ISBN 978-82-326-3782-9 (printed ver.)
ISBN 978-82-326-3785-0 (electronic ver.)
ISSN 1503-8181

Emre Kantar

Doctoral thesis

Doctoral theses at NTNU, 2019:93

Emre Kantar

Longitudinal AC Electrical Breakdown Strength of Polymer Interfaces

Experimental and theoretical examination of solid-solid interfaces considering elasticity, surface roughness, and contact pressure

NTNU
Norwegian University of Science and Technology

Thesis for the Degree of Philosophiae Doctor
Faculty of Information Technology and Electrical Engineering
Department of Electric Power Engineering

Doctoral theses at NTNU, 2019:93

NTNU
Norwegian University of Science and Technology

NTNU

Emre Kantar

Longitudinal AC Electrical Breakdown Strength of Polymer Interfaces

Experimental and theoretical examination of solid-solid interfaces considering elasticity, surface roughness, and contact pressure

Thesis for the Degree of Philosophiae Doctor

Trondheim, June 2019

Norwegian University of Science and Technology
Faculty of Information Technology and Electrical Engineering
Department of Electric Power Engineering

NTNU
Norwegian University of
Science and Technology

NTNU
Norwegian University of Science and Technology

Thesis for the Degree of Philosophiae Doctor

Faculty of Information Technology and Electrical Engineering
Department of Electric Power Engineering

ISBN 978-82-326-3782-9 (printed ver.)
ISBN 978-82-326-3785-0 (electronic ver.)
ISSN 1503-8181

Doctoral theses at NTNU, 2019:93

Printed by NTNU Grafisk senter

To those who inspired it
and will not read it...

Preface

This thesis is submitted in partial fulfillment of the requirements for the degree of Philosophiae Doctor (PhD) at the Norwegian University of Science and Technology (NTNU) in Trondheim, Norway. The PhD work has been carried out at the Department of Electric Power Engineering, between August 2014 and July 2018. It has been supervised by the main advisor Prof. Erling Ildstad, the first co-advisor Assoc. Prof. Frank Mauseth from the Department of Electrical Power Engineering, NTNU, and the second co-advisor, Dr. Sverre Hvidsten from SINTEF Energy Research in Trondheim, Norway.

The PhD work was part of a large KPN[1]project administrated by SINTEF Energy Research with the title "High Voltage Subsea Connections (SUBCONN)."

The PhD work was conducted within the work package of "electric breakdown of interfaces." The project was funded and supported by The Research Council of Norway (Project No. 228344), and by the SUBCONN Project Consortium amongst SINTEF Energy Research and the following industrial partners: ABB AS, Aker Solutions AS, Chevron Norge AS, Det Norske Oljeselskap ASA, Deutsch Offshore, Nexans Norway AS, Shell Technology Norway AS, and Equinor ASA (formerly [Statoil Petroleum AS]).

[1]KPN: Knowledge-building projects for industry.

Acknowledgments

"*Everything should be made as simple as possible, but not simpler.*"
Albert Einstein

First and foremost, I wish to thank the Department of Electrical Power Engineering, Faculty of Information Technology and Electrical Engineering and Norwegian University of Technology for having given me the opportunity to attain this degree. Also, I wish to thank Norwegian Research Council, SINTEF Energy Research and the SUBCONN Project Consortium for their support.

I would like to thank my main supervisor, Prof. Erling Ildstad for giving me the opportunity to accomplish this research, and for all his guidance and critiques throughout my PhD.

I express my deepest gratitude to my co-supervisor, colleague and friend Assoc. Prof. Dr. Frank Mauseth for having been so friendly and hospitable to me from day one. He not only helped me in technical aspects during the PhD but also encouraged me to start skiing and even taught me to get the hang of it with patience. Luckily, I have been a quick learner and did not cost him a vast stiff back when he was trying to help me stand up with my skis. We also enjoyed several biking trips together except for the very first one. All in all, I feel indebted to you and express a huge thank you once again!

I own my other co-supervisor from SINTEF Energy Research, Dr. Sverre Hvidsten, many thanks for his invaluable advice and insightful discussions during these four years. His ideas and suggestions are greatly appreciated in making this work an original one.

I would like to express my deepest gratitude to my best friend and my beloved wife Cansu for her unconditional, endless love, support, and encouragement in all aspects of my life. In August 2014, we opened a new chapter together in our lives and made Norway our new home. Her warm embrace has been the safest harbor that tranquilized me at the end of every day and made me appreciate every moment I spent by her side.

I am very thankful to my parents for their material and spiritual support in my life. With hindsight, I now see it more clearly that their sacrifice to enable me to

receive the best education possible and anything I need has made me the person I am today. I owe all my success to their unconditional love and constant support. *Anneme ve babama, hayatımdaki maddi ve manevi desteklerinden dolayı en derin şükranlarımı sunarım. Tecrübelerime dayanarak, şimdi daha net görüyorum ki, mümkün olan en iyi eğitimi almamı ve ihtiyaç duyduğum her şeye kavuşmamı sağlayan fedakarlıkları beni bugün olduğum insan yaptı. Tüm başarımı koşulsuz sevgilerine ve daimî desteklerine borçluyum.*

My special thanks go to my colleagues and friends at the Department of Electric Power Engineering at NTNU who have been of great support and have made this mostly lonely journey a bearable one. I am also grateful to the administrative and technical staff at the department, NTNU Service Lab and Workshop who were always ready to help.

I feel lucky to have had the Head of the Office, Bodil Wold, not only as a co-worker but also as a friend. Her arrival brought a breath of fresh air to the workplace that led to many positive changes. She is an asset to the department, and I am glad that my new office is very close to the cookie box which is replenished every morning by her tirelessly.

I was employed at SINTEF Energy Research, Department of Electric Power Technology in November 2018. I would like extend my gratitude to Sverre Hvidsten, Hans Lavoll Halvorson, Dag Eirik Nordgård, and Nora Gullbekkhei for having given me the chance to be part of one of the best research institutes in Europe. I also would like to thank my colleagues at SINTEF Energy Research for their understanding and support during the finishing phase of my thesis. I extend my special thanks to Torbjørn Andersen Ve and Cedric Lesaint for being not only colleagues but also friends outside of work.

Beyond all doubt, I feel incredibly grateful and indebted to Norway and its good people for the fantastic five years I have had so far.

Last but not least, I feel fortunate to have the coolest Turkish friends in town. We have been a family to one another, and their friendship not only made me feel home in Norway but also led to many hangovers and crazy videos. You are too many to be named one by one. Thank you for making these years unforgettable.

Emre Kantar
Trondheim, Norway
March 2019

Abstract

All electrical insulation systems consist of a combination of different insulating and conductive materials. The alternating current (AC) breakdown strength (BDS) of insulation systems is limited by the lowest BDS of either the insulating bulk materials or the interface between adjacent insulating materials. The interfacial breakdown between two solid dielectric surfaces has been reported to represent one of the principal causes of failure for insulation systems; thus, a better understanding of the mechanisms governing the solid-solid interface breakdown is vital. Therefore, the main objectives of this work are to examine the practical limitations regarding electrical breakdown strength of interfaces between solid-solid insulating components and to address the main mechanisms leading to a solid-solid interface breakdown. Individual effects of the contact pressure, surface roughness, elastic modulus of the polymers, and insulating dielectric medium surrounding the interfaces (i.e., air, water, or oil) on the longitudinal/tangential AC breakdown strength of solid-solid interfaces are studied, both theoretically and experimentally.

When two nominally flat solid materials are brought into a contact, an interfacial contact occurs at discrete spots, resulting in numerous microcavities between adjacent contacting areas at the interface due to imperfect, non-ideal surfaces. An interface thus consists of cavities and contact spots connected to each other. A hypothesis is proposed considering the imperfect surface texture of solid-solid interfaces: the breakdown strength of a solid-solid interface can be represented by the breakdown strength of strings of cavities and contact spots formed at the interface between the electrodes. In other words, size, shape and surrounding medium inside the cavities are assumed to determine the dielectric strength of the cavities whereas the insulating properties of the contact spots presumably also have a significant impact on the interfacial breakdown strength. To fulfill the objectives of the thesis presented above, the hypothesis was tested using experimental and theoretical studies conducted during the PhD period. To structure and represent the hypothesis analytically, an *interface breakdown model* was developed that focuses on the discharge of cavities and breakdown of contact areas, separately.

Two different theoretical approaches for modeling contact surfaces at solid-solid interfaces were used: a statistical and a deterministic/numerical interface contact models, that were developed based on *tribology* of polymeric materials. The statistical model was primarily used to develop the interface breakdown model. The main

purpose of developing the deterministic model was, on the other hand, to support the outputs of the interface breakdown model by simulating the deformation of the surface asperities in 2D and 3D as a function of the contact pressure, surface roughness, elasticity, and hardness of the solid material. Simulation results on the interfacial deformation cast light on how cavities are connected in 3D and elucidate the resulting gas pressure inside the cavities, which could not be estimated using the 2D statistical interface contact model solely.

Experimental studies on the solid-solid interfaces consisted of three different types of testing: AC breakdown strength testing, AC partial discharge inception field testing, and interface discharge-monitoring testing under AC excitation. In the experiments, two rectangular prism-shaped samples were placed vertically between two Rogowski-shaped electrodes. In the AC breakdown experiments and partial discharge (PD) inception field measurements, four different interfaces formed between identical polymers were used. The selected polymers were silicone rubber (SiR), cross-linked polyethylene (XLPE), filled epoxy resin (EPOXY), and polyether ether ketone (PEEK) that have different elasticity and electrical insulation properties. In addition, the surface roughness was varied by sanding the surfaces using four different sandpapers of different roughnesses with grit numbers: #180, #500, #1000, and #2400 from roughest to the smoothest in a sequence. In the discharge-monitoring experiments, in contrast to the AC breakdown and PD experiments, a very smooth glass sample in the same size of the polymer sample at the bottom was utilized as a transparent solid material to enable the camera to monitor light originating from the discharges at the glass-polymer interface.

The results of the experimental and theoretical studies have indicated that different mechanisms are involved in the breakdown of solid-solid interfaces. The main hypothesis has been verified through the results of the experimental and theoretical studies. The main findings are briefly summarized below.

The interfacial breakdown in the cases of materials with low elastic moduli (softer materials) such as SiR and XLPE has been found to be strongly dominated by the discharged cavities due to their low estimated interface tracking resistances. (The estimated interface tracking resistance is linearly correlated with the fourth root of elastic modulus). In other words, discharged cavities have led to an interfacial failure more easily because the contact spots could not withstand the enhanced fields. Besides, varied surface roughness in the case of XLPE–XLPE interfaces has yielded parallel results such that the clear correlation between the cavity discharge and the interface breakdown have been maintained irrespective of the surface roughness. On the other hand, in the cases of materials with higher elastic modulus such as EPOXY and PEEK, the endurance of the contact spots against the local enhanced fields has been observed to be higher due to the increased estimated micro-tracking resistance. To summarize, the results have suggested that the influence of the contact spots on the interface breakdown becomes more prominent at higher contact pressures, higher elastic modulus (harder materials), or smoother surfaces.

Contents

List of Abbreviations, Glossary and Nomenclature

Abbreviations

2D	Two-dimensional
3D	Three-dimensional
AC	Alternating current
AFM	Atomic force microscopy
BD	Breakdown
BDS	Breakdown strength
CCD	Charge-coupled device
CI	Confidence interval
DC	Direct current
EHV	Extra high voltage
EPDM	Ethylene propylene diene monomer
EPOXY	Cured end product of epoxy resins
EPR	Ethylene propylene rubber
FDM	Finite difference method
FEA	Finite element analysis
FEM	Finite element method
GUI	Graphical user interface
HV	High voltage
LDPE	Low-density polyethylene
MV	Medium voltage
NB	Nota bene
NOP	Non-contact optical profiler
PD	Partial discharge
PDF	Probability density function
PDIE	Partial discharge inception field strength
$PDIE^{e}$	Estimated partial discharge inception field strength
$PDIE^{m}$	Measured partial discharge inception field strength

PDIV	Partial discharge inception voltage
PEEK	Polyether ether ketone
PRPDA	Phase-resolved partial discharge analysis
PSA	Pulse-sequence analysis
PTFE	Polytetrafluoroethylene
PU	Per unit
RMS	Root mean square
SEM	Scanning electron microscope
SiR	Silicone rubber
SP	Stylus profiler
TO	Test object
XLPE	Cross-linked polyethylene

Glossary

#180	Interface/Sample surface sanded using #180 grit sandpaper
#500	Interface/Sample surface sanded using #500 grit sandpaper
#1000	Interface/Sample surface sanded using #1000 grit sandpaper
#2400	Interface/Sample surface sanded using #2400 grit sandpaper
A_a	Apparent/Nominal contact area
a_c	Radius of a circular contact area
A_{cav}	Total area of cavities
A_{cav_j}	Area of the j^{th} cavity
$\overline{A}_{cav}$	Average area of a cavity
A_{cnt_j}	Area of the j^{th} contact spot
A_i	Elastic contact area of an individual contact spot
A_{re}	Total real (elastic) contact area in the statistical model
$A_{re,d}$	Total real contact area in the deterministic model
AY	Average of AY^i of the motifs
AY^i	Horizontal distance between the peaks of the i^{th} motif
C_k	Coupling capacitor
D	Dimensionless separation
d	Nominal distance between the reference planes of two rough surfaces
d_{avg}	Average length of cavities in 2D
$d_{avg_{ref}}$	Initial average cavity size in the longitudinal direction
d_{int}	Nominal thickness of the interface
E	Elastic modulus
E'	Composite/Effective elastic modulus of two contacting surfaces
E_{app}	Applied electric field
E_{cav}	Discharge inception field strength of a cavity
E_{cnt}	Field strength at contact spots
E_{tr}	Estimated interfacial tracking resistance
F_m	Parabolic cylinder function
G	Material toughness

H	Material hardness
H^i	Height difference between the left peak and the deepest valley in a motif
H^{i+1}	Height difference between the right peak and the deepest valley in a motif
h_g	Gap between undeformed surfaces of a measured profile and a rigid plane
H_s	Hardness of the softer material
h_z	Length of a microcavity in the normal field direction
K	Integral kernel
l	Thickness of the bulk of the insulation between the electrodes
l_{avg}	Average length of contact spots in 2D
l_{eff}	Total/effective length of the contact spots
l_s	Sampling length of a 2D profile
N	Number of asperities
n	Number of cavity and contact spot pairs
$\overline{n}$	Number of average-sized cavity and contact spot pairs in a row vector
N_{cnt}	Number of discretized elements having a pressure value higher than zero
N_d	Number of discrete elements
n_i	Number of discrete data points in a row vector of the surface data matrix
n_j	Number of discrete data points in a column vector of the surface data matrix
n_{PD}	Number of partial discharges
x_{ref}	Nominal longitudinal distance
$\mathbb{P}$	Primary surface profile
p_0	Atmospheric pressure
p_a	Apparent contact pressure
p_c	Pressure inside the cavity
p_r	Mean real contact pressure
p_{ref}	Initial applied pressure
$p^*(s)$	Standardized peak-height probability density function
$P(x)$	Probability function where x is the variable
$p(z)$	Peak-height probability density function
q_a	Apparent charge magnitude
$\mathbb{R}$	Roughness profile
r	Radius of the main tubular branch of the interface tracking path
R_a	Arithmetic mean of the absolute ordinate values
r_n	Radius of the needle tip
s	Standardized/Normalized height of asperities in a profile
S_a	Arithmetic mean height (S-amplitude parameters)
S_q	Root mean square height (S-amplitude parameters)
S_p	Maximum peak height (S-amplitude parameters)
S_v	Minimum dip/pit height (S-amplitude parameters)
S_z	Maximum height of the surface (S-amplitude parameters)
SAY	Root mean square of AY^i of the motifs
SAY_{eq}	Root mean square of AY^i of the motifs in the sum surface
SW	Root mean square of height values W^i of the waviness motifs

SW_{eq}	Root mean square of height values W^i of the waviness motifs in the sum surface
V_{app}	Applied voltage
V_{cav_j}	Voltage drop across j^{th} cavity
V_{cav}	Discharge inception voltage of a cavity
V_{cnt_j}	Voltage drop across j^{th} contact spot located between two cavities
$\mathbb{W}$	Waviness profile
W	Root mean square of height values W^i of the waviness motifs
W_{eq}	Root mean square of height values W^i of the waviness motifs in the sum surface
W_m	Total load
$W_{m\,i}$	Load on an individual contact spot
Y	Average of the height values Y^i of the motifs
Y^i	is the mean height (of H^i and H^{i+1}) of the i^{th} motif
AY_{eq}	Average of AY^i of the motifs in the sum surface
Y_{eq}	Average of the height motifs in the sum surface
z	Height of asperities in a profile

Nomenclature

$\mathscr{A}$	Sampling area of a 2D surface profile
β_m	Asperity radius
$\mathscr{D}$	Density of asperities on a profile
δ	Total peak displacement
δ_e	Amount of elastic deformation
δ_p	Amount of plastic deformation
$\digamma$	Integral of contact energy function
ε_0	Permittivity of vacuum
ε_r	Permittivity of dielectric material/medium
η	Surface density of asperities
γ	Shape factor for cavity geometry
λ	Rate parameter of the exponential distribution
λ_c	Long wave cut-off wavelength for roughness profile
λ_f	Long wave cut-off wavelength for waviness profile
λ_s	Short wave cut-off noise filter
μ	Mean or expectation of the Gaussian distribution
Ω	Arbitrary area in the integration domain for 2D / 3D contact
ϕ	Voltage phase
σ	Standard deviation of the random variable
σ^2	Variance of the random variable
σ_p	Standard deviation of asperity radius

Chapter 1

Introduction

Power cable connectors are vital components of oil and gas installations and future ocean renewable energy systems because they allow quick, reliable and in situ connection of offshore modules to main components while providing versatility and modularity of expensive equipment and cables [1–14].

Subsea cable connectors are a pertinent example of modern, sophisticated connector solutions available for cable connectors. They are categorized as wet-mate connectors, dry-mate connectors, and penetrators [4]. Recent and future subsea extensions stipulate significant and cost-effective developments in wet-mate connector technologies, which should be able to provide higher power ratings and operate at higher voltages, higher temperatures, deeper waters, and longer tiebacks [1–3]. Moreover, weight and size restrictions, limitations arising due to the presence of solid-solid and solid-liquid interfaces between dielectric materials in the connectors, and environmental difficulties challenge the design and implementation of new solutions. To date, wet-mate cable connectors up to 36 kV are commercially available, but connectors up to 150 kV should be available within the next decade to fulfill the driving force to provide higher power at elevated voltage ratings with reduced losses [1, 2]. The connectors used in subsea applications are usually oil-filled and contain solid-solid and solid-liquid interfaces. They may potentially be placed at depths down to 3000 meters, which poses a significant challenge as water penetration or diffusion into a liquid dielectric reduces the performance of the insulation [1, 4]. Consequently, cable connectors and accessories constitute critical components in the power supply system since the majority of direct failures are related to those components [5, 6]. To tackle these failures and to fulfill the growing demands of industry for higher power at elevated voltage ratings, weak parts of the connections must be thoroughly examined.

1.1 Background

All electrical insulation systems consist of a combination of different insulating and conductive materials. The series connection of two or more dielectric materials constitutes the electrical insulation system in most high-voltage (HV) equipment and accessories. The alternating current (AC) breakdown strength (BDS) of insulation systems is limited by the lowest BDS of either the bulk insulating materials or the interface between adjacent insulating materials [15].

When two nominally flat, rough, solid surfaces are brought into contact, contacts occur at discrete spots, leading to numerous defects such as cavities between adjacent contacting areas at the interface [16].

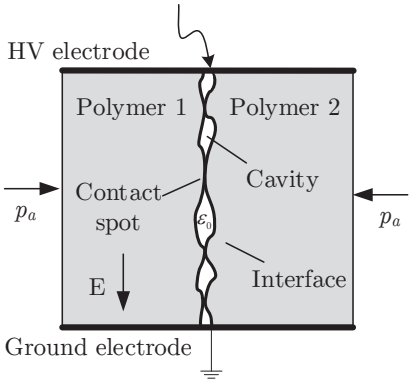

Figure 1.1: Illustration of a solid-solid interface, consisting of cavities and contact spots. The electric field is applied tangentially, and p_a stands for the contact pressure.

An interface thus consists of microcavities and contact spots connected to each other, as illustrated in Figure 1.1. Imperfections at interfaces such as cavities, protrusions, and contaminants reduce the longitudinal AC electric breakdown strength of the interface since they cause local electric field enhancements [5–10, 17–19].

Elasticity and surface roughness of the solid materials and applied contact pressure (interfacial pressure) significantly affect the shape, size, and number of cavities and contact spots [6, 8–13, 20–22]. Cavities are likely to cause partial discharges (PD) and trigger interfacial tracking that can eventually lead to premature electrical breakdown (BD) failures [5, 6, 23–35]. In addition, the medium inside the cavities influences the PD inception field strength (PDIE) of interfaces [5, 6, 10]. Once the cavities are filled with air, the dielectric strength of the cavities is lower than that of the surrounding bulk insulation [5–10]. In the presence of electrical stress applied longitudinally to the interface, PD initiation is very likely to occur inside these cavities. Therefore, the longitudinal/tangential BDS of the interface is lower than that of the bulk insulation enclosing these cavities.

1.2 Motivation

Cable accessories such as power cable joints, outdoor composite terminations, and subsea connectors incorporate solid-solid interfaces, which undergo locally enhanced electrical stresses during service life. It is thus of paramount importance to achieve a high interfacial BDS. By studying and identifying the parameters affecting the BDS of such interfaces, cost-effective, long-lasting, and most importantly,

reliable HV equipment can be developed. With this motivation, polymers have been extensively studied in the literature as insulating materials in HV equipment. However, current designs for practical applications are based solely on know-how and type testing. The majority of experimental results and research are, however, limited to studies on complete designs of connectors or joints without dissecting the solid-solid interfaces separately [11]. Nevertheless, the polymer interfaces should be scrutinized separately and diligently by considering the roughness of contact surfaces, dielectric medium surrounding the interfaces, elasticity modulus and contact pressure. In this respect, comprehensive theoretical/analytical models incorporating these parameters should be developed in addition to extensive experimental studies because the understanding of the mechanisms dominating the solid-solid interface breakdown phenomenon paves the way for the successful design of advanced, reliable apparatus.

1.3 Objectives

In a broad sense, the main objective of this study is to come up with more tangible design criteria for HV apparatus in which solid-solid interfaces are present. The findings of this work are intended to serve as a guide for the development of more reliable HV equipment with higher breakdown strength and longer service life.

In particular, the primary objectives are to examine the practical limitations regarding the electrical breakdown strength of interfaces between solid-solid insulating components and to address the main mechanisms leading to a solid-solid interface breakdown. For these purposes, individual effects of the contact pressure, surface roughness, elastic modulus of the polymers, and insulating dielectric media surrounding the interfaces (i.e., air, water, and oil) on the longitudinal AC breakdown strength of solid-solid interfaces are to be studied, both theoretically and experimentally.

1.4 Main Hypothesis and Research Questions

As a starting point, a premise is made on the basis of limited evidence/knowledge in the literature on the interfacial breakdown phenomenon. The following hypothesis is proposed as the starting point for further investigation:

- The breakdown strength of a solid-solid interface can be represented by the dielectric strength of strings of cavities and contact spots between the electrodes, as illustrated in Figure 1.1. In particular, size, shape and insulating medium inside the cavities are postulated to strongly affect the dielectric strength of the cavities whereas the insulating properties of the contact spots presumably also have a significant impact on the interfacial breakdown strength.

In order to fulfill the objectives stated above, the hypothesis will be tested using the results of the experimental and theoretical studies conducted during the PhD period. As the hypothesis incorporates different breakdown mechanisms (discharge of cavities and breakdown of contacting areas), several research questions are formulated to dissect the hypothesis in submodules. The findings for the following questions are addressed in the discussion and conclusion:

Q-i. How do the elasticity, contact pressure, and surface roughness influence the sizes of the cavities and contact spots? How can the deformation of the cavities and contact spots be modeled/simulated in two-dimensional (2D) or three-dimensional (3D) space as a function of the contact pressure, surface roughness, and elasticity of the insulation material?

Q-ii. In turn, what would be the impact of physical changes in the structure of interfacial cavities and contact spots (as a function of elasticity, contact pressure, and surface roughness) on the longitudinal AC breakdown strength? This question is split into four subsections to investigate the impacts of the breakdown mechanisms in minute detail:

- main the mechanisms controlling the interfacial breakdown in dry-mate conditions: Effect of discharged cavities and contact spots on the interfacial breakdown strength;
- initiation, development, and propagation of discharge streamers at the interface in dry-mate conditions;
- expected gas pressure inside the cavities at solid-solid interfaces in dry-mate conditions; and
- impacts of ingress of water or oil into the cavities on the longitudinal AC breakdown of solid-solid interfaces.

1.5 Scope

To structure and represent the hypothesis analytically, an *interface breakdown model* is developed that focuses on the discharge of cavities and breakdown of contact areas, separately.

Two different theoretical models for contact surfaces at solid-solid interfaces are used: a statistical and a deterministic/numerical model, that are developed based on *tribology* of polymeric materials. The statistical model is the backbone of the theoretical work and is primarily used to develop the interface breakdown model.[2] The primary purpose of developing the deterministic model is, on the other

[2]The interface breakdown model incorporates two submodels for cavity discharge and breakdown of the contacting surface area (see Figure 1.1). The statistical model is used to develop the submodel for the cavity discharge whereas another empirical model, based on the interfacial tracking resistance of the solid materials, is utilized to develop the submodel for the breakdown of contacting spots.

hand, to support the outputs of the interface breakdown model by simulating the deformation of the surface asperities in 2D and 3D as a function of the contact pressure, surface roughness, elasticity, and hardness of the solid material.

The interfacial breakdown strength between solid-solid interfaces is experimentally studied by incorporating four different polymers (which are widely used in practical applications) with different surface roughnesses at various contact pressures. Experiments carried out on the solid-solid interfaces consist of three different types of testing: AC breakdown testing, AC partial discharge inception field testing, and interface discharge-monitoring testing under AC excitation. AC breakdown experiments incorporate dry-, wet-, and oil-mate interfaces whereas PD and discharge-monitoring experiments are carried out only for dry-mate interfaces. Last, field element method (FEM) is also used to simulate electric field distribution at dry-, wet-, and oil-mate interfaces studied in real experiments by defining air, water and oil as the dielectric media filling the cavities, respectively.

1.6 Contributions

The list of the articles generated during the PhD period is provided at the end of this chapter. The publications that form the foundation of the thesis (i.e., Papers I–V) are appended to Appendix G. The author wrote all the articles listed. He planned and performed the experimental and theoretical work and produced the results presented in these papers while each co-author contributed to the discussion of the results.

Contributions from the selected articles and novel findings presented for the first time in this thesis are summarized below.

Effect of Contact Pressure, Elastic Modulus and Surrounding Dielectric Medium on the AC BDS of Interfaces [Papers I and II]

Papers I and II offer a thorough experimental methodology that ensures generating reproducible trends given the stochastic nature of breakdown experiments. Secondly, in contrast to the methodology adopted in these papers, the effects of water- or oil-filled cavities on the interface BDS have not been studied in the literature by isolating (i.e., only focusing on) the solid-solid interfaces. Instead, the complete set of cable accessories have been tested against water or oil ingress that yielded only assumptions regarding the performance of the solid-solid interfaces. Lastly, field simulations for air-, water-, and oil-filled cavities performed in Paper II provide original results such that the data of real, rough surface texture of the samples used in the study were exported to field element analysis (FEA) software to investigate the field intensification/distribution likely to take place at the interfaces in the performed experiments. Nonetheless, in the literature, field enhancements only in perfect cylindrical, ellipsoidal or spherical, air-filled voids were examined.[3]

[3]Cavity and void are used interchangeably in this thesis.

The experimental and simulation results indicated that air-filled cavities or water penetration at the interface are the main limiting factors in the overall BDS of solid-solid interfaces. The addition of insulating liquids such as oil prior to assembly, on the other hand, has shown promise in ensuring a high breakdown strength and long service life for practical applications.

Effect of Surface Roughness and Contact Pressure on the AC BDS of Interfaces [Paper III]

The primary contribution of this paper is the clear correlation presented between the surface roughness and AC breakdown strength of dry-mate XLPE–XLPE interfaces. The breakdown strength of the interfaces was recorded to be the highest when the contact pressure was relatively high, and the contact surface was the smoothest (among the chosen variables). Moreover, the use of a non-contact profilometer that can precisely calculate 3D surface height parameters to quantitatively determine the surface roughness was a unique approach. This uniqueness stems from the fact that relevant studies in the literature—where the effect of surface roughness on the interfacial breakdown strength was investigated—employed stylus profilometers that can only scan a limited surface area in 2D. Thus, the data of the 3D surface profiles are believed to be more reliable when correlating the surface roughness with the results of the AC breakdown experiments.

Effect of Elasticity, Surface Roughness and Contact Pressure on the Sizes of Cavities and Contact Areas [Paper IV]

In this paper, tribological principles were used to develop a statistical approach that models the contact surface between two rough, solid materials. To the best of author's knowledge, the proposed roughness model is one of the first models blending tribology and high voltage engineering in the literature. In the model, the motif approach was utilized to characterize rough surfaces quantitatively because the contact model requires these statistical parameters to estimate the ratio of the real area of contact to the nominal rough surface area. The use of motif parameters to map polymeric surfaces is also considered to be a novel approach. It was observed in the motif roughness profiles that the rougher the surface, the higher the peaks and the deeper the dips.

N.B.: In this paper, the results of the AC breakdown experiments, presented in Paper III, are correlated with the estimated results that are calculated using the cavity discharge submodel presented in Section 4.1.1. However, the proposed theoretical model in Section 4.1 was not in its current form at the time of the publication, thus only the effect of the cavity discharge on the interface BDS was studied. Therefore, the complete model in the thesis should be considered.

Effect of Contact Pressure and Elastic Modulus on the AC BDS of Interfaces [Paper V]

In the course of the PhD study, following an extensive literature review, a lack of a thorough investigation on the impact of the material elasticity on longitudinal AC breakdown strength of interfaces between polymers has been detected. No publications were found that directly focused on the impact of the elastic modulus on the interfacial breakdown strength. Thus, the experimental results on the correlation between the elasticity and AC breakdown strength are considered as contributing to the originality of this work. The interfacial breakdown strengths of solid-solid interfaces were studied by incorporating four different polymers which are widely used in practical applications. Secondly, in the wake of the finalization of Paper IV, which covers the correlation between the discharge of average-sized cavities and interface breakdown at solid-solid interfaces, the contact model was extended/improved to not only incorporate the mechanisms controlling the cavity discharge but also those governing the breakdown of contact spots. The newly introduced submodel for the breakdown of contact spots utilizes the interfacial tracking resistance of the materials and estimates the non-homogeneous field strength at the edges of discharged cavities. Using the upgraded interface breakdown model for the electrical breakdown of solid-solid interfaces, we postulated a hypothesis on the effective mechanisms in the interfacial breakdown, and its validity was tested by utilizing the results of the AC breakdown experiments covered in the paper. The results indicated that discharged cavities influence the interfacial BDS while the impact of the interfacial tracking resistance of contact spots (the bulk of the insulation) was found to be significant.

Correlation between PD Inception and Breakdown Strength at Interfaces, Monitoring of Interfacial Discharges, 3D Simulations of Rough Surface Textures [Thesis]

A laboratory test setup was developed to monitor the discharge activity at solid-solid interfaces, that incorporates a charge-coupled device (CCD) camera, an HV source, and PD detection equipment. Captured discharge images elucidated where and how PD is initiated at the interface, how discharged cavities develop to larger channels, and eventually how discharge channels lead to a complete flashover depending on the interfacial tracking resistance of the materials. The discharge images together with the simultaneously obtained PD data complement the results from the proposed theoretical interface breakdown model, AC breakdown experiments and PD experiments performed using polymer-polymer interfaces.

The numerical contact surface model, namely, the deterministic interface contact model was employed. The primary purpose of using the deterministic model was to verify the trends observed in the results of the statistical interface contact model. In addition, the deterministic model enabled us to simulate the effects of elasticity, surface roughness and contact pressure on the size of cavities and con-

tact area at the interface. The deterministic model introduced in [36] is built on the tribological friction model proposed in [37]. However, the use of the proposed model in a MATLAB® script in [36] is limited because it can only work with 2D surface profiles. In this work, the MATLAB® script developed for simulating the contact asperities has been upgraded to span surfaces in 3D as well by extending the mathematical expressions/formulae used to develop the 2D model introduced in [37]. To the best of the author's knowledge, the 3D simulation results of the surface cavities varying as a function of elasticity, hardness, surface roughness, and contact pressure are unique.

These results are presented in this thesis for the first time; however, they are to form the basis for the Papers VI, VII, and VIII listed in Section 1.8.

1.7 Thesis Outline

This thesis is based on the work presented in the selected publications and on the results of continued experimental and theoretical work that have not been published elsewhere but in the thesis. For the sake of self-completeness and in order for the thesis to be a standalone document, details are included in the appendices. In addition, the parts that could not be elaborated upon in the articles due to limited space, especially the experimental methodology, are provided extensively in order to ensure reproducibility of the results.

The main outline of the thesis is summarized in Table 1.1. Brief information on the scope and objective is provided at the beginning of each chapter.

Table 1.1: The structure of the thesis shown chapter by chapter.

Content	Chapter
Introduction, scope, objectives	1
Background and literature survey	2
Theory and modeling	3, 4, 5
Experimental methodology	6
Experimental results	7, 8, 9, 10
Results of theoretical models	11
Discussion	12
Conclusion and future work	13
Appendices*	A, B, C, D, E, F
Selected publications	G

* Appendices A–F present more detailed analyses containing raw/additional experimental results, results from electric field simulations run in an FEA software, results from the deterministic contact model, experimental methodology and test setups, respectively.

Only the major results from the appended articles are used in the main body of the thesis while the results shown for the first time in this thesis are reported in detail. However, the inclusion of the new unpublished results increased the volume significantly. Consequently, this thesis has a format closer to that of a monograph although the parts already covered in the selected articles have a style similar to the format of a compendium of several academic papers.

1.8 List of Publications

A significant number of the PhD research outputs have been published in the top-tier, international journal transactions and conference proceedings listed below:

I. **E. Kantar**, D. Panagiotopoulos, and E. Ildstad, "Factors Influencing the Tangential AC Breakdown Strength of Solid–Solid Interfaces,"*IEEE Transactions on Dielectrics and Electrical Insulation*, vol. 23, no. 3, pp. 1778–1788, June 2016.

II. **E. Kantar**, F. Mauseth, and E. Ildstad, "Effect of Pressure and Elastic Modulus on Tangential Breakdown Strength of Solid–Solid Interfaces," *IEEE Electrical Insulation Conference (EIC)*, Montreal, QC, 2016, pp. 431–435.

III. **E. Kantar**, F. Mauseth, E. Ildstad, and S. Hvidsten, "Longitudinal AC Breakdown Voltage of XLPE–XLPE Interfaces Considering Surface Roughness and Pressure," *IEEE Transactions on Dielectrics and Electrical Insulation*, vol. 24, no. 5, pp. 3047–3054, Oct. 2017.

IV. **E. Kantar**, S. Hvidsten, F. Mauseth, and E. Ildstad, "A Stochastic Model for Contact Surfaces at Polymer Interfaces Subjected to an Electrical Field," *Tribology International*, vol. 127, pp. 361–371, Nov. 2018.

V. **E. Kantar**, S. Hvidsten, and, E. Ildstad, "Effect of Material Elasticity on the Longitudinal AC Breakdown Strength of Solid-Solid Interfaces," *IEEE Transactions on Dielectrics and Electrical Insulation*, vol. 26, no. 2, pp. 655–663, Apr. 2019.

VI. **E. Kantar** and S. Hvidsten, "Initiation and Propagation of Discharge Streamers at Solid-Solid Interfaces," *IEEE Transactions on Dielectrics and Electrical Insulation*, manuscript submitted for publication.

VII. **E. Kantar** and S. Hvidsten, "A Deterministic Surface Contact Model for Contact Surfaces at Polymer Interfaces Subjected to an Electrical Field," *IEEE Transactions on Dielectrics and Electrical Insulation*, manuscript in preparation.

VIII. **E. Kantar** and S. Hvidsten, "Discharge Mechanisms Monitored at Solid-Solid Interfaces using a CCD-Camera," *IEEE Conference on Electrical Insulation and Dielectric Phenomenon (CEIDP)*, Richland, WA, 2019, abstract submitted, manuscript in preparation.

IX. **E. Kantar**, D. Panagiotopoulos, and E. Ildstad, "Impact of Contact Pressure on Breakdown Strength of Solid–Solid Interfaces," *Proceedings of the Nordic Insulation Symposium*, no. 24, 2015.

X. **E. Kantar** and E. Ildstad, "Modeling Longitudinal Breakdown Strength of Solid–Solid Interfaces Using Contact Theory," *IEEE International Conference on Dielectrics (ICD)*, Montpellier, 2016, pp. 398–401.

XI. **E. Kantar**, S. Hvidsten, and E. Ildstad, "Examination of Longitudinal AC Breakdown Strength of Dielectric Surfaces as a Function of Elastic Modulus," *Proceedings of the Nordic Insulation Symposium*, no. 25, 2017.

XII. **E. Kantar**, S. Hvidsten, F. Mauseth, E. Ildstad, "Tangential AC Breakdown Strength of Solid-Solid Interfaces Considering Surface Roughness," *IEEE Conference on Electrical Insulation and Dielectric Phenomenon (CEIDP)*, Fort Worth, TX, 2017, pp. 580–583.

XIII. **E. Kantar**, S. Hvidsten, F. Mauseth, E. Ildstad, "Interfacial Breakdown between Dielectric Surfaces Determined by Gas Discharge," *IEEE Conference on Electrical Insulation and Dielectric Phenomenon (CEIDP)*, Fort Worth, TX, 2017, pp. 556–559.

XIV. **E. Kantar**, S. Hvidsten, F. Mauseth, E. Ildstad, "On the Tangential AC Breakdown Strength of Polymer Interfaces Considering Elastic Modulus," *IEEE Conference on Electrical Insulation and Dielectric Phenomenon (CEIDP)*, Fort Worth, TX, 2017, pp. 816–819.

The publications published during the PhD period, but not incorporated in this thesis are:

XV. **E. Kantar** and A. M. Hava, "Optimal Design of Grid-Connected Voltage Source Converters Considering Cost and Operating Factors," *IEEE Transactions on Industrial Electronics*, vol. 63, no. 9, pp. 5336–5347, Sept. 2016.

XVI. **E. Kantar** and A. M. Hava, "*LCL*–filter Design for Low-Voltage High-Power Grid-Tied Voltage-Source Converter Considering Various Damping Methods," *IEEE 17th Workshop on Control and Modeling for Power Electronics (COMPEL)*, Trondheim, 2016, pp. 1–8.

Chapter 2

Literature Survey on Longitudinal Breakdown of Polymer Interfaces

In this chapter, first, a brief introduction to state-of-the-art subsea connectors and cable apparatus that contain interfaces is provided. Particular attention is paid to the solid-solid interfaces, considering the causes of interfacial failure and important factors that influence the dielectric strength of an interface. Second, publications relevant to the scope of the PhD work found in the literature are summarized into two main categories: empirical studies on solid-solid interfaces and theoretical studies on modeling the rough contact surfaces at solid-solid interfaces. The scope of the literature survey is illustrated in Figure 2.1.

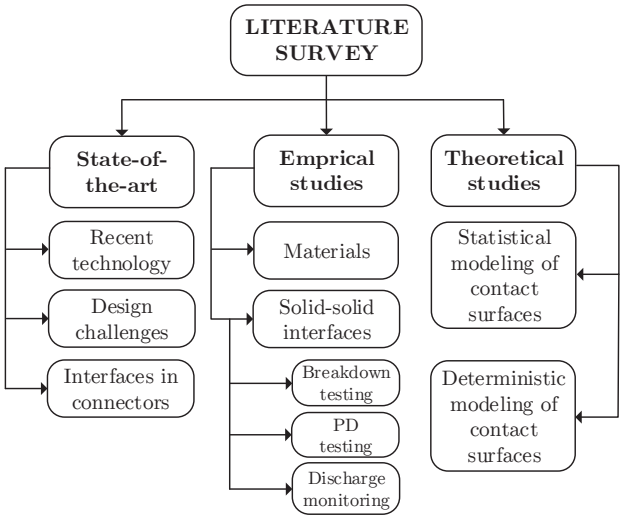

Figure 2.1: Categories covered in the literature survey.

2.1 Interfaces in State-of-the-Art Cable Connectors

In this section, a brief introduction to the modern subsea connectors and the limiting factors involved in the design phase and in practice are given. In addition, a more general overview of solid-solid interfaces in polymer-insulated power cables is provided.

2.1.1 Interfaces in Subsea Cable Connections

Subsea cable connectors are a pertinent example of modern, sophisticated connector solutions available for cable connectors. They are categorized as wet-mate connectors, dry-mate connectors, and penetrators. A modern, wet-mate connector is composed of a plug and a receptacle, as presented in Figure 2.2 [38]. In subsea applications, to retrieve a pump or a transformer to the surface for repair is of paramount importance, and wet-mate connectors significantly facilitate performing this task [1–3]. Wet-mate connectors can be connected and disconnected underwater, allowing the equipment to be disconnected before retrieval to the surface and to be connected after being installed in the subsea grid [1–4, 39]. On the other hand, dry-mate connectors require equipment to be assembled on a vessel along with the cable before being lowered to the seabed. A penetrator is, in essence, a cable termination, enabling HV cables to be fed through a wall in the equipment [1]. Penetrators often withstand high differential pressures and hence allow connecting equipment requiring a 1-atm environment [1].

Subsea connectors have been in operation in oil and gas industry for years due to their ease in plugging underwater [1–3, 6, 39]. Recently, wet-mate connectors are gaining a place in the renewable industry such as in offshore wind farms, tidal energy systems, and floating-type solar panels. However, recent and future subsea extensions stipulate significant and cost-effective developments in wet-mate connector technologies, which should be able to provide higher power ratings and operate at higher voltages, higher temperatures, deeper waters, and longer tiebacks [1–3]. To date, 36-kV-rated wet-mate cable connectors are commercially available, but connectors up to 150 kV should be available within the next decade to provide the driving force for ensuring higher power with reduced losses [1, 2].

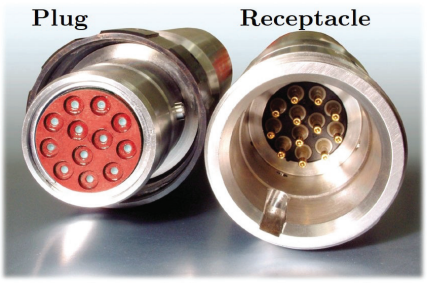

Figure 2.2: Plug and receptacle of a subsea connector [38].

In a connector operating with the principle of a controlled environment, there are two separate insulation systems. Two oil chambers are used, one inside the other, separated by a diaphragm, as shown in Figure 2.3. The main potential weak parts in subsea connectors are the interfaces between the solid-solid insulation and

solid-liquid dielectric. Leading causes of failure are the presence of imperfections, defects, and impurities at the interfaces and water intrusion [5]. They are likely to result in locally high field stresses that, in turn, initiate surface discharges along the guide pin, potentially causing tracking and eventually breakdown. Moreover, water ingress affects the performance of insulating oil significantly [4]. The causes of failure presented here are not inherent only to subsea connectors. In the next section, the focus will be on solid-solid interfaces.

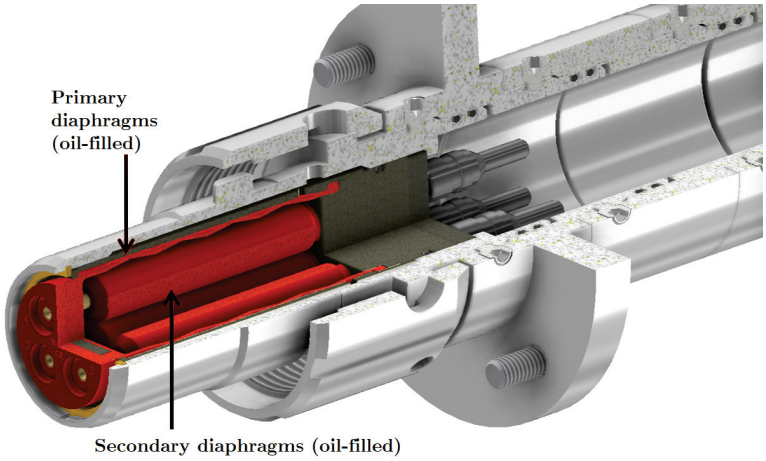

Figure 2.3: Illustration of the insulation system of a subsea connector with two nested, oil-filled diaphragms [38].

2.1.2 Interfaces in Polymer-Insulated Cable Connections

The simple structure of the insulation in XLPE cables led to the early development of easy-fit prefabricated joints and terminations, whose field control elements are prefabricated and are tested in the factory [6]. In the past, such accessories were initially developed for medium-voltage (MV) applications, which were then upgraded for the high-voltage (HV) and extra-high-voltage fields (EHV). However, nowadays, a large number of alternative solutions are competing with these prefabricated elements.

Recent developments have progressed to prefabricated and routine-tested slip-on units even for straight joints for polymer-insulated cables [6]. Field control components are already incorporated in these joints [40]. Accessories with slip-on stress cones for HV and EHV cables usually utilize field control deflectors, as shown in Figure 2.4(a) [6]. Properly contoured deflectors made from an elastic conductive material are positioned into a similar elastic insulator permanently, then pressed in one piece onto the suitably prepared polymer-insulated cable (EPR, LDPE, or XLPE)[4] precisely.

[4]EPR: Ethylene propylene rubber, LDPE: Low-density polyethylene, XLPE: Cross-linked polyethylene.

Figure 2.4(a) shows the cross-section of a slip-on joint, consisting of two opposing control deflectors and a field smoothing sheet for the conductor connection [6]. A conductive coating for the surface of the joint is needed to provide the outer screening. Lastly, a metal housing (durable against corrosion) is used to avoid ingress of moisture and mechanical damage [6].

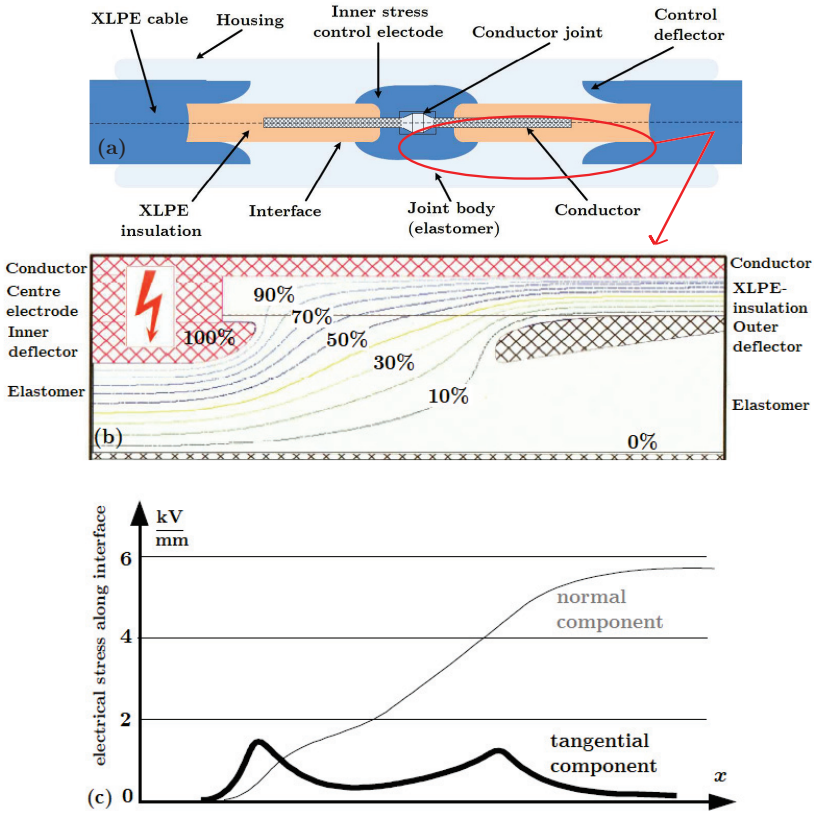

Figure 2.4: Illustration of a cable joint highlighting the parts where the solid-solid interfaces exist, and why the tangential electric field is of concern: (a) Prefabricated EHV silicone joint for 400-kV-XLPE-insulated cables [36]. (b) Calculated potential distribution in a prefabricated slip-on joint [5]. (c) Calculated field patterns in a prefabricated slip-on joint [5].

2.1.3 Factors Affecting the Interfacial Breakdown Strength

Solid-solid interfaces in cable joints usually arise between a soft material (elastomer/polymer) and a hard (polymer) material such as XLPE–EPDM[5], XLPE–SiR[6], XLPE–EPR, and PEEK–XLPE, or between two identical polymers. Soft material provides better contact and sealing even under low/moderate contact pressure.

[5]EPDM: Ethylene propylene diene monomer.
[6]SiR: Silicone rubber.

Despite the presence of deflectors with identical structure, different field conditions arise in joints than in sealing ends. In particular, the tangential component of the electrical field that is locally enhanced at the interface between cable dielectric and joint insulation becomes more significant relative to the maximum field strength within the body of the joint [6]. Accurate field calculations, as illustrated in Figure 2.4, are essential to avoid intolerably high stresses and to optimize the shape of the joint. Figures 2.4(b)–(c) depict the results of field calculations in the form of the potential distribution and the field distribution of the normal and tangential components in a 400 kV slip-on joint, respectively [6].

Electrical performance of solid-solid interfaces are dependent on:

- surface roughness;
- contact force;
- mechanical and electrical characteristics of the insulation materials such as elasticity and tracking resistance;
- surrounding/insulating dielectric medium; and
- care exercised and conditions during assembly.

2.1.4 Contact Surfaces at Solid-Solid Interfaces

Although cable accessories are prefabricated and pretested for partial discharges (PD), they are assembled/fitted on-site under sub-optimal and less controllable conditions [6]. Therefore, the assembly procedure does not incorporate an automated process under clean-room conditions, which makes the interfaces vulnerable during installation. As a consequence, interfacial surfaces are likely to become rife with imperfections such as cavities, protrusions, and contaminants/impurities [5]. The existence of such imperfections at the interface causes the local electric field enhancements illustrated in Figure 2.4(c). To be more specific, rough surfaces lead to various cavities at the interfaces whereas contact force affects the size and deformation of the cavities and contact areas, as shown in Figure 2.5. Mechanical and electrical characteristics of the insulation materials such as elasticity and interfacial tracking resistance strongly affect the interfacial BDS. Type and quantity of lubricant/grease used during assembly, water penetration to the interface, or assembly at dry and optimal conditions change the insulating dielectric medium filling the cavities. Lastly, poor workmanship, wear and tear of materials, contaminants, and impurities cause a substantial reduction in the BDS [6].

The presence of the solid-solid interfaces increases the risk of local electric field enhancements, caused by the imperfections at the interface, and is likely to initiate PD and hence give rise to a premature tracking failure [5–9, 11–14]. In fact, the interfacial breakdown between two solid insulating materials accounts for one of the principal modes of failure for power cable joints reported to date [5–7, 9, 12, 13]. When dimensioning the thickness of the insulation walls of the cable and joint body, Peschke and Olshausen [6] recommend restricting the operational stress on the outer

Figure 2.5: Illustration of surface asperities leading to cavities and contact spots at solid-solid interfaces at: (a) No-load. (b) Increased contact area and reduced cavity size under load [41].

conductive layer to around 6–7 kV/mm even if the installation is performed with due care and the mechanical and electrical design of the apparatus is optimal [6].

The cavities on a solid dielectric surface have various sizes and distributions depending on the methods concerning surface roughness, contact force, mechanical properties of the material as well as the care taken during manufacturing and assembly [5, 6]. When two rough, nominally flat surfaces are placed in contact, surface asperities cause contact to occur at discrete contact spots whereas numerous cavities arise between the contact spots, as schematically represented in Figure 2.6(a)–(b). The real contact area is therefore significantly smaller than the nominal area, as illustrated in Figure 2.6(b). A typical cavity formed at the interface is considerably larger in the tangential direction ($x-$axis or $y-$axis), as delineated in Figure 2.6(c) [16].

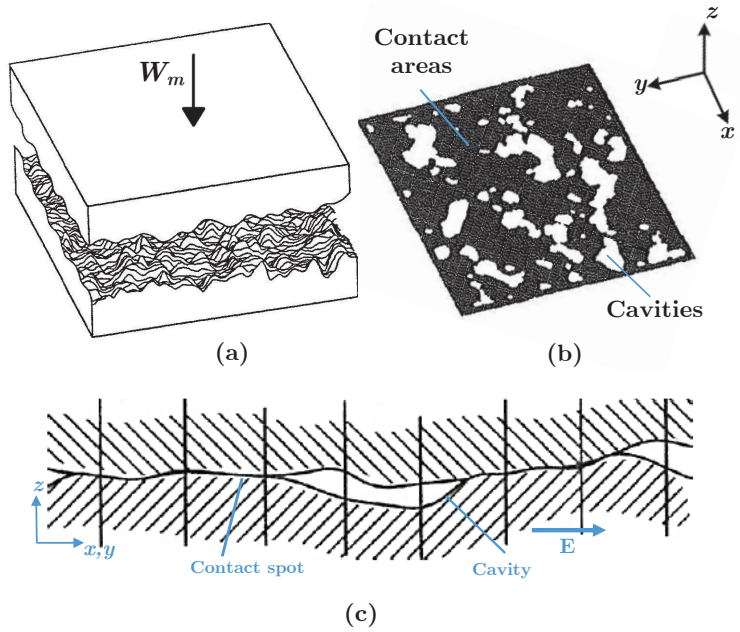

Figure 2.6: (a) Illustration of two rough surfaces in contact. (b) Contact area and cavities at the interface in 3D. (c) Illustration of cavities at the interface in 2D [42].

The parameters that influence the distribution and size of the contact spots and the cavities are discussed in Section 2.1.3. In addition, *Section 2.2* in Paper IV illustrates the effects of surface roughness, elasticity and contact pressure on the interface breakdown strength.

2.2 Empirical Studies on Dielectric Strength of Polymers and Solid-Solid Interfaces

Experimental studies regarding the electrical properties of solid-solid interfaces in insulating materials, HV apparatus, and cable accessories have been covered to a large extent in the literature. The papers referred to in this section have predominately focused on the breakdown strength and PD inception field strength of solid-solid interfaces by focusing on interfacial discharge and breakdown mechanisms induced by enclosed cavities (either spherical or elongated in the field direction) and interfacial tracking resistance (PD resistance) of the polymers. Besides this, a few papers correlated the intensity of discharge images with the interfacial BDS values. In the experiments, cable joints as a whole, interfaces assembled between pieces of polymers cut from commercial cables or polymers cast in laboratories have reportedly been used. Casting custom-made polymers in the laboratories using molds in desired shapes and sizes has been popular among researchers because it allows embedding metal electrodes or air-filled cavities in diverse shapes and sizes in the specimens. Below, a summary of findings from the selected publications is provided.

2.2.1 Studies on Dielectric Strength of Solid-Solid Interfaces

In the 1990s, Fournier et al. [8–11, 20, 21] studied solid-solid interfaces thoroughly using needle-plate electrodes under AC or direct current (DC) excitation across the interfaces formed between XLPE–XLPE, EPDM–EPDM, and EPDM–XLPE samples. In [8, 9, 20], dry interfaces and greased/lubricated interfaces were examined. In both cases, the interfacial breakdown strength was reported to be increasing by a factor of 2.7 and 1.5, respectively, when the applied pressure was increased from 0 kPa to 80 kPa. It was also shown that lubricated interfaces had six times higher breakdown strength than that of an interface without grease. Moreover, Fournier [11] studied effects of surface roughness at dry and greased EPDM–XLPE and EPDM–EPDM interfaces. It was concluded that the dielectric strength of EPDM–XLPE interfaces increased by a factor of 3–4 when the XLPE surface was sanded and greased, while that of unsanded EPDM–XLPE interfaces improved slightly when grease was present. It was also observed that EPDM–EPDM interfaces showed higher dielectric strength compared to EPDM–XLPE interfaces, where their strength depended on the grease used. Since EPDM is softer than XLPE, the interfaces between softer materials achieve higher BDS than those between hard materials. Last, Dang and Fournier [8, 10] addressed that the

interfacial breakdown voltage increased at elevated interface pressures; however, aged cable accessories could cause a reduction in the interface pressure, leading to a reduced interface dielectric strength.

Kunze et al. [5] studied the design of interfaces in HV cable accessories by varying the surface roughness and contact pressure. XLPE–SiR interfaces under AC and impulse voltages were tested, and the experimental results indicated that surface roughness and radial pressure significantly affect the longitudinal electrical strength of interfaces. To be more specific, the increase of the surface roughness (mean height of surface asperities varied from 5 µm to 50 µm) of the XLPE samples reduced the interfacial BDS by 50%.

Takahashi et al. [7] studied interfacial breakdown strength and PD patterns of interfaces between the SiR and epoxy resin using two types of model samples on which the electric field can be applied in parallel (tangentially) or perpendicularly to their interface. The effect of delaminations between interfaces that are filled with air, on the breakdown voltage along the interface was also discussed. They concluded that tangential component of the electrical field is governing the interfacial breakdown, and AC surface breakdown voltages increase by a factor of 1.5 with decreased thickness of the air layer from 1 mm to 0.01 mm.

Du et al. [12, 22] studied the impact of contact pressure using XLPE and SiR samples under AC voltage using needle-plane electrodes. It was concluded that initial discharge voltage increased by a factor of 1.7 with the increase of interfacial pressure from 20 kPa to 300 kPa. Therefore, loss of interfacial pressure between XLPE and SiR should be avoided in practice to extend the life-span of power cables. The effects of interfacial pressure on the interface discharge and the interfacial tracking failure between XLPE and SiR were also investigated by processing the discharge images. Based on the distribution characteristics of discharge light and carbonization patterns, the process and mechanism of interfacial tracking failure were revealed under different interfacial pressures. It was found that the increase in the interfacial pressure significantly restrains the propagation of discharges, further delaying the accumulation of carbonization and the tracking failure at the interface. Both the discharge channels and carbonization pattern decrease with the increase of interfacial pressure. In [13], the effect of surface roughness on the tracking mechanisms at XLPE–SiR interfaces under AC voltage was studied. The results concluded that as the surface roughness was decreased (surfaces sanded with #100 to #1000 in a sequence), the initial discharge voltage, the tracking failure voltage, and the time to tracking failure increased by factors of 1.8, 1.4, and 2.3, respectively, whereas the intensity of the emitted discharge light decreased. In a similar research paper, Chen et al. [43] investigated the tracking failure of XLPE–SiR interfaces under AC and impulse voltages, and concluded that AC voltage has a longer time of over voltage in each cycle and easily leads to interface tracking failure.

Gu and He [44] examined the effect of microcavity on the interfacial breakdown between XLPE and SiR from an artificial cable joint with image processing methods

by analyzing the channel width distribution of discharge light and carbonization. They found that microcavities significantly reduce the interfacial dielectric strength and lead to discharge and tracking failure, while an elongated cavity parallel to the tangential component of the electric field leads to interfacial discharge more easily.

Hasheminezhad [36, 45–49] studied the interfacial breakdown strength of solid-solid interfaces between 2007 and 2011 within the scope of his PhD work an NTNU. During this time, he investigated the BDS and PD inception field of XLPE–XLPE interfaces under a homogeneous AC field by varying the contact pressure and surface roughness. The core results from his thesis are summarized in Figure 2.7 and they agree with the reported results in the literature above and with the results shown in Chapter 8.

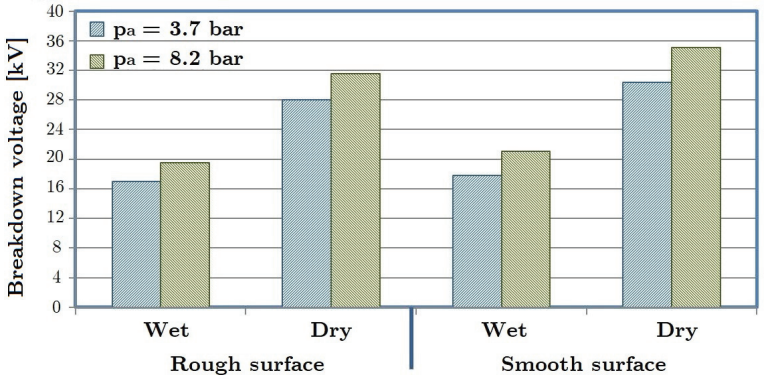

Figure 2.7: Summary of the measured breakdown strength of dry- and wet-mate interfaces using XLPE-insulated cable samples in Hasheminezhad's PhD thesis [36].

Illias et al. [50–52] performed thorough studies on the measurement and modeling of partial discharges in solid dielectric materials and at polymer interfaces. They extensively used phase-resolved partial discharge analysis (PRPDA) and pulse sequential analysis (PSA) techniques to display both experimental and simulation results. When processing the experimental results of the PD measurements in this work, the methods and discussion provided in [50] served as a valuable source of inspiration.

Finally, Stewart et al. [53–58] examined factors affecting the PD activity in internal voids and surface properties of the voids and reported on the characteristics of PD in artificially created voids. The studied void types were enclosed voids, vented channels, and unvented channels in [53,54], and they reported that variation in gas content and by-products generated by the PD activity in voids affect the space charge build-up on the void walls, generation rate of initiating electrons, and alter the collision energy; thus changing the PD characteristics. These studies are found very relevant in determining the effect of gas pressure inside the cavities and the surface roughness on the overall BDS of insulation materials. They also suggested in [53] that vented channels were likely to be subjected to decreased

degradation due to by-products dispersing and gas refresh through the vent. These findings are consistent with the results of the experimental and the theoretical work performed in this thesis.

2.2.2 Studies on Insulation Properties of Polymers

Albayrak et al. [59], Roy et al. [60], and Ding and Varlow [61] observed improved electrical insulation properties when the elastic modulus was increased by adding micro- and nano-scaled zinc oxide, nano-scaled zirconia particles, and silica nanoparticles. In these studies, dielectric strengths of different dielectric materials were tested by changing the chemical and material properties of the bulk insulation material.

Tracking failure in HV cable insulations has been the subject of considerable study, as it is one of the major breakdown mechanisms for solid dielectrics subjected to high electrical stresses [62]. Needle-plane type experimental configurations are extensively used in the literature to examine tracking resistance of insulation materials by inducing a high divergent field to promote the initiation of surface or interface tracking [24, 62–64]. Using empirical data, Fothergill [63] developed an analytical expression to estimate the interfacial tracking resistance of polymers. There, the interfacial tracking resistance is linearly correlated with the fourth root of elastic modulus. Chen et al. [24] used Fothergill's model to investigate the interfacial tracking behavior in XLPE cable insulation samples. Both Fothergill [63] and Chen et al. [24] used needle-plane electrode configurations to generate a strong electric field owing to the non-homogeneous field generated. Mason [65] investigated the PD resistance XLPE samples using nine different combinations of needle, plane and rod electrodes.

Eichhorn [64] published a review paper on interfacial tracking in solid dielectrics in 1977. He concluded that the most familiar and most commonly investigated interfacial tracking phenomena were those resulting from internal electrical discharges which decompose organic materials and most dielectrics. Although the presence of internal voids and contaminants is undesirable, the damage which results from the application of moderate AC voltages to electrode/insulation interfaces which contain imperfections is more commercially significant [64]. In this case, very high, localized stress gradients may exist and lead to the initiation and growth of trees with sufficient time, which may be followed by breakdown. To estimate these localized stress gradients, Eichhorn [64] provided a thorough review of the expressions for stress enhancement at the tip of sharp conductive electrodes.

Gao et al. [66] used the simplified interface contact model, which was formerly proposed in our publications [45, 46, 67, 68]. In the model, the interface voltage is expressed as the sum of the voltages applied across the voids and contact spots. Using the model, they studied the interface breakdown mechanisms at the interfaces formed between polypropylene and SiR under AC excitation. They examined the breakdown of contact spots in two separate stages, namely the initiation stage

and propagation stage, and addressed possible mechanisms responsible for the local deterioration of the contact area at the initiation stage. They suggested that once the contact surface between two discharged cavities is broken down, the cavities are connected, resulting in a larger discharge channel. It was concluded that the degradation and the breakdown of the local contact area are essential for the discharge channel to propagate at the interface.

Finally, Gubanski et al. [27, 29, 62, 69–76] contributed to the literature with numerous extensive and thorough studies on interfacial tracking resistances of polymeric materials, such as SiR, PE, XLPE, LDPE under AC excitation. The essence of the findings from [27, 29, 62, 69–76] is that the electric field at the needle tip was found to be strongly limited by the charges injected from the needle. The results indicated that the maximum electric field emerges in the bulk material very close to the needle tip and is likely to induce changes in the material, leading to the initiation of an electrical tree.

2.3 Theoretical Studies on Contact Surface Modeling Using Tribology

There are various approaches to the description of rough engineering surfaces in the history of tribology, such as statistical analysis of contacts, fractal analysis of contacts [16], and approaches based upon the surface power spectrum [77]. Recently, the use of numerical/deterministic roughness models has been widespread as fast processors become available [16, 37].

Archard [78] worked on the multilevel structure of the roughness where a sphere of radius consists of spherical asperities whose radii are significantly smaller. The idea of the iterative hierarchical structure of roughness was further developed in [79]. In addition, Nayak [80] and Whitehouse and Archard [81] studied modeling of surfaces as random processes; however, it later turned out that the mean radius of curvature is scale-dependent [77]. More recently, fractal approaches have been introduced with the aim of providing a scale-invariant characterization of roughness to more accurately obtain the contact area [77, 82, 83]. Fractal characterization supplies information of the surface roughness at all the length scales that depict the fractal behavior [83]. Several distinguished tribology researchers, however, argued that empirical fractals do not yield scale-independent parameters for description of rough surfaces [77, 84]. Thus, the fractal approach is still an active area of research [77]. Approaches to surface roughness based on the surface power spectrum have also been frowned upon due to lack of mathematical justification [77]. In the following sections, further details on the statistical and deterministic roughness models are provided.

2.3.1 Statistical Interface Contact Models

One of the earliest statistical models of contact between rough elastic solids was offered by Zhuravlev (1940) [85]. Johnson (1975) [86] and Greenwood (1990) [87] are among the first scientists to have cited the Zhuravlev model. Intending to develop the Zhuravlev model, Greenwood and Williamson [88] later proposed a contact model of nominally flat surfaces, where both Gaussian and the exponential distribution of the asperity peaks were tested to show that the real contact area is proportional to the applied load. Greenwood and Williamson's model [88] analyzed a rough surface pressed against a smooth surface considering contacts that are either elastic or plastic. More recently, Borodich's introduction to Zhuravlev's historical paper [89] highlighted that the Greenwood-Williamson's theory (1966) [88], which assumes the asperities having the same radii with various heights was a developed version of Zhuravlev's model for purely elastic contact published in 1940 [85]. Actually, Greenwood and Williamson [88] modified the Zhuravlev model by covering the transition of surface asperities from elastic behavior to plastic behavior. The Greenwood and Williamson model [88] together with Bhushan's modifications to it [16] are utilized to propose a statistical contact model in Chapter 3.

Lastly, Zhu et al. [90] also used the simplified interface contact model, which was formerly proposed in our publications [45, 46, 67, 68]. They studied the relationship between the interfacial DC breakdown voltage of the XLPE–SiR interface and the interface morphology using the interface contact model. They combined the analytical model with an image processing algorithm that yielded similar surface simulations as those we obtained by using the deterministic contact model, that will be introduced below. They concluded that although the density of real contact asperities is high, the real contact area is considerably lower than the nominal contact area. Consequently, there are a large number of connected voids at the interface, and they are the main channel of interfacial breakdown, while the contact asperities become the obstacles of breakdown. These deductions are found to be strongly agreeing with the main findings reported in Chapter 12.

2.3.2 Deterministic Interface Contact Models

With the advent of supercomputers that can perform heavy computations of big data in a matter of hours if not minutes, deterministic models have increasingly been favored. The outcome is becoming increasingly realistic as computational speed increases. However, simplified models of material topographies are needed, that make it necessary to minimize the computing time. In this respect, Almqvist's PhD thesis [37] is found to be of immense benefit, which was built on the numerical model proposed by Tian and Bhushan [42].

Almqvist [37] proposed a contact model that requires a measured surface profile, where the interface of contact between two surfaces is governed by the theory of minimum potential complementary energy. The resulting displacement of peaks

and valleys of the profile is then computed by minimizing an integral energy equation with respect to the applied contact pressure and material properties.

The outcome of the model is a simulated deformed surface profile at the interface between a rigid plane and the measured surface profile [37]. The sizes of all cavities at the interface and total area of contact are definite. Hasheminezhad [36] employed Almqvist's deterministic model [37] to estimate the length of the largest cavity (in the direction of the electric field) at the XLPE–XLPE interfaces. His study covered scanned 2D surface profiles of XLPE specimens. In this thesis, the proposed model in [36] is further extended using the analytical expressions addressed in [37] so that the model incorporates 3D surface profiles in addition to the 2D surface profiles.

An illustration of the original surface profile, displacement of surface asperities along with the deformed surface profile of a 2D surface is presented in Figure 2.8(a). The discrete distribution of contact pressure at the surface asperities is illustrated in Figure 2.8(b). Details regarding the deterministic theory are given in Chapter 5.

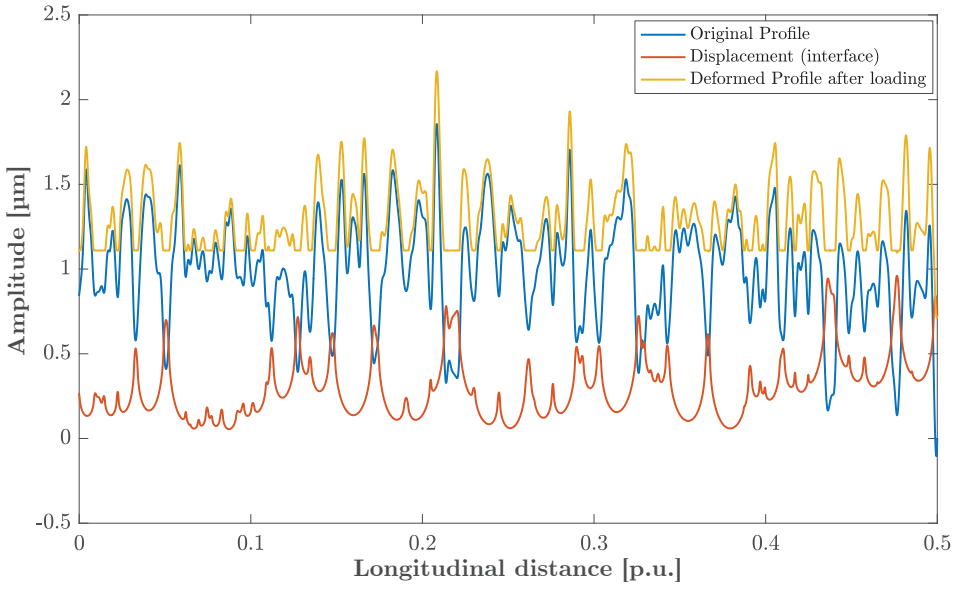

(a)

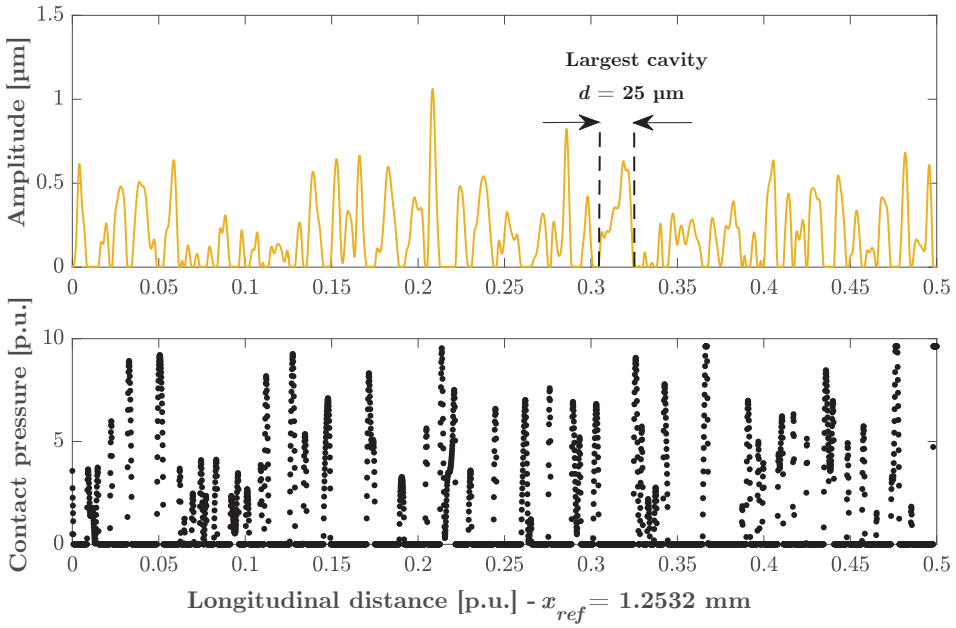

(b)

Figure 2.8: (a) Illustration of a measured 2D surface profile of an XLPE sample (polished by sandpaper grit #2400), displacement of peaks after loading (1.16 MPa), and the resulting deformed profile. (b) Deformed profile and distribution of contact pressure at contact spots. Nominal longitudinal distance (x_{ref}) is 1.2532 mm.

Chapter 3

Statistical Contact Model for Estimation of Average Sizes of Cavities and Contact Spots

This chapter shows how the statistical model, introduced in Section 2.3.1, is used to describe multiple-asperity dry contacts formed at a solid-solid interface in a 2D plane using the tribological principles presented in [16, 42, 88, 91–95]. The model estimates the average size of cavities and contact areas at solid-solid interfaces as a function of the contact pressure, surface roughness, and elastic modulus.

3.1 Dry Multiple-Asperity Contacts

If the two rough surfaces, as presented in Figure 3.1, which are both nominally flat, are brought into contact by being pressed together until their reference planes are separated by a distance d, numerous discrete contact spots then arise at those asperities where the sum of total heights $z_1 + z_2$ are greater than the nominal distance between the surfaces, d [16, 91, 92].

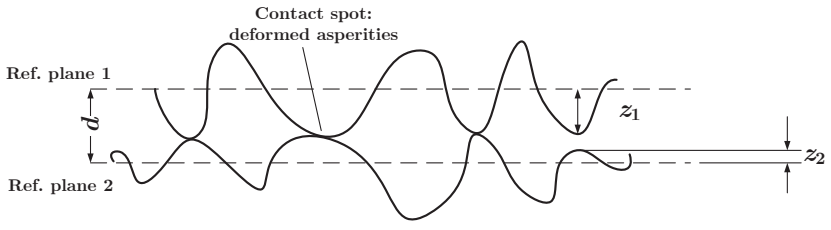

Figure 3.1: Schematic representation of a contact between two rough surfaces [92].

Williamson et al. [93] addressed that assessing surfaces with cumulative processes (either single-point processes or extreme-value processes) resulted in a Gaussian-height distribution, whereas peak heights had a Gaussian distribution in all cases. On the other hand, Greenwood and Tripp [95] discovered that as long as the peak heights follow a Gaussian distribution, the asperity shape and whether the asperities exist on one or both surfaces are unimportant. Besides, Greenwood and Tripp [95] showed that the contact of two rough surfaces could be reduced to a so-called equivalent sum surface, consisting of a single, rough surface with a smooth, rigid plane. In agreement with this, O'Callaghan and Cameron [96], and Francis [97] reported similar findings such that the contact of two rough surfaces negligibly differs from the equivalent sum surface consisting of a perfectly smooth and an equivalent rough surface, as illustrated in Figure 3.2.

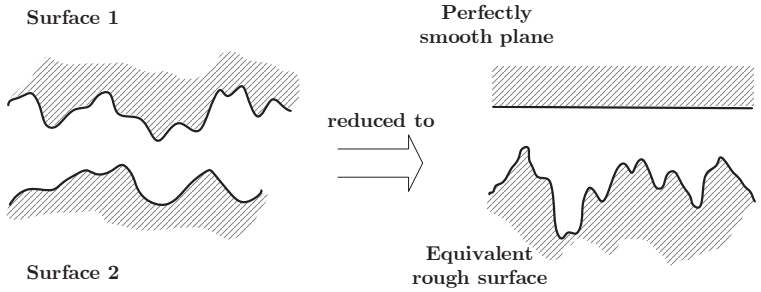

Figure 3.2: Contact asperities between a perfectly smooth surface and a rough surface.

Considering these findings, Greenwood and Williamson [88] assumed that:

- The rough surface incorporates a large number of asperities, which are of spherical geometry at least near their summit.
- Asperities on each surface have a constant summit radius, whereas their heights vary randomly.
- Most surfaces found in engineering applications have normally distributed asperities and peak heights (Gaussian distribution).

The curvature of the asperity-peak , β_m of the equivalent rough surface (sum surface) is then defined as the sum of surface asperities of each rough surface, β_{m1} and β_{m2} using [16, 92]:

$$1/\beta_m = 1/\beta_{m1} + 1/\beta_{m2}. \tag{3.1}$$

Moreover, elementary statistics suggest that if the peak-height distributions of two rough surfaces are independent (as is likely when two surfaces are prepared separately) and are distributed randomly (not necessarily Gaussian) with standard deviations of the asperities σ_{p1} and σ_{p2}, the distribution of the equivalent rough surface, σ_p, will have a standard deviation of [16, 92]:

$$\sigma_p = \sqrt{\sigma_{p1}^2 + \sigma_{p2}^2}\,. \tag{3.2}$$

When the contact pressure between the two contacting samples is applied, elastic deformation initially takes place as a function of their elastic moduli of elasticity [88]. As the load is further increased, the mechanically weaker/softer sample (or both if they are identical) begins to deform plastically. The load at which the plastic flow begins depends on the hardness of the softer material [16, 88].

3.2 Statistical Analysis of Surface Contacts at Solid-Solid Interfaces

In the light of the assumptions/simplifications made by Greenwood and Williamson [88], Bhushan [16], showed that the apparent pressure p_a, mean real pressure p_r, (elastic) real area of contact A_{re}, the number of contact spots n, and mean asperity real area of contact as a function of separation d can be calculated. For this purpose, the contact between a plane and a nominally flat surface incorporating numerous spherically tipped asperities of the same radius β_m was considered, with their peak heights represented by a probability density function of $p(z)$, as shown in Figure 3.3. Contact mechanics of an individual cavity under a particular load are known from the Hertzian equations [88, 98], in which the contact radius a_c, the individual contact area A_i, and the individual load W_{mi} are represented in terms of total peak displacement δ. Each elastic contact area for a peak displacement δ equals to $A_i = \pi\beta_m\delta$ and is circular with the radius $a_c = (\beta_m\delta)^{1/2}$ as depicted in Figure 3.3 and Figure 3.4, while the load is given by $W_{mi} = (4/3)E'\beta_m{}^{1/2}\delta^{3/2}$ [98].

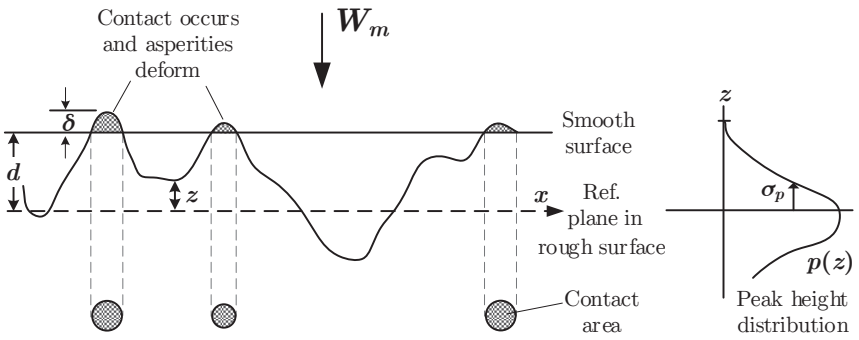

Figure 3.3: Schematic representation of the contact between a rough surface and a smooth surface (rigid plane) [16].

When two surfaces are brought into contact until their reference planes are separated by d, contact spots will arise at any asperity whose height was formerly greater than d. Thus, the probability of having a contact at a given asperity height z, $P(z > d)$ is [16, 88, 98]:

$$P(z > d) = \int_d^\infty p(z)\, dz, \tag{3.3}$$

where $p(z)$ is the probability density function (pdf).

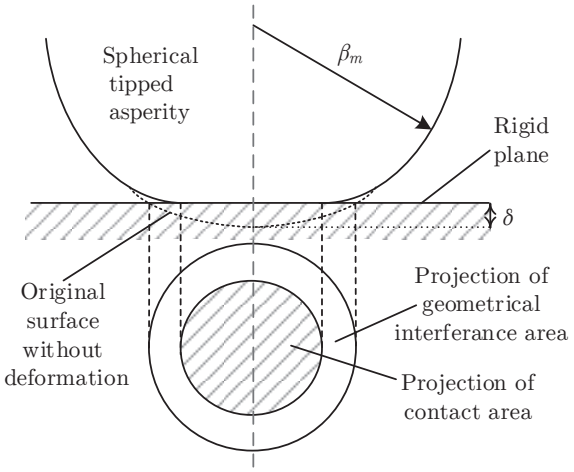

Figure 3.4: Contact area between a spherical asperity and a rigid plane, which is circular $\pi\beta_m\delta$ with the radius of $a_c = (\beta_m\delta)^{1/2}$ [94].

Moreover, if there are N asperities in total, the expected number of contacts n will then become:

$$n = N \int_d^\infty p\,(z)\,dz. \tag{3.4}$$

In addition, since the total displacement δ is equal to $z - d$, the total real (elastic) area of contact (A_{re}) becomes:

$$A_{re} = \pi N \beta_m \int_d^\infty (z-d)\,p\,(z)\,dz. \tag{3.5}$$

Similarly, the expected total load ($W_m = NW_i$) is:

$$W_m = p_r A_{re} = p_a A_a = \frac{4}{3} N E' {\beta_m}^{1/2} \int_d^\infty (z-d)^{3/2}\,p\,(z)\,dz, \tag{3.6}$$

where p_r is the mean real pressure, p_a is the apparent contact pressure in Pa, A_a is the nominal surface area in m^2, and E' is the composite/effective elastic modulus (i.e., Young's modulus) of two materials in contact. The contact pressure is expressed by $p_a = W_m/A_a$ (in $\mathrm{N/m^2} \equiv \mathrm{Pa}$). The effective elastic modulus, E', is calculated as the composite elastic modulus of each material in contact E, using the relation below:

$$\frac{1}{E'} = \frac{1}{2}\left(\frac{1-{v_1}^2}{E_1} + \frac{1-{v_2}^2}{E_2}\right), \tag{3.7}$$

where E_1, v_1 and E_2, v_2 are the elastic modulus in Pa and Poisson's ratio of each material, respectively [37]. Note that the Equations (3.3)–(3.6) are valid for any type of surface peak-height distribution. In the case of Gaussian peak-height dis-

tribution, the distribution of asperity heights is expressed by:

$$p\,(z) = \frac{1}{\sigma\sqrt{2\pi}}\; e^{-\frac{1}{2}\left(\frac{z-\mu}{\sigma}\right)^2}, \tag{3.8}$$

where μ is the expected mean value and σ^2 is the variance of the random variable.

To benefit from the convenience of scale-independent variables, Bhushan [16, 91, 92] modified the above formulae by introducing non-dimensional variables and standardized probability density functions as follows:

$$\frac{p_a}{\eta\,\sigma_p\,\beta_m\,E'\,\sqrt{\sigma_p/\beta_m}} = \frac{4}{3}F_{3/2}\,(D)\,, \tag{3.9}$$

$$\frac{p_r}{E'\,\sqrt{\sigma_p/\beta_m}} = \frac{4}{3\pi}\,\frac{F_{3/2}\,(D)}{F_1\,(D)}\,, \tag{3.10}$$

$$\frac{A_{re}\,E'\,\sqrt{\sigma_p/\beta_m}}{p_a\,A_a} = \frac{3\pi}{4}\,\frac{F_1\,(D)}{F_{3/2}\,(D)}\,, \tag{3.11}$$

$$\frac{n\,\sigma_p\,\beta_m\,E'\,\sqrt{\sigma_p/\beta_m}}{p_a\,A_a} = F_0(D)/\frac{4}{3}F_{3/2}(D)\,, \tag{3.12}$$

$$(A_{re}/n)\,\sigma_p\,\beta_m = \pi F_1\,(D)/F_0\,(D)\,, \tag{3.13}$$

where D is the dimensionless separation (d/σ_p), η is the density of asperity summits per unit area (N/A_a), and $F_m(D)$ is a parabolic cylinder function provided by:

$$F_m(D) = \int_D^\infty (s-D)^m\,p^*(s)\,ds, \tag{3.14}$$

where $p^*(s)$ is the standardized peak-height-probability density function. The function $p^*(s)$ has, by definition, zero mean and is scaled to render its standard deviation unity [92]. It should be noted that the dimensionless, scaled Equations (3.9)–(3.13) are also valid for all surface distributions as for Equations (3.3)–(3.6).

In the case of a Gaussian peak-height distribution, transforming $p\,(z)$ in Equation (3.8) into $p^*(s)$ yields:

$$F_m(D) = \frac{1}{\sqrt{2\pi}}\int_D^\infty (s-D)^m\,e^{-s^2/2}\,ds. \tag{3.15}$$

Using Equations (3.9)–(3.13), correlation between D and p_a as well as those between p_a and p_r, A_{re} and n are acquired in dimensionless forms. Bhushan [92] then further studied these relationships via least-square fit functions and concluded the mathematical model that correlated the real area of contact A_{re} with the nominal contact area A_a in the elastic regime as:

$$A_{re} \cong 3.2 \frac{p_a\, A_a}{E' \sqrt{\sigma_p / \beta_m}}. \tag{3.16a}$$

The real area of contact can directly be represented as a function of the contact pressure p_a and effective elastic modulus E' by further simplifying Equation (3.16a):

$$A_{re}/A_a \triangleq \mathcal{Z}\, \frac{p_a}{E'}, \tag{3.16b}$$

where $\mathcal{Z}$ is a parameter equal to $3.2\sqrt{\beta_m/\sigma_p}$ since σ_p and β_m are constant values computed for characterizing the surface under consideration. In addition, the expected number of contact spots n is given by:

$$n = 1.21 \eta A_a \left(\frac{p_a}{\eta \sigma_p \beta_m E' \sqrt{\sigma_p / \beta_m}} \right)^{0.88}, \tag{3.17}$$

where η stands for the surface density of asperities [16, 91, 92]. With the help of Equations (3.16a)–(3.17), the number of contact spots and the area that the contact spots take up as a fraction of the nominal contact area can be computed.

3.3 Contact Surface Modeling

In this study, a simplified, 2D interface contact model is aimed to be developed. For the sake of simplicity, the average size of the cavities and contact spots are favored. As the model is developed in 2D, the average size is defined with respect to the axis parallel to the direction of tangential electric field since the minimum value of the cavity discharge inception field is associated with the maximum path length in the field direction (critical avalanche length [99]). In addition to this, the number of contact spots is assumed to be equal to the number of cavities as each cavity is enclosed between two contact spots.

3.3.1 Average Size of Contact Spots

By manipulating Equations (3.16a) and (3.17), the total contact area is computed. As stated in Section 3.1, the simplification to the equivalent rough surface does not affect the real area calculation and causes negligible differences [95]. The average length of the contact spot l_{avg} is derived as follows:

$$A_{re} = \sum_{j=1}^{n} A_{cnt_j} = n\pi \left(\frac{l_{avg}}{2} \right)^2, \tag{3.18}$$

$$l_{avg} = 2\sqrt{\frac{A_{re}}{n\pi}} = 1.84\, \frac{\beta_m^{0.47}\, \sigma_p^{0.41} p_a^{0.06}}{E'^{0.06}\, \eta^{0.06}}, \tag{3.19}$$

where A_{cnt_j} stands for the respective area of the j^{th} contact spot.

3.3.2 Average Size of Cavities

To calculate the average size of the cavities, the shape of cavities, arising at the polymer surfaces after sanding/polishing with abrasive sandpapers, should initially be determined. This procedure is illustrated by examining the surface morphology of a polished XLPE sample by following the methodology described in Section 6.1.2. Figure 3.5(a) shows the obtained 3D surface profile whereas Figure 3.5(b) and Figure 3.5(c) depict 2D profiles at the cursor position in x- and y-axes, respectively.

It should be noted that these profiles account for the interface between an equivalent rough surface and a perfectly smooth plane. The gray-solid lines represent the displaced asperity position under a heavier load, whereas the difference between the lines is the peak displacement, δ. The details on how to transform two rough surfaces into an equivalent rough surface and a smooth, rigid plane can be found in Chapter 5.

As observed in Figure 3.5(b) and Figure 3.5(c), the surface topographies in both the x- and y-axes have comparable amplitudes and widths of peaks and valleys. The cavities formed in xz- or yz-planes can be approximated with an ellipsoid whose length parallel to the electric field (d_{avg}) is approximately 8–9 times larger than the length normal to the field (h_z). Approximated average-sized interfacial cavities are illustrated in Figure 3.6, whose tangential length d_{avg} is considerably larger than the height of the asperity peaks h_z. As previously mentioned, regardless of the cavity shape, the cavity size parallel to the electric field component is of importance when determining cavity discharge inception field because the minimum value of the inception field is associated with the maximum path length in the field direction [14].

Based on the defined shape of an average cavity, the projection area of a cavity on the xy-plane is determined with the assumption that there are n pairs of cavities and contact spots where the number of the contact spots is assumed to be equal to the number of cavities. For simplicity, the projection area on the xy-plane is considered to be square with the side length d_{avg}. On that account, d_{avg} is calculated as follows:

$$A_{cav} = \sum_{j=1}^{n} A_{cav_j} = A_a - A_{re}, \tag{3.20a}$$

$$\overline{A}_{cav} = \frac{A_a - A_{re}}{n}, \tag{3.20b}$$

$$d_{avg} = \sqrt{\frac{A_a - A_{re}}{n}}, \tag{3.21a}$$

$$d_{avg} = \frac{\left(E' \sqrt{\frac{\sigma_p}{\beta_m}} - 3.2 p_a\right)^{0.5} \beta_m^{0.47} \sigma_p^{0.41}}{\sqrt{1.21}\, E'^{0.06}\, \eta^{0.06}\, p_a^{0.44}}, \tag{3.21b}$$

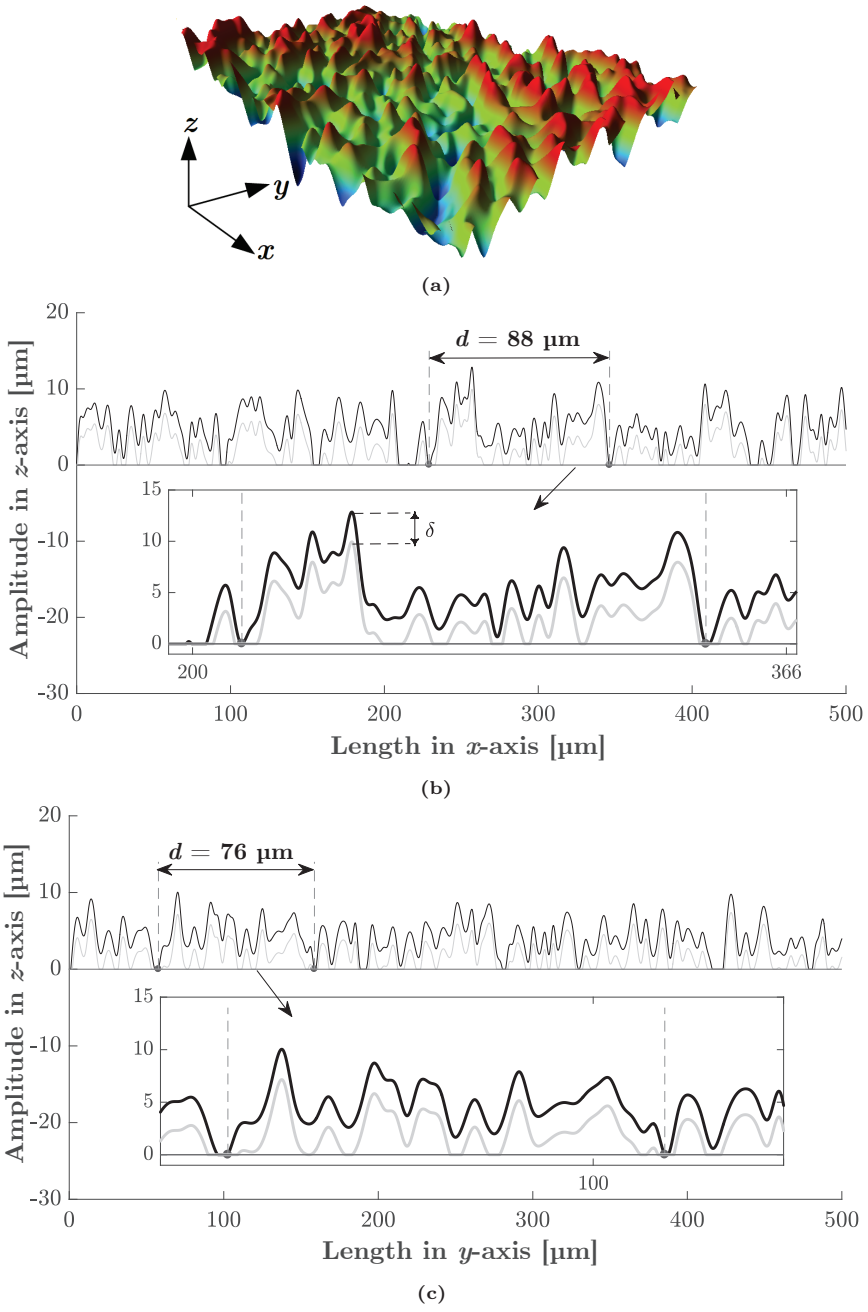

Figure 3.5: (a) Example of a surface profile of an XLPE sample polished with #500 sandpaper. Interface between an equivalent rough surface and a perfectly smooth plane: (b) x-axis data are placed in a row vector out of 640 available planes where the thickness of each plane is 1.9581 µm. (c) y-axis data are placed in a column vector out of 480 available planes (see Section 6.6.1).

where A_{cav}, A_{cav_j}, and $\overline{A}_{cav}$ stand for the total area cavities take up, the area of the j^{th} cavity, and the average area of a cavity, respectively. The correlation between the cavity size and the interfacial contact pressure p_a, the effective elastic modulus E', and the average length of cavities d_{avg} is estimated by Equation (3.21b).

The three surface characterization parameters; σ_p, β_m, and η in Equations (3.19) and (3.21b) need to be determined to calculate the average size d_{avg} and the average contact spot length l_{avg}, respectively. For this purpose, the motif profiles, namely the roughness and waviness profiles proposed in [100, 101], are employed as explained in the following section.

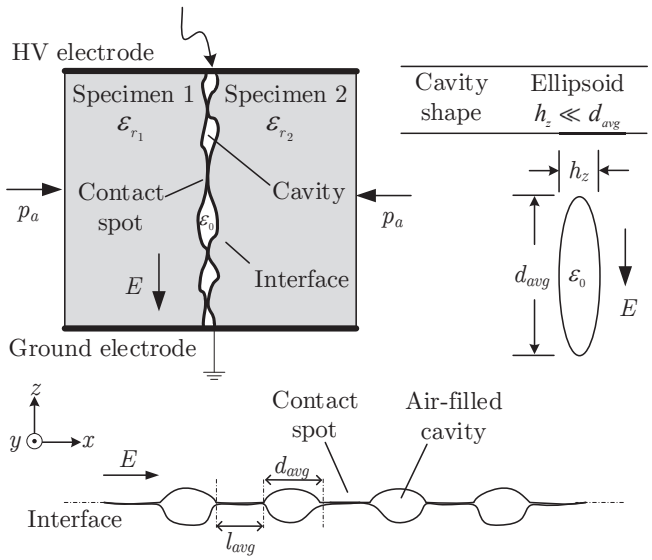

Figure 3.6: Air-filled cavities formed at the polymer interface.

3.3.3 Number of Cavity and Contact Spot Pairs

The interface model displayed in Figure 3.6 is composed of identical average-sized cavities and contact spots. The average sizes of cavities and contact spots, d_{avg} and l_{avg}, are derived using the data of scanned surface stored in a 480 × 640 matrix that incorporates 640 xz-planes and 480 yz-planes with a thickness of 1.95 µm (see Section 6.6.1). The simplified interface model shown in Figure 3.6 represents the average of the surface data, which is represented in the xz-plane (yz-plane could also be used since both planes have identical distributions and size of asperities as shown in Figure 3.5 and Figure 7.5). Thus, a row vector with a size of 1×640 represents an area of 1.95 µm x 1.25 mm in the total area of 0.94 mm× 1.25 mm. Analogously, if the model is to represent the average data of the yz-planes, a vector with the size of 480×1 represents the entire data. For instance, the data of the profiles shown in Figures 3.5(b)–(c) are stored in a 1×640 row vector and 480×1 column vector, respectively.

The surface characterization parameters, σ_p, β_m, and η, are computed using the matrix that contains the surface data. Thus, the number of cavity and contact spot pairs n in Equation (3.17) represent the number of pairs over the entire surface in the xyz-plane. In the results section, n (dimensionless) is normalized with the nominal surface area A_a and is represented by the unit mm^{-2}. To determine the number of contact spots and cavities existing in an area, the normalized n times the area provides the number of cavity and contact spot pairs.

3.4 Characterization of Surface Roughness

Surface texture characterization requires a large array of parameter calculations and filtering methods. The software toolboxes/packages that are provided with surface texture measuring instruments, along with some stand-alone software applications, usually offer an overwhelming range of options for surface texture characterization. If possible, those taking current international standards as their point of reference, such as ASME B.46 [102], ISO 25178–2 [103], ISO 12085 [104] and ISO 4287 [105] should be favored [106].

The sum surface approach, which is used to transform two rough surfaces to an equivalent rough surface and a smooth surface as delineated in Figure 3.2, requires the use of motif parameters, as explained in [101]. Moreover, the motif approach is essential when computing the statistical surface characterization parameters of σ_p , β_m , and η. On the other hand, as performed in Paper II, S-parameters are used to compare the surfaces according to their degree of roughness in a less complicated way, without delving into the motif approach. Therefore, in this thesis, both the motif parameters and S-amplitude parameters have been used when characterizing the areal surface textures of the studied samples.

3.4.1 Motif Parameters Approach

Motif parameters offer a statistical description of asperity shapes and locations spread out on a broad range of micro-geometry from periodic to random profiles, where the primary asperities on isotropic rough surfaces are scrutinized by employing the summit and the radius of the altitude of each asperity [100]. Statistical analysis using probability density functions, for instance, Gaussian or log-normal, are used to describe each of these geometrical characteristics, where the distributions are redimensioned with the extracted characteristic values of the *roughness* and *waviness* parameters following the *motif* procedure [100, 101].

The procedure for determining the motif parameters is described according to ISO 12085 [104] and is represented by the illustration in Figure 3.7(a). First, the total surface profile is obtained using a surface characterization instrument. Second, a short-wave cut-off noise filter with the wavelength λ_s is applied to the total profile to obtain the primary profile. The roughness profile $\mathbb{R}$ is then extracted by applying a band-pass filter with the short-wave cut-off wavelength λ_s and the long-wave cut-off wavelength λ_c to the primary profile $\mathbb{P}$ [106].

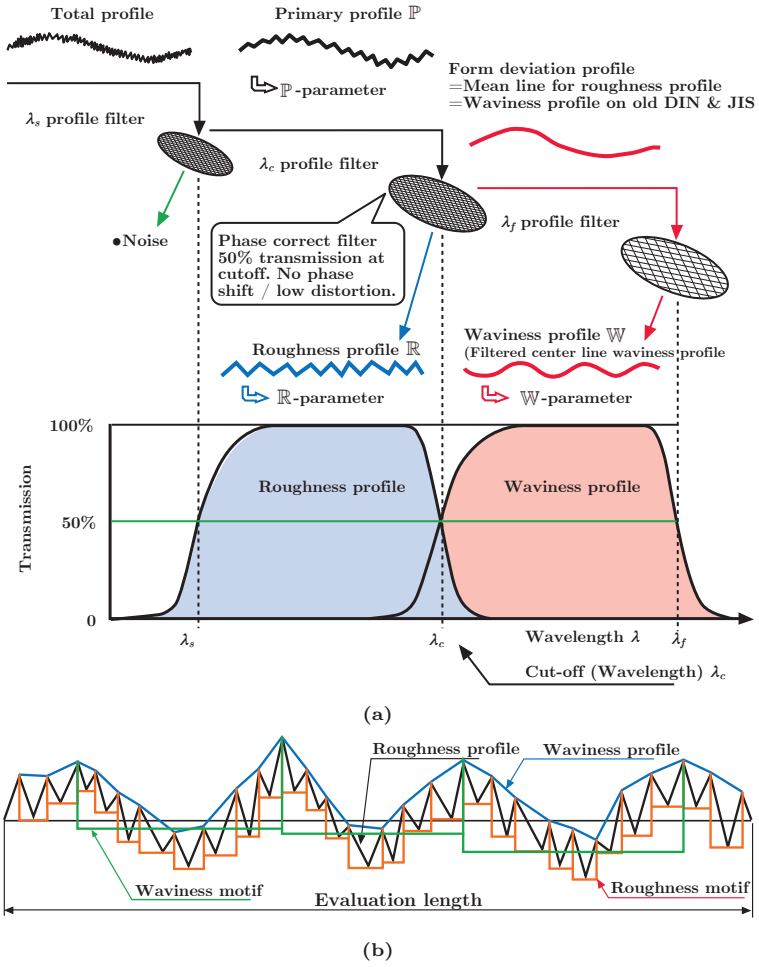

Figure 3.7: (a) Extraction methods of roughness and waviness profiles from the primary profile [107]. (b) Illustration of extracted roughness and waviness motifs and profiles [107].

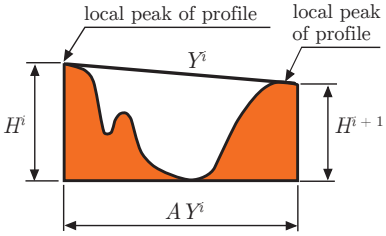

Figure 3.8: Sketch of a motif [107].

Likewise, a band-pass filter with a short-wave cut-off wavelength λ_c and long-wave cut-off wavelength λ_f is applied to extract the waviness profile $\mathbb{W}$ [106]. ISO 4287 [105], ISO 25178 [103] or ASME B46.1 [102] list suggested values for the cut-off lengths. The resulting profiles and motifs are illustrated in Figure 3.7(b). A motif stands for a portion of the primary profile between the highest points of two local peaks of the profile, which are not necessarily adjacent [107]. The geometrical attributes of a motif with the index i are as follows (see Figure 3.8):

- H^i is the height difference between the left peak and the deepest valley.
- H^{i+1} is the height difference between the right peak and the deepest valley.
- Y^i is the mean height (of H^i and H^{i+1}) of the i^{th} motif.
- AY^i is the horizontal distance between the peaks of the i^{th} motif.

The following four conditions give the principal peaks and permit the calculation of roughness parameters of a surface consisting of several motifs:

- Y is the average of the height values Y^i of the motifs (i.e., arithmetic mean asperity height).
- AY is the average of the width values AY^i of the motifs.
- SY is the root mean square (rms) of the Y^i of the motifs.
- SAY is the root mean square of the AY^i of the motifs.

Likewise, waviness parameters W and SW—the mean value and root-mean-square of the height values W_i of the waviness motifs, respectively—are determined following the same procedure as for the roughness profile, using the waviness profile.

Belghith et al. [101] derived geometric characteristics of the sum surface (i.e., an equivalent rough surface and a smooth surface) from each surface in contact. Thus, the parameters of the sum surface result from parameters of each surface with the subscripts 1 and 2 as [101]:

$$Y_{eq} = Y_1 + Y_2, \tag{3.22a}$$

$$W_{eq} = W_1 + W_2, \tag{3.22b}$$

$$AY_{eq} = \frac{1}{2}\left(AY_1 + AY_2\right), \tag{3.23}$$

$$SY_{eq} = \sqrt{SY_1^2 + SY_2^2}, \tag{3.24}$$

$$SAY_{eq} = \sqrt{SAY_1^2 + SAY_2^2}, \tag{3.25a}$$

$$SW_{eq} = \sqrt{SW_1^2 + SW_2^2}. \tag{3.25b}$$

Belghith et al. [101] suggested that the arithmetic mean asperity height Y represents a brief overview of surface texture. Therefore, surfaces with different roughness degrees can roughly be compared using Y or Y_{eq}.

Robbe-Valloire [100] addressed that transforming a profile into a surface requires modifications in densities. In this respect, the density of asperities on a profile $\mathscr{D}$ are converted to the surface density of asperities η by using the correlation:

$$\eta = 1.2\,\mathscr{D}^2, \tag{3.26a}$$

$$\mathscr{D} = {}^{1}\!/_{AY_{eq}}. \tag{3.26b}$$

The standard deviation of the distribution of the peak heights σ_p and the mean value of the summit radius β_m—considering two spherically shaped summits—are respectively given by:

$$\sigma_p = 0.35\sqrt{W_{eq}^2 + SW_{eq}^2}, \tag{3.27}$$

$$\beta_m = \frac{AY_{eq}^2 + SAY_{eq}^2}{16Y_{eq}}. \tag{3.28}$$

To sum up, the motif parameters of the equivalent rough surface are computed using Equations (3.22a)–(3.25b). The resulting parameters are then substituted in Equations (3.27) and (3.28).

Note that Equations (3.19) and (3.21b) are derived based on the assumption that peaks and valleys are normally distributed. In case the peak-height distribution fits a different probability density function, then the new probability density function $p(z)$ should be substituted in Equation (3.14) to modify the mathematical expressions for the d_{avg} and l_{avg}. To determine the type of the peak-height distribution of the surfaces utilized in this work, histograms of surface peak height distributions are obtained (see Appendix D.3.3.1). A Gaussian distribution function was selected for $p(z)$ considering the obtained histograms as shown in Appendix D.3.3.1 and the normality tests carried out in Appendix D.3.3.2.[7]

Last, Archard [108] observed that the three surface parameters of engineering surfaces which are sanded or machined are usually correlated by the relation of:

$$\sigma_p \, \beta_m \, \eta \simeq 0.03 - 0.05. \tag{3.29}$$

In Section 7.2.3, the multiplication of the motif parameters is checked if it agrees with Equation (3.29).

3.4.2 Surface Height Parameters Approach

Stout et al. [109] have developed the 3D surface texture height parameters (S-parameters) to specifically address the 3D nature of surface textures. Modern surface profilometers mostly employ the S-parameters as part of their software packages when characterizing rough surfaces [106]. The use of S-parameters is straightforward by merely adding the toolbox to the measured data and software returns the S-parameters for the selected profile.

S-parameters incorporates the following subgroups: S-amplitude, S-hybrid, S-spatial, S-functional index family, and S-functional volume family parameters with reference to ASME Y.14 and ISO 25178–2 [103, 110]. The definitions and detailed information are available in [103, 106, 109, 110].

[7] For instance, in the case of an exponential asperity height distribution $p(z)$ would be: $p(z) = \lambda e^{-\lambda z}$, where λ is the rate parameter provided that $\lambda > 0$ [16].

S-amplitude parameters are defined as below and are illustrated in Figure 3.9:

- arithmetic mean height (S_a);
- root mean square height (S_q);
- maximum peak height (S_p);
- maximum pit height (S_v)[8]; and
- maximum height of the surface (S_z).

The arithmetic mean height, S_a parameter is defined as the arithmetic mean of the absolute value of the surface asperities, $z(x, y)$, within the sampling area:

$$S_a = \frac{1}{\mathscr{A}} \iint\limits_{\mathscr{A}} \left| z(x, y) \right| \, dxdy \,, \tag{3.30}$$

where $\mathscr{A}$ is the sampling area, $\mathscr{A} = xy$. The S_a parameter is the closest alternative to the R_a parameter.[9] However, they are fundamentally different because the areal, S parameters use areal filters in 3D whereas profile, R parameters, use profile filters in 2D [111]. Thus, utmost care must be exercised when they are compared. Similarly, the root mean square height, S_q parameter is designated as the root mean square value of the height within the sampling area, $\mathscr{A}$:

$$S_q = \sqrt{\frac{1}{\mathscr{A}} \iint\limits_{\mathscr{A}} z^2(x, y) \, dxdy} \,. \tag{3.31}$$

The S_a and S_q parameters are strongly correlated to each other [112]. The S_q parameter has more statistical significance as it is the standard deviation and is directly associated with surface energy and the angle of scattered light from a surface [111]. As heights are counted from the mean plane, S_p is always positive and S_v is always negative [106]. Thus, the S_z parameter is the sum of the absolute values of S_p and S_v:

$$S_z = \left| S_p \right| + |S_v| = S_p - S_v \,. \tag{3.32}$$

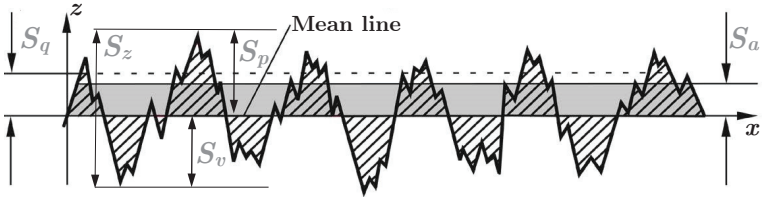

Figure 3.9: Reference sketch illustrating the $S-$amplitude parameters in a 2D profile.

[8] Absolute minimum height of the lowest point of the surface.

[9] The R_a parameter is the arithmetic mean of the absolute ordinate values, $z(x)$, within the sampling length, l_s [111].

Chapter 4

Modeling the Longitudinal AC Breakdown of Solid Interfaces

The purpose of this chapter is to develop a model to estimate the longitudinal AC breakdown strength of solid-solid interfaces. First, the electrical model of a solid-solid interface, consisting of cavities and contact spots, is provided. Second, the breakdown mechanisms involved in the discharge of cavities and breakdown of contact spots are modeled in individual submodels. Next, the complete breakdown model is constructed using the mechanisms modeled in the submodels. Finally, the main theoretical hypothesis based on the complete breakdown model is postulated to address the mechanisms dominating the longitudinal interfacial breakdown phenomenon in a sequence.

The shape, size, and number of cavities and contact spots strongly affect the breakdown strength of an interface. Since the dielectric strength of a gas-filled cavity is notably lower than that of bulk insulation, cavities are one of the weakest parts of the interface limiting the electrical breakdown strength [14]. Accordingly, cavity discharge (i.e., PD activity) can be presumed to start in the cavities first [51]. According to the postulated hypothesis in Section 1.4, it is assumed that the discharged cavities do not necessarily lead to the breakdown of contact spots immediately. The PD/interfacial tracking resistance of the material determines the endurance of the contact spots against breakdown [24, 63–65]. The electrical breakdown model of a solid-solid interface can then be reduced to the discharge of air-filled cavities and breakdown of contact spots enclosing those cavities.

Series connections of cavities and contact spots compose the electrical breakdown model of the interface where the applied voltage is distributed along the interface, as illustrated in Figure 4.1:

$$V_{app} = \sum_{j=1}^{n} V_{cav_j} + \sum_{j=1}^{n} V_{cnt_j}, \tag{4.1}$$

where V_{app} is the applied voltage across the dry interface, n is the number of cavity and contact spot pairs, V_{cav_j} is the voltage drop across j^{th} cavity, and V_{cnt_j} is the voltage drop across j^{th} contact spot located between two cavities, as presented in Figure 4.1. Note that the contact spots in the model stand for ideal void-free contact areas.

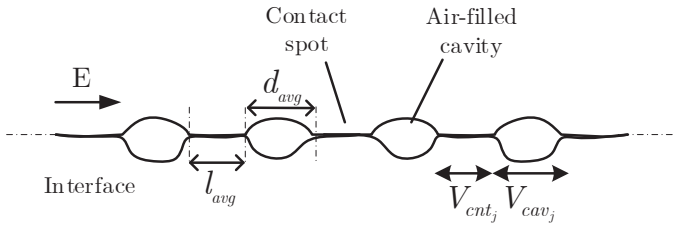

Figure 4.1: Illustration of an interface consisting of cavities and contact spots. Voltage drops at the cavities and contact spots are illustrated where E is the electric field strength at the interface in the longitudinal direction.

4.1 Estimation of the Longitudinal AC Breakdown Strength of Solid-Solid Interfaces

The interface breakdown model at solid-solid interfaces is based on two main mechanisms: discharge of cavities and breakdown of contact spots. Therefore, the interface breakdown model incorporates two submodels consisting of a model for the discharge of cavities and a model of the breakdown of contact spots. The statistical model proposed in Chapter 3 is used to develop the submodel for the cavity discharge, which estimates the breakdown strength of average-sized cavities, while the average cavity size varies depending on the elasticity, surface roughness, and contact pressure. The submodel for the breakdown of contact spots is developed using an empirical model, based on the interfacial tracking resistance of the solid materials. In this submodel, enhanced field strengths at the edges of discharged cavities are approximated by needle-needle electrode configuration.

4.1.1 Estimation of the Discharge Inception Field Strength of Air-filled Cavities

The field at which the dielectric strength of the gas in the cavity is exceeded is defined as cavity discharge inception field or, analogously, partial discharge inception field–PDIE. Under a homogeneous electric field, the PDIE of an air-filled cavity (E_{cav}) can be estimated using the well-known Paschen's law [14, 113]. The Paschen's approach is favored due to the lack of any better model [114, 115]. Illias [50] utilized an analytical expression to estimate the cavity inception field for streamer-type discharge in cavities as a function of cavity geometry, the pressure in

the cavity, the dielectric permittivity, characteristics of ionization process in the gas and the distance between the two electrodes [116–119]. In Figure E, Illias' model and Paschen's approach are compared for a wide range of electrode distances where both analytical expressions yield very similar results.

Regarding the size of the cavities arising at the interfaces in the light of the experimental and theoretical work, the portion of the Paschen's curve to the right of the minimum value, which covers a cavity size within 10 µm–1 mm, is considered and is plotted in Figure 4.2 for five different air-pressures in the cavity (p_c). The curves suggest a reduced inception field strength as the cavity size increases. Note that the curves represent the electric field values, not the voltage waveforms. The slopes of the voltage and field waveforms are opposite in the covered range of d. Readers are referred to Appendix E for the details.

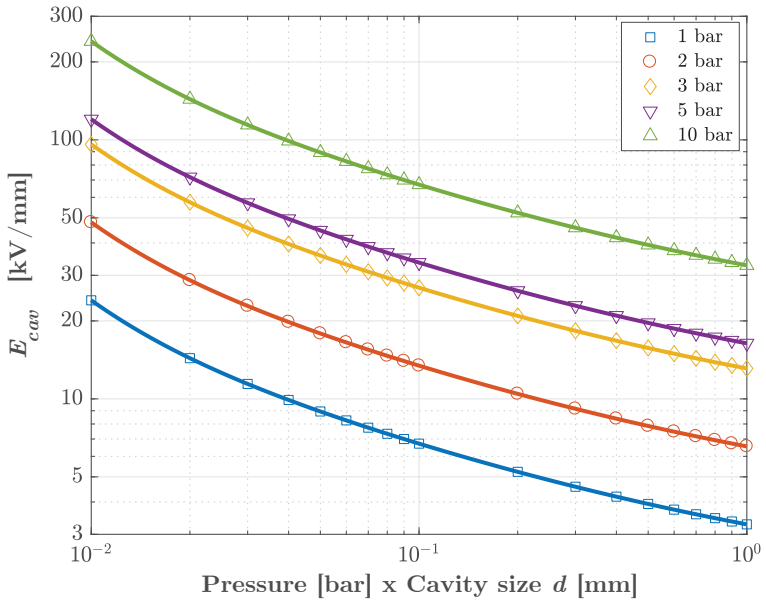

Figure 4.2: The Paschen's curve for air at various air pressure (1 bar = 0.1 MPa).

The BDS of a cavity, E_{cav} at a given pressure is analytically represented by the polynomial fit:

$$E_{cav}\,(p_c, d) = A\frac{p_0/p_c}{d^{\,2}} + B(p_c/p_0) + \frac{C}{d} + D\sqrt{\frac{p_c/p_0}{d}}\,, \tag{4.2}$$

where p_c is the pressure inside the cavity, atmospheric pressure $p_0 = 1\,\text{bar}$, $A = 0.00101\ \text{kV}\cdot\text{mm}$, $B = 2.4\ \text{kV/mm}$, $C = -0.0097\ \text{kV}$, $D = 2.244\ \text{kV}\cdot\text{mm}^{-0.5}$ [14]. The waveforms in Figure 4.2 are plotted using Equation (4.2).

Since the permittivity of air is less than the permittivity of the bulk material, the electric field strength in air-filled cavities is enhanced in the field direction by

the enhancement factor f with reference to the interfacial cavities and contact spots illustrated in Figure 3.6:

$$f = \frac{\gamma\, \varepsilon_{r_i}}{1 + (\gamma - 1)\, \varepsilon_{r_i}}\,, \tag{4.3}$$

where ε_{r_i} is the relative permittivity of the material (contact spots), and γ is the shape factor varying as a function of the geometry of the cavity [50]. As illustrated in Figure B.2 in Appendix B, γ varies based on the ratio of the axis parallel to the field to the axis normal to the field. γ is displayed as a function of the axis ratio for oblate and prolate spheroids in Figure B.3. For spherical cavities, $\gamma = 3$, whereas for ellipsoidal cavities elongated in the field direction, $\gamma \geq 50$. Enhanced fields within cavities with different geometrical shapes are also provided in Appendix B.

The estimated PDIE, i.e., PDIE^{e} stands for the field strength at the contact spots (E_{cnt}[10]), calculated by dividing the value read from the Paschen's curve by the enhancement factor f:

$$\text{PDIE}^{\text{e}} = E_{cnt} = E_{cav}/f. \tag{4.4}$$

For the determined cavity shape shown in Figure 3.6, $f \approx 1$ according to Equation (4.3). Since any direction of the field within the ellipsoid (with respect to the defined cavity shape in Figure 3.6) can be resolved into three orthogonal components, it is sufficient to consider the axis parallel to the field since the minimum value of PDIE is associated with the maximum path length in the field direction (critical avalanche length) [99,114,115]. Hence, the average length of the cavities in the direction of the applied field d_{avg} (calculated using Equation (3.21b)) is substituted for d in Equation (4.2). Depending on the elasticity and contact pressure, cavities can either be enclosed or form larger cavities or channels by connecting with other cavities at the interface. In the case of large cavities or channels, initially compressed air is assumed to be squeezed out and is vented to the surroundings. According to the right of Paschen minimum, however, the BDS of vented cavities, in which the gas pressure settles around the ambient pressure ($p_c \approx 1$ bar), is significantly lower than that of interlocked/enclosed cavities with p_c greater than 1 bar. Consequently, the vented cavities are assumed to dominate the mechanisms governing the interfacial cavity discharge, and PD activity starts in a cavity whose length, parallel to the electric field, is equal to or greater than d_{avg}, whereas it can be presumed that there is no discharge activity in cavities smaller than d_{avg} or in enclosed cavities having gas pressure higher than ambient pressure.

A flow diagram recapitulating all the steps in the model to estimate the discharge inception field of average-sized cavities is shown in Figure 4.3.

[10] **Important note:** The conventional abbreviation, PDIE, is modified here, where PDIE^{e} stands for the estimated PDIE values at the interface described in this section. PDIE^{m}, on the other hand, will later be defined to represent the experimentally measured PDIE values at the interfaces.

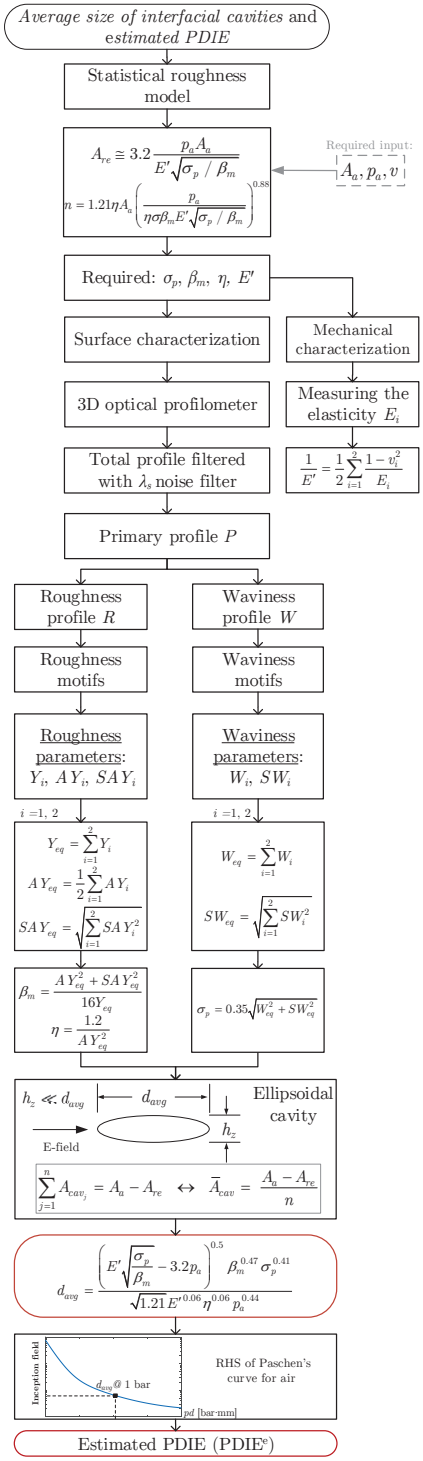

Figure 4.3: Flow diagram summarizing the steps of estimating the average size of the cavities and calculating the estimated discharge field strength of average-sized cavities.

4.1.2 Estimation of the Breakdown Strength of Contact Spots

The submodel for the estimation of the breakdown strength of contact spots (solid bulk material) incorporates two empirical models to estimate the enhanced local fields at the edges of the discharged cavities and the interfacial tracking resistance of the contact spots.

4.1.2.1 Estimation of Enhanced Local Fields at the Edges of Discharged Cavities

As Illias et al. [51] reported in their respective studies that strong non-homogeneous local fields occur at the edges of the discharged cavities enclosed by contact spots despite the uniform electric field (see Figure 4.4). The field strength reduces considerably in a discharged cavity due to the high electrical conductivity of the discharge spark. Until the discharge is quenched, the contact spots undergo an increased electric field, as illustrated in Figure 4.4, due to the increased voltage at the contact area. However, the enhanced fields may not be sufficiently high to induce a breakdown on the contact area [66]. Whether the resulting strong local fields can cause a complete flashover across the interface strongly depends upon the interfacial tracking resistance of the insulation [24, 63, 64].

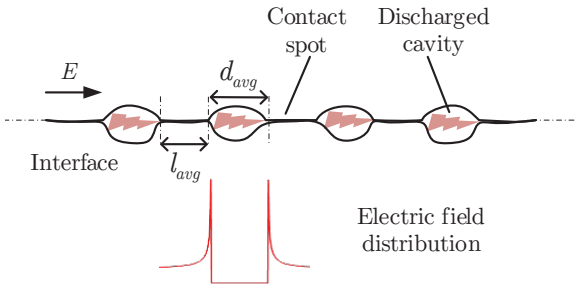

Figure 4.4: An illustration of the field lines at the interface in 2D profile from the field simulations performed using FEA software shown in Appendix B. The dimensions of the defined cavities are so small that the internal field is deemed effectively uniform [51].

We assume that the local enhanced fields at edges of contact spots can be emulated by a needle-plane (point-plane) or a needle-needle electrode configuration. The crest values of the field can then be estimated via empirical models as if the needle tips cause them. Subsequently, the interfacial tracking resistance of the contact spots can be checked to see if the contact spots could withstand the local field spikes or if an interfacial discharge would occur.

The field strength at the tip of a needle is a few orders of magnitude higher than the estimated intrinsic BDS of polymers [64]. The enhanced field at the edges of a discharged cavity emulated with a needle-needle geometry can be estimated by:

$$E_{enh} = \frac{V_{app}\sqrt{1 + r_n/l}}{r_n \operatorname{arctanh}\left[\frac{1}{\sqrt{1 + r_n/l}}\right]}, \tag{4.5}$$

where r_n is the radius of the tip of needle, V_{app} is the applied voltage, l is the thickness of the bulk polymer between the electrodes [64]. To calculate the V_{app}, the applied field E_{app} is multiplied by the the nominal thickness of the interface, d_{int}, since the applied field is homogeneous (Rogowski electrodes). In addition, to compute the thickness of the bulk insulation, l between the electrodes, the total length of the contact spots, i.e., effective interface length (l_{eff}) is required to be substituted for l in Equation (4.5). Based on the contact model shown in Figure 4.4, effective interface length l_{eff} is calculated by the summation of the average-sized contact spots:

$$l_{eff} = \sum_{j=1}^{\overline{n}} l_{avg} = l_{avg} \cdot \overline{n}\,, \tag{4.6}$$

where $\overline{n}$ is the number of the average-sized cavity and contact spot pairs in a single row vector as shown in Figure 6.13 and as illustrated in Figure 4.4.

4.1.2.2 Estimation of Interfacial Tracking Resistance of Contact Spots

Needle-plane type experimental configurations with different needle tip radii are extensively studied in the literature to examine interfacial tracking resistance of insulation materials under AC, DC or impulse [24, 63, 64]. Using empirical data, Fothergill [63] developed the following expression to estimate the interfacial tracking resistance E_{tr}:

$$E_{tr} = \left(\frac{16GE'}{{\varepsilon_0}^2{\varepsilon_r}^2\, r}\right)^{1/4}, \tag{4.7}$$

where the toughness G is a constant in $\mathrm{J/m^2}$, E' is Young's/elastic modulus in Pa, ε_0 is the permittivity of vacuum in F/m, ε_r is the relative permittivity of the dielectric medium, and r is the radius of the main tubular branch of the breakdown channel (i.e., interface tracking path) in m [14, 63]. The mechanism proposed here is operative at higher local electric fields and is a breakdown rather than an aging mechanism that predicts a breakdown time of $\lesssim 10^{-7}$ s from the initiation of interfacial tracking to discharge [14, 63]. Therefore, Equation (4.7) does not incorporate time as a parameter. In Figure 4.5, breakdown mechanisms in solid dielectric materials are categorized according to the time to breakdown. The proposed model for the interfacial tracking resistance could be deemed to belong to the electrical and/or electro-mechanical mechanisms [14]. Value of radius r depends on the agent initiating the breakdown streamer; such as a microvoid, an impurity particle, an

electrode irregularity, an electrical tree, or a feature of the polymer morphology and is assumed constant in a specimen [63]. In this model, the radius of the BD channel is assumed to be equal to the radius of the needle tip, i.e., $r = r_n$.

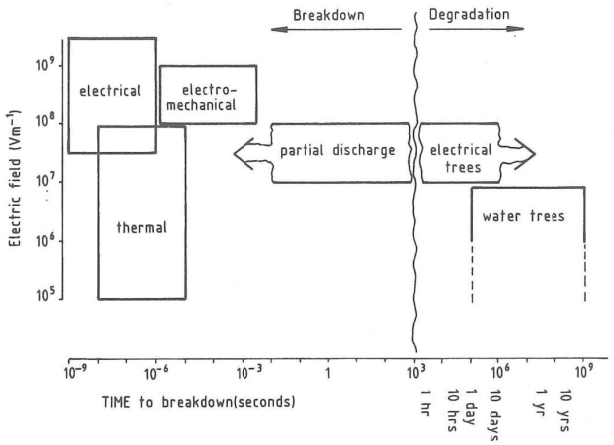

Figure 4.5: Time to breakdown and degradation vs. electric field amplitude for various electrical breakdown mechanisms in solid dielectric materials [14].

4.2 Sequence of Mechanisms Contributing to Breakdown under AC Ramp Excitation

The complete model to estimate the longitudinal AC BDS of solid-solid interfaces is illustrated in Figure 4.6. Using the submodels proposed in this chapter, a possible sequence from no discharge activity to a complete flashover at the interface (longitudinal BD of the interface) is proposed.

Since the dielectric strength of a gas-filled cavity is considerably lower than that of bulk insulation, the breakdown of air-filled cavities is assumed to take place initially. Therefore, cavity discharge and breakdown of contact spots will be initiated at different instants in a sequence. The order of these mechanisms can be explained with the help of the illustration shown in Figure 4.6. Note that the red waveform represents the AC ramp voltage applied in the experiments. The instants at which the mechanisms become active are represented with reference to the applied ramp voltage/field.

First, the inception of the cavity discharge takes place (represented by *instant I*), before which no discharge activity is assumed to occur at the interface. Until *instant II*, the contact spots endure the enhanced local fields across them, and in case the interfacial tracking resistance of the insulation is exceeded (at the *instant II*), the breakdown of the contact spots takes place, bridging the electrodes.[11]

[11]The submodels for the cavity discharge and contact spot discharge are based on the average size of the cavities [Equation (3.21b)] and the effective length of the contact spots [Equation (4.6)].

To elaborate on the activation order of the BD mechanisms, the time frame of a breakdown is dissected in four consecutive periods, as listed below:

1. *No PD:* This is the period from the application of AC voltage until the *instant I* in Figure 4.6. The electric field is not sufficiently strong to accelerate a free electron to start an avalanche mechanism in the cavities or absence of free electrons cause the delay of PD inception. Thus, no PD activity is observed in this period.
2. *Onset of PDs*: At *instant I*, the electric field is sufficiently high to initiate the persistent discharge activity in the cavities. However, the breakdown of contact spots does not occur as yet, because the interfacial tracking resistance of the polymeric contact spots can withstand the locally enhanced fields. Thus, only PD is observed.
3. *Initiation and propagation of the interfacial tracking*: It is represented by the *instant II*. As mentioned earlier, the submodel for the interfacial tracking mechanism is operative at higher local electric fields with a breakdown time of around 10^{-7} s [63]. Therefore, it takes only a fraction of a microsecond from the inception of the interfacial tracking to the breakdown of the contact spots between two discharged cavities.
4. *Breakdown of the interface*: The electrodes are bridged, and the destructive effects of the interfacial breakdown are clear at the material surfaces (as revealed in Chapter 8 and Appendix A.2).

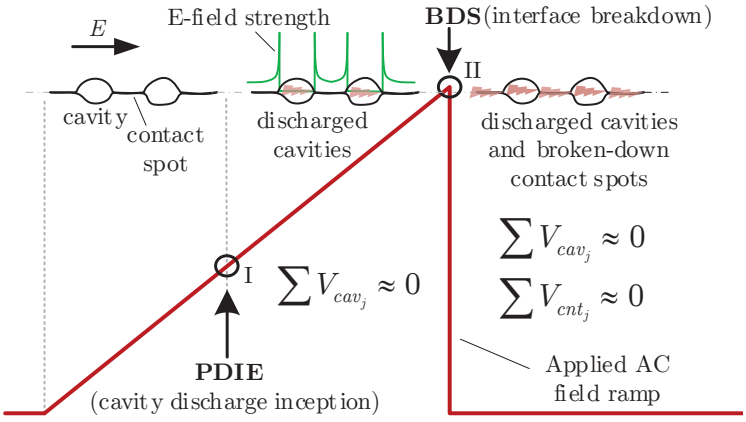

Figure 4.6: Activation sequence of the mechanisms with respect to the applied field ramp. Roman numerals, I and II stand for *instant I* and *instant II*, as referred to in the text.

Chapter 5

Deterministic Contact Model for Asperities at Solid-Solid Interfaces

This chapter provides a brief theoretical background for the deterministic interface contact model introduced in Section 2.3.2. The primary motivation for developing the deterministic model is to verify the output of the statistical model that is the backbone of the theoretical hypothesis. Secondly, the deterministic model is also used to simulate the deformation of the surface asperities in 3D as a function of the contact pressure, surface roughness, elasticity, and hardness of the favored insulation material, which provides a reliable, supporting basis for the discussion chapter. The model is based on the equivalent rough surface model, illustrated in Figure 3.2 and incorporates linear elastic and perfectly plastic materials in which the energy dissipation due to plastic deformation being considered. With this model, 3D in-contact topography and the respective pressure distribution are acquired.

5.1 Introduction to Variational Principle

The contact between real-life topographies leads to plastic deformations at the contact spots even under relatively small loads, as illustrated in Figure 2.8. Tian and Bhushan [42] built their theoretical model on a variational principle for both linear elastic and linear elastic-perfectly plastic materials. The use of the variational principle leads to a standard quadratic mathematical programming problem after an infinite-to-finite dimension transformation [16]. In the variational method, the real area of contact and contact pressure distributions are the variables, which minimize the total complementary potential energy [16, 42].

The variational principle employs a direct, quadratic numerical programming method that returns a unique solution for rough surface contact problems. Its computation time is substantially shorter compared to the conventional matrix in-

version technique because there is no additional iteration process involved in the variational approach [42]. Therefore, the solution for 3D rough surface contact problems with a large number of contact points becomes feasible. Solving a variational problem is identical to solving a minimum value of integral equation that can be approximated to a boundary value problem of differential equations for a mechanical system [16]. Two minimum energy principles, namely total elastic strain energy and total complementary potential energy, can be used for solving mechanical problems in the variational approach [16, 42].

In the cases where the real area of contact and the pressure distribution are uncertain, the minimum total complementary potential energy principle for rough surface contacts requires the minimum value of an integral equation that minimizes the total complementary potential energy of the contacting system. In Tian and Bhushan's model [42], the proposed theoretical model is based on the variational principle for both linear-elastic and linear elastic-perfectly plastic materials, where the plastic deformation of contact spots is covered for real contact surfaces. To solve the contact problem covering linear elastic-perfectly plastic surface contacts, the model depicted in [37] has been modified to account for the energy dissipation due to plastic deformations.

Almqvist [37] followed the Tian and Bhushan's model [42] when developing the deterministic roughness model utilized in this work. As mentioned in Section 2.3.2, the deterministic numerical roughness model in this thesis is based on Almqvist's diligent work [37].

5.2 Equations to Define the Mechanical Contact Problem

The elastic and plastic deformation of the surfaces and contact pressure are computed by minimizing the following energy equation that allows both 2D and 3D topographies [37]:

$$\min_{0\leq p_a\leq H_s}(F) = \min_{0\leq p_a\leq H_s}\left(\frac{1}{2}\int_{\Omega} p_a\,\delta_e\,d\Omega - \int_{\Omega} p_a\,(h_2 - h_1 - \delta_p)\,d\Omega\right), \tag{5.1}$$

$$W_m = \int_{\Omega} p_a\,d\Omega = \iint_{\Omega} p_a\,dx\,dy\,, \tag{5.2}$$

where Ω is an arbitrary area, H_s is the hardness of the softer material, p_a is the contact pressure, $\delta_e = z - d$ is the elastic deformation with reference to Figure 3.3, $h_g = h_2 - h_1$ is the gap between the undeformed surfaces, δ_p is the amount of plastic deformation, and W_m is the applied load. Equation (5.1) is limited by two main constraints such that the maximum pressure is limited to the hardness of the softer material i.e., $p_a \leq H_s$, while it is assumed equal to or greater than zero.

In this way, the local contact pressure increases with increasing normal force for elastic contact spots, resulting in larger real contact area.

For two elastic half spaces, the amount of deflection of elastic surface $\delta_e(x)$ at a given pressure is expressed as [37]:

$$\delta_e(x) = \int_{-\infty}^{\infty} K\,(x-s)\,p_a(s)\,ds + \text{constant}\,, \tag{5.3}$$

where the integral kernel K is given by [37]:

$$K\,(x-s) = -\frac{4}{\pi E'}\ln|x-s|\,, \tag{5.4a}$$

and

$$K\,(x_1-s_1, x_2-s_2) = -\frac{2}{\pi E'}\,\frac{1}{\sqrt{(x_1-s_1)^2+(x_2-s_2)^2}}\,, \tag{5.4b}$$

for 2D and 3D contacts, respectively and E' is calculated as shown in Equation (3.7).

5.3 Discretization of Surface Profiles

In order to obtain an approximate value of minimum complementary potential energy, the integral Equation (5.1) for the total complementary potential energy and Equation (5.3) relating surface displacement to the surface pressure are discretized into a mesh of small elements over the entire contact area.

As described in Figure 6.13, the measured surface profile of each specimen as shown in Figure 7.5 is stored in a 480×640 matrix. The assessment length in the row vectors of the measured profile is discretized into 10240 elements, resulting in an equivalent, discrete matrix with a size of 480×10240. The measured profile by the profilomoter is considered to have an assessment length of L, which is a fraction of thickness of the sample T, the total applied load W_m is thus scaled by L/T as described in [36]. The samples studied are of $L_x = 1.25$ mm, $L_y = 0.94$ mm, and $T = 4$ mm.

The integral equation describing the relation between contact pressure and elastic deflection Equation (5.3) is by the application of a finite difference method (FDM), discretized into:

$$\delta_{ei} = \sum_{j}^{M} K_{ij}\,p_j\,, \tag{5.5}$$

where M is the total number of initial contact points, K_{ij} is the arbitrary discretization of K, and p_j is the discretized contact pressure in each element.

Numerically, the equation defining F is a quadratic form, because of the specific relation between the elastic deflection and the pressure:

$$F_i = \frac{1}{2}\sum_{i}^{M} p_i \sum_{j}^{M} K_{ij}\, p_j - \sum_{i}^{M} p_i \left(h_{2i} - h_{1i} - \delta_{p_i}\right), \tag{5.6}$$

which can be reformulated in the following matrix form [37]:

$$F = \frac{1}{2}\,\mathbf{p}\,\mathbf{K}\,\mathbf{p} - \mathbf{p}\left(\mathbf{h_2} - \mathbf{h_1} - \boldsymbol{\delta}_\mathbf{p}\right). \tag{5.7}$$

In order to minimize the total complementary potential energy F, the value of pressure p should be determined such that $\nabla F = 0$. The gradient $\nabla \triangleq \partial/\partial\,\mathbf{p}$ of F with respect to pressure p is [37]:

$$\begin{aligned} \nabla F &= \mathbf{K}\,\mathbf{p} + \boldsymbol{\delta}_\mathbf{p} - (\mathbf{h_2} - \mathbf{h_1}) \\ &= \boldsymbol{\delta}_\mathbf{e} + \boldsymbol{\delta}_\mathbf{p} - (\mathbf{h_2} - \mathbf{h_1}). \end{aligned} \tag{5.8}$$

5.4 Solution Technique

The solution method proposed in this section minimizes the total complementary potential energy F using a nested iterative process finding p such that $\nabla F = 0$. The force-balance condition is controlled by an inner loop in the iterative process, and the outer loop continues to iterate until all contacting points lie sufficiently close the contact plane [37]. Since forces in the opposite direction to the motion of contacting surfaces are permitted at the contact interface, the quest for a minimum value of Equation (5.6) is limited by $p_j \geq 0$ where $j = 1, ..., M$. It should be noted that the number of final contact spots satisfying the restriction, $p_j \geq 0$, is likely to be lower than M. Overall, this solution technique is claimed to be very robust as the algorithm never diverged [16, 37].

In the computer program running the algorithm, initially, 3D surface profiles of the two surfaces forming the interface are imported. Following this, the equivalent rough contact surface (sum surface) is generated. Subsequently, the contacting surface is discretized into smaller elements corresponding to the surface asperities. For a given rigid body, then, an iteration loop is executed to compute elastic deformation. In case the pressure at any contact spots exceeds the material hardness (main constraint of the algorithm, as mentioned at the beginning of the chapter), a fraction of the surface at that particular node is discarded, and the type of the contact spot is then marked as plastic. A new solution is then attained based on the modified surface containing plastically deformed spots. In case the pressure at plastic contacts does not reach a predefined level, a part of the plastic deformation at those specific points must be removed [37]. Thus, the iterative process

continues until the pressure at all plastically deformed points lies within the region spanned by the specified lowest level and the hardness of the softer surface material at the applied load [37]. When the inner loop is complete, an influence matrix is constructed to correlate the contact pressure to the displacements based on the location of the pressure element and contact points. Following this, the minimum value of the total complementary potential energy incorporating the information of the displacement and pressure is obtained using direct quadratic mathematical programming technique [42]. The analysis is run for contacts with positive pressure $p_j > 0$. The iterations continue until $\delta_{\mathbf{e}}$, $\delta_{\mathbf{p}}$ and $\mathbf{p}$ satisfy Equation (5.7). Figure 5.1 presents a flow chart of the main algorithm. The main advantage of this algorithm is that the corresponding contact pressure for a given rigid body approach can be obtained directly from a single minimization process [42]. Hence, the additional iteration cycles due to the conventional matrix inversion methods are eliminated, and the iteration cycle is significantly accelerated [42].

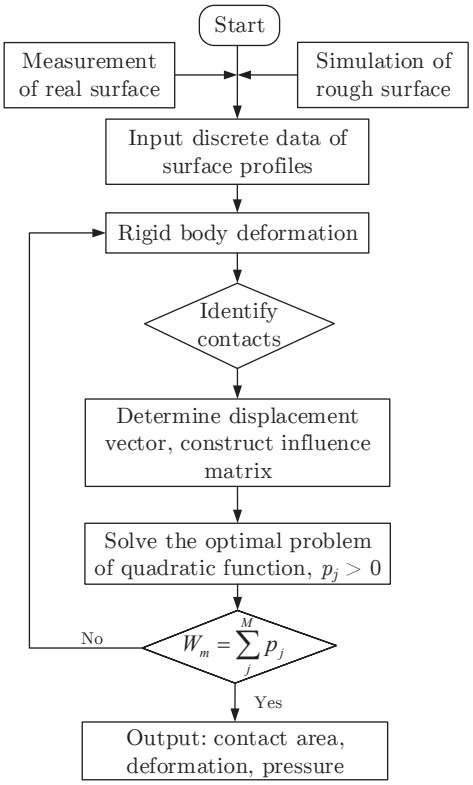

Figure 5.1: Flow chart of the computer program for contact analysis of two rough surfaces [42].

5.5 Computation of Real Area of Contact

The number of discretized elements that have a pressure value higher than zero (N_{cnt}) is given by:

$$N_{cnt} = \frac{1}{n_i} \sum_{i=1}^{n_i} \sum_{j=1}^{n_j} \left| \operatorname{sgn}(p_{ij}) \right|, \tag{5.9}$$

where sgn represents the signum function that extracts the sign of the contact pressure. In the deterministic model, the contact pressure is zero at the asperity peaks whereas it is a nonzero positive real number at the contacting points, represented as:

$$\operatorname{sgn}(p_{ij}) = \begin{cases} 1 & \text{if } p_{ij} > 0\,, \\ 0 & \text{if } p_{ij} \leq 0\,. \end{cases} \tag{5.10}$$

Based on Equation (5.10), $\left| \operatorname{sgn}(p_{ij}) \right|$ in Equation (5.9) reduces to $\operatorname{sgn}(p_{ij})$. The number of discrete elements, N_d, is then given by: $N_d = n_i \times n_j$. The ratio of the total contact area to the nominal area $A_{re,d}/A_a$ can then be calculated as a fraction of the number of discretized elements N_d such that:

$$A_{re,d}/A_a\,(\%) = \frac{N_{cnt}}{N_d} \times 100\,, \tag{5.11}$$

where the subscript d in $A_{re,d}$ represents the estimated real contact area in the discrete environment of the deterministic model to differentiate it from the A_{re} in the statistical model. As mentioned in Section 5.3, the discretized surface data are stored in a 480×10240 matrix, where $n_i = 480$ and $n_j = 10240$.

5.6 Representation of Numerical Data

The output of the deterministic model is displayed in various types of plots. First and foremost, contour plots and surface plots are extensively used to visualize the variation of surface texture from light load to heavy load where large cavities are broken into smaller ones as the contacting area expands. Furthermore, scatter plots are favored when displaying the simulated contact pressure values at each contact spot in a 3D plane, which is an extended version of the distribution displayed in Figure 2.8(b). The main results are shown in Section 11.2 whereas supplementary information and detailed results are provided in Appendix C.

Use of contour lines facilitates the representation of lines of equal height on a map of a topographic surface. Points on microscale surface maps represent heights

measured from a reference surface, which is represented by a horizontal plane defining the zero level by convention [106].

Contour lines are extracted from the intersection of the surfaces with horizontal planes at different heights as illustrated in Figure 5.2(a). An array of contour lines is generated by shifting the plane to evenly spaced height levels, as illustrated in Figure 5.2(b).

Contour plots in this work are utilized to represent the amplitudes of the asperities and area of cavities and contact spots at the interface. With the aim of increasing readability, different levels are colored using color maps, where red indicates the highest peak and white indicates the zero level.

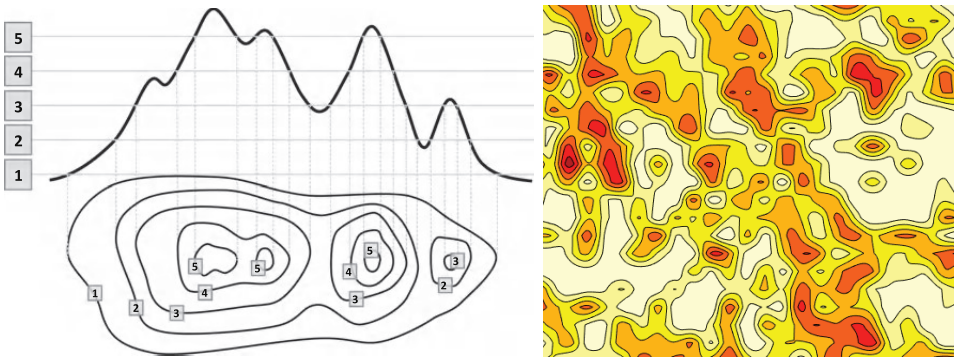

(a) (b)

Figure 5.2: (a) Contour lines representing the surfaces with planes at different amplitudes [106]. (b) Filled-contour lines colored based on height/amplitude.

Chapter 6

Experimental Methodology

This chapter provides a detailed overview of the methodology adopted when performing the experimental work. Three types of experiments were executed: AC breakdown tests, PD tests under AC excitation, and discharge-monitoring tests using a camera.

6.1 Test Samples

As mentioned in Chapter 2, the elastic modulus can be increased for the same material by adding micro- and nano-scaled zinc oxide, nano-scaled zirconia particles, and silica nanoparticles [59–61]. However, due to time, scope and facility constraints, we used different materials with different moduli to vary the elastic modulus.

For the AC breakdown and PD measurement experiments, four different polymers were used: silicone rubber (SiR), cross-linked polyethylene (XLPE), filled epoxy resin (EPOXY), and polyether ether ketone (PEEK). Source materials and methods to prepare each material in the desired dimensions are shown in Table 6.1. *Cast* refers to the polymers we molded and cast in our laboratories whereas *cut* stands for re-dimensioning from bulk insulation ordered in large chunks. The relative permittivities of SiR, XLPE, EPOXY, PEEK, and glass are 2.8, 2.3, 4.6, 2.8, and 3.8, respectively [120–124].

For the discharge-monitoring experiments, one of the polymers is replaced with a glass sample of the same size as the polymer sample. We had the glass samples (see Figure 6.1) produced in the desired dimensions at the Glass Workshop at NTNU (Glassblåserverksted). They are extremely smooth especially at the surfaces normal to the direction of the camera lens and are durable against applied contact force. The surface smoothness degrees of the glass samples are quantitatively presented in the next chapter.

Table 6.1: List of polymers and the preparation method.

Polymer	Source	Method
SiR	Two component, liquid silicone rubber	Cast
XLPE	145 kV power cable (Super clean peroxide cross-linked)	Cut
EPOXY	Alumina pre-filled epoxy resin	Cast
PEEK	High-viscosity, unreinforced PEEK	Cut
Glass	–	Ordered*

* Cast and polished by the glass workshop at NTNU.

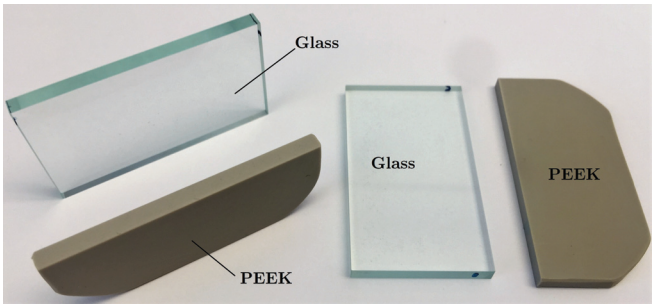

Figure 6.1: Glass samples prepared for the discharge-monitoring experiments.

6.1.1 Sample Preparation

All XLPE and PEEK used were cut in the size of 4 mm × 55 mm × 25 − 30 mm rectangular prisms. The thickness of the samples (i.e., the length of the interface) is 4.0 mm. Likewise, the molds manufactured to cast SiR and EPOXY samples are designed such that the end products become in the same size with XLPE and PEEK samples, which is 4 mm × 55 mm × 25 − 30 mm (see Figure 6.2). Note that the heights of the samples vary within 25 − 30 mm to compensate for extra sanding in case it is needed or for imprecision upon cutting. The details regarding the casting of SiR and EPOXY samples are provided briefly in Appendix D.1.

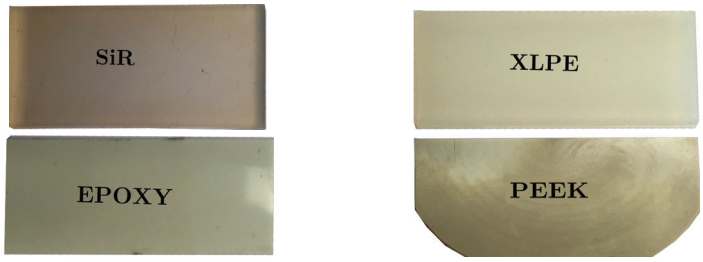

Figure 6.2: Four different polymers utilized to form solid-solid interfaces.

6.1.2 Contact Surface Preparation

The contact surfaces of the samples were prepared using a STRUERS Abramin tabletop, rotating grinding machine (see Figure 6.3(a)). The specimens were fixed on a steel rotating disk, as shown in Figure 6.3(b), and a round, silicon carbide sandpaper of the desired grit was placed on the rotating plane. Four different sandpapers with different grits (#180, #500, #1000, and #2400) were used. The speed of the rotating plane was set to 150 rpm, and the force pressing the steel disk towards the sandpaper was fixed to 300 N during the polishing of all the samples, ensuring that all surfaces underwent the same procedure.

Since the SiR is somewhat soft, attaining an unstrained surface contact was challenging. To cope with this challenge, SiR samples were sandwiched between XLPE samples when grinding, as shown in Figure 6.3(b). The samples were sanded for 2–3 minutes with a continuous flow of water to remove any loose materials and polymer remnants, and to avoid heating caused by friction. After assessing if the polishing was successful, samples were rinsed in tap water and were then dried using filtered compressed air. Finally, they were briefly washed with isopropanol to remove any remnants that might have adhered to the samples and were left to dry at room temperature. Note that the terms; *grinding*, *sanding*, and *polishing* are used interchangeably in this work.

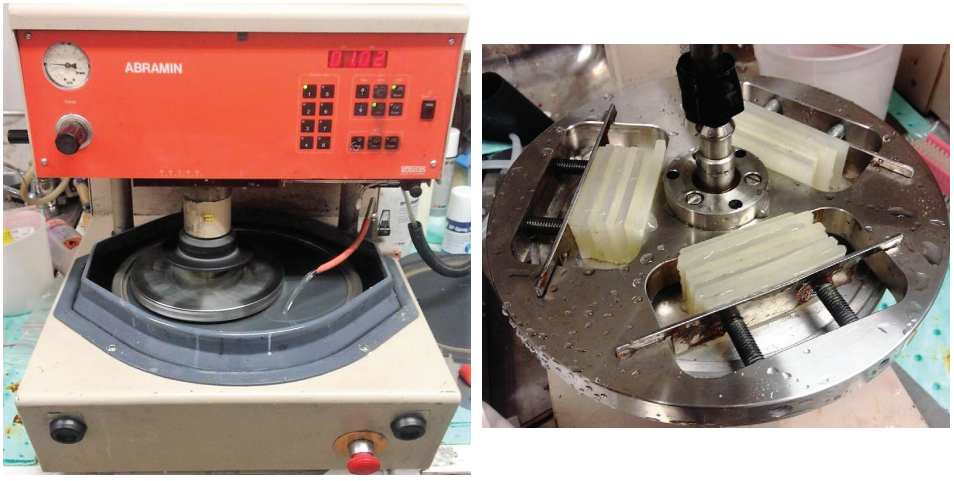

(a) **(b)**

Figure 6.3: (a) The STRUERS Abramin rotating grinding machine while in use. (b) Surface polishing of the samples. SiR samples are sandwiched between XLPE samples and are fixed on the rotating disc with the help of steel plates.

6.1.3 Dry-, Wet- or Oil-Mate Samples

Dry-, wet- and oil-mate interfaces have been tested in the AC breakdown experiments. To assemble dry-mate interfaces, polished surfaces were mated using clean lab gloves and were placed between the electrodes, and then the contact pressure was applied. Last, the container was filled with oil. For the wet-mate interfaces, the surface of the bottom sample was subjected to tap water with a volume of approx. 10 µl using a laboratory pipette prior to placing the top sample. A similar methodology was pursued in the case of oil-mate samples. In fact, some of the injected water droplets or oil droplets are likely to be squeezed out due to the applied contact pressure. Likewise, they are likely to have been broken into smaller droplets which spread out and span a larger area at the interface.

6.2 AC Breakdown Experiments on Polymer Interfaces

6.2.1 Experimental Setup for AC Breakdown Testing

A simple illustration of the test arrangement with the dimensions of the core components is depicted in Figure 6.4. There, two polymer samples were positioned on top of each other between two Rogowski electrodes, forming a 4 mm-wide interface. Detailed sketches and photos from the setup used in the HV laboratory can be found in Appendix F.

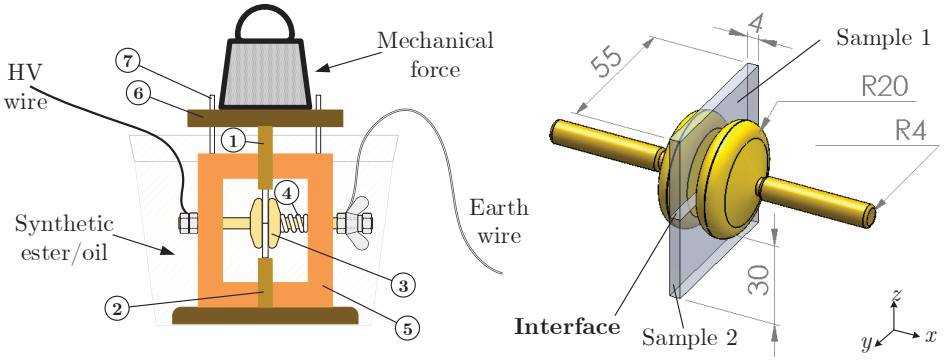

Figure 6.4: Mechanical test setup used in the AC breakdown experiments: (1) Movable (upper) pressure transfer block. (2) Fixed (lower) interface pressure keeper block. (3) Rogowski-shaped electrodes. (4) Helical spring. (5) Supporting frame. (6) Epoxy plate. (7) Weight stabilizing epoxy bars.

Figure 6.5 presents the complete electrical test setup. A 50-Hz variac ($0 - 230$ V) was used to energize the primary side of a 100 kV transformer, generating AC ramp voltage on the secondary winding at the rate of 1 kV/s. A water resistor with the resistance of 300–400 kΩ was employed to limit the breakdown current. In addition, a voltage divider was connected in parallel to the test object to transmit secondary voltage information to a PC via a data acquisition unit.

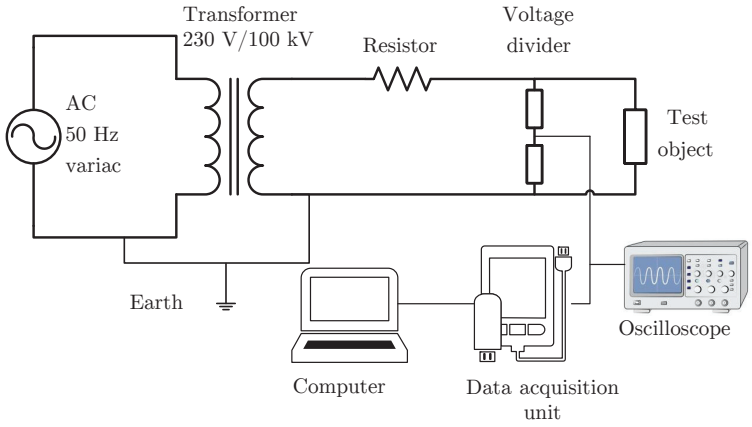

Figure 6.5: Sketch of the electrical circuit used in the AC breakdown experiments.

6.2.2 Test Procedure for AC Breakdown Testing

The desired contact pressure was exerted using weights varying between $3 - 75$ kg to press the samples vertically against one another, as illustrated in Figure 6.4. The average contact pressure is then calculated using the nominal contact area of $A_a = 4\,\text{mm} \times 55\,\text{mm} = 220\,\text{mm}^2$. The applied pressure levels were determined via preliminary tests, where the samples and the interface were checked against deformation and ester (oil) penetration. For instance, the interface between XLPE–XLPE could not be tested above 1.67 MPa due to deformation of the samples. Likewise, the SiR samples deforming beyond 0.27 MPa prevented them from having been tested at higher contact pressures. All the breakdown tests were performed with the setup submerged in a container filled with synthetic ester oil (Midel 7131 [125]) to prevent any external flashover. To avoid ester from penetrating the interface, we applied the contact pressure before filling the container with the ester. The interface was also tested against ester penetration under oil-mate conditions, as explained in the next section.

6.2.3 Data Processing Techniques for AC Breakdown Tests

For each interface at each contact pressure, eight measurements were performed using a virgin pair of samples every time. The obtained results were statistically assessed using the two-parameter Weibull distribution. Details regarding the analytical description of the Weibull distribution are provided in Paper I as well as in [14, 114, 126]. In most of the figures, the nominal value of the Weibull (i.e., 63.2%) with the 90% confidence intervals (CI) were used. Also in the results and discussion, the 63.2% values were used to make comparisons. Goodness-of-fit in each case was tested following the guidelines in [127]. Note that data represented in Weibull graphs, as well as the 63.2 percentile and 90% CI values, make use of the rms voltage values since the experiments were executed under AC excitation.

6.3 AC Partial Discharge Experiments on Polymer Interfaces

6.3.1 Experimental Setup for PD Testing

Figure 6.6 shows the setup used for the PD inception field detection. The setup incorporates an AC (50 Hz) high voltage supply (100 kV PD free transformer), a test object, a 100-pC-coupling capacitor, a coupling device (Omicron CPL measuring impedance unit), a PD detector (Omicron MPD 600) with a rechargeable battery pack (MPP 600), which is connected to a USB controller/converter (MCU 504) via fiber optic cables, and a personal computer that shows the PD output using the Omicron software MPD and MI 1.6.7. The system noise was lower than 100 fC, and the PD detection threshold was set to 0.5 pC during tests, which is the PD sensitivity of the system. The time resolution of PD patterns is less than 2 ns, which ensures a high degree of accuracy for the detected discharge pulse. Detailed information and photos from the real setup can be found in Appendix F.

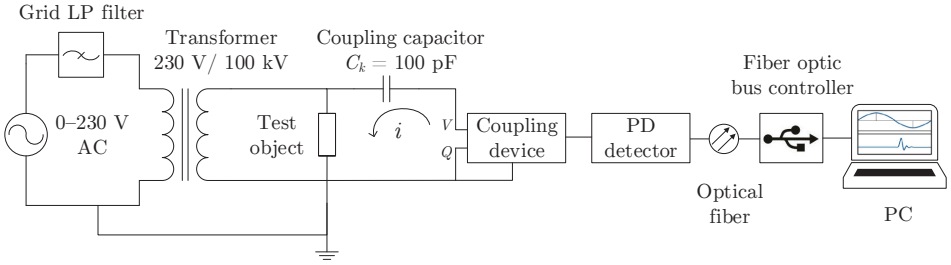

Figure 6.6: Illustration of the PD detection circuit used in the PD experiments. Fiber optic bus controller converts optical signals transmitted by the PD detector into electrical signals processable by the PC. Coupling device stands for a sophisticated measuring impedance.

The value of the coupling capacitor, C_k is selected as 100 pF with the voltage rating of 140 kV. The PD detection unit is placed in series with the coupling capacitor to prevent any damages in case the test object fails during the experiment. Thus, the short circuit current does not pass through the PD unit, and the PD detector is protected by C_k if the test object fails. The concept of the PD detection system is based on measuring the current pulse across the test object (i.e., direct measuring technique). A brief explanation of how the PD detection unit works is as follows: when a discharge occurs in the test object, charges are transferred from the coupling capacitor, C_k to the test object to compensate the voltage drop across the test object. As a result, a current pulse i of short duration, which is within the nanoseconds range flows in the circuit and a voltage pulse, V is generated across the coupling device. The amount of charge transferred is called the apparent charge q_a [128].

Before each experiment, the system is calibrated. The MPD 600 system allows charge calibration to be performed digitally using its graphical user interface (GUI). A charge calibrator is connected across the terminals of the test object during calibration, which injects a calibration charge at a predefined amplitude and polarity. Details on how the calibration was performed is given in Appendix F.2.

6.3.2 Test Procedure for PD Testing

To provide reasonable grounds for the comparison between the AC breakdown and PD tests, the same type of AC voltage ramp of 1 kV/s was applied as performed in the AC breakdown tests. When the PD activity started, the voltage was maintained for 2 minutes at the inception voltage V_i. Following this, the voltage was reduced to zero, and a five-minute interval was given before repeating the procedure. Four virgin pairs of samples were used in each experiment, and each pair was tested three times with five-minute breaks in between. Hence, 12 measurements in total were recorded for each set of PD tests. An illustration on a PD measurements is provided in Appendix F.2.

Furthermore, the sources of PDs were checked if they were caused by microvoids at the interface before the results were deemed acceptable. The procedure was as follows:

First, the setup was tested without any polymers between the electrodes. The electrodes were separated by a 4-mm gap which was filled with oil (setup immersed in the oil-filled container). If no PD was recorded at relatively high voltages, the electrodes and the setup were deemed to be PD-free. Secondly, the test arrangement was tested without the presence of a polymer interface by using a single piece of 4-mm-thick XLPE sample whose length and height was approximately as large as two samples combined. If no PD was recorded, then microvoids were considered as the sole source of PD, which was further validated by testing the system using polymer interfaces. Then, the PD inception field strength, PDIE, values for the test setup was determined for each case.

6.3.3 PD Data Processing Techniques

The main results are displayed by using the phase-resolved partial discharge analysis, PRPDA, as the phase information is critical when interpreting the PD results shown in Chapter 9. The PRPD data-sets obtained by the PD acquisition unit are exported to MATLAB® compatible format (ASCII) using a script developed at NTNU, a simple version of which is available in [129]. The data are then post-processed using another MATLAB® script to generate statistical data such as the number of PDs per cycle, mean charge magnitude, and total charge magnitude, which is available in [50].

On the other hand, pulse-sequence analysis, PSA, enables to find out the sequence of PDs whereas PRPDA allows the statistical data to be extracted from the phase-charge magnitude information. The PD sequence information is lost in the PRPDA while statistical data cannot be extracted in the PSA [52].[12]

PSA is also carried out for the PD data obtained in the experiments. The results obtained by the PSA are shown in Appendix A.3.1.2 to complement the PRPDA data. A MATLAB® script developed at SINTEF Energy Research to generate/extract PSA data from PRPDA data is also available in [129].

Finally, for some PD experiments, the obtained results were statistically assessed using the two-parameter Weibull distribution, as in the case of AC breakdown experiments.

6.4 Experiments on Monitoring of Interfacial Discharges

The main purpose of the discharge experiments is to monitor discharge activities taking place at solid-solid interfaces, that might lead to a complete flashover at the interface. Simultaneously, PD inception field strength values and the energy involved in the discharge activities are also measured to be correlated with the images of discharge activity at the interface.

6.4.1 Experimental Setup for Discharge-Monitoring

The test setup used in the AC breakdown experiments could not be used to monitor the light originating from the discharges because the direction of the force and camera coincides (in the vertical direction). Therefore, a new setup was designed to enable a CCD camera to be placed above the setup. In the new design,

[12] Phase-resolved partial discharge analysis (PRPDA) is based on the charge magnitude with reference to voltage phase whereas pulse-sequence analysis (PSA) is based on time and voltage data of PDs. The PSA enables users to find out the sequence of PDs whereas PRPDA allows the statistical data to be extracted from the phase-charge magnitude information. Therefore, the PD sequence information is lost in the PRPDA while statistical data cannot be extracted in the PSA [52].

the mechanical load is achieved with the help of screws and bolts, while the applied force is measured using two identical S-shaped load cells connected to two separate PCE Digital Force Gauges (PCE-FB 2K [130]) to ensure the same pressure magnitude is exerted at both edges of the top sample. A pair of Rogowski-shaped electrodes similar to those fixed in Figure 6.4 is used.

Figure 6.7 illustrates the complete setup incorporating the CCD camera, the mechanical setup, and the electrical components used in the BD testing: the variac and the transformer. In addition, the coupling capacitor and the MPD 600 PD acquisition unit used in the PD experiments are also connected to the system to simultaneously obtain discharge patterns.

Core parts of the test object are illustrated in Figure 6.8 whereas Figure 6.9 provides the top view and section view of the setup. The electrode with the spring allows the movement in the horizontal direction to place the samples conveniently and accurately. It also adjusts to the thickness of the samples and provides firm contact between the electrode and the samples. An O-ring is placed for sealing outside the container. The other electrode is fixed with the help of a bolt with threads.

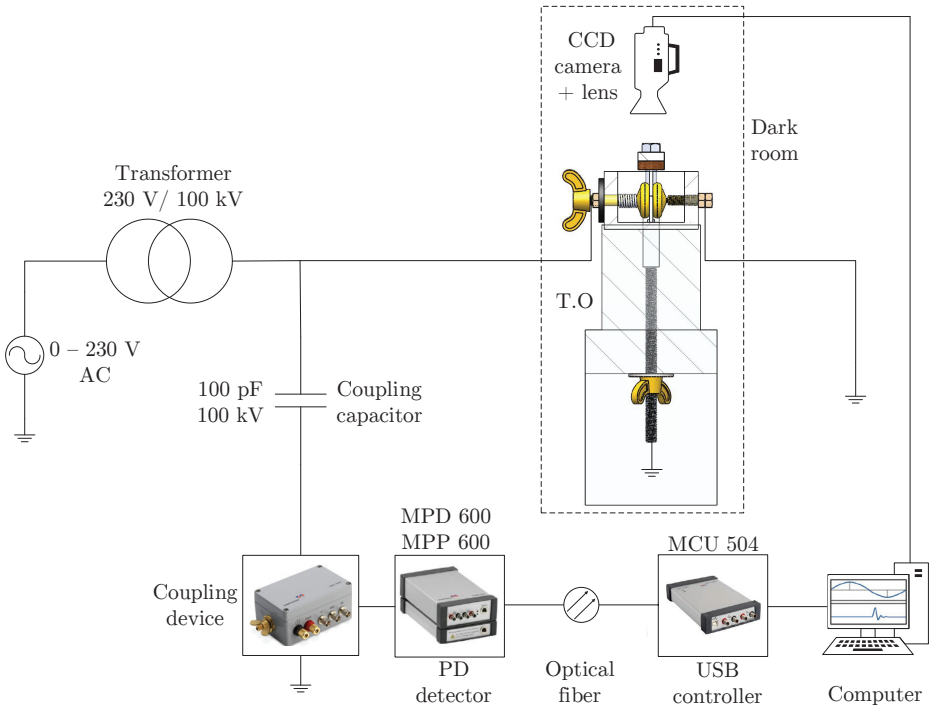

Figure 6.7: Illustration of the test setup for the interface discharge-monitoring experiments. The voltage values are given in rms. (T.O: Test object).

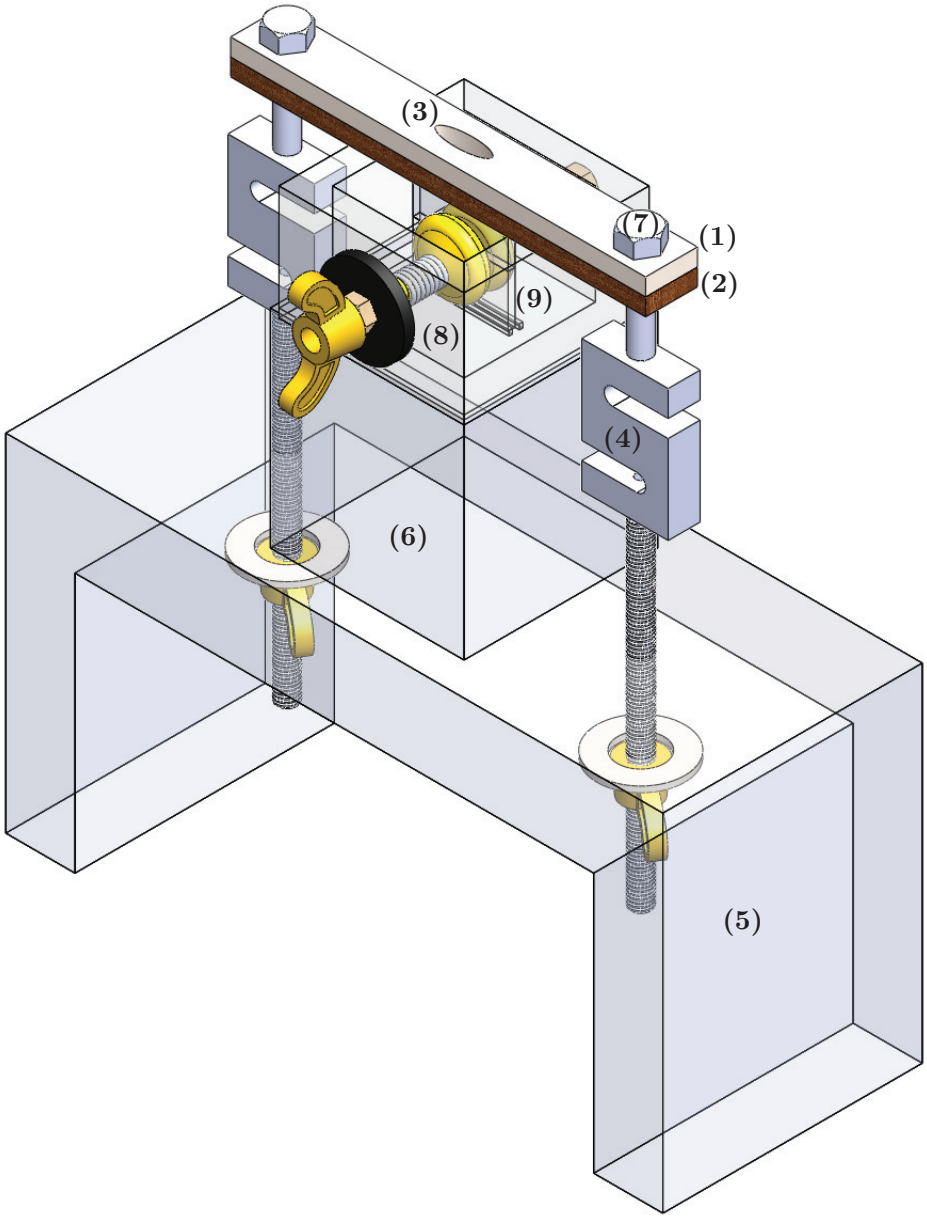

Figure 6.8: Isometric view of the setup used for discharge-monitoring tests: (1) Stainless steel metal plate with hollow window for camera monitoring. (2) Wooden plate with hollow window (identical to 1). (3) Punched window for the camera monitoring. (4) Load cell connected to the digital force measurement gauge. (5) Main wooden base. (6) Upper support base for the glass container. (7) Bolts attached to force gauge for clamping. (8) Plexiglass container with the electrodes (40-mm diameter). (9) Polymer (bottom) and glass (top) samples (4 mm $\times$ 55 mm $\times$ 25 $-$ 30 mm).

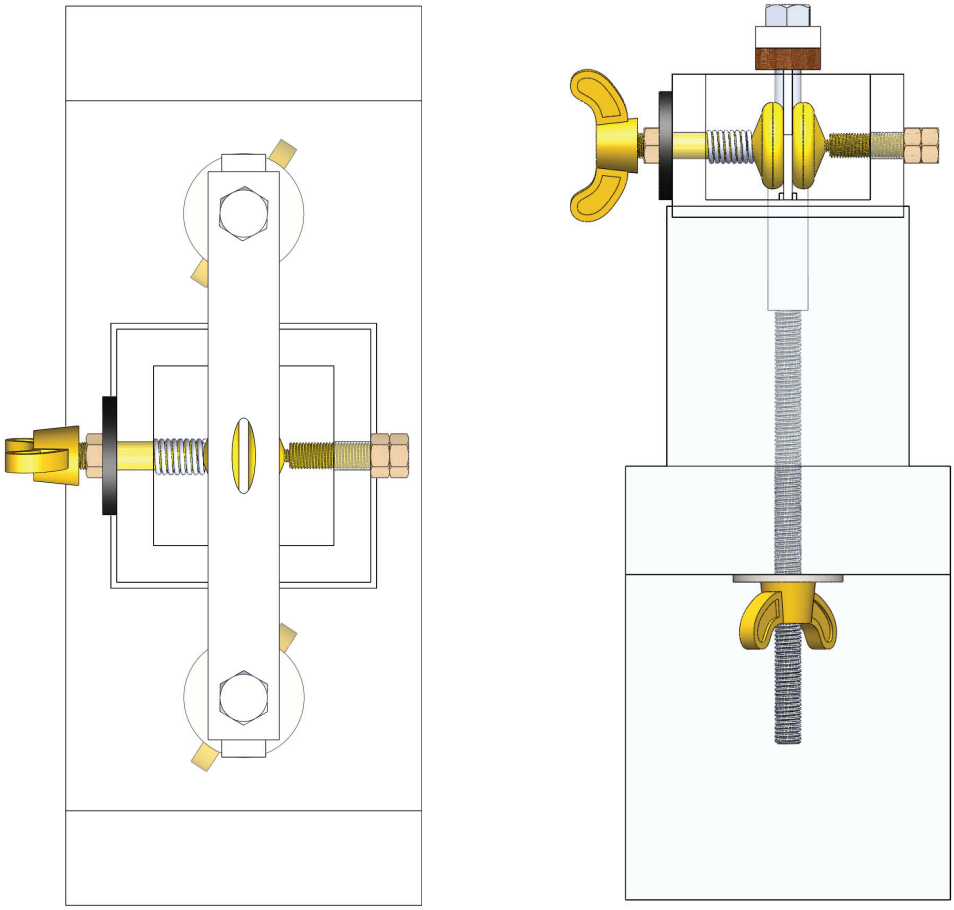

(a) (b)

Figure 6.9: Additional views for the test setup shown in Figure 6.8: (a) Top view to highlight how the CCD camera overlooks the interface. (b) Section view to show the configuration of samples placed between the electrodes.

6.4.2 Type of Samples

Discharge-monitoring tests were performed using glass–polymer interfaces, as explained in Figure 6.1. The top sample is a smooth glass sample in the same dimensions as the bottom polymer sample. The primary purpose of using a glass sample is to monitor the interface through a transparent test sample. For the bottom sample, PEEK was selected because it is the hardest material among the studied materials that can withstand the pressure from the glass without being considerably deformed. Besides, its (estimated) interfacial tracking resistance is the highest of all, which means that it is more likely to withstand the discharge activity longer at the interface. EPOXY samples could have been used for the same

purpose since they are equally hard and have high (estimated) interfacial tracking resistance. However, as explained in Section 6.1, EPOXY samples were cast in the laboratory, which is a time-consuming process yielding only 16 new samples in a batch in the best case (see Figure D.4(b)) in contrast to the easy procurement of PEEK samples in large amounts. Therefore, PEEK was favored over EPOXY.

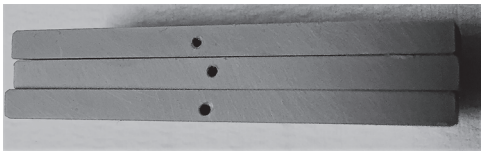

Figure 6.10: Three PEEK samples with cylindrical cavities of 1 mm diameter.

In Chapter 10, it is addressed that the experimental challenges prompted the use of a large artificial cavity at the interface to initiate PD at a lower voltage without inducing an interfacial breakdown immediately. Cylindrical-shaped artificial cavities with diameters of 1 mm were drilled at the surfaces of polymer samples as shown in Figure 6.10. Scanned surfaces of the PEEK samples with the cylindrical cavities will be shown in Section 7.2.2.

6.4.3 Camera

A CCD camera with an image sensor from Photometrics Model no. QuantEM 512SC is used for monitoring the interfacial discharge activity (see Figure 6.11(a)).[13] It will be referred to as "CCD camera" henceforth. A computer is used to control the camera via MetaMorph software version 7.6. A long-distance microscope lens is attached to the CCD camera to be able to monitor the interface through the open window. The lens provides focus adjustments to maximize the quality of the images obtained.

The camera and the metal part of the base are electrically grounded to protect the camera from any damage should unexpected flashovers occur. This is rather unlikely due to the wide gap between the camera and the HV electrode being immersed in oil. As the CCD camera is extremely sensitive to light, a dark-room environment is established using a thick black fabric fold with a couple of layers, as depicted in Figure 6.11(b).

[13] CCD image sensors use top-notch imaging technology to maximize pixelation and exposure times. They employ a small, rectangular chip of silicon called a charge-coupled device to muster and record incoming light rather than a film. The silicon chip is a solid-state electronic component composed of light-sensitive cells called photo-sites. Each photo-site is its own pixel, so a minuscule area in a photograph can contain hundreds of thousands of pixels. When incoming light strikes the photo-site, the photoelectric effect creates and builds an electron charge for as long as exposure occurs. The electrons are then "stored" in their individual cells until the analog-to-digital converter unloads the array, counts the electrons, and reassembles them into the main picture that is sent to the computer [131].

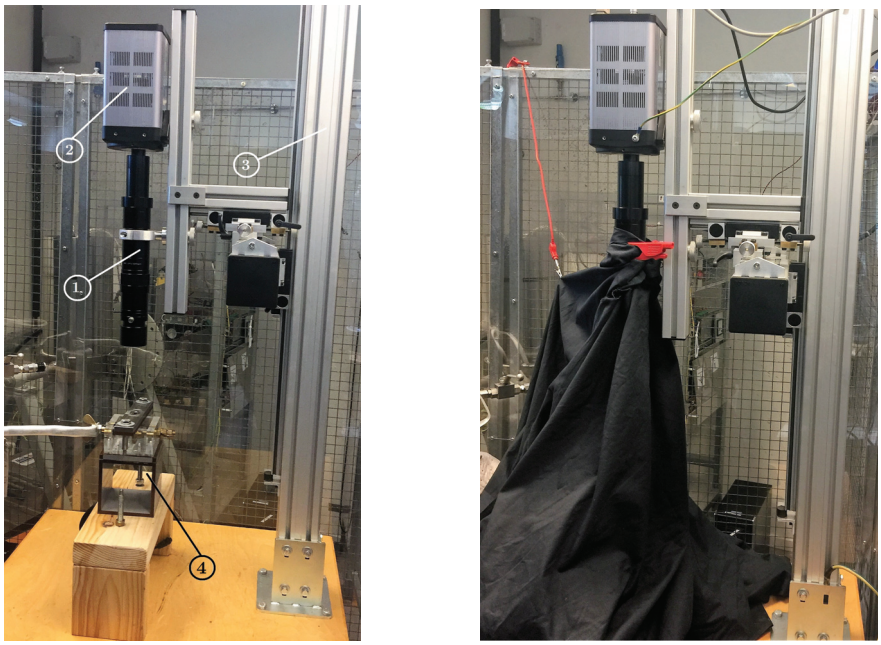

(a) (b)

Figure 6.11: Photos of the experimental setup for discharge-monitoring tests with the CCD camera: (a) (1) External camera lens. (2) CCD camera. (3) Camera base. (4) Mechanical setup. (b) Thick fabric to emulate a dark-room setting along with the lights being switched off.

6.4.4 Test Procedure for Discharge-Monitoring

Adopting a valid methodology to successfully capture discharge activity at the interface was quite challenging. For the sake of simplicity, the challenges are listed in Appendix F.3.1. Having overcome those challenges led to the following step-by-step procedure:

First, samples are assembled at dry conditions between the electrodes following the same procedure that is adopted for AC breakdown and PD experiments. Then, the plates (no. 1–2 in Figure 6.8) are securely fixed, and the desired amount of force is applied while checking the displays of the force gauges to set the amount equally on both load cells. Next, the plexiglass container (no. 8) is filled with Midel 7131 [125]. The CCD camera is switched on and the optimal exposure time is found (for details refer to Appendix F.3.1). Following this, several images of the interface are shot to check if the interface is visible through the window (no. 3) after filling the container with oil. Subsequently, the dark-room environment is set by fixing the black fabric, as shown in Figure 6.11(b) and all lights are switched off. Next, the PD acquisition system is calibrated. The optimal exposure time is reset in the dark environment. Then, the setup is powered by a ramp voltage of 1 kV/s, and the PD pattern is observed in the meantime. When the discharge activity is

detected, the camera software displays it in its GUI. The detailed experimental procedure is provided in Appendix F.3.2.

6.5 Elastic Modulus Measurement of the Samples

The elastic moduli of the SiR, XLPE, EPOXY, and PEEK were measured by tensile testing using a Lloyd LR5K gauge following the ASTM D 790 standard [132]. Five measurements for each material were carried out using dog-bone-shaped samples. The initial slope of the applied force (stress) to the elongation of the specimen (strain) curve in the initial linear region was used to determine the value of the elastic modulus E. Subsequently, the effective elastic moduli E' of the assembled surfaces are calculated using the relation shown in Equation (3.7).

Elastic modulus of each material was also measured under compressive testing to verify the modulus values acquired by the tensile testing. Compressive testing was executed using two rectangular specimens in the same dimensions as the materials used in the AC breakdown experiments. The two specimens were placed in a composite housing holding them on top of each other. The machine was pressing the top specimen at a given speed until the pre-defined force value was reached. The optimal values for these pre-defined values of the speed and force were determined by running some initial tests. The range of the force was selected considering the chosen contact pressure values in the AC breakdown experiments. The details on test-samples, along with background information on the test methodology for tensile and compressive testing are provided in Appendix D.2.

6.6 Characterization of Surface Morphology of the Samples

To quantitatively determine the surface texture of the studied polymers, an optical 3D profilometer was used. The statistical packages embedded in the computer software of the profilometer yields various roughness parameters with reference to [102, 105]. In addition, a modern scanning electron microscope (SEM) and a digital microscope are used to obtain additional qualitative information of sample surfaces with different roughnesses and different polymers polished using the same sandpaper grit.

6.6.1 3D Optical Profilometer

A 3D-optical profilometer (Bruker Contour GT − K [133]) was used to characterize the surface topography of the polished sample surfaces (see Figure 6.12). 50X magnification was opted with 0.2 µm lateral sampling resolution and 3 nm vertical

resolution that led to a scanned surface area of 1.25 mm × 0.94 mm. Several scans were performed at different sections to examine consistency or any scatter. It should be noted that higher magnification results in a smaller scan area. Therefore, the number of scans on the surface should be increased when testing the consistency or if the mean value of all the measurements is used, then the number of trials should be sufficiently high to reduce the standard deviation. In Appendix D.3, details on how to determine the optimal magnification, scan size, and sampling length are provided.

The surface data of the scan area of 1.25 mm × 0.94 mm is stored in a 480×640 matrix with 1.95 µm being the thickness of each row and column vector, as depicted in Figure 6.13.

Various digital toolboxes for 3D statistical post-processing of the data as well as various digital filtering toolboxes are available in the profilometer GUI. Parameters can be computed for any surface profile, raw data, filtered data, masked data and so forth. Filters such as low-pass, high-pass, band-pass, and notch are also available to reduce noise and to remove outliers due to measurement errors.

Roughness and waviness profiles can be extracted using a similar embedded, software package. In this package, digital filters are applied to the raw surface data with the proper cut-off wavelengths, that are selected according to the procedure explained in Section 3.4.1.

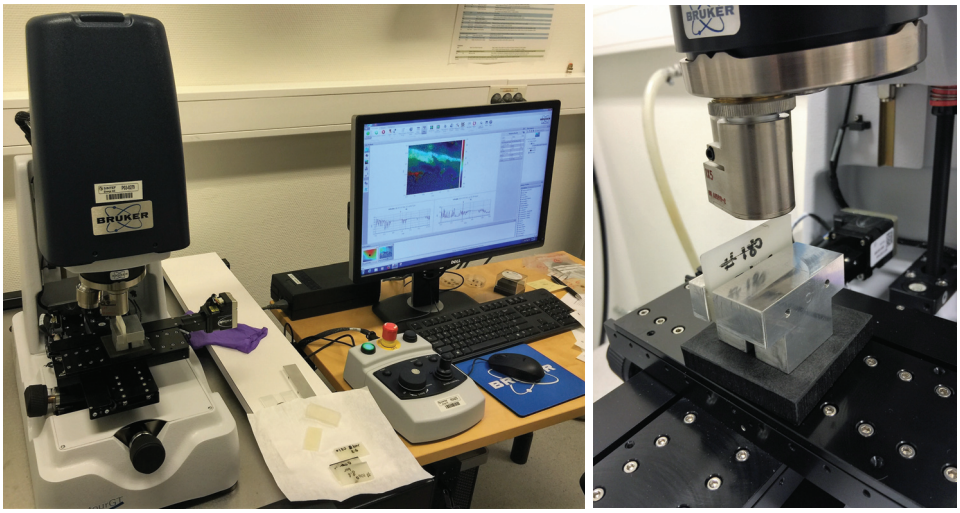

(a) **(b)**

Figure 6.12: Bruker Contour GT–K optical profilometer: (a) The profilometer and motor unit connected to PC for controlling the instrument. (b) Objectives with various magnification settings.

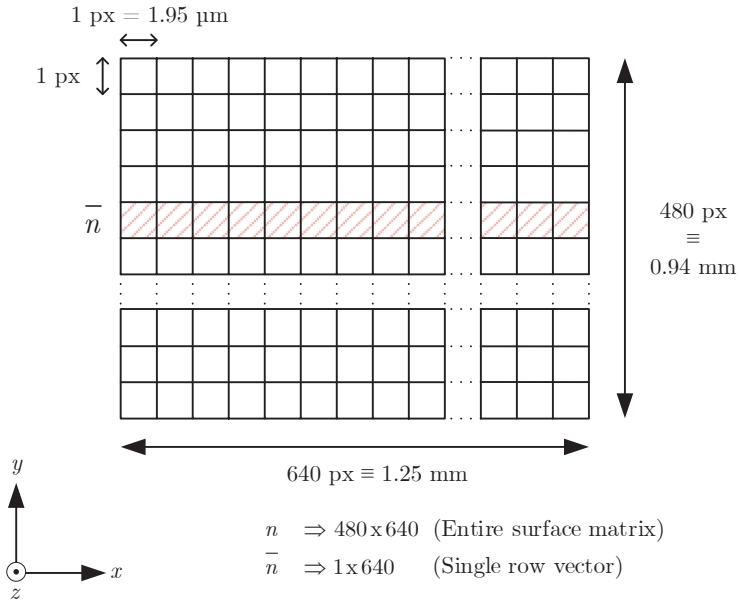

Figure 6.13: Image data stored in a 480 × 640 matrix at the favored scan, sampling and magnification settings.

6.6.2 Scanning Electron Microscope

The samples to be scanned by the SEM should be small in size because they are placed on the pins presented in Figure 6.14), whose diameters are around 1.5 mm. Therefore, first, the samples were cut and sanded as usual by following the procedure explained in Section 6.1. Their sizes were then reduced to the pin size (approx. 4 cm in diameter).

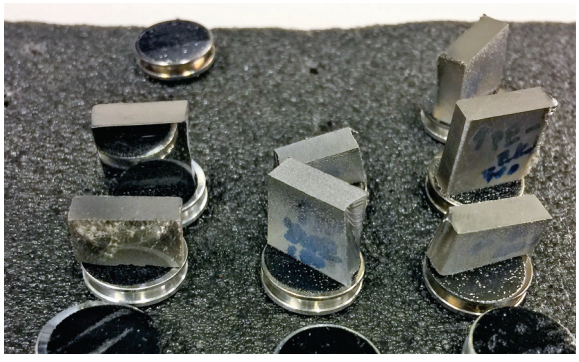

Figure 6.14: Sample surfaces coated for the SEM scanning.

A scalpel was used to cut XLPE and SiR samples whereas an electrical saw was used for the PEEK and EPOXY. Following this, the edges were smoothened using a sandpaper. In case the polished surfaces were damaged during cutting, the samples were polished again with the appropriate sandpapers, resulting in smaller but identical polymer samples in the pin size. Before placing the samples in the SEM, the samples were coated with Au-sputtered films. Non-conducting materials are usually coated with an ultra-thin coating of electrically conducting material (favorably Au), deposited on the sample by low-vacuum sputter coating. A Polaron E5100 sputter coater [134] was used was to used coat the samples. The coated samples are shown in Figure 6.14. Seven samples in total were scanned: the coated surfaces of XLPE samples with four different roughness degrees (#180, #500, #1000, and #2400), and those of SiR, EPOXY, and PEEK samples at the same roughness (#500).

6.6.3 Digital Microscope

A table-top digital microscope (Keyence VHX-500FE [135]) is used to examine the interface surfaces before and after the AC breakdown and PD experiments. The digital microscope used is a derived form of a traditional optical microscope that uses optics and a digital camera to produce an image by means of software running on a computer. Some of the obtained images of samples subjected to electrical breakdown using the digital microscope are shown in Appendix A.2.

Chapter 7

Results of Sample Characterization Tests

This chapter presents a summary of the sample characterization results, which constitute surface roughness measurements and elastic modulus measurements performed by following the methodology described in Chapter 6. Surface characterization analyses incorporate surface images obtained using the SEM and the optical profilometer. The raw surface data are post-processed using the S-amplitude parameters and motif parameters (introduced in Chapter 3) to extract quantitative information of each interface surface.

Section 7.1 provides the SEM images of all types of samples used in this work. They are intended to provide visual/qualitative results whereas the quantitative results shown in Section 7.2 and Section 7.3 are extensively used for the analytical model proposed in Chapter 3.

7.1 SEM Images

Figure 7.1 shows the SEM images of SiR, XLPE, EPOXY and PEEK samples polished using #500-grit sandpaper. The scales of the images are shown at the bottom right of each image. The images view the samples from the top; it is thus not possible to differentiate protrusions and dents, which eventually lead to the formation of cavities and contact spots when the interface is assembled. Despite having been sanded with the same sandpaper grit, the surface textures of the samples appear to be different in such a way that, the harder the material, the fewer the number of imperfections visible at the same magnification.

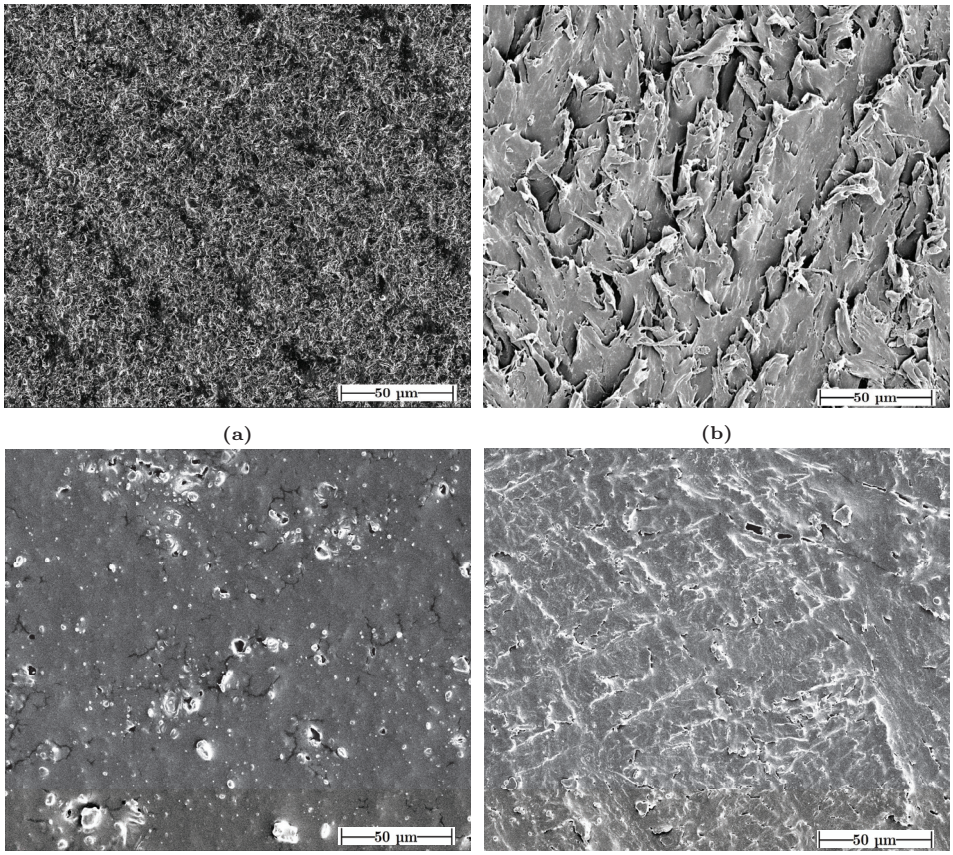

Figure 7.1: SEM images at 667X magnification: (a) SiR #500. (b) XLPE #500. (c) EPOXY #500. (d) PEEK #500.

Figure 7.2 depicts the images of the XLPE samples sanded with four sandpapers with different roughnesses. Figures 7.3 and 7.4 provide a closer glance at the surfaces at a higher magnification, where the scales of the images are shown at the bottom right corner of each image. As expected, sanding using rougher sandpapers leads to more rugged surface texture. Lines indicating the sanding pattern are visible in the cases of #180 and #500. On the other hand, in the cases of #1000 and #2400, these lines are not as discernible. Only a few protrusions are visible with no cracks on their surfaces.

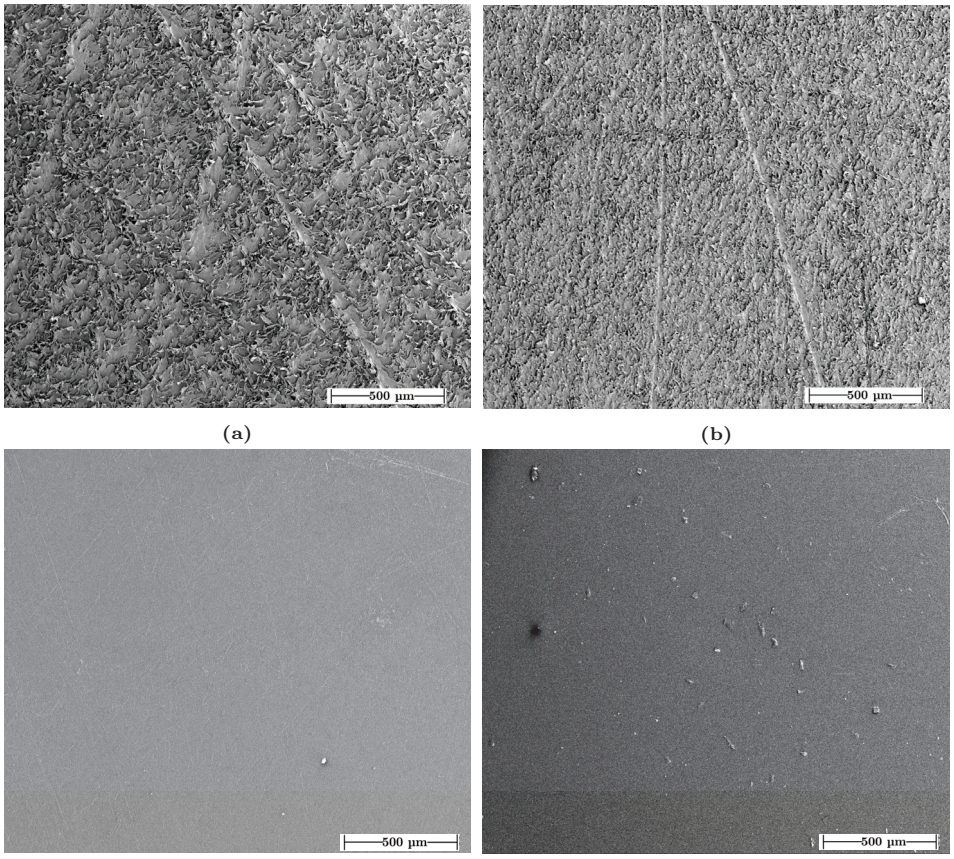

Figure 7.2: SEM images of XLPE samples at 67X magnification: (a) #180. (b) #500. (c) #1000. (d) #2400.

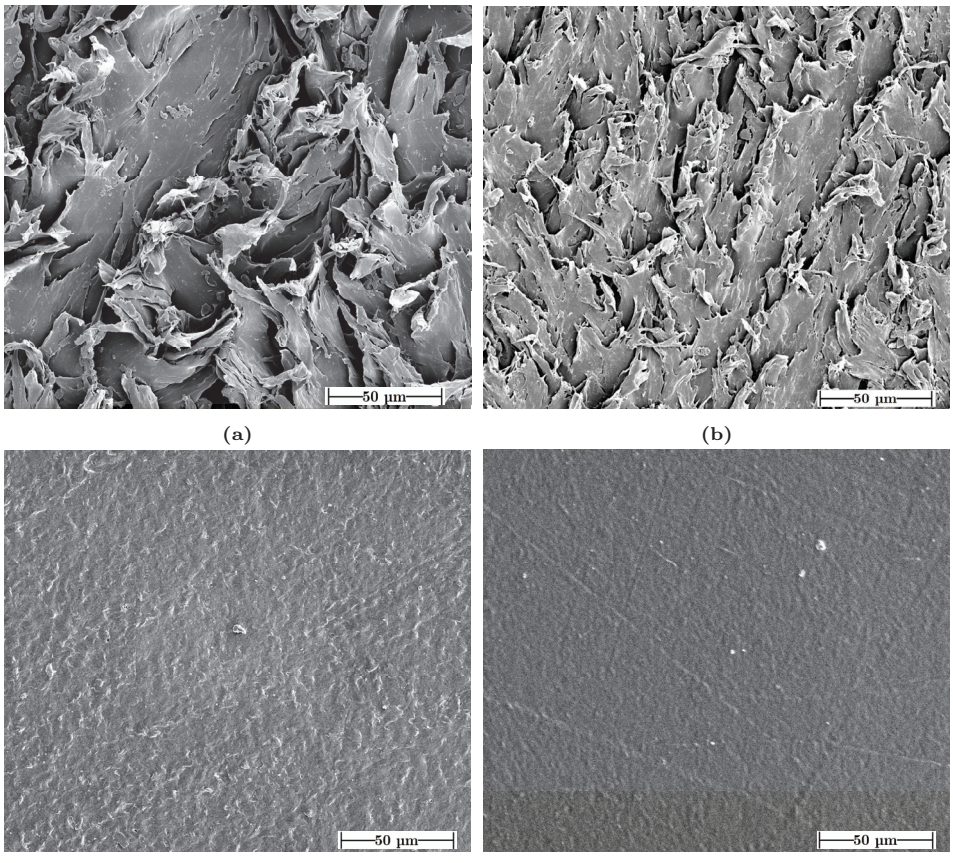

Figure 7.3: SEM images of XLPE samples at 667X magnification: (a) #180. (b) #500. (c) #1000. (d) #2400.

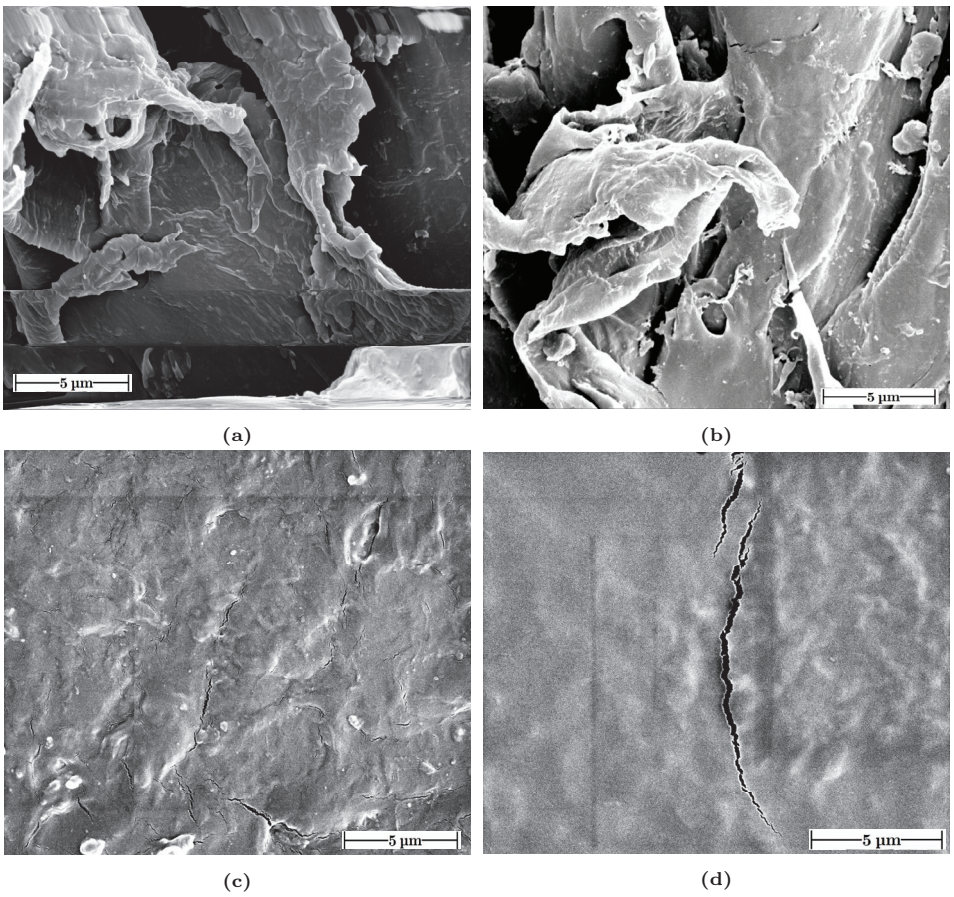

Figure 7.4: SEM images of XLPE samples at 6667X magnification: (a) #180. (b) #500. (c) #1000. (d) #2400.

7.2 Surface Measurements by the Optical Profilometer

3D and 2D surface profiles of the samples were generated using the 3D optical profilometer, as illustrated in Figure 7.5. The 3D surface data are stored in a 640×480 matrix, where each row and column stand for an xz- and yz-plane, respectively (see Section 6.6.1). In the following sections, 3D views of the surface textures of the selected samples are displayed, which are categorized based on the type of the experiments they were used in.

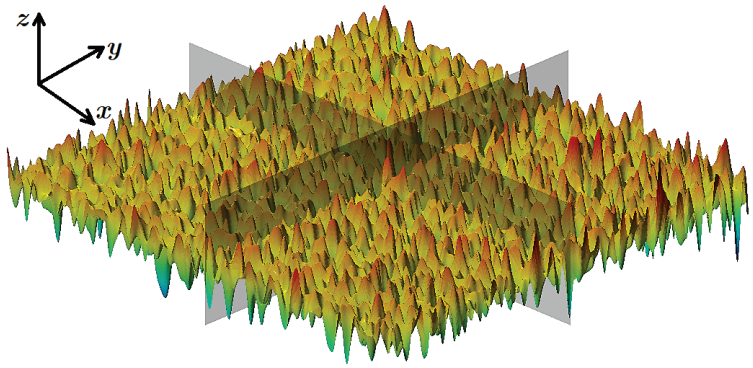

(a) 3D surface profile with planes.

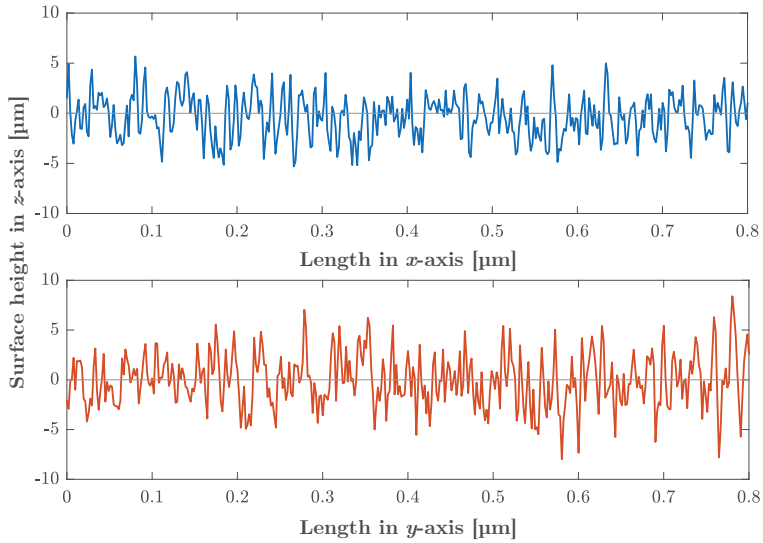

(b) 2D surface profiles that the planes represent.

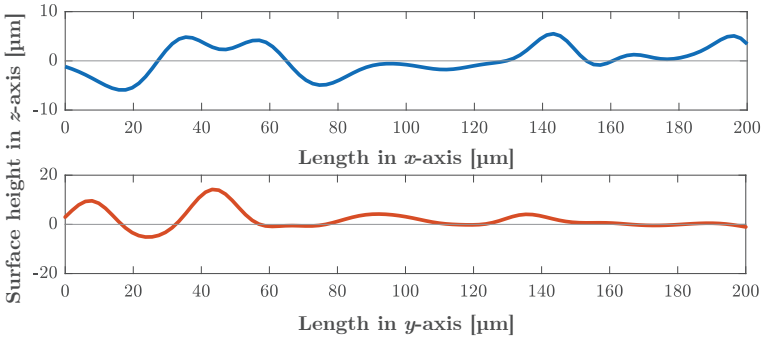

(c) 1:1 aspect ratio of the 2D surface profiles.

Figure 7.5: Surface roughness data obtained by the optical profilometer. The $xz-$ and $yz-$planes are one of the 640 and 480 available planes, respectively. The $xz-$plane is a row vector of 1×640 while the $yz-$plane is a column vector of 480×1 (see Section 6.6.1). Thickness of each plane is 1.9581 µm.

7.2.1 3D Surface Topographies of the Samples Used in AC Breakdown and PD Experiments

Figure 7.6 shows the 3D surface profiles of the XLPE samples with different surface roughnesses whereas Figure 7.7 displays the smoothest and roughest surfaces of PEEK samples. In addition, Figure 7.8 shows the surface profiles of the selected polymers used in the AC breakdown and PD experiments. The surface topographies indicate that the amplitude of the surface asperities significantly decreases in smoother surfaces. Moreover, the asperity heights differ notably in the samples sanded using the identical sandpapers.

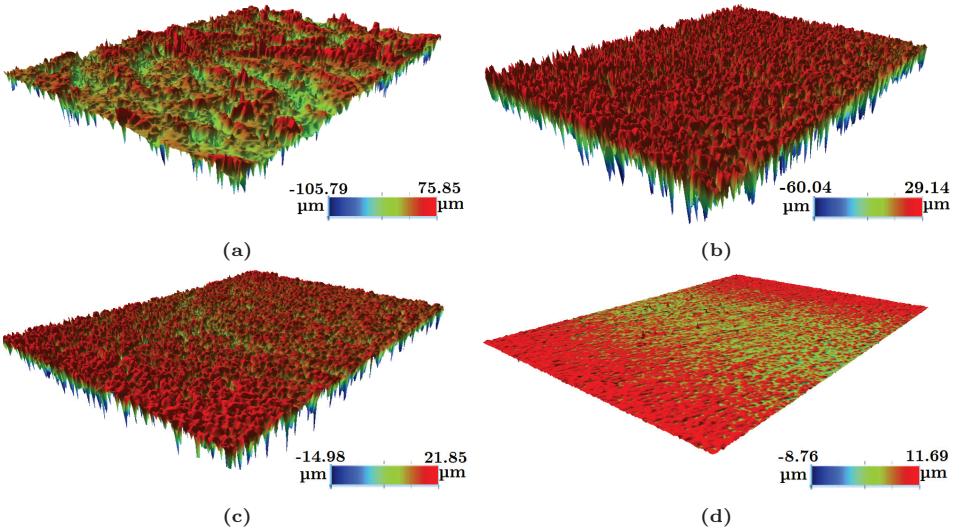

Figure 7.6: 3D view of the surface texture of XLPE samples polished using the sandpaper grit: (a) #180. (b) #500. (c) #1000. (d) #2400.

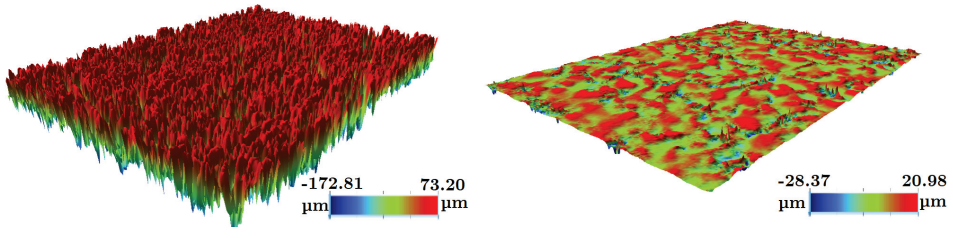

(a) PEEK #180. **(b)** PEEK #2400.

Figure 7.7: 3D view of the surface texture of PEEK samples sanded using the sandpaper grit: (a) #180. (b) #2400.

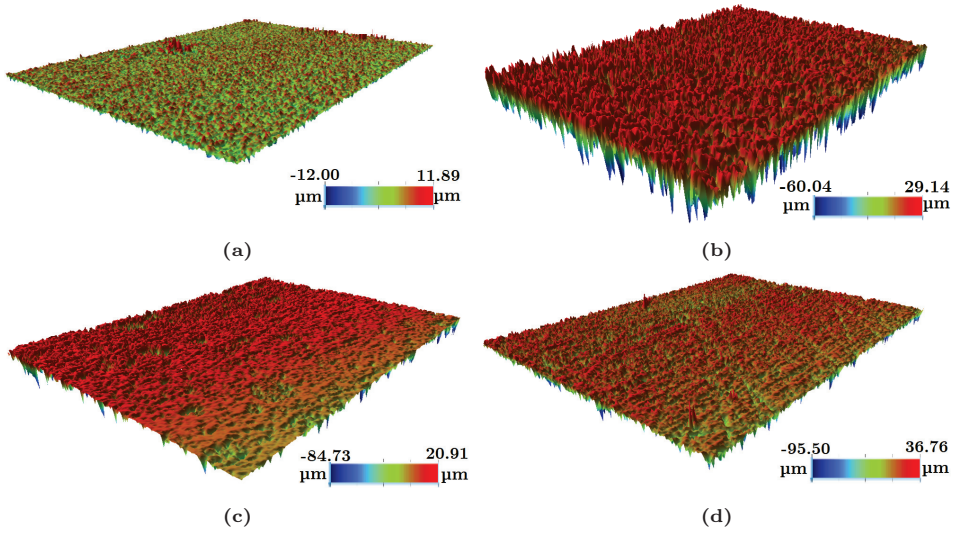

Figure 7.8: 3D view of the surface texture of the polymers polished using the sandpaper grit #500: (a) SiR. (b) XLPE. (c) EPOXY. (d) PEEK.

7.2.2 3D Surface Topographies of the Samples Used in Discharge-Monitoring Experiments

The PEEK samples used in discharge-monitoring experiments were scanned using the profilometer immediately after a cylindrical cavity, with a diameter of 1 mm, had been drilled (see Figure 7.9). To flatten out the protruding edges around the brim of the drilled, artificial cavity, we sanded the sample surfaces again using the same sandpaper type that was used before drilling the cavity. Figure 7.10 displays the depth and size of the cavity in X- and Y-profiles after the sample was polished again. Evidently, the protruding edges around the cavity vanished after repolishing.

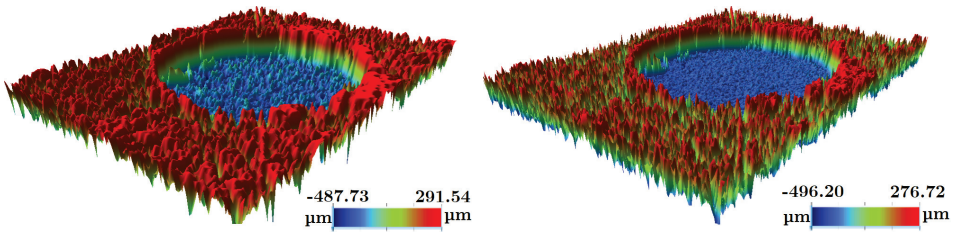

(a) PEEK #180. **(b)** PEEK #500.

Figure 7.9: Scanned surfaces of PEEK samples immediately after cylindrical cavities, with diameters of 1 mm, were drilled (before repolishing).

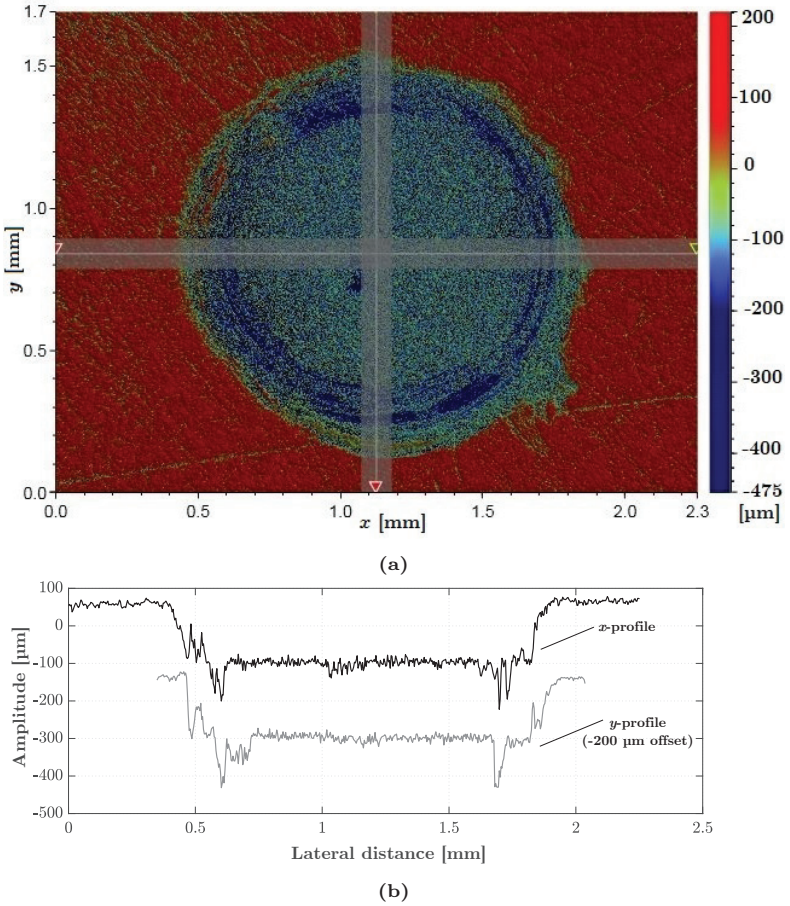

Figure 7.10: 2D x-axis profile and y-axis profiles of the PEEK #500 surface with the cylindrical cavity. An offset of -200 µm is added to the amplitude of the y-profile to juxtapose both profiles clearly.

7.2.3 Quantification of Surface Roughness Using Motif Parameters

As briefly mentioned in Section 3.4.1, the motif parameters provides surface characterization parameters required by the theoretical model in Chapter 3.

Surface roughness and waviness profiles were extracted by following the procedure described in Section 3.4.1. Short and long wavelength cut-off lengths were set as follows: $\lambda_s = 8\,\mu$m, $\lambda_c = 0.08$ mm, $\lambda_f = 0.25$ mm. (ISO 4287 [105], ISO 25178 [103] or ASME B46.1 [102] list suggested values for the cut-off lengths). Obtained roughness and waviness profiles are shown in Figure D.9 in Appendix D.3.3. In addition, the calculated roughness and waviness motif parameters of the inter-

faces with varying surface roughness and elastic modulus are shown in Table 7.1 and Table 7.2, respectively. Finally, Table 7.3 and Table 7.4 show the resulting statistical parameters of η, σ_p, and β_m using Equations (3.26a), (3.27), and (3.28).

Equation (3.29) is used to test if the calculated surface characterization parameters are reliable. Multiplication of $\sigma_p \, \beta_m \, \eta$ in Table 7.3 and Table 7.4 lie within 0.031–0.046. Therefore, all the surface parameters seem reliable as all the $\sigma_p \, \beta_m \, \eta$ values lie within 0.03–0.05.

Table 7.1: Motif parameters of XLPE–XLPE interfaces.

Interface	Roughness [µm]			Waviness [µm]	
	$\boldsymbol{Y_{eq}}$	$\boldsymbol{AY_{eq}}$	$\boldsymbol{SAY_{eq}}$	$\boldsymbol{W_{eq}}$	$\boldsymbol{SW_{eq}}$
#180	17.79	19.30	13.97	11.39	9.80
#500	5.65	20.61	12.38	5.43	4.87
#1000	1.98	21.47	13.23	1.25	1.08
#2400	0.50	27.59	13.44	0.34	0.35

Table 7.2: Motif parameters of the interfaces polished using #500 grit sandpaper.

Interface	Roughness [µm]			Waviness [µm]	
	$\boldsymbol{Y_{eq}}$	$\boldsymbol{AY_{eq}}$	$\boldsymbol{SAY_{eq}}$	$\boldsymbol{W_{eq}}$	$\boldsymbol{SW_{eq}}$
SiR–SiR	2.97	27.69	14.17	2.31	2.01
XLPE–XLPE	5.65	20.61	12.38	5.43	4.87
EPOXY–EPOXY	9.88	21.04	10.18	7.63	6.53
PEEK–PEEK	11.18	12.81	9.11	6.31	5.77

Table 7.3: Surface characterization parameters of XLPE-XLPE interfaces at various surface roughnesses.

Interface	$\boldsymbol{\sigma_p}$ **[µm]**	$\boldsymbol{\beta_m}$ **[µm]**	$\boldsymbol{\eta}$ **[µm]**
#180	5.26	1.94	$3.22 \cdot 10^{15}$
#500	2.55	6.39	$2.83 \cdot 10^{15}$
#1000	0.58	19.91	$2.64 \cdot 10^{15}$
#2400	0.17	118.19	$1.58 \cdot 10^{15}$

Table 7.4: Surface characterization parameters of the studied polymers polished using #500 grit sandpaper.

Interface	$\boldsymbol{\sigma_p}$ **[µm]**	$\boldsymbol{\beta_m}$ **[µm]**	$\boldsymbol{\eta}$ **[µm]**
SiR–SiR	1.07	20.39	$1.6 \cdot 10^{15}$
XLPE–XLPE	2.55	6.39	$2.8 \cdot 10^{15}$
EPOXY–EPOXY	3.51	3.45	$2.7 \cdot 10^{15}$
PEEK–PEEK	2.99	1.38	$7.3 \cdot 10^{15}$

7.2.4 Quantification of Surface Roughness Using *S*-Amplitude Parameters

As seen in Figure 7.6, in the case of surfaces sanded using #180-grit sandpaper, the surface is rife with high peaks and deep pits, resulting in a large peak-to-peak distance; in contrast, shorter peaks and shallower dips are observed when a sandpaper with a higher grit intensity is used. The obtained roughness *S*-amplitude parameters from the measurements are tabulated in Table 7.5.

Table 7.5: Surface roughness height parameters of XLPE–XLPE interfaces.

Grit No.	Roughness $S-$parameters [µm]				
	S_a	S_q	S_p	S_v	S_z
#180	8.86	12.50	75.85	−105.79	181.64
#500	7.79	9.57	29.14	−60.04	89.18
#1000	1.65	2.19	21.85	−14.98	36.86
#2400	0.27	0.60	11.69	−8.76	20.44

Similarly, *S*-amplitude parameters of the four polymers polished using #500-grit sandpaper are shown in Table 7.6. Although the samples were sanded with identical sandpapers of the same grit, the amplitudes of peaks and dips deviate from each other due to differences in tribological features (i.e., friction, adhesion) of the samples [41, 91]. A schematic guide is depicted in Figure 3.9, where the *S*-amplitude parameters are demonstrated on a 2D surface profile.

Table 7.6: Surface roughness height parameters of polymer interfaces sanded using #500 sandpaper.

Grit No.	Roughness $S-$parameters [µm]				
	S_a	S_q	S_p	S_v	S_z
SiR	2.29	2.88	11.89	−12.00	23.89
XLPE	7.79	9.57	29.14	−60.04	89.18
EPOXY	9.31	12.28	20.91	−84.73	105.64
PEEK	8.74	11.42	36.76	−95.50	132.26

7.3 Elastic Modulus Measurements

The performed stress vs. strain measurements for each material are shown in Figure 7.11. Based on the methodology described in Section 6.5, the elastic modulus E values are obtained using the initial slope of the stress vs. strain curves. The effective moduli E' values are then calculated using Equation (3.7). The resulting values including the selected Poisson's ratios are depicted in Table 7.7. Poisson's ratio values are taken from the data sheets. As the interfaces are formed between identical materials, $E = E_1 = E_2$ and $v = v_1 = v_2$ with reference to Equation (3.7). The results indicate that the harder (stiffer) the material, the higher the elastic modulus. These results are in line with the findings in literature [136].

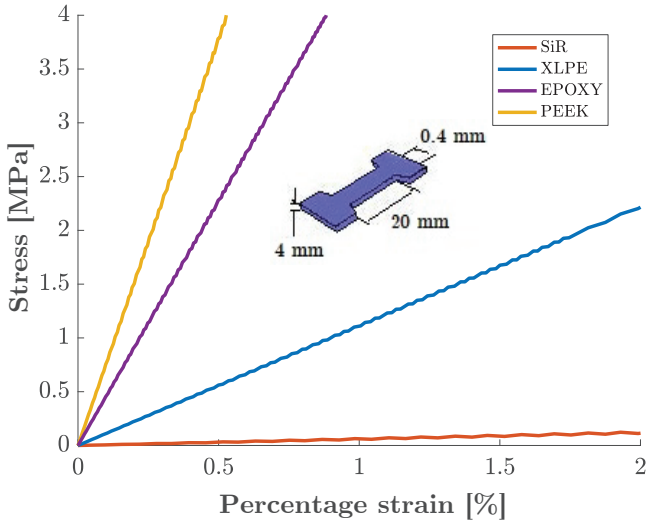

Figure 7.11: Stress-strain tensile test results using dog-bone shaped samples.

Table 7.7: Measured elastic modulus of each sample and calculated effective/composite modulus of each polymer interface formed between identical materials using Equation (3.7).

Polymer	Elastic modulus E [MPa]	Poisson's ratio v	Interface	Effective Modulus E' [MPa]
SiR	59	0.48	SiR−SiR	109
XLPE	200	0.46	XLPE−XLPE	226
EPOXY	4425	0.38	EPOXY−EPOXY	5166
PEEK	7515	0.38	PEEK−PEEK	8808

Chapter 8

Results of AC Breakdown Experiments

Since all the results from the AC breakdown experiments are published in the appended articles, this chapter presents a summary of the main results along with brief comments on the results.

The experimental setup and methodology used for the AC breakdown testing are described in Chapter 6 and also in the appended papers. Raw data obtained from the AC breakdown experiments (that are not available in the appended articles) are presented in Appendix A.

The main parameters in the AC breakdown experiments are contact pressure, elastic modulus, surface roughness, and the surrounding medium (i.e., the insulating dielectric environment that fills the interfacial cavities such as air, water, or oil).

In order to be able to interpret the experimental results as simply and accurately as possible, two of the parameters were varied in steps at a time while the remainder were kept constant throughout each experiment to focus on the individual impact of each parameter on the interfacial breakdown strength. Table 8.1 summarizes the parameters studied in each article. As can be seen in the table, the contact pressure is the only parameter that was varied in all studies.

Moreover, Table 8.3 provides a good overview of the type of the studied interfaces and the covered pressure range for each interface, which were determined through the initial tests mentioned in Section 6.2.2. We aimed to keep the electrical properties of the polymer interfaces the same at an interface by assembling them between identical samples, as seen in Table 8.3. In addition, experiments with PEEK–XLPE interface were carried out to check the performance of an interface between a relatively soft material and a hard material, as found in some real-life applications [8, 20, 137, 138]. The SiR–XLPE interface was studied in Papers I and

II for the same purpose, however, the covered applied contact pressure range had to be quite limited due to the SiR samples easily becoming deformed even under low contact pressures. It should be noted that the main focus of this work is kept on the interfaces between identical materials to dissect the impact of each parameter as accurately as possible.

It should also be highlighted that the experimental data are represented using rms voltage values in Weibull plots since the data showed a good fit to Weibull distribution. When presenting the results, the term BDS and 63.2% BDS are used interchangeably as the nominal/mean value of Weibull distribution is 63.2%, analogous to the mean value in Gaussian distribution.

Unless otherwise stated or if not mentioned explicitly, interfaces at stake are dry-mate, are assembled between identical polymers and are sanded using #500. Since the majority of the results will represent the interfaces formed between identical materials, in the text, only the name of the polymer will be used to represent the interface to reduce wordiness while names of the entire interfaces will be written explicitly in necessary cases.

Table 8.1: Scope of the selected publications containing AC breakdown experimental results.

Papers	**Contact pressure**	**Elastic modulus**	**Surface roughness**	**Void-filling medium**
Paper I	✓	✓✘*	✘	✓
Paper II	✓	✓✘*	✘	✓
Paper III	✓	✘	✓	✘
Paper IV	✓	✘	✓	✘
Paper V	✓	✓**	✘	✘

* Only two different polymers were tested.
** Four different polymers were tested.
✓: Studied, ✘: Not studied, ✓✘: Partially studied.

8.1 Influence of Surface Roughness [Papers III and IV]

In this section, the main findings from Papers III and IV are presented. The scopes of these papers were limited in order to determine the effect of surface roughness on the interfacial BDS. In order to study the correlation between surface roughness and electrical interface breakdown, XLPE samples of four different surface roughnesses were used in the experiments to form the dry-mate polymer interfaces.

The effect of the surface roughness on the interfacial BDS at 0.5, 0.86, and 1.16 MPa contact pressures were studied. For clarity, only 63.2% values with 90% CI are plotted against the sandpaper grit in Figure 8.1, while each bar graph illustrates the arithmetic mean height S_a of the asperities at each interface. Table 8.2 provides the quantitative data points from Figure 8.1.

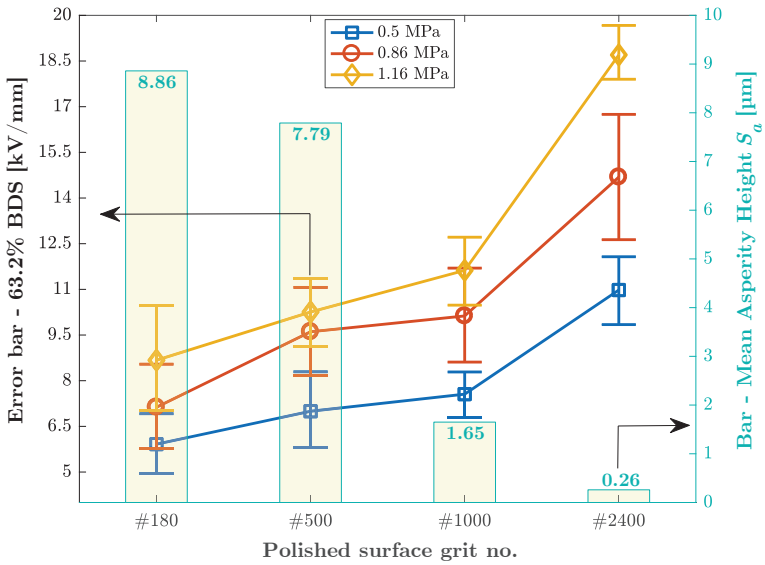

Figure 8.1: (i) Left y-axis: Experimental results of longitudinal AC BDS of interfaces versus the polished rough surface grit no. of XLPE samples. (ii) Right y-axis: Arithmetic mean asperity height S_a shown by the bars.

Table 8.2: Overview of the experimental results on the effect of surface roughness.

XLPE-XLPE interface	63.2% BDS [kV/mm]		
	0.5 MPa	0.86 MPa	1.16 MPa
#180 ($S_a = 8.9$ µm)	5.92	7.13	8.67
#500 ($S_a = 7.8$ µm)	6.99	9.61	10.26
#1000 ($S_a = 1.7$ µm)	7.56	10.13	11.62
#2400 ($S_a = 0.3$ µm)	10.98	14.69	18.70

The results suggest that increased surface roughness results in reduced BDS whereas increased contact pressure results in increased BDS. The 63.2% BDS in the case of the surface polished by #2400 is nearly twice as high as that in the case of #180 at each contact pressure. As the mean asperity height S_a is reduced by a factor of 30 from #180 to #2400, the BDS increases by a factor of 1.85 at $p_a = 0.5$ MPa and by 2.15 at $p_a = 1.16$ MPa. The increase in the BDS from #1000 to #2400 culminates under all pressures, as evident in Figure 8.1, where the highest increase is detected at 1.16 MPa by a factor of 1.6. The results indicated that surface roughness has a considerable effect on the BDS of the interfaces at dry-mate conditions.

As the pressure is raised from 0.5 to 1.16 MPa, the 63.2% BDS rises by a factor of 1.4 in the case of #180 ($S_a = 8.9\,\mu m$), while it increases by a factor of 1.7 in the case of #2400 ($S_a = 0.30\,\mu m$). Thus, the smoothest interface shows the strongest dependency on the contact pressure. Besides, the overlap in the 90% CIs dwindles as the surface roughness is decreased. In the case of the smoothest surface, #2400, 90% CIs do not even overlap, as seen in Figure 8.1. The less the overlap in CIs, the more pronounced the difference between cases at different pressures.

8.2 Influence of Elastic Modulus

In this section, the main findings from Paper V are shown by studying the effect of the elastic modulus on the tangential AC breakdown strength of solid-solid interfaces. Interfaces between identical polymers of SiR, XLPE, EPOXY, and PEEK were tested at various interfacial contact pressures, and all samples were polished using the same sandpaper with grit no #500. In addition, XLPE–PEEK #500 and SiR–XLPE #500 interfaces were tested in a similar manner. The main motivation was to test the performance of the interfaces between soft and hard materials and to correlate their AC BDS values with those of the interfaces between identical materials.

8.2.1 Interfaces between Identical Polymers [Paper V]

The 63.2% values for each interface are shown in Figure 8.2 and Table 8.3 with corresponding 90% CI values. The results demonstrate that the increase of elastic modulus results in a reduced BDS. The effect of the contact pressure is also discernible such that increase of contact pressure by a factor around 3 elevates the interfacial BDS by a factor of 1.4 in the case of the lowest elastic modulus (SiR–SiR) whereas the BDS value in the case of highest modulus (PEEK–PEEK) is 2.4 times higher. The results of the AC breakdown experiments indicate that the elastic modulus is one of the prominent electrical insulation properties affecting the BDS of solid-solid interfaces. It is observed that materials with relatively low moduli such as SiR and XLPE yield higher interfacial BDS values even at relatively low contact pressures.

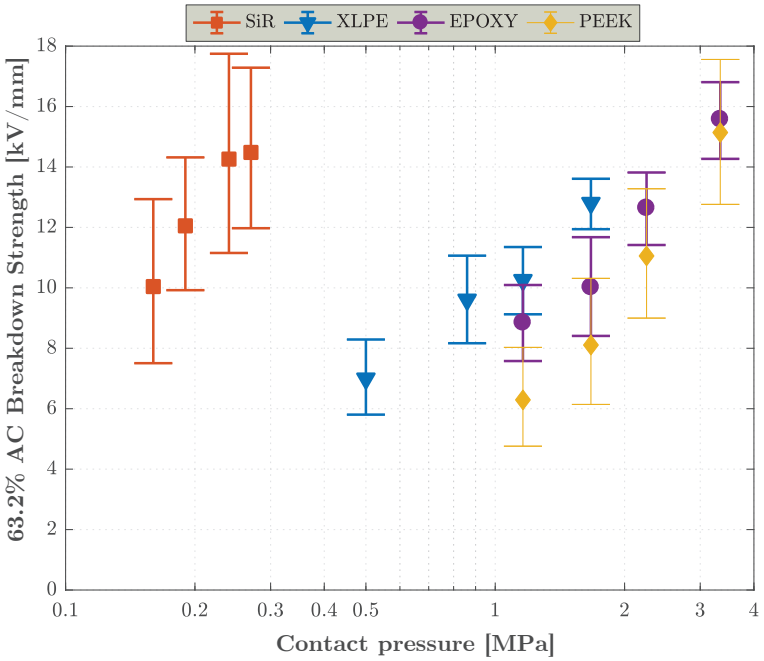

Figure 8.2: Results of the AC breakdown experiments vs. the contact pressure in which interfaces between the identical materials of SiR, XLPE, EPOXY, and PEEK tested whose surfaces were sanded using #500 grit sandpaper. The markers of the error bars in Figure 8.2 stand for the 63.2% BDS while error bars represent the 90% CI of the 63.2% values.

Table 8.3: Overview of the experimental results on the effect of elasticity.

Contact pressure	SiR–SiR		XLPE–XLPE		EPOXY–EPOXY		PEEK–PEEK	
	p_a [MPa]	63.2% [kV/mm]	p_a [MPa]	63.2% [kV/mm]	p_a [MPa]	63.2% [kV/mm]	p_a [MPa]	63.2% [kV/mm]
p_{a1}	**0.16**	10.0	**0.5**	7.0	**1.16**	8.9	**1.16**	6.3
p_{a2}	**0.19**	12.1	**0.86**	9.6	**1.67**	10.0	**1.67**	8.1
p_{a3}	**0.24**	14.3	**1.16**	10.3	**2.25**	12.6	**2.25**	11.1
p_{a4}	**0.27**	14.5	**1.67**	12.8	**3.34**	15.6	**3.34**	15.1

8.2.2 Interfaces between Soft and Hard Materials

In addition to the results covered in the articles, AC breakdown results on interfaces formed between a relatively soft and relatively hard material are shown in this section. Figure 8.4 displays the obtained results for the XLPE–XLPE, PEEK–PEEK and PEEK–XLPE interfaces. As seen in the figure, the BDS values of the XLPE–XLPE, XLPE–PEEK and PEEK–PEEK interfaces line up from highest to the lowest in a sequence.

In the case of the PEEK–XLPE interface at 0.86 MPa, the mean BDS (63.2%) is half the BDS of the XLPE–XLPE interface, whereas, it is lower by factors of 0.67 and 0.83 at 1.16 MPa and 1.67 MPa, respectively. On the other hand, the BDS of the PEEK–XLPE is found to be higher than that of the PEEK–PEEK by factors of 1.1 and 1.3 at 1.16 MPa and 1.67 MPa, respectively.

To highlight the effect of the pressure, the BDS of PEEK–XLPE with the 90% CIs are presented in Figure A.16 in Appendix A.1 at the lowest and highest pressures. Note that the PEEK–XLPE interface could not be tested above 1.67 MPa due to the deformation of XLPE samples.

Figure 8.5 provides the obtained results of XLPE–XLPE, SiR–SiR and SiR–XLPE interfaces from the Papers I and II at $p_a = 0.27$ MPa. This pressure was the highest pressure level used in the SiR–SiR case, ensuring no deformation of SiR samples. As evident in Figure 8.5, the presence of SiR made a significant difference with a greater measurement dispersion in such a way that the BDS of the XLPE–SiR interface increases by a factor of 1.43 compared to the XLPE–XLPE interface whereas it is lower than that of the SiR–SiR interface, by a factor of 0.39. Figure 8.3 is also provided to demonstrate the differences between the interfaces using the Weibull plots with their 90% CIs as they could only be tested at a single pressure value. The similar slopes of the Weibull curves of XLPE–SiR and SiR–SiR suggest that the presence of SiR is likely to affect the resulting breakdown strength.

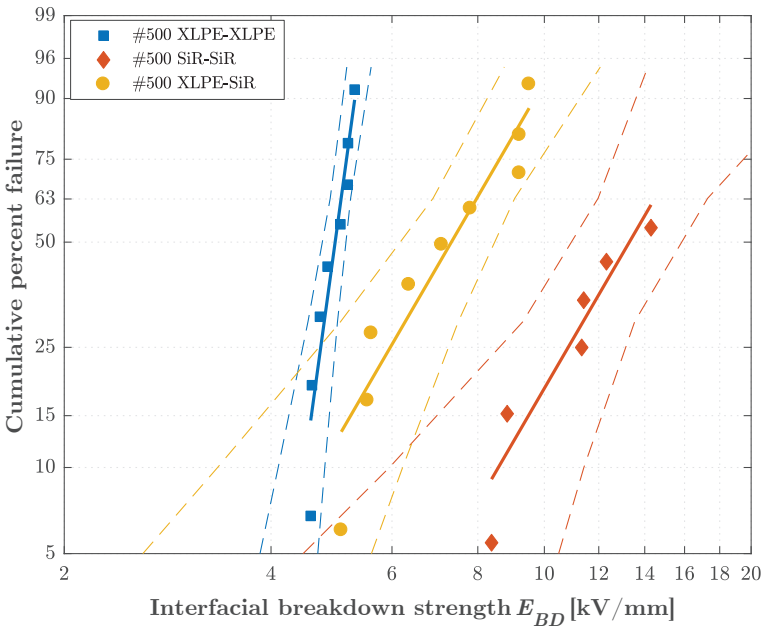

Figure 8.3: Weibull plot of cumulative percent failure vs. BDS of SiR-XLPE interface with full CI at 0.27 MPa.

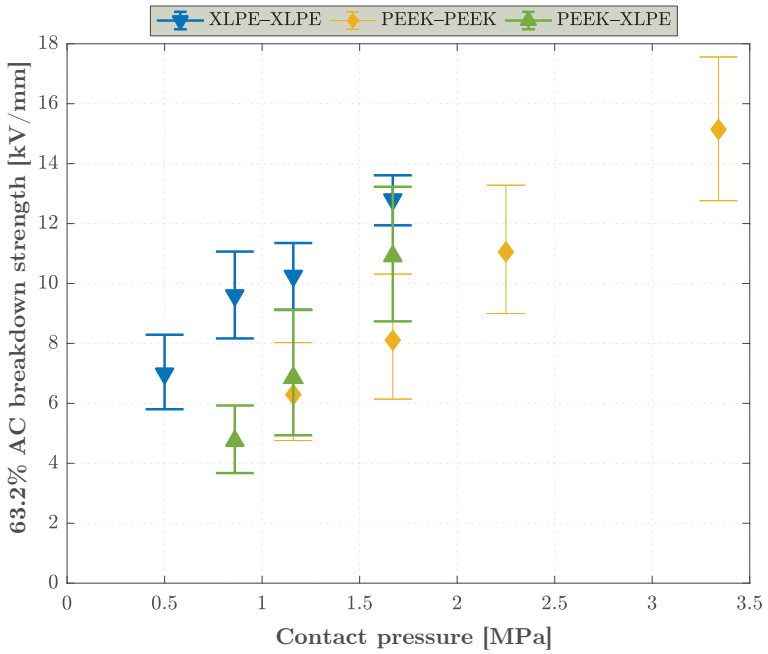

Figure 8.4: Longitudinal AC BDS values of XLPE-XLPE, PEEK-PEEK, and XLPE-PEEK interfaces. (Error bars represent the 63.2% BDS with the 90% CIs).

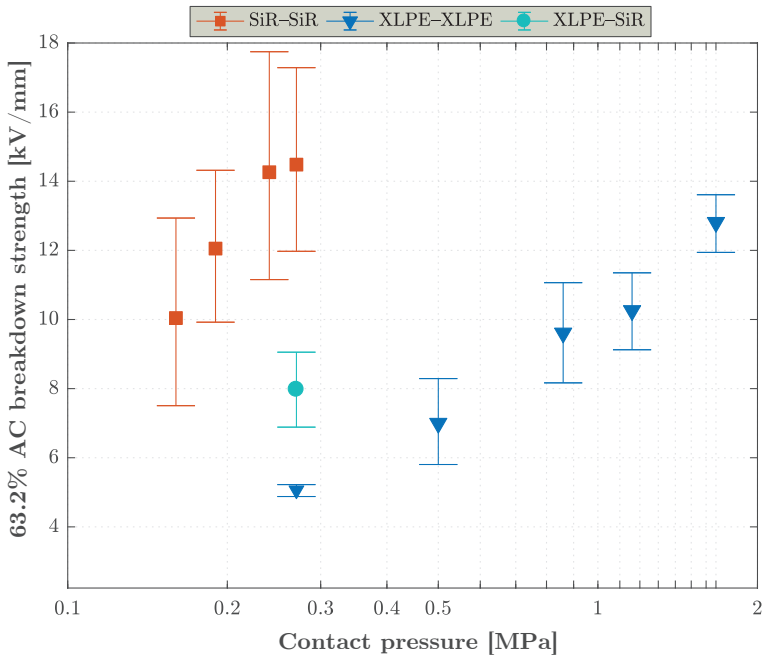

Figure 8.5: Longitudinal AC BDS values of SiR–SiR, XLPE–XLPE, and XLPE–SiR interfaces at 0.27 MPa. (Error bars represent the 63.2% BDS with the 90% CIs).

8.3 Influence of Dielectric Medium Inside Cavities [Papers I and II]

In this section, the main results from Papers I and II on the effect of the insulating medium inside interfacial microcavities are summarized. With reference to Table 8.1, the effects of the applied contact pressure and elastic modulus on the tangential AC BDS of dry-mate, wet-mate and oil-mate XLPE–XLPE and SiR–SiR interfaces, sanded using only #500 grit sandpapers, were studied experimentally.

8.3.1 Dry-mate vs. Wet-mate Interfaces

The results of the dry-mate and wet-mate interfaces formed using the XLPE #500 and SiR #500 samples are summarized in Figure 8.6. The 63.2% BDS values in the case of dry-mate XLPE–XLPE #500 are higher than those in the case of wet-mate XLPE–XLPE #500 by a factor ranging from 2.6 to 2.9 as the contact pressure is increased from 0.5 to 1.16 MPa. Increasing the contact pressure from 0.5 to 1.16 MPa results in an increase by a factor of 1.2 in the 63.2% BDS in the case of dry-mate XLPE–XLPE. On the other hand, in the case of wet-mate XLPE–XLPE, when the pressure is increased from 0.5 to 1.16 MPa, the 63.2% BDS increases by a factor of 1.7. These findings indicate that the increase in contact pressure is likely to squeeze some water droplets out of the interface. Thus, air-filled and water-filled cavities are likely to coexist at higher contact pressures, which, in turn, increases the BDS significantly.

In Figure 8.6, the BDS of air is also shown for reference. It was measured using the same setup in the air with a 4-mm distance between the electrodes. In accordance with the field simulations shown in Paper II and Appendix B, Figure 8.6 indicates that the presence of water at the interface has a detrimental effect on the BDS in the AC breakdown experiments. Particularly at low contact pressures, the BDS of an interface is comparable with that of air.

Similarly, the 63.2% BDS values in the case of dry-mate SiR–SiR #500 are higher than those in the case of wet-mate SiR–SiR #500 by a factor ranging from 3.3 to 3.9 as the contact pressure is increased from 0.16 to 0.27 MPa. In the case of dry-mate SiR–SiR #500, the 63.2% BDS increases by a factor of 1.4 as the pressure is increased from 0.16 to 0.27 MPa. Similar to wet-mate XLPE–XLPE, the BDS of the wet-mate SiR–SiR at 0.16 MPa is comparable with that of air. The increased pressure from 0.16 to 0.27 MPa increases the BDS of the wet-mate SiR–SiR interface by a factor of 1.2. It can be argued that the SiR samples are more hydrophilic than those of the XLPE samples [139], which might have resulted in the removal of fewer water droplets from the interface.

The Weibull plots of the BDS values containing the raw data for the dry-mate and wet-mate interfaces between the XLPE–XLPE and SiR–SiR are shown in *Fig. 6* in Paper II.

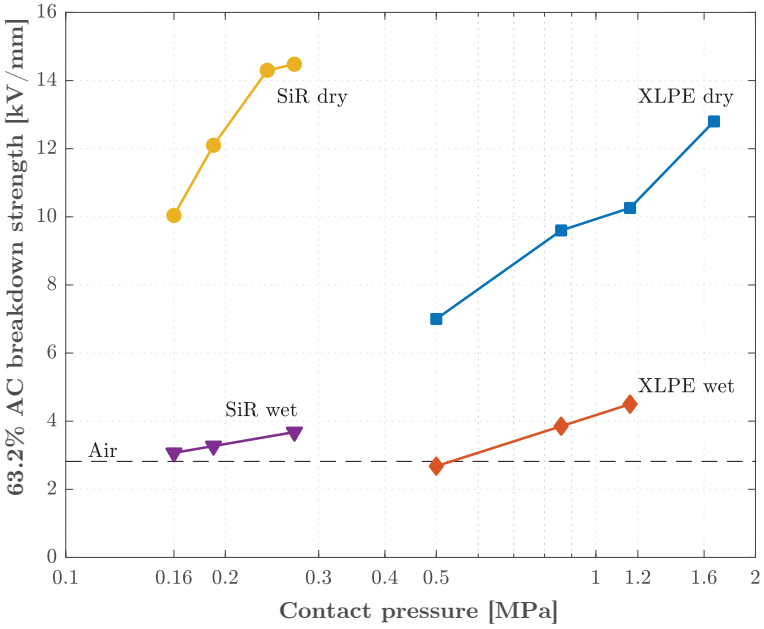

Figure 8.6: Longitudinal AC BDS values of dry-mate and wet-mate XLPE–XLPE #500, and SiR–SiR #500 interfaces vs. the contact pressure. (The BDS of air (∼ 2.8 kV/mm (rms)) is measured using the same experimental setup in ambient air at the laboratory with an electrode distance of 4 mm, as performed in the interface breakdown experiments).

8.3.2 Oil-mate (Lubricated) Interfaces

The BDS of the oil-mate XLPE–XLPE #500 at 0.5 MPa and SiR–SiR #500 at 0.16 MPa are presented in Figures 8.7(a) and 8.7(b), respectively. As can be seen, the presence of oil at the interface leads to significantly higher BDS values. In the case of XLPE–XLPE #500, the 63.2% value increases by a factor of 2.8 whereas the already high BDS of dry-mate SiR–SiR #500 rises by a factor of 1.6 (63.2% value).

The BDS of the oil-mate XLPE–XLPE #500 increases by a factor of 2.8 compared to that of the dry-mate XLPE–XLPE. Similarly, in the case of oil-assembled SiR–SiR, there is a significant increase by a factor of 1.6 in the 63.2% BDS. In some of the experiments, the BDS of the oil-mate SiR–SiR #500 interface was so high that the breakdown channel bypassed the interface along the electrodes through the oil; thus, the breakdown did not occur at the interface. This data were then recorded as singly censored data and treated accordingly [127]. An experiment of oil-assembled SiR–SiR #500 at 0.27 MPa was also attempted, but breakdown never occurred at the interface. The Weibull plots of air and the ester oil at 0.1 MPa (≃ 1 atm) are also incorporated in Figures 8.7(a) and 8.7(b) for comparison.

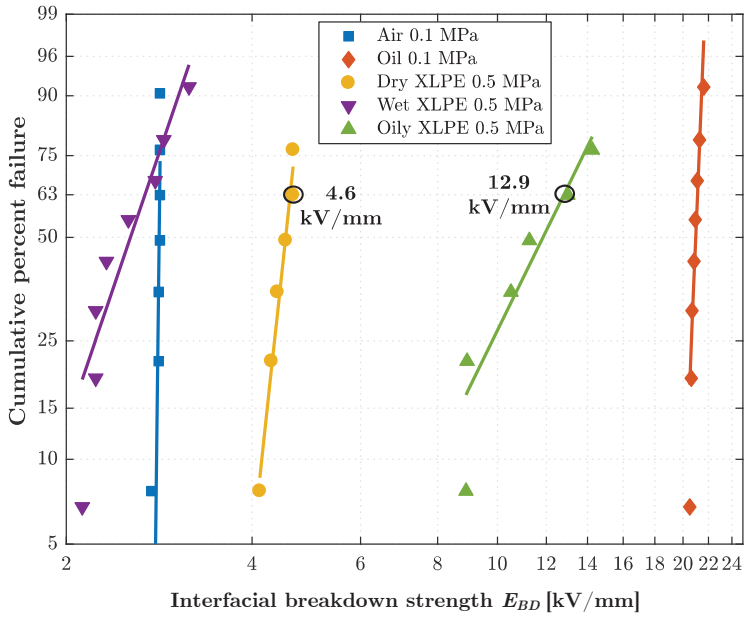

(a)

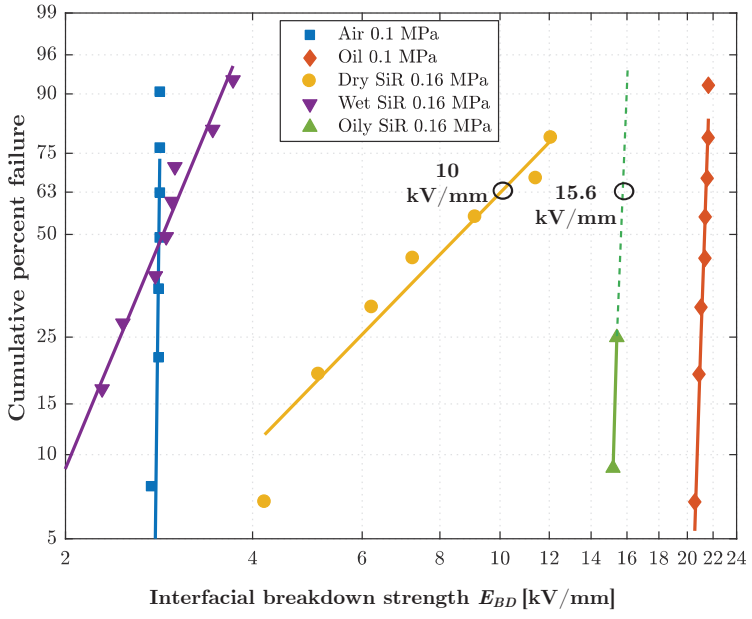

(b)

Figure 8.7: Weibull plot of cumulative percent failure in terms of BDS of dry-mate, wet-mate and oil-mate interfaces: (a) XLPE–XLPE #500 interface at 0.5 MPa contact pressure. (b) SiR–SiR #500 interface at 0.16 MPa contact pressure.

8.4 Summary of Findings

The results of the experimental work regarding the longitudinal AC breakdown testing of interfaces are summarized in this chapter. Summaries of the findings are grouped according to the studied variables.

Effect of Insulating Dielectric Medium on the AC Breakdown Strength

- Increased contact pressure from 0.5 to 1.16 MPa resulted in an increase of 63.2% BDS by factors of 1.2 and 1.7 in the cases of dry- and wet-mate interfaces, respectively.
- Dry SiR–SiR interface showed higher BDS despite the considerably lower applied pressure compared to dry XLPE–XLPE interface. These results together with the results of XLPE–SiR interface indicated that the presence of a more elastic material such as SiR made a significant improvement in the interfacial BDS.
- The differences in the BDS values of the dry, wet and oil-mate interfaces are very clear. The results indicated that air-filled cavities and water-filled cavities yielded BDS values significantly lower than those in the case of oil-mate interfaces. The presence of water at the interface reduced the BDS significantly due to the strong local field enhancements at the edges of the contact spots, as shown by the field calculations in Paper II and Appendix B. On the other hand, the lubricated interfaces yielded notably higher BDS. Especially the SiR–SiR interface showed an exceptional performance, so much so that in some cases breakdown did not occur at the polymer interface. Considering practical connectors, injection of insulating liquids such as ester oil prior to mating (i.e., oil-mate interfaces) appears of considerable value in practical applications in ensuring a high breakdown strength and long service life.

Effect of Surface Roughness on the AC Breakdown Strength

- The experimental results showed that the surface roughness has a significant influence on the interfacial BDS. A high correlation between the interfacial BDS and the surface roughness was observed. The BDS was doubled from the roughest to the smoothest surface. Likewise, increased contact pressure yielded increased BDS values by a factor of 1.5 irrespective of the surface roughness.
- The breakdown strengths of the dry-mate interfaces were recorded to be the highest when the contact pressure is relatively high, and the contact surface is as smooth as possible. Therefore, it is possible to improve the performance of solid-solid interfaces by introducing a smoother surface and by retaining the interfacial pressure high enough during service life.

Effect of Elastic Modulus on the AC Breakdown Strength

- The measured BDS results indicated that the elastic modulus is one of the most prominent properties of solid materials, affecting the BDS of polymer interfaces. More specifically, the lower the elastic modulus, the higher the BDS, where a much higher BDS is achieved using softer materials with low elastic moduli such as SiR and XLPE. Besides, the interfacial BDS increases with the increased contact pressure in all cases independently on the elastic modulus.
- The measured BDS results indicate that the elastic modulus is one of the prominent material properties affecting the BDS of polymer interfaces.
- The BDS of the PEEK–XLPE interface suggested that the presence of the XLPE made a significant increase in the BDS as compared to the BDS of PEEK–PEEK interface, while the XLPE–XLPE interface has yielded the highest BDS at all pressure values.
- A similar trend is observed in the case of XLPE–SiR interface. It is, thus, concluded that interfaces between a soft and hard material (relative to each other) achieve a higher BDS than the BDS of interfaces formed between the identical, relatively hard materials.

Surface Tracks of Interfacial Breakdown

Breakdown tracks damaged the surface of each sample at the interface. Images of the tracks at surfaces of the SiR, XLPE, EPOXY, and PEEK samples that were polished using #500 sandpaper, are shown in Figure 8.8. The results reported in this chapter stand for the BDS values that took place at the interface in each case except for a few cases which occurred in the oil that are represented by singly censored data, as mentioned in Section 6.2.3. After each breakdown test, the condition of each sample at the interface was inspected. Breakdown tracks at the surfaces of the selected samples in the cases of dry-, wet-, and oil-mate were inspected using the digital microscope. Selected images of the breakdown tracks are shown in Appendix A.2. Apart from the main breakdown track, the images exhibit compelling evidence via the traces caused by the discharge activity at the interface before the breakdown took place at some other place at the interface.

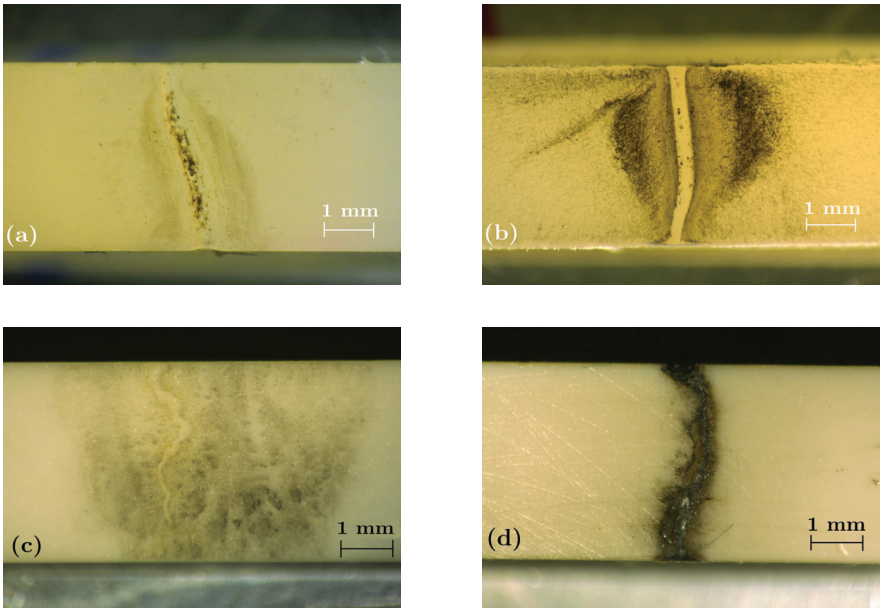

Figure 8.8: Surfaces of broken-down interfaces inspected using the digital microscope: (a) SiR #500. (b) XLPE #500. (c) EPOXY #500. (d) PEEK #500.

Chapter 9

Results of AC Partial Discharge Experiments

In this chapter, the results of the AC PD experiments, that were performed to measure PD inception field values at solid-solid interfaces, are shown.

9.1 Scope of the PD Experiments

The main purposes of performing the PD experiments are to address:

i. The correlation between the measured PD values and measured BDS values i.e, the correlation between the discharged cavities and the interface breakdown.
ii. The correlation between the measured PD inception field values ($PDIE^m$) and the estimated PD inception field values ($PDIE^e$) using the estimated, average length of cavities under fully vented conditions to test the applicability of the interface breakdown model proposed in Chapter 4 in two submodules:[14]
    - The applicability of the statistical interface contact submodel (see Section 4.1.1).
    - The applicability of the tip field-based interfacial tracking resistance model (see Section 4.1.2).

[14] To eliminate any ambiguity, it is again highlighted here that $PDIE^e$ denotes the analytically estimated cavity discharge field whereas $PDIE^m$ stands for the experimentally measured PD inception field values.

The reason why the AC breakdown testing was performed more extensively compared to the PD testing is explained as follows: the proposed contact surface model shown in Figure 3.6 transforms/reduces the 3D surface asperities to a 2D profile, which is traversed only by the tangential/parallel electric field component. It is unclear if the experimentally obtained (measured) PD inception field values, PDIE^{m} stand for the PDIE of discharged cavities parallel to the electric field (that are likely to cause the interface BD) or for significantly larger connected cavities not parallel to the field (that are unable to bridge the electrodes). Due to this uncertainty, the AC breakdown testing was used to ensure that the discharged cavities had caused interfacial breakdown along the tracking path parallel to the electric field as those shown in Appendix A.2.

For the PD testing, dry-mate PEEK–PEEK #500 and XLPE–XLPE #500 interfaces were tested at various contact pressures (0.5–2.25 MPa) using the setup illustrated in Figure 6.6 (real setup is shown in Figure F.3). Wet-mate and oil-mate cases were not covered. The reason why XLPE and PEEK were investigated is that one relatively soft interface and one relatively hard interface were intended to be tested to observe the influence of the modulus more clearly.

The PRPDA is utilized to assess the PD patterns obtained from the PD experiments. First, the PD patterns were used to check if the source of the PD is the air-filled cavities at the interface by following the methodology explained in Section 6.3.2. Concentrated PD clusters near the voltage zero crossing points in Figure 9.1(a)–(b) validate that the PD source is the discharged microcavities at the interface [140]. Furthermore, PD patterns are shown using 3D histograms in Figure A.22 in the format of $\phi - q_a - n_{_{PD}}$ plots in Appendix A.3. There, ϕ on the x-axis is the voltage phase, q_a on the y-axis is the apparent charge magnitude and $n_{_{PD}}$ on the z-axis is the number of PDs occurring at a specified phase of the applied voltage.

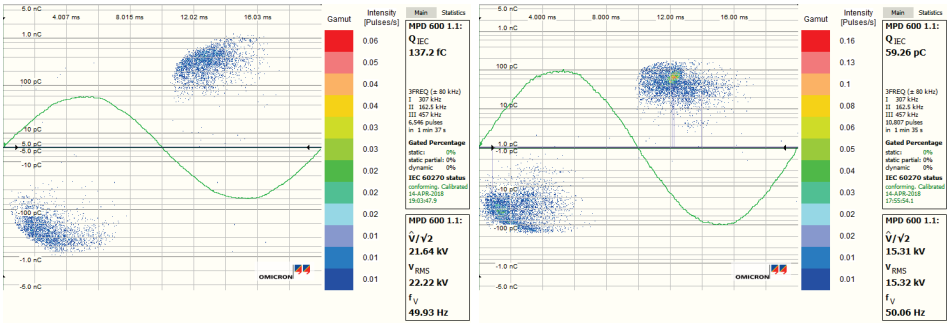

(a) **(b)**

Figure 9.1: Measured PD patterns at 1.16 MPa of the interfaces: (a) XLPE–XLPE #500. (b) PEEK–PEEK #500.

9.2 Results of the PD Inception Field Tests [Paper V]

The plots in Figure 9.2 show the measured PDIE^{m} results using the cumulative probability of Weibull distribution. Figure 9.2 indicates that 63.2% PDIE^{m} in the case of XLPE is higher than that of the PEEK at 1.16 MPa by a factor of 2.3. In the case of PEEK #500 interface, increased pressure from 1.16 MPa to 2.25 MPa has also increased the 63.2% PDIE^{m} by a factor of 1.8 while the 63.2% PDIE^{m} augmented by a factor of 1.6 in the case of XLPE #500. These results agree with the observations from the AC breakdown experiments although the extent of PD experiments is limited compared to that of AC breakdown experiments. In the AC breakdown experiments, breakdown strength decreased at higher elastic modulus. In accordance with this finding, in the PD tests, XLPE–XLPE #500 has yielded higher PDIE^{m} than that of the PEEK–PEEK #500.

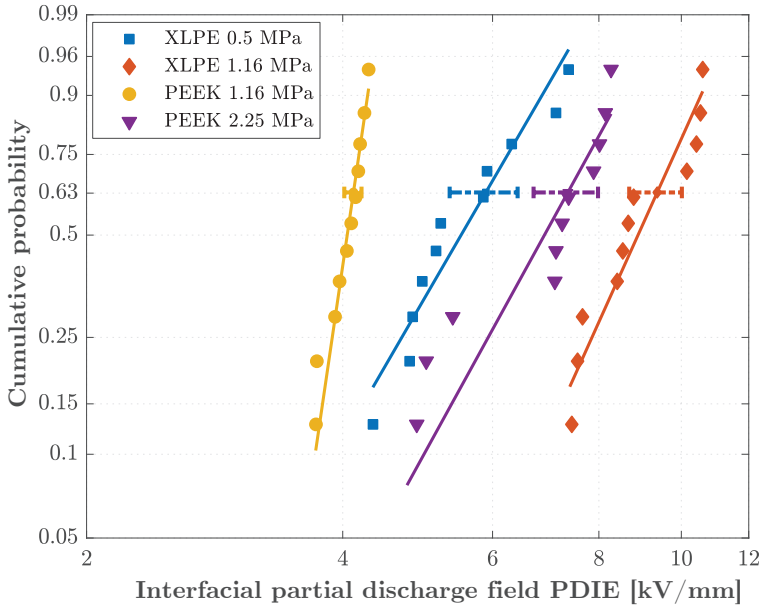

Figure 9.2: Measured PDIE values of dry-mate XLPE–XLPE #500 and PEEK-PEEK #500 interfaces.

The graphs in Figures 9.3(a)–(d) provide statistical quantitative examination using each PD value. The PD data were exported to MATLAB® and were further processed, as presented in Appendix A.3. In the analysis, XLPE and PEEK are compared at the same pressure 1.16 MPa as well as PEEK being examined at 2.25 MPa to show the effect of pressure increase. Figure 9.3(a) shows that the number of PDs per cycle is the highest in the case of the PEEK, and it further increases at a higher contact pressure. The majority of discharges occur at the rising edge

of the voltage whereas fewer discharges occur at the end of the falling edge of the applied voltage since the electron generation rate is higher at the rising edge (first and third quadrants of the applied voltage) [51]. As seen in Figure 9.3(a), the earliest phase at which the PD onsets is slightly shifted forward in phase when the applied voltage is increased due to an enhanced electron generation rate [51]. In contrast, the mean charge magnitude in Figure 9.3(b) is higher in the second (90°–180°), and fourth quadrants (270°–360°) of the applied voltage since fewer PDs per cycle occur in those regions. Overall, XLPE has higher mean charge amplitude. In Figure 9.3(c), the total charge amplitudes per cycle have skewed distributions because a higher number of PDs occur at the rising edge than at the peak.

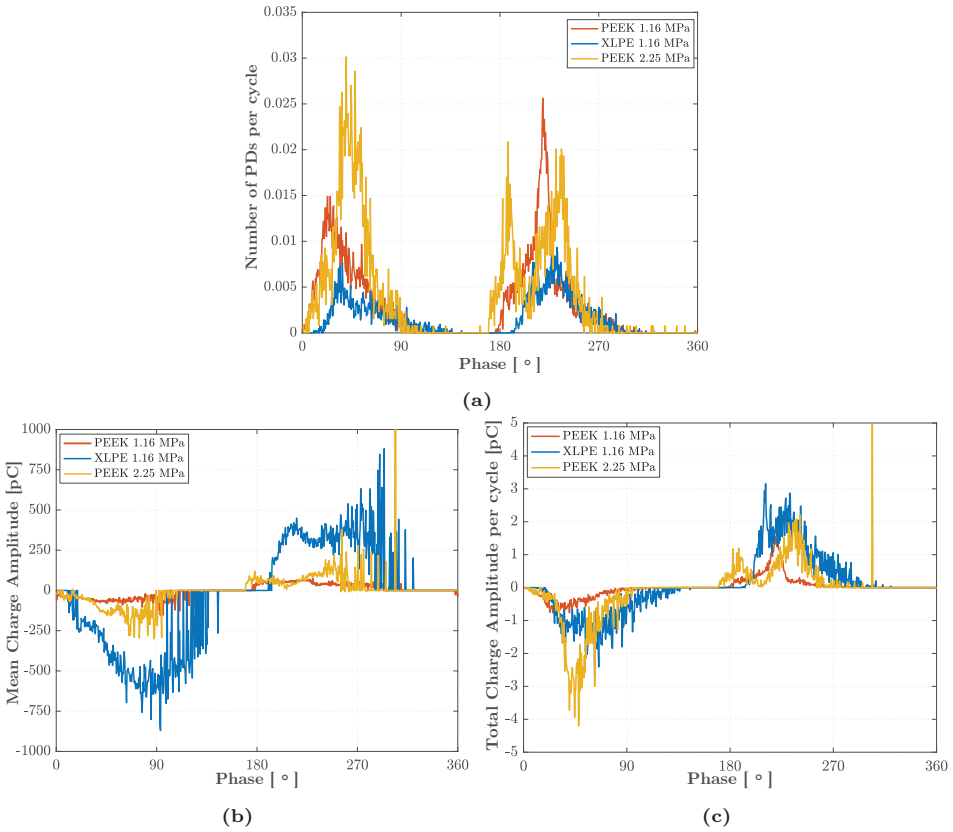

Figure 9.3: Post-processed PD data: (a) Number of PDs per cycle vs. phase angle. (b) Mean charge amplitude vs phase angle. (c) Total charge amplitude per cycle vs. phase angle.

Additional studies using the PSA to extract information of the PD sequence are provided in Appendix A.3.1.2. Finally, the approximation of the tip field-based model introduced in Section 4.1.2.1 to estimate the local field enhancements in the contact spot discharge submodel is verified by obtaining the PD pattern from zero voltage until breakdown. Details are available in Paper V (see *Section 5.4*).

Chapter 10

Results of Interfacial Discharge Monitoring Experiments

Discharge-monitoring tests were performed using PEEK–glass interfaces by following the procedure explained in Section 6.4. PEEK–glass interfaces were tested with the PEEK samples at two different surface roughnesses, where PEEK samples were sanded using sandpapers with grit #180 and #500.

By following the procedure explained in Section 6.4.4, initial experiments were carried out. First, a PEEK–glass interface was placed between the electrodes. The voltage was increased with a rate of 1 kV/s. PRPD pattern was monitored simultaneously to check if the PD activity started. When PD clusters, reminiscent of interface discharge, appeared in the PRPD diagram, the voltage was kept at its current value. However, no discharge activity could be monitored with the CCD camera at the PD inception voltage (PDIV) value. Next, to ensure that the interfacial cavities were the source of the PDs on the PRPD diagram, a large polymer piece (without an interface) was tested, but no PD was recorded at the PDIV value that was the value recorded in the presence of an interface in the previous case. As the next step, the settings of the camera, as well as the darkness condition of the room, was checked, and many different combinations of camera settings, rough interfaces, and voltage values were tried out to manage to obtain a discharge image. Despite numerous trials, the discharge activity could not be captured by the CCD camera. Then, the same procedure was repeated at increased voltages with the expectation of monitoring the discharge activity. However, the increased voltage caused the failure of the interface before any discharge images could be captured.

To overcome this problem, an artificial cylindrical cavity of 1-mm diameter was drilled at the surface of one of the samples (see Figure 6.10) to initiate the PD activity at a lower voltage without causing an interfacial breakdown immediately.

Thus, a "main" cylindrical cavity perpendicular to the field direction—similar to the bottom half of the ellipsoid in Figure B.5(a) resulting in the highest field enhancement factor—was punched, leading to a high field enhancement at the edges of the discharged "main" cavity and subjecting the contact spots and microcavities to high local, non-homogeneous fields, as illustrated in Figure 4.4. The presence of the main cavity caused the PD to start in the cavity at a relatively low voltage that enabled discharge images to be captured without evolving to a complete flashover.

10.1 Representation of the CCD Camera Images

A large number of experiments were performed to visualize the discharge activity taking place at the interface. Identical experiments were repeated 10 times in each case (i.e., PEEK #180 and PEEK #500) to differentiate between the discharge mechanisms due to the stochastic nature of discharges. Before assessing the discharge images, some information on the interpretation of the images will now be provided.

Figure 10.1 depicts the arrangement of the electrodes and the sample in the experimental setup. The top view of the electrode container is the same view as the CCD camera, except that the interface can partially be seen through the window of the steel and wooden plates (not shown in Figure 10.1).

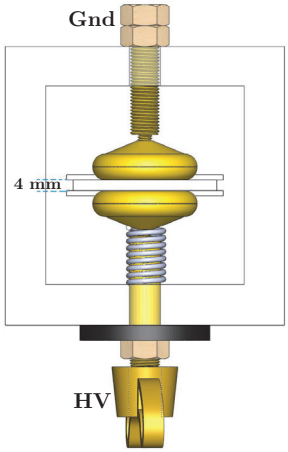

Figure 10.1: Top view of electrode housing. HV: High voltage terminal, Gnd: Earth terminal.

A pseudo-color filter is used to distinguish between different intensities of the emitted light in the images. The intensity of discharges in the cavity is hardly discernible in Figure 10.2(c) whereas pseudo filter highlights it with red considerably more clearly in Figure 10.2(d). In the pseudo color filter, the red color is assigned to the most intense light emission while colder colors such as shades of blue represent reduced intensity.

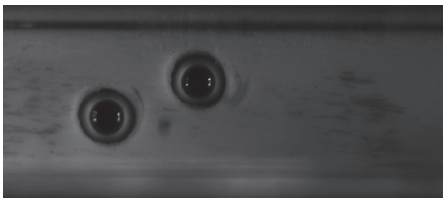

(a) Double cavities with 1-mm diameter before the voltage is applied.

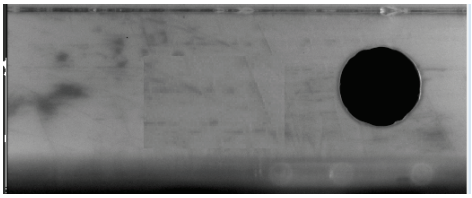

(b) Single cavity with 2-mm diameter before the voltage is applied.

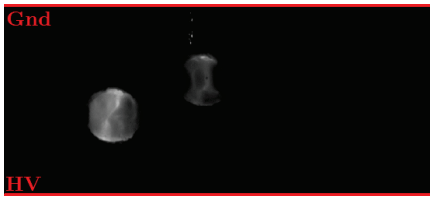

(c) Discharged cavities (no filter).

(d) Discharged cavity bridging with the HV electrode (pseudocolor filter).

Figure 10.2: Captured images using the CCD camera setup. The distance between the electrodes is 4 mm in all cases.

10.2 Streamer Discharge Channels Observed at Polymer–Glass Interfaces

In the experiments, interfaces between PEEK #180–glass and PEEK #500–glass were tested at a contact pressure ranging between 2.5–3.5 MPa. Based on the characteristics of the glow discharge, the results of the experiments that yielded similar characteristics are grouped together in Figures 10.3, 10.5, and 10.6. In a few experiments, two identical cavities were drilled to observe the interaction between discharged cavities.

The first group of images in Figure 10.3 consist of discharged microcavities connected to each other which are induced by the high local field generated by the discharged main cavity. The discharged cavities form a semi-conductive filament bridging the main cavity with one of the electrodes. The reason why it is called semi-conductive is that there are likely contact spots isolating these discharged microcavities.

Figure 10.4(a) displays the size of a microcavity in terms of pixels as compared to that of the main cavity with a diameter of 1 mm. Thus, the ratio of 1/15 between the pixels yields a microcavity size of 67 µm in the direction of the field. Similarly, the smallest cavity size is found to be around 36 µm considering the ratio of 5/140 in Figure 10.4(b). These images indicate that sizes of the microcavities are comparable with the estimated cavity sizes (in the direction of the field) ranging between 32–137 µm as listed in Tables 11.1 and 11.2.

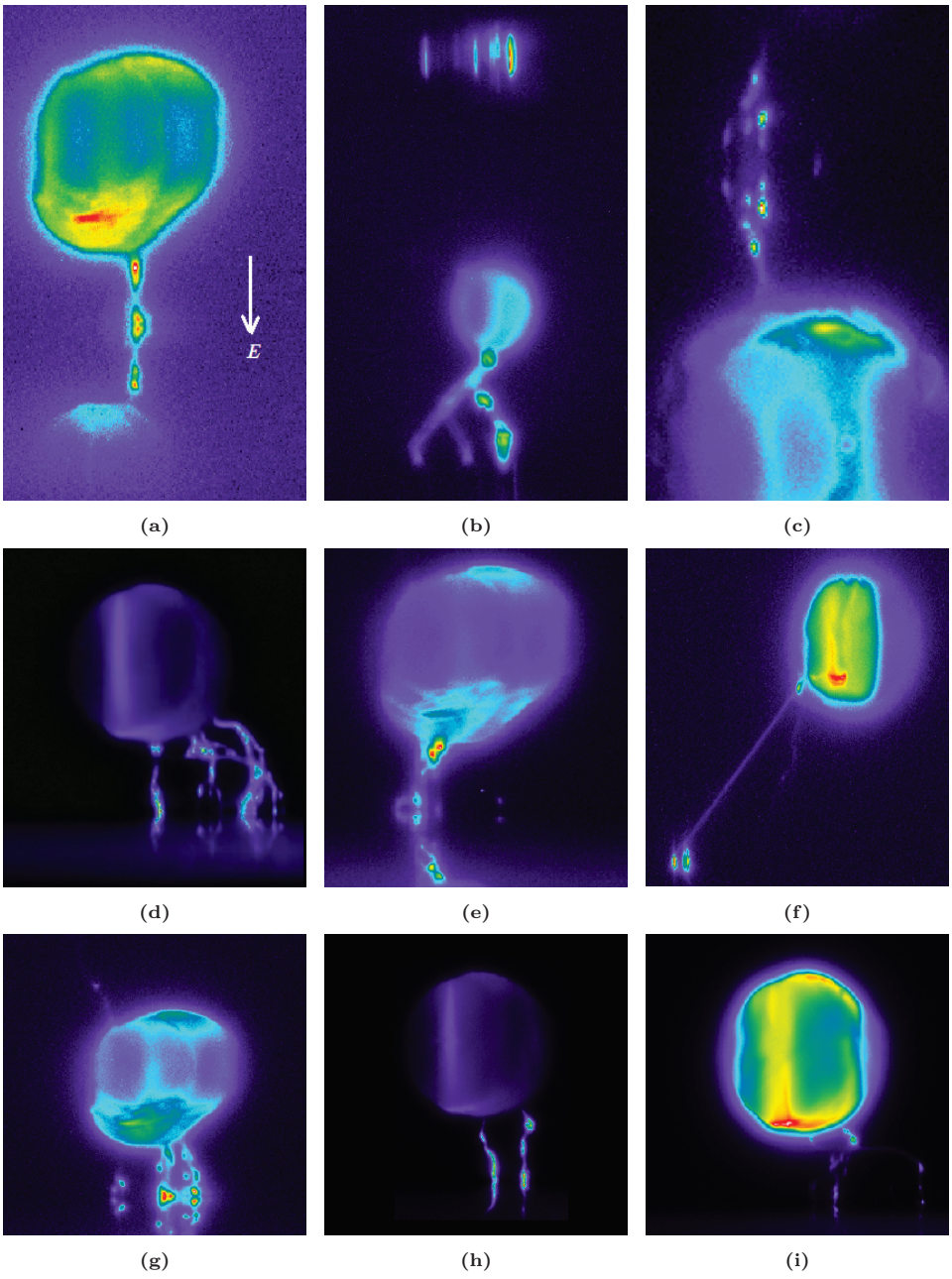

Figure 10.3: Interfacial discharges induced by the 1-mm artificial cavity that were formed by isolated, discharged cavities at the PEEK #500–glass interfaces. The electric field direction shown in (a) is the same for all the images. Exposure time is 60 s. The images do not necessarily follow a sequence in any rows and columns.

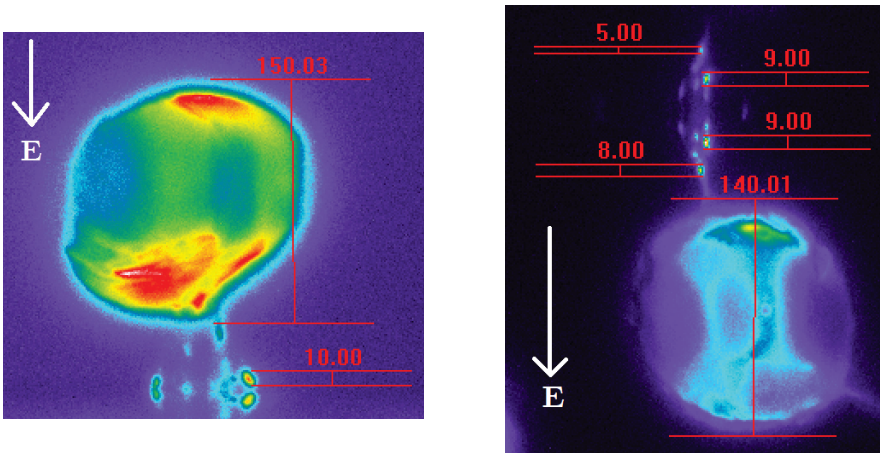

(a) (b)

Figure 10.4: Size of a discharged microcavity as compared to 1-mm artificial cavity (in pixels).

The next group of captured images displayed in Figure 10.5 depict continuous glow discharges bridging the main cavity with either of the electrodes based on the direction of the electric field. The continuous discharge channels suggest that streamers chase air-filled openings composed of a number of connected cavities in 3D space. In particular, the images in the first two rows indicate that the progressing discharge channels could not follow the shortest path to the electrode due to the contact spots obstructing the discharges from directly proceeding towards the electrode. Instead, the discharges presumably followed the air-gaps connected to each other. The simulated structure of the surface asperities—shown in Figure 11.9 by using the data from real, measured surface profiles—support the presence of continuous air-gaps.

Figure 10.6 displays the results obtained in the case of PEEK #180–glass interfaces. As seen, the discharge channels are significantly wider compared to those shown in Figure 10.5. Based on the difference between the simulated surface textures of PEEK #180 and PEEK #500 displayed in Figure 11.9, there are larger air-gaps and fewer isolated cavities in the case of PEEK #180, likely to result in streamers with a higher cross-section as observed in the captured images. Thus, the impact of the surface roughness on the width of the air-gaps is clearly observed, which, in turn, results in stronger interfacial discharges with higher energy.

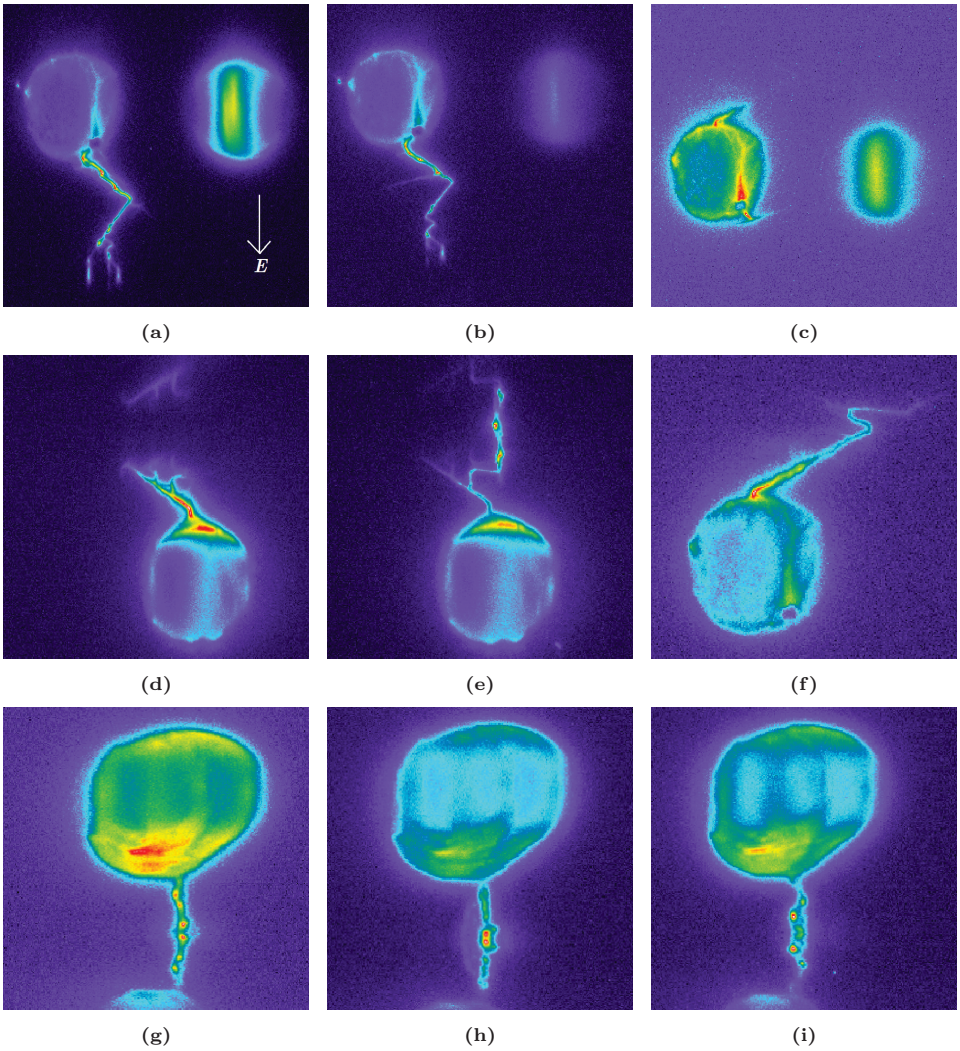

Figure 10.5: Interfacial discharges induced by the 1-mm artificial cavity that were formed by continuous channels with low cross-section at the PEEK #500–glass interfaces. The electric field direction shown in (a) is the same for all the images. Exposure time is 60 s. The images do not necessarily follow a sequence in any rows and columns.

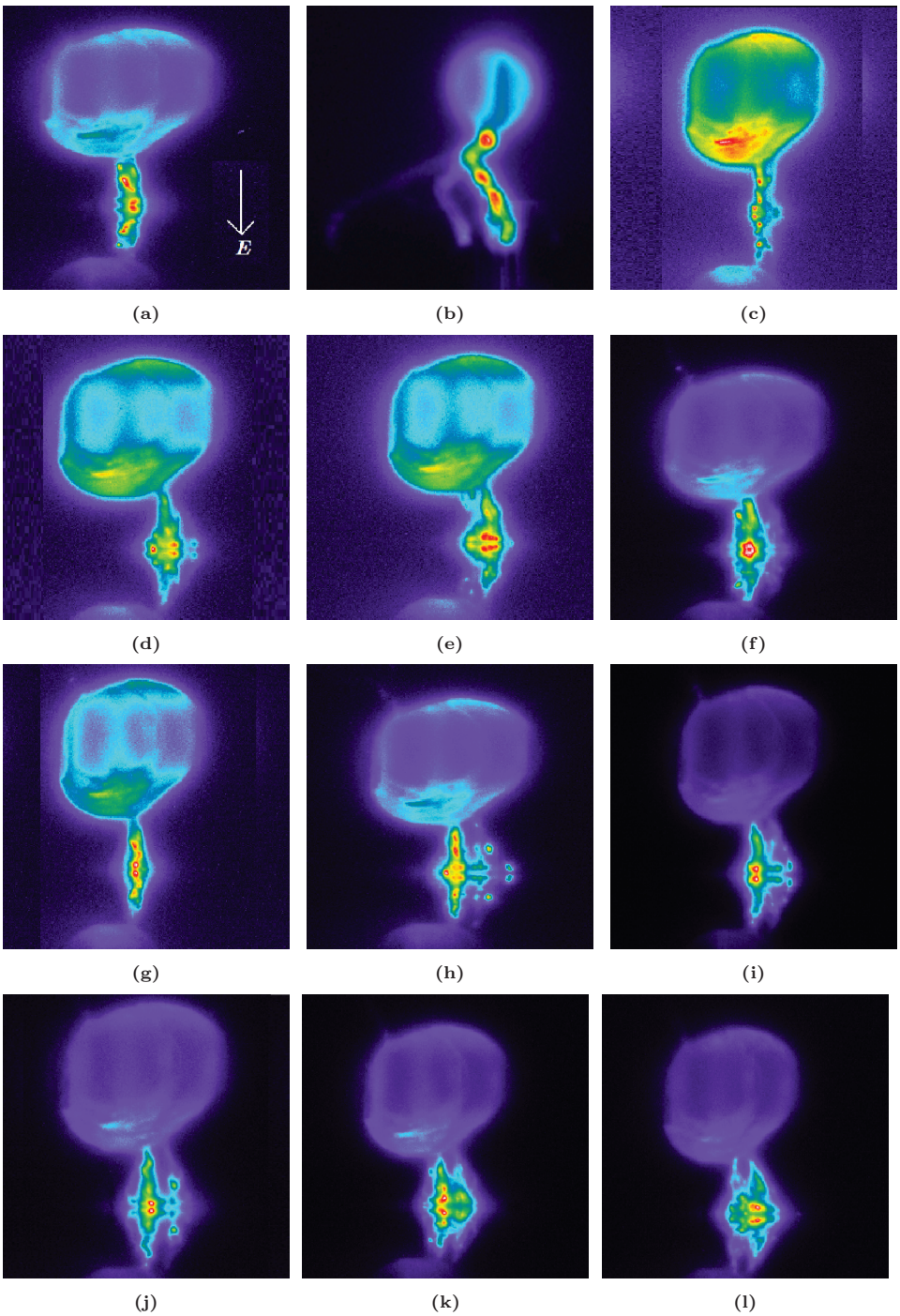

Figure 10.6: Interfacial discharges induced by the 1-mm artificial cavity that were formed by continuous channels with high cross-section at the PEEK #180–glass interfaces. The electric field direction shown in (a) is the same for all the images. Exposure time is 60 s. The images do not necessarily follow a sequence in any rows and columns.

10.3 Discussion on the Interfacial Discharge Mechanisms based on the Discharge Images

In the experiments, whose results are shown in Figure 10.3, the cavities might have been broken into smaller ones, resulting in no large air-filled openings as opposed to those observed in the case of Figures 10.5 and 10.6 although identical samples were used and the same experimental procedure was followed. It is, thus, fair to claim that the stochasticity involved in the discharge mechanisms, the statistical distribution of the surface asperities (normal distribution according to the results in Appendix D.3.3.2), and even tiny, involuntary methodological differences occurred in the experiments are likely to cause deviations in the results.

Another possibility could be that the contact spots enclosing the discharged cavities broke down due to very high local fields at their terminals, as modeled in Figure 4.4. To check the likelihood of this mechanism, we scanned the surfaces of the samples using the profilometer and the digital microscope if there were permanent damages at the surface (i.e., contact spots subjected to electrical BD) after the experiments.

Nonetheless, a number of the experiments ended up with a complete flashover at the interface, as illustrated in Figure 10.7(a) due to propagating streamers over time at the same voltage. The scanned surfaces of the samples subjected to an electrical breakdown are displayed in Figure 10.8. On the other hand, in the majority of the experiments, the discharge activity was confined only to the artificial main cavity and did not spread to the interfacial microcavities. In a few cases, discharges ceased soon after the inception of the PDs.

In the majority of the experiments, the discharges did not cease; neither did they evolve to a complete flashover. After these experiments, the surfaces of the samples were scanned using the profilometer and the digital microscope. Figure 10.9 demonstrates the images of the PEEK samples acquired by using the digital microscope. These samples were exposed to the discharged main cavity and other discharges induced by the main cavity and/or other intrinsic cavities at the interface for a short period of five minutes. As can be seen in Figures 10.9(a) and 10.9(b), discharges left visible marks at the surfaces. In addition to this, high local fields at the brim of the cavity caused morphological changes, probably due to temperature caused by the persistent discharges in the main cavity. In some sections at the interface close to the main cavity, permanent damages caused by the destructive effects of the strong local discharges were also observed, as shown in Figure 10.9(c), which did not exist before the experiments. Moreover, the surface of the glass sample exposed to interfacial discharges was scanned using the profilometer and is shown in Figure 10.10(b) while Figure 10.10(a) depicts the scanned surface of a virgin glass sample.

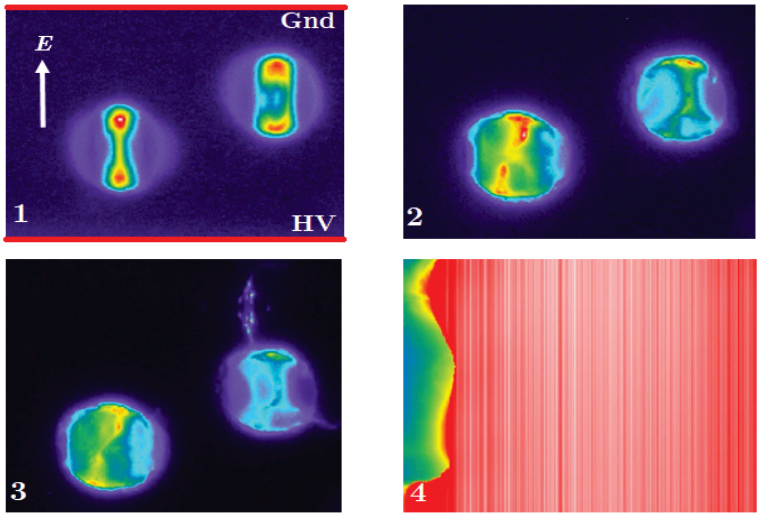

(a) Interfacial discharge activity in a sequence (1–4) that evolved to a complete flashover.

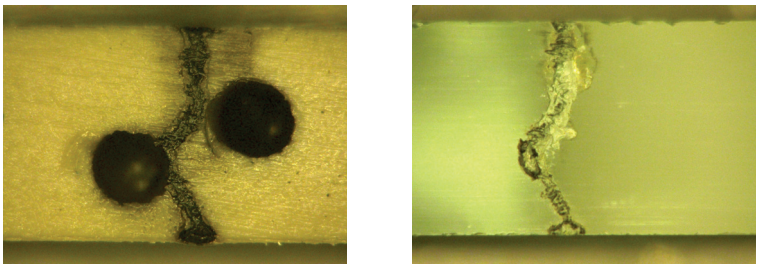

(b) PEEK sample exposed to interface BD. **(c)** Glass sample exposed to interface BD.

Figure 10.7: Experiments resulted in a complete flashover due to cavity-induced discharges. The artificial cavities are of 1 mm diameter and the interface width is 4 mm.

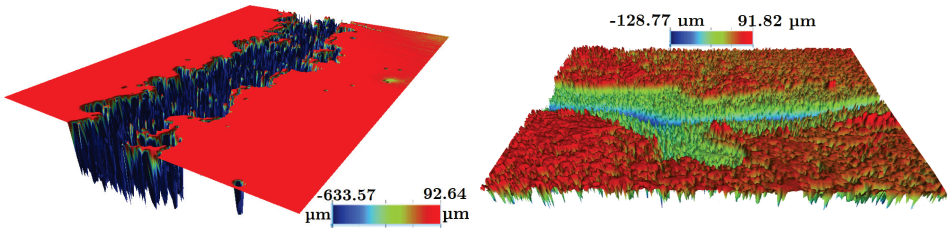

(a) Glass sample exposed to BD. **(b)** PEEK sample exposed to BD.

Figure 10.8: 3D surface inspection of PEEK samples with cylindrical cavities (1.25 mm × 0.94 mm). Samples are scanned before being polished again.

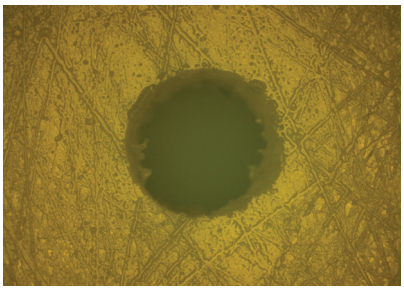

(a) PEEK surface before a test.

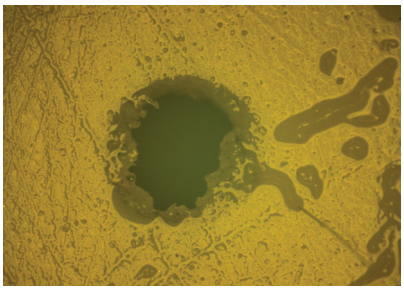

(b) PEEK surface after the test.

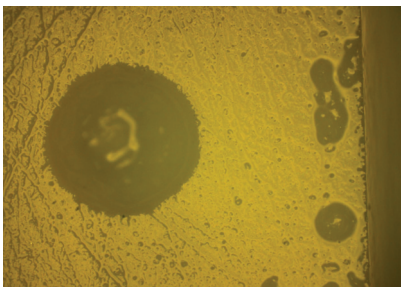

(c) Another PEEK surface after a new test.

Figure 10.9: Surface inspection of interfaces before and after discharge-monitoring tests. The artificial cavities are of 1-mm diameter.

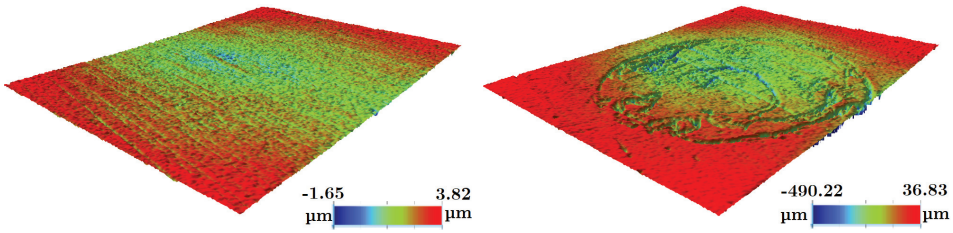

(a) **(b)**

Figure 10.10: 3D surface inspection of glass samples (1.25 mm × 0.94 mm). (a) Virgin glass sample. (b) Glass sample exposed to discharges caused by the PD activity in a PEEK sample with a 1 mm artificial cavity.

Possible mechanisms responsible for the local destruction of contact area/spots are further elucidated here by referring to the following study that focused on the mechanisms of the breakdown of contact spots.

Gao et al. [66] used our interface model, that was formerly proposed in [45, 46, 67, 68], to study the interface discharge behavior between polypropylene and silicone rubber under AC voltage. The author used a part of their discussion on possible mechanisms responsible for the local deterioration of contact area at the initiation stage, and, since they used our interface model, the discussion is highly

relevant to the main hypothesis of this thesis. The duration between the *instants I* and *II* in Figure 4.6 is divided into two substages: initiation stage and propagation stage. Initiation stage is assumed to be considerably longer than the propagation stage since the propagation of the interfacial tracking is assumed to take place momentarily, i.e., in 10^{-7} s as modeled in Section 4.1.2.2.

The initiation stage is illustrated in Figure 10.11(a) [66]. In the case that the average-size cavities are discharged (at the *instant I*), the discharge activity in the cavities leads to energetic particle bombardment and light emission from recombination of particles with opposite polarities [66]. The thermal effect of the discharge is not taken into consideration at this point since the discharge has low energy; the heat generated at this stage could thus be neglected [66].

The energetic particle bombardment is likely to disrupt the covalent bonds that hold the polymer together. The light emission also gives rise to the acceleration of the chain scission [66]. As illustrated in Figure 10.11(a), the bombardment of particles is likely to cause the loss of part of their energies, and trapped carriers (electron or hole) arise at the contact areas at the interface [66]. Such carriers are subjected to a de-trapping process and recombine with each other, leading to further light emission as well as local field distortion [66]. Consequently, at the interface, low-density regions are formed that are relatively easy to permit electrical breakdown under AC voltage [141]. Once the contact surface between two cavities is broken-down, the discharged cavities are connected, resulting in a larger discharge channel. Hence, the degradation and the breakdown of the local contact area are essential for the discharge channel to propagate at the interface. At the propagation stage, as illustrated Figure 10.11(b), the discharge activity is considerably stronger than the discharge in the initiation stage [66]. In this case, the thermal effect of the discharge channel cannot be neglected, since gas expansion is likely to take place within the discharged cavities due to the heat generated from the strong discharge channel [66]. Moreover, the gaseous byproducts are generated from the degradation of the polymer sample by the discharge activity, leading to a gas expansion in the deformation of the cavity, as depicted in Figure 10.11(b)). Due to the strong discharge activity, degradation and subsequent breakdown triggered by the particle bombardment and the light emission from the discharge channel seem to play an essential role in the propagation of the discharge channel. On the other hand, the charge injection, trapping, and de-trapping mechanisms have a subordinate role in the degradation of contact area [66].

To sum up, different microtracking resistances of the polymers studied in this thesis tend to affect the primary discharge propagation mechanisms of particle bombardment and the light emission from discharge channel, whereas the charge injection, trapping, and de-trapping mechanisms have indirect effects as they result in further light emission as well as local field distortion in the initiation stage. The initiation and propagation stages discussed above seem to agree with the observed discharge propagation mechanisms. For instance, the discharged cavities displayed in Figures 10.3 and 10.5 can stand for the initiation and propagation stages of the

contact spot breakdown, respectively, such that only microcavities are discharged in the initiation stage whereas the contact areas isolating the discharged cavities are bridged in the propagation stage as illustrated in Figure 10.11(b).

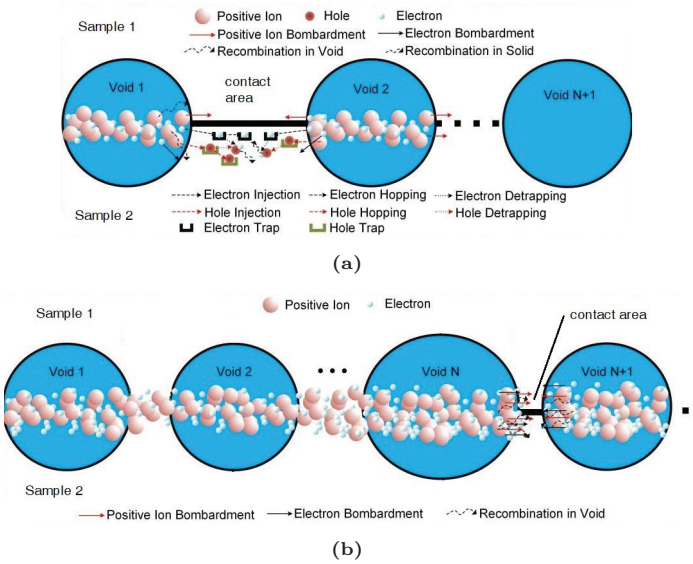

Figure 10.11: Mechanisms for the degradation and breakdown of perfect/ideal contact area at various discharge stages [66]: (a) Initiation stage. (b) Propagation stage.

10.4 Additional Results from Discharge Experiments

The results of a discharge experiment run for 48 hours are shown in Appendix A.4.1 rather than in this chapter because the main focus of this thesis is centered around the instantaneous mechanisms leading to an interface breakdown. The long-term impact of cavity discharges at the interface is not directly related to the main research questions, but it still provides supplementary information on the interfacial breakdown mechanisms.

The PD inception field values and the corresponding patterns from PRPDA were also measured in the experiments. A summary of the main PD results is given in Appendix A.3.2 to correlate the discharge images with the PD patterns along with the histogram of emitted light during the discharge event. Similarly, since these results only serve as supplementary/supporting information, they are placed in the appendix for coherence and clarity.

Chapter 11

Results of Theoretical Models

In this chapter, the results of the theoretical models introduced in Chapter 4 and Chapter 5 are briefly shown.

11.1 Results of the Interface Breakdown Model

The results calculated using the theoretical model proposed in Section 4.1 are shown in this section. The results are categorized into two main sections, where the influence of the elastic modulus and surface roughness are considered separately along with the effect of contact pressure.

11.1.1 Results of the Cavity Discharge Submodel

Using the statistical contact model described in Chapter 3, A_{re}, n, and the average cavity size d_{avg} are computed for the SiR, XLPE, EPOXY, and PEEK samples sanded with #500 (see Table 11.1). As mentioned in Section 3.3.3, though the number of cavity and contact spot pairs, n is a dimensionless quantity according to Equation (3.17), the tabulated values are normalized with the nominal sample area $A_a = 220\,\mathrm{mm}^2$.

For a complete assessment, sizes of average cavities are calculated with two-sigma significance (i.e., equivalent to 90% CI [142]) using the standard deviation of the asperity radius σ_p. Thus, an estimated cavity size is represented with its 90% CI by a shaded region while the markers in Figure 11.1(a) signify the experimentally applied pressure values for reference. A similar procedure is followed to calculate the l_{avg} values with their 90% CIs. However, in the interface breakdown model, the total length of the contact spots i.e., effective interface length, l_{eff} is to be substituted for l in Equation (4.5). Therefore, l_{eff} values are calculated at this stage by substituting the l_{avg} values from Equation (3.19) into Equation (4.6) to

omit the intermediate steps. The estimated l_{eff} are displayed in Figure 11.1(b) with the shaded regions standing for the 90% CIs.

Table 11.1: Estimated cavity size, number, and real contact area of the SiR, XLPE, EPOXY, and PEEK.

Param. / Pressure	SiR – SiR #500				XLPE – XLPE #500			
	p_a [MPa]	A_{re}/A_a [%]	n [mm^{-2}]	d_{avg} [µm]	p_a [MPa]	A_{re}/A_a [%]	n [mm^{-2}]	d_{avg} [µm]
p_{a1}	0.16	2.05	432	47.6	0.50	0.99	319	55.7
p_{a2}	0.19	2.43	503	44.0	0.86	1.72	515	43.7
p_{a3}	0.24	3.07	618	39.6	1.16	2.32	670	38.2
p_{a4}	0.27	3.45	685	37.5	1.67	3.33	923	32.4

Param. / Pressure	EPOXY – EPOXY #500				PEEK – PEEK #500			
	p_a [MPa]	A_{re}/A_a [%]	n [mm^{-2}]	d_{avg} [µm]	p_a [MPa]	A_{re}/A_a [%]	n [mm^{-2}]	d_{avg} [µm]
p_{a1}	1.16	0.10	57	132.0	1.16	0.03	52	137.6
p_{a2}	1.67	0.14	79	112.4	1.67	0.04	72	117.2
p_{a3}	2.25	0.19	102	98.6	2.25	0.06	94	102.8
p_{a4}	3.34	0.29	145	82.8	3.34	0.08	133	86.4

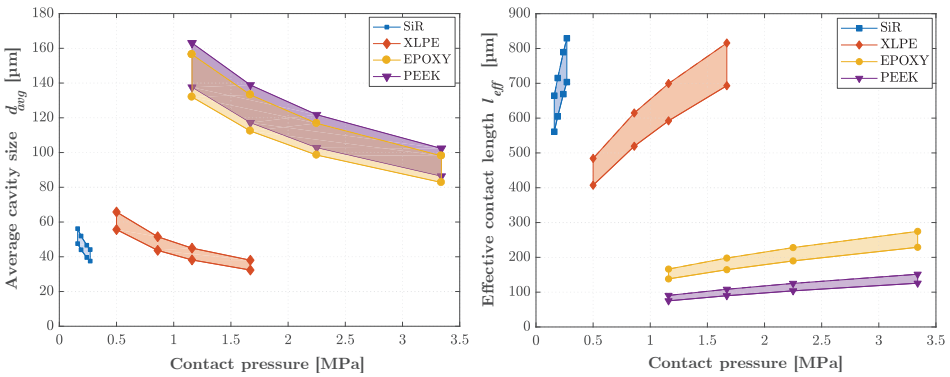

(a) (b)

Figure 11.1: SiR, XLPE, EPOXY, and PEEK sanded with #500: (a) Estimated average cavity size via Equation (3.21b) plotted against the applied contact pressure. (b) Estimated effective contact length via Equation (4.6).

A_{re}/A_a decreases in harder materials, as seen in Table 11.1 because the increased modulus cause larger cavities to arise at the interface, and in turn, a smaller contact area is predicted. In this regard, the average cavity size d_{avg} increases by a factor of $2.3 - 2.9$ from the softest interface SiR to the hardest interface PEEK as the contact pressure p_a is increased. To sum up, reduced real contact area results in a substantial reduction in the number of contact spots n and hence larger average cavities arise.

Similarly, A_{re}, n, and the average cavity size d_{avg} are computed for the XLPE samples with different surface roughnesses (see Table 11.2). The average cavity sizes d_{avg} are calculated with their standard deviation (equivalent to 90% CI) and are shown with the shaded regions in Figure 11.2(a) while the markers signify the pressure values used in the experiments for reference. Likewise, the estimated l_{eff} values are displayed in Figure 11.2(b) with their 90% CIs.

Table 11.2: Estimated cavity size, number and real contact area of the XLPE samples with different roughnesses.

Param. / p_a / Interface	0.5 MPa			0.86 MPa		
	A_{re}/A_a [%]	n [$\mathrm{mm^{-2}}$]	d_{avg} [µm]	A_{re}/A_a [%]	n [$\mathrm{mm^{-2}}$]	d_{avg} [µm]
#180	0.41	221	75.6	0.70	357	59.7
#500	1.06	335	61.3	1.82	540	48.1
#1000	3.91	1433	29.2	6.73	2309	22.7
#2400	17.55	3082	18.5	30.18	4967	13.4

Param. / p_a / Interface	1.16 MPa		
	A_{re}/A_a [%]	n [$\mathrm{mm^{-2}}$]	d_{avg} [µm]
#180	0.94	464	52.1
#500	2.45	703	42.0
#1000	9.08	3005	19.6
#2400	40.71	6464	10.8

The A_{re}/A_a values in Table 11.2 indicate that the real area of contact considerably increases in smoother surfaces. The most significant change in A_{re}/A_a is observed from #1000 to #2400 by a factor of 4.5 under each contact pressure. Likewise, the average cavity size d_{avg} decreases by a factor of $4.08 - 4.82$ from the roughest interface #180 to the smoothest interface #2400 as the contact pressure p_a is increased from 0.5 to 1.16 MPa. In essence, expanded real contact area results in a substantial increase in the number of contact spots n and hence a reduced average cavity size.

The d_{avg} values of the polymers sanded using #500 with their CIs (from Figure 11.1(a)) are substituted in Equations (4.2) and (4.4), respectively to estimate the minimum and maximum values of the estimated PDIE (i.e., $\mathrm{PDIE^e}$). The PDIE results for the studied polymers are shown in Figure 11.3(a). The proposed interface breakdown model (Chapter 4) simplifies the 3D surface topography of the surface asperities into cavities and contact spots in 2D, which are traversed by the tangential electric field component. However, cavities are shown to be connected with each other in 3D that form larger air gaps, as the simulated interface surfaces indicate via the deterministic model in the next section. As a result, the pressure inside the cavities is assumed to be equal to the ambient pressure ($\simeq$ 1 atm) when calculating the estimated PDIE values.

Analogous to the procedure above, the d_{avg} values of the XLPE samples with different roughnesses from Figure 11.2(a) are substituted in Equations (4.2) and (4.4), respectively. The resulting estimated PDIE values of the XLPE samples are shown in Figure 11.3(b).

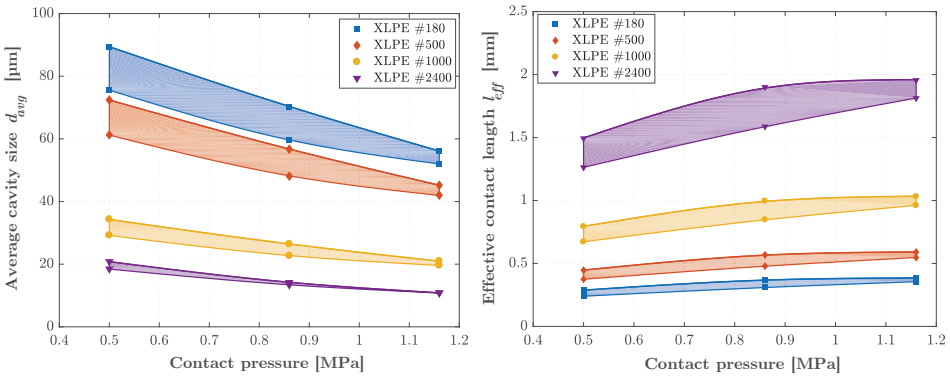

Figure 11.2: XLPE samples with different roughnesses: (a) Estimated average cavity sizes via Equation (3.21b) vs. the applied contact pressure. (b) Estimated effective contact length via Equation (4.6) vs. the applied contact pressure.

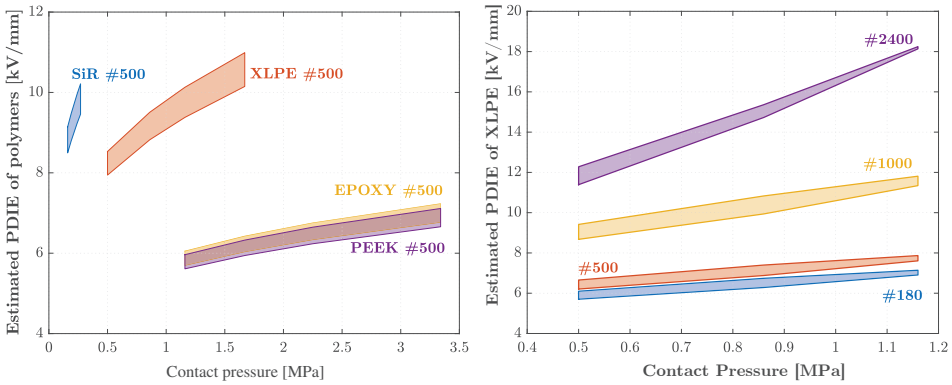

Figure 11.3: Estimated PDIE values of: (a) SiR #500, XLPE #500, EPOXY #500, and PEEK #500. (b) XLPE samples with the roughnesses of #180, #500, #1000, and #2400.

11.1.2 Results of the Contact Spot Breakdown Submodel

The average l_{eff} values from Figures 11.1(b) and 11.2(b) are substituted in Equation (4.5) to estimate the locally enhanced field strength values, E_{enh}. The estimated values of E_{enh} are shown in Figures 11.4 and 11.5 at the *instants I* and *II* with reference to the model shown in Figure 4.6. *instant I* stands for the inception of discharge in the averaged-sized cavities whereas *instant II* represents the moment when electric breakdown takes place at the contact spots due to the

intense local fields generated by the discharged cavities. For the *instant I*, the mean estimated PDIE values are multiplied by the nominal dielectric thickness (d_{int}) of 4 mm and are then substituted for V_{app} in Equation (4.5) along with the mean value of the calculated l_{eff}. Likewise, for the *instant II*, the measured BDS values are multiplied by the distance between the electrodes (i.e., $d_{int} = 4$ mm) and are substituted for V_{app}. The estimated local field enhancements at the edges of the discharged cavities, E_{enh}, along with the estimated interfacial tracking resistances E_{tr} of XLPE, EPOXY and PEEK are plotted in Figure 11.4.[15]

Figure 11.4(a) indicates that when discharge activity starts in the cavities at the XLPE–XLPE interface at the *instant I*, the enhanced fields at the edges of the contact spots are higher than the interfacial tracking resistance, which is likely to cause local electronic breakdown and bond scission [63]. Thus, the growth rate of the breakdown channel tends to accelerate further, which eventually leads to an interfacial failure [63]. At the *instant II* in Figure 11.4(b), the estimated local fields are already higher than the estimated interfacial tracking resistance of the XLPE. Until the cavity discharge inception, presumably, no stress arises at the contact spots in the case of XLPE. According to the average-sized cavity model, once the cavities are discharged, the low estimated interfacial tracking resistance of the XLPE cannot endure the enhanced local fields, and this leads to interfacial failure. Conversely, at the *instant I*, the enhanced local fields are not sufficiently high to exceed the interfacial tracking resistances in the cases of the EPOXY and PEEK. Although the average-sized cavities are assumed to be discharged, the high estimated interfacial tracking resistances of the EPOXY and PEEK can withstand the high local fields longer than the XLPE could last. At the *instant II*, however, the estimated enhanced field values exceed the estimated interfacial tracking resistances of the EPOXY and PEEK.

In a similar manner, Figure 11.5 shows the comparison between the estimated local field enhancements at the edges of the discharged cavities E_{enh} and the estimated interfacial tracking resistances E_{tr} of the XLPE samples with four different surface roughnesses. When discharge activity starts in the average-sized cavities at the *instant I*, amplitudes of the estimated enhanced fields at the edges of the contact spots are close to the estimated interfacial tracking resistance of the XLPE, as displayed in Figure 11.5(a). At smoother surfaces, the estimated enhanced field values seem sufficiently strong to lead to the breakdown of the contact spots. Based on Equation (4.5), this is due to the higher estimated PDIE^{e} owing to smaller d_{avg} at smoother surfaces. At the *instant II* (Figure 11.5(b)), amplitudes of the estimated local fields do not increase to any great extent because the estimated PDIE^{e} values are close to the measured BDS values.[16]

[15] The pressure ranges in which SiR–SiR interfaces were tested in are considerably lower than those determined for harder polymers. There are not any common pressure values for a fair comparison. Therefore, SiR is omitted in this analysis.

[16] As the mean values of PDIE^{e} and the measured BDS are substituted for V_{app} in Equation (4.5)—where PDIE^{e} and BDS are multiplied by $d_{int} = 4$ mm to be converted to voltage values—higher PDIE^{e} values caused higher enhanced fields at the *instant I* in Figure 11.5(a).

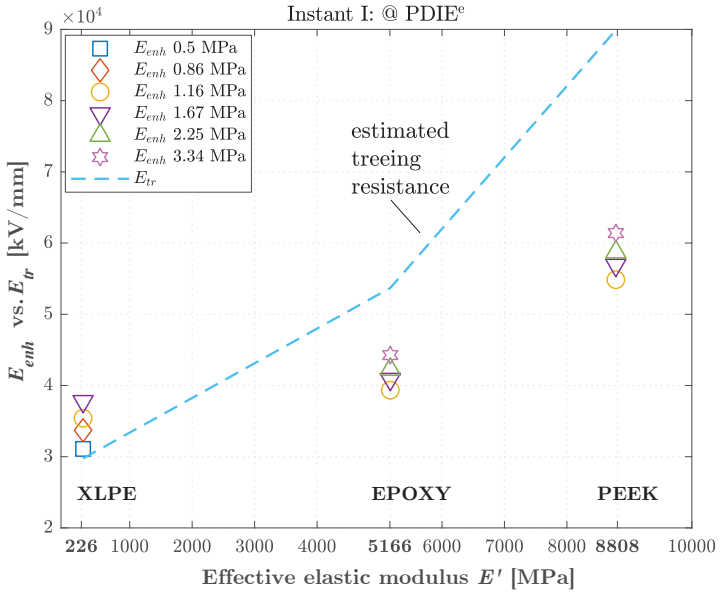

(a)

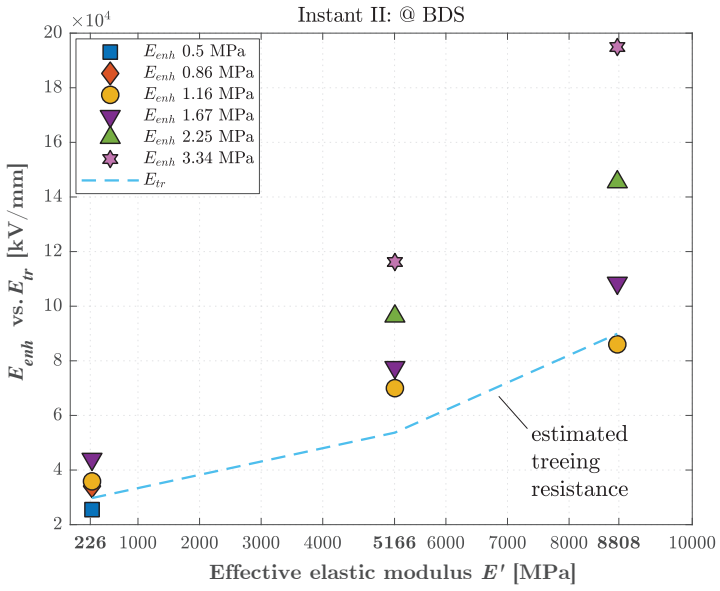

(b)

Figure 11.4: Estimated enhanced field E_{enh} vs. tracking resistance E_{tr} within the covered p_a for each interface. (a) Instant I: Estimated PDIE of average-sized air-filled cavities (PDIE^e). (b) Instant II: Breakdown of contact spots. Vertical axes are adjusted according to the min-max data values so that the data points can be seen clearly. ($\varepsilon_r = 2.3$, $G = 20000\,\mathrm{J/m^2}$ and $r = 0.3\,\mu\mathrm{m}$ for the XLPE; $\varepsilon_r = 4.6$, $G = 20000\,\mathrm{J/m^2}$ and $r = 0.12\,\mu\mathrm{m}$ for the EPOXY; and $\varepsilon_r = 2.8$, $G = 20000\,\mathrm{J/m^2}$ and $r = 0.12\,\mu\mathrm{m}$ for the PEEK [14, 63]).

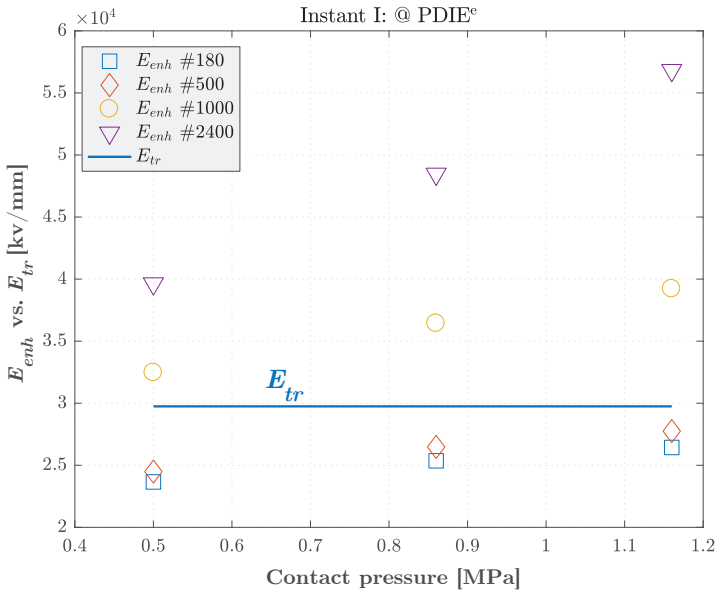

(a)

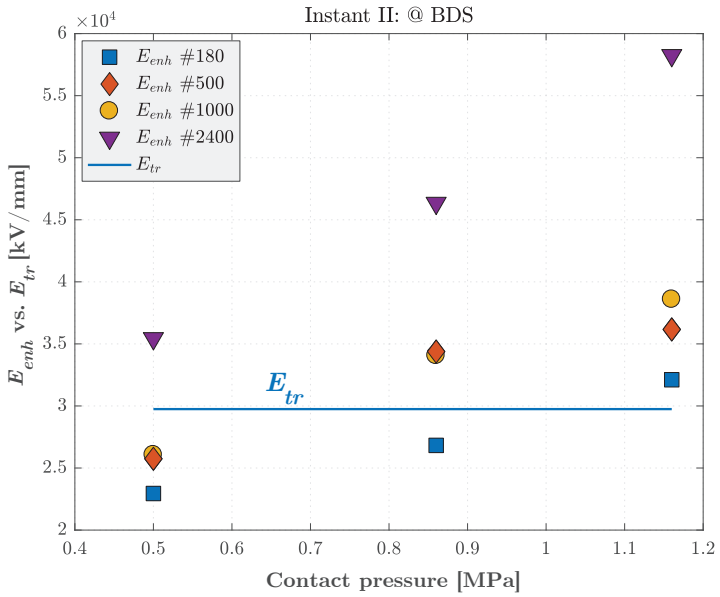

(b)

Figure 11.5: Enhanced field E_{enh} vs. tracking resistance E_{tr} of the XLPE samples with different surface roughnesses. (a) Instant I: Estimated PDIE of average-sized air-filled cavities (PDIE^e). (b) Instant II: Breakdown of contact spots. Vertical axes are adjusted according to the min-max data values so that the data points can be seen clearly. ($\varepsilon_r = 2.3$, $G = 20000\ \mathrm{J/m^2}$ and $r = 0.3\,\mu\mathrm{m}$ for the XLPE [14, 63]).

11.2 Results of the Deterministic Roughness Model

Results of the deterministic model introduced in Section 2.3.2 are briefly provided in this section. Some background information, the numerical solution method, and the methodology in discretizing the surface data are presented in Chapter 5. It is important to recall that the interface between two rough surfaces is transformed into an interface between one perfectly smooth plane and one equivalent rough surface [17] both in the statistical model and in the deterministic model (see Figure 3.2). An illustration of an equivalent rough surface is plotted in the 3D Cartesian coordinates in Figure 11.6. Moreover, the projection of the asperity amplitudes on a 2D plane is mapped using contour plots. With the help of color bars next to the contour plots, the amplitudes of the peaks are displayed quantitatively, where red represents the highest peak, and light yellow/white stands for the contact points. Details on how to obtain a contour plot are briefly provided in Section 5.6. Materials with two different elastic moduli and surface roughnesses are examined in this chapter: XLPE and PEEK, where XLPE stands for the soft material and PEEK represents the hard material.

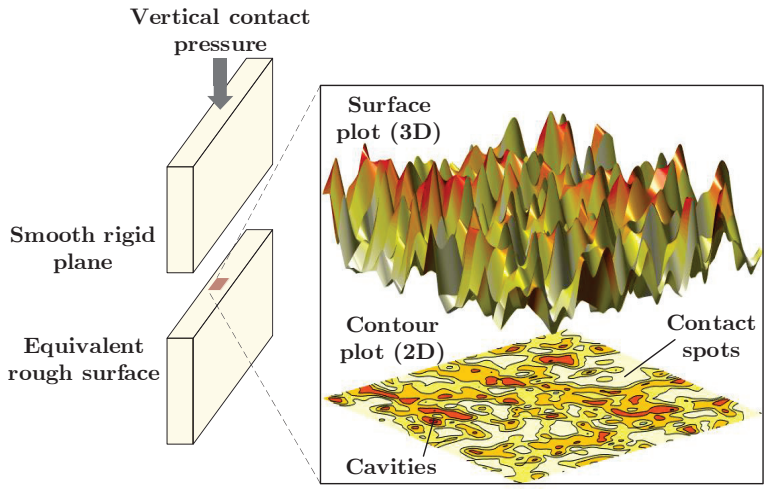

Figure 11.6: Contact asperities between a perfectly smooth surface and a rough surface. Red color represents the highest peak and light yellow/white represents the contact points.

[17] Sum surface of the roughnesses of both surfaces.

11.2.1 Effect of Surface Roughness and Contact Pressure

Figures 11.7 and 11.8 show contour plots of the surface asperities of the XLPE samples with four different surface roughnesses, while those of the PEEK samples with two different surface roughnesses are presented in Figure 11.9. In order to ensure consistency, the variations of the asperities are simulated at the lowest and highest contact pressure values determined for the XLPE and PEEK samples in the AC breakdown experiments.

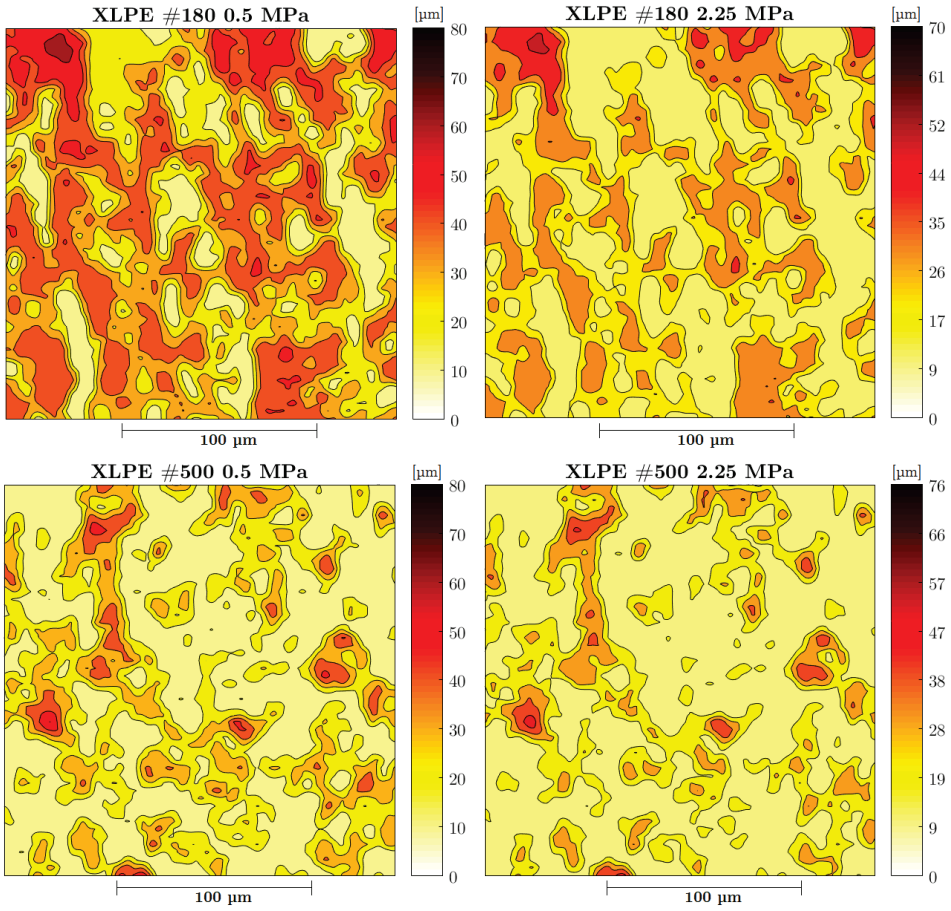

Figure 11.7: Filled-contour plots of the surface asperities of the XLPE samples polished with #180 and #500 at 0.5 MPa (lowest p_a) and 2.25 MPa (highest p_a), respectively. Color bars are in µm, where light yellow color represents the contact areas and darker colors imply cavities.

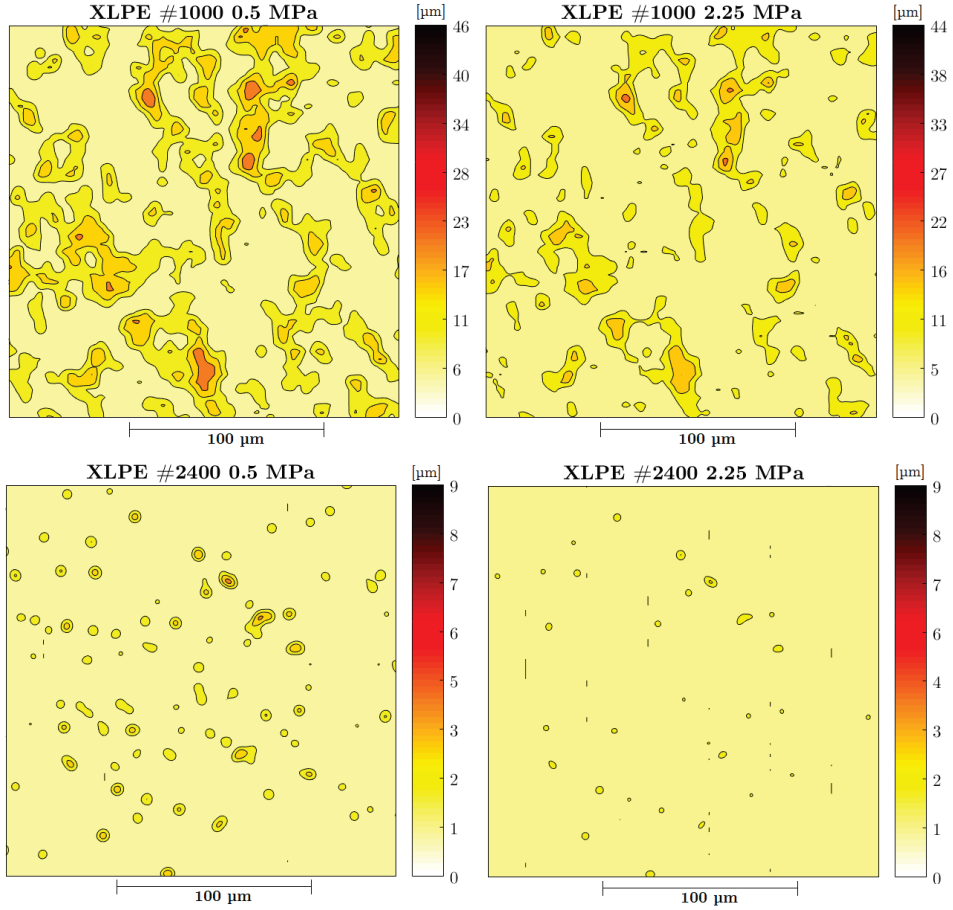

Figure 11.8: Filled-contour plots of the surface asperities of the XLPE samples polished with #1000 and #2400 at 0.5 MPa (lowest p_a) and 2.25 MPa (highest p_a), respectively. Color bars are in µm, where light yellow color represents the contact areas and darker colors imply cavities.

The contour plots indicate that increased pressure pushes the asperity tips further, leading to the formation of new contact spots. As a result, more cavities are formed due to channels being broken into smaller channels and cavities. Towards smoother surfaces, the density of the peaks reduces considerably, and the impact of the increased pressure becomes even more discernible. Particularly in the case of XLPE #2400, there are a limited number of protruding peaks at the surface while the rest of the surface is simulated to be a perfect contact.

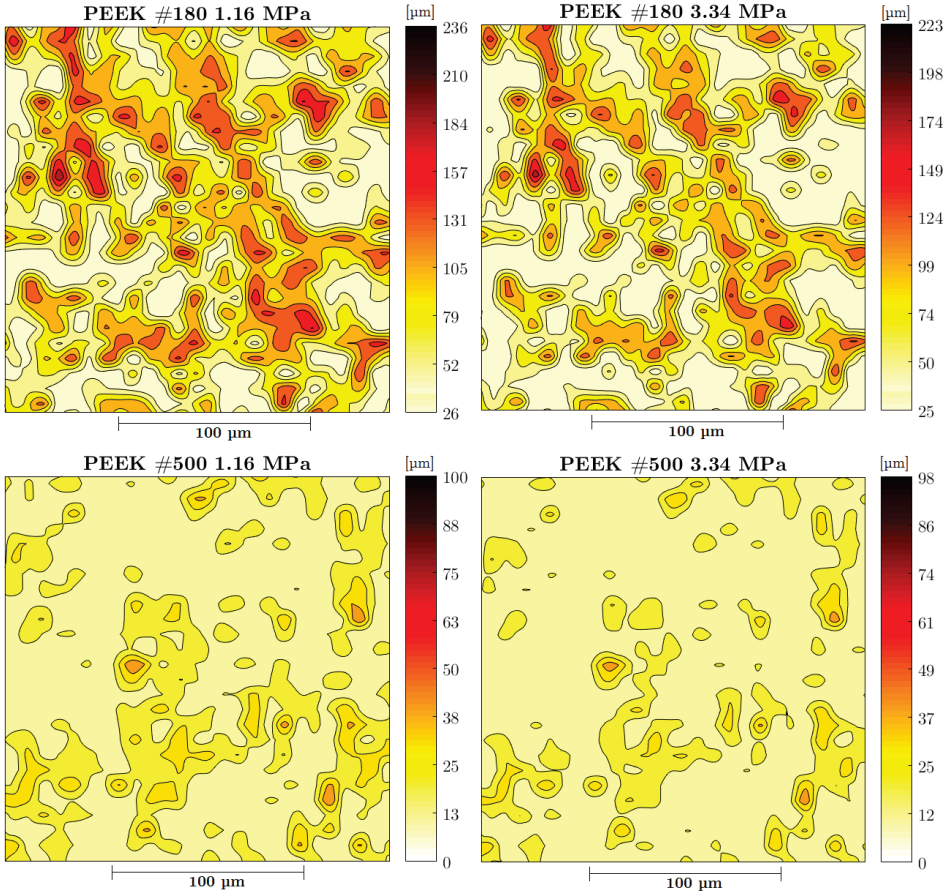

Figure 11.9: Filled-contour plots of the surface asperities of the PEEK samples polished with #180 and #500 at 1.16 MPa (lowest p_a) and 3.34 MPa (highest p_a), respectively. Color bars are in µm, where light yellow color represents the contact areas and darker colors imply cavities.

11.2.2 Effect of Elastic Modulus and Contact Pressure

The displacement of the asperities in 2D is simulated in Figure 11.10 at the increased pressure, while the deformation of asperities in XLPE samples in 3D with respect to the applied contact pressure is presented Figure C.2. The deformation of the protrusions at the surfaces of PEEK samples in 2D and 3D are presented in Figures 11.11 and C.4, respectively. In accordance with what the motif parameters in Tables 7.1 and 7.2 suggest, the amplitude of peaks in the PEEK samples are larger than those of XLPE samples despite having been sanded by #500 grit sandpaper. This difference in amplitudes, in turn, yields larger cavities in the direction parallel to the tangential electrical field, as highlighted by the maximum size of the cavities in Figures 11.10 and 11.11. They are also in line with the d_{avg} and A_{re}/A_a values in Table 11.1.

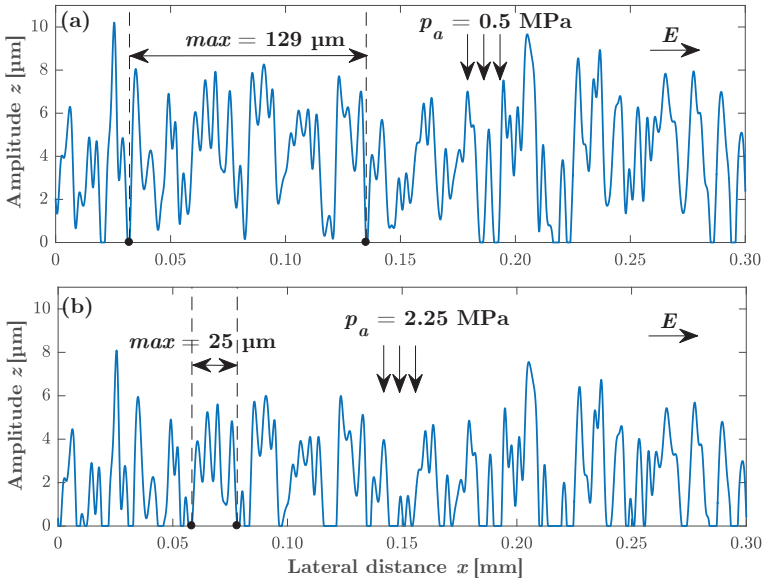

Figure 11.10: The displacement of peaks at the XLPE #500 surface at: (a) 0.5 MPa. (b) 2.25 MPa. E shows the direction of the tangential field component.

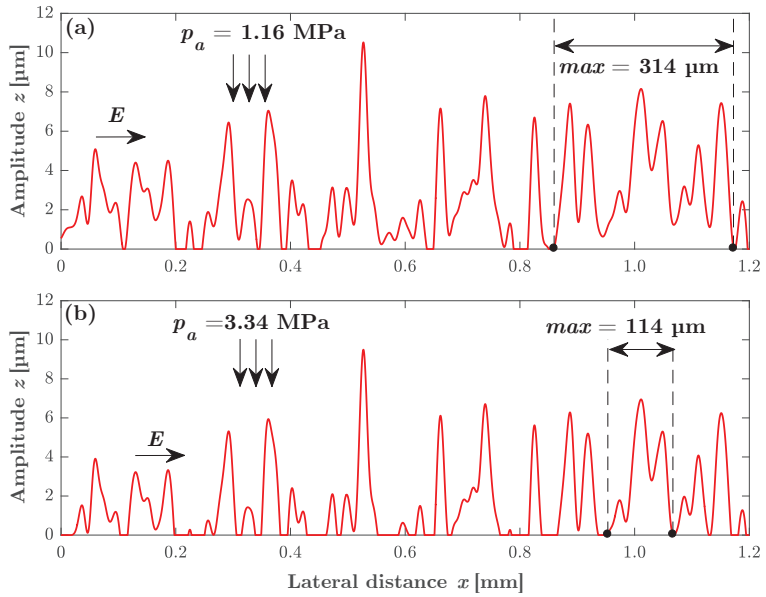

Figure 11.11: The displacement of peaks at the PEEK #500 surface at: (a) 1.16 MPa. (b) 3.34 MPa. E shows the direction of the tangential field component.

Consequently, the increased pressure pushes the asperity tips further, leading to the formation of new contact spots. As a result, cavities and channels are broken into smaller cavities. The deformation of the peaks can be envisaged in such a way that the perfectly smooth rigid plane (no asperities hypothetically—see Figure 3.2) is pressed against the equivalent rough surface as more of the afloat asperities come into contact with the smooth surface, resulting in more contact spots and hence smaller cavities. Figures C.1–C.4 display the discretized surface data from the obtained profiles, as shown in Figure 7.5.

Note that these profiles constitute a small portion of the complete surface data, as illustrated in Figure 11.6. The complete surface data set are too large to be demonstrated in a single graph. The unrevealed parts of the surfaces have similar, uniform patterns. With reference to Figure 6.13, the complete 3D surface data as shown in Figure C.2 is stored in a 480 x 640 matrix, whereas a row vector in the size of 1 x 640 represents a 2D roughness profile similar to those shown in Figure 11.10.

Pressure distributions at the contact surfaces of the XLPE and PEEK samples at two different pressures are shown in 3D plots to gain a clear understanding of elastic and plastic deformations in Figures C.6–C.10 in Appendix C.2 for simplicity while two illustrative plots are shown in Figure 11.12. Each spherical marker in Figure 11.12 represents the contact pressure at the shown position. If the contact is elastic, then the contact pressure will lie between zero and the hardness of the material. On the other hand, when the hardness of the material is reached, elastic contact spots transition to plastic contacts, and the contact area does not increase any further, irrespective of the applied force. In this regard, the pressure distribution plots indicate that the deformation of contact asperities are significantly lower in the case of PEEK even at higher contact pressures. At plastic contacts, the pressure is limited by the hardness of the material, as illustrated in Figure 11.12(b).

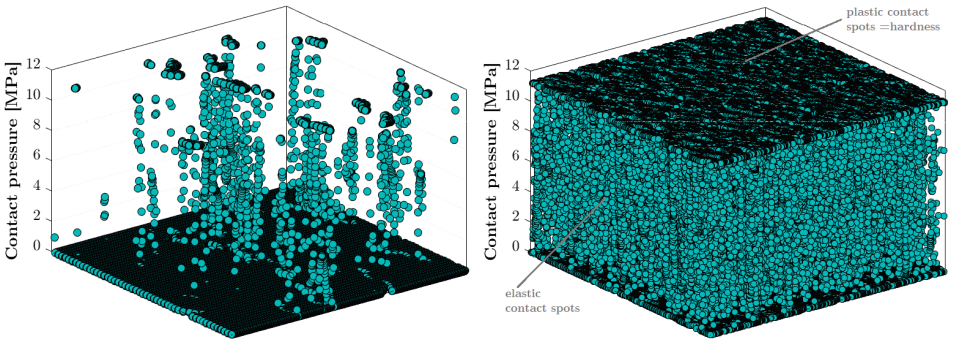

(a) Elastic contacts **(b)** Elasto-plastic contacts

Figure 11.12: Pressure distribution at contact spots. When the plastic contact occurs, contact pressure saturates at the hardness of the material and becomes independent of the applied force. Each spherical marker represents the contact pressure at the shown position.

11.3 Correlation between the Deterministic and the Statistical Model

In this section, the similarities and differences between the deterministic and statistical models are briefly addressed. The ratio of the real contact area to the nominal contact area A_{re}/A_a is calculated for each case using the statistical model and the deterministic model (see Figure 11.13).

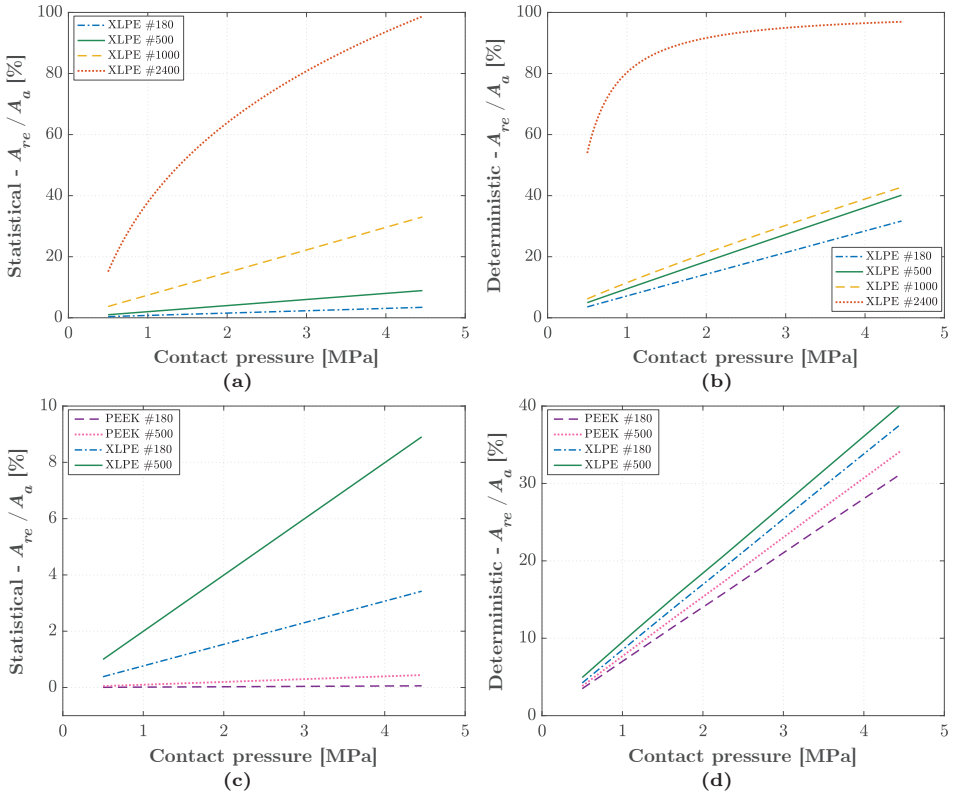

Figure 11.13: Correlation between the results of the statistical model and the deterministic model. Ratio of real area of contact to nominal area of contact: (a) Statistical model for rough XLPE samples. (b) Deterministic model for rough XLPE samples. (c) Statistical model for rough XLPE and PEEK samples. (d) Deterministic model for rough XLPE and PEEK samples.

Figures 11.13(a)–(b) indicate that smoother XLPE surfaces yield a higher contact area, especially at higher pressure, in both models. On the other hand, in the case of PEEK in Figures 11.13(c)–(d), the statistical model estimates significantly lower contact area compared to the values computed by the deterministic model although the same trends and sequence in amplitudes are observed. Moreover, in the deterministic model, the difference in A_{re}/A_a between the XLPE and PEEK samples in Figure 11.13(d) is not as significant as that in Figure 11.13(c).

The initial portion of the waveform of #2400 in Figure 11.13(b) shows an almost linear relationship between the total area of contact and the contact pressure in the range from 0.5 to 1.16 MPa. These correlations indicate that the increased interfacial pressure reduces the number of large air-filled gaps and thus creates more isolated cavities at the interface, as verified by the contact surface simulation results shown in Figures 11.7 and 11.8.

The largest cavities measured between two adjacent contact areas are estimated using the deterministic model. Figures 11.14(b)–(d) display the largest cavities for XLPE and PEEK samples with the shown roughness degrees. Figures 11.14(a)–(b) reveal that the largest cavities could be 3–4 times as large as the average-sized cavities in the case of XLPE. On the other hand, sizes of the largest cavities are close to each other in the cases of PEEK and XLPE despite the significant difference observed in the average-sizes in Figure 11.14(c).

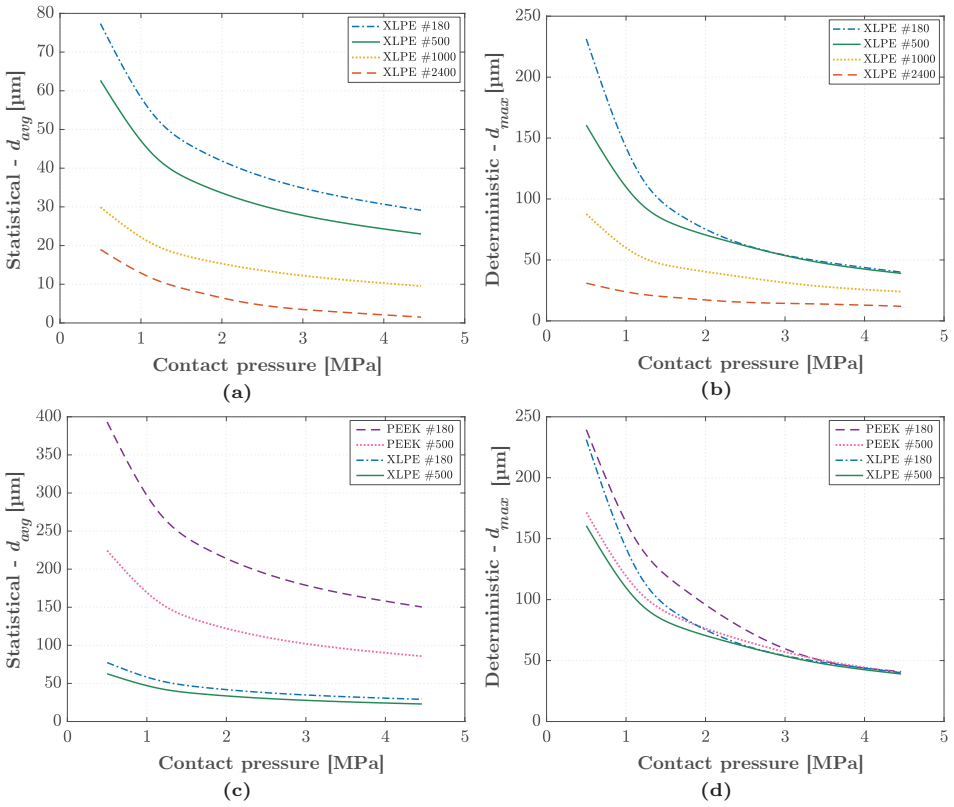

Figure 11.14: Correlation between the estimated cavity sizes using the statistical model and the deterministic model: (a) Average cavity sizes from the statistical model for rough XLPE samples. (b) Maximum cavity sizes from the deterministic model for rough XLPE samples. (c) Maximum cavity sizes from the statistical model for rough XLPE and PEEK samples. (d) Maximum cavity sizes from the deterministic model for rough XLPE and PEEK samples.

Chapter 12

Discussion

In this chapter, answers to the research questions presented in the introduction are sought and discussed based on the results of the performed experiments, simulation studies, and theoretical models. Scopes of the research questions are summarized below in a compact format:

- [Q-I]: How do the elasticity, contact pressure, and surface roughness influence the sizes of the microcavities and contact spots? (Discussed in Section 12.1).
- [Q-II]: What are main the mechanisms controlling the interfacial breakdown? (Discussed in Section 12.2). This question is dissected in four subsections that are:
  - effect of discharged cavities and contact spots on the interfacial breakdown strength (discussed in Sections 12.2.1 and 12.2.2);
  - initiation, development, and propagation of streamers at the interface in dry-mate conditions (discussed in Section 12.2);
  - expected gas pressure inside the cavities at solid-solid interfaces in dry-mate conditions (discussed in Section 12.2.3); and
  - impacts of ingress of water or oil into the cavities on the longitudinal AC breakdown of solid-solid interfaces (discussed in Section 12.2.4).

12.1 Sizes of the Microcavities and Contact Spots

In Chapters 3 and 5, two different theoretical approaches are proposed for the modeling of interfacial cavities and contact spots, namely, statistical and deterministic interface contact models. The statistical interface contact model provides a simplified, 2D interface contact model that can predict average sizes of the cavities and contact spots as a function of surface roughness, contact pressure, and elasticity. With the interface breakdown model presented in Chapter 4, impacts of varied sizes of cavities and contact spots on the AC breakdown strength are estimated (Section 11.1). These estimated results will be used in the next section alongside the results of the AC breakdown experiments and PD experiments to test the correlation between the cavity discharge and interface breakdown and comment on the validity of the interface breakdown model. Additionally, with the deterministic model, deformations of the contact spots are simulated in 3D (Section 11.2). Simulation results on the interfacial deformation will cast light on how cavities are connected in 3D and elucidate the resulting gas pressure inside the cavities, which could not be estimated by solely using the 2D statistical contact model.[18]

The deterministic interface contact model provides insight into how the real area of contact at solid-solid interfaces varies as a function of the contact pressure, surface roughness, elasticity, and hardness of the solid material in 3D. The model indicates that an increase in the interfacial pressure reduces the number of long air-filled channels and thus creates more enclosed cavities at the interface (see Figures 11.7–11.9). Likewise, the smoother the surface, the more enclosed, smaller cavities are present. Conversely, the harder the material, the larger the resulting cavities, and in turn, long channels are formed by the interconnected, larger cavities. Consequently, cavities are interconnected in 3D space, forming longer air-filled channels in the cases of rougher surfaces, harder materials, and/or lower contact pressures.

The proposed interface breakdown model (Chapter 4) simplifies the 3D surface topography of the surface asperities into cavities and contact spots in a 2D plane parallel to the electric field. The simplified 2D model requires the cavities and contact spots between the electrodes to be broken-down in order to lead to an interface failure. In the 2D model, the breakdown of cavities and contacts spots is assumed to be connected on a 2D line. This simplification does not diverge from the real situation because a discharge streamer at an interface follows a line-like path in the field direction (see the interface tracking shown in Chapter 8 and Appendix A.2). Interface tracking path is not necessarily straight; in most cases, it is tortuous (non-straight) due to contact spots being in the way of a propagating streamer. As in the simplified 2D model, a string of cavities and contact spots, depending on the location of the weaker cavities and contact spots, is tracked by

[18] Note that the *interface breakdown model* presented in Chapter 4 is built on the *statistical interface contact model*, which is also referred to as *statistical model*, *simplified 2D model*, or *statistical roughness model* in this work. They all are used interchangeably.

a propagating breakdown streamer. The results of the discharge-monitoring experiments also support these observations and thus the simplified 2D model. In addition, images of discharge activity shown in Chapter 10 indicate that sizes of microcavities parallel to the electric field are similar in sizes to those of the estimated cavities calculated using the statistical interface contact model. Furthermore, as shown in Section 11.3, the statistical model yields consistent results with those of the deterministic model in terms of the average cavity size and the ratio of the real contact area to the nominal contact area, A_{re}/A_a. Increased contact pressure, lower elastic modulus, and/or decreased surface roughness generated smaller cavities and higher ratios of A_{re}/A_a.

When developing the 2D interface breakdown model in Chapter 4, all cavities are assumed to be isolated/enclosed between two contact spots. However, the theoretical and experimental results indicate that the simplified assumption of only enclosed cavities is not entirely valid in the cases of rough surfaces under low contact pressures and/or hard materials subjected to low contact pressures. For instance, the simulation results from the deterministic model suggest significantly fewer enclosed cavities while there are manifold, vented air-gaps/channels. Consequently, vented channels and enclosed cavities at the interface are likely to coexist, especially in the cases of moderate roughnesses, contact pressures, and elasticities. The state of coexistence of vented and enclosed cavities can be deemed/envisaged as a transition from soft, smooth interfaces under high contact pressure to hard, rough interfaces at low pressure. Figures 12.1(a) and (c) illustrate the case when only enclosed cavities are present at the interface such as in the cases of soft materials, high contact pressure and/or smooth surfaces. Conversely, Figures 12.1(b) and (d) demonstrate that, nearly, only vented channels exist at the interfaces, similar to the cases of hard materials, rough surfaces, and/or low contact pressure. Possible surface paths that are likely to be tracked in the event of an interface breakdown are drawn in Figures 12.1(a)–(b) for each case. In the case of "only enclosed cavities", contact spots must be subjected to electrical breakdown in addition to the discharge of cavities. On the other hand, in the case when air-filled interconnected cavities are prevalent at the interface, an interface tracking path can be formed by incorporating only the interconnected cavities (vented channels) as illustrated in Figure 12.1(b).

Lastly, the continuous discharge streamers, shown in Figures 10.3 and 10.5, also suggest that streamers chase air-filled channels composed of several connected cavities in the real 3D-interfacial surface. Therefore, streamers do not necessarily follow the shortest path to the electrode due to the presence of the contact spots that obstruct the propagation of streamers. Instead, they presumably follow a tortuous channel consisting of air-filled cavities connected to each other. In the case of PEEK #180–glass interface, wider, continuous discharge channels were observed as compared to the discharge images in the case of PEEK #500–glass interface. Based on the difference between the simulated interface surfaces of PEEK #180 and PEEK #500 shown in Figure 11.9, longer air-gaps, and fewer isolated cavities

will exist in the case of rougher surfaces. Similarly, as previously mentioned, the statistical roughness model estimates larger cavities in the case of PEEK #180.

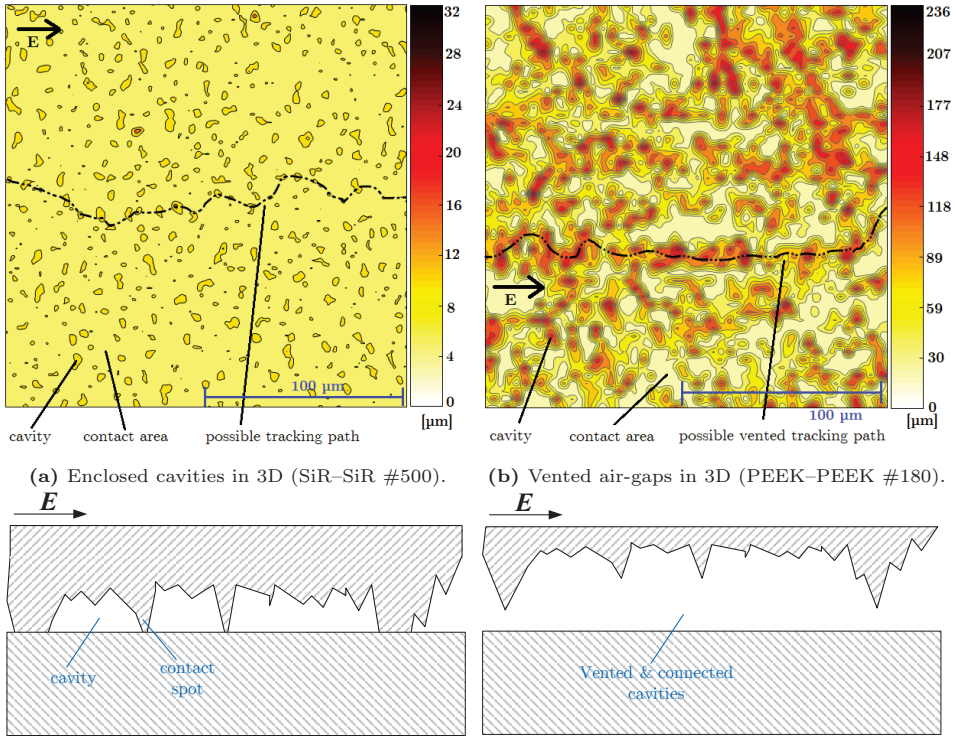

(a) Enclosed cavities in 3D (SiR–SiR #500).

(b) Vented air-gaps in 3D (PEEK–PEEK #180).

(c) Enclosed cavities in 2D.

(d) Vented air-gaps in 2D.

Figure 12.1: Simulated interfacial surfaces incorporating only enclosed cavities and vented air-gaps formed by interconnected cavities.

12.2 Mechanisms Controlling the Interfacial Breakdown

In this section, to elucidate main mechanisms controlling the interfacial breakdown (Q-II), the results of the entire experimental and theoretical studies are used. The results will also clarify the impacts of different sizes of cavities and contact spots on the longitudinal AC breakdown strength, that are part of the research question Q-I. The effect of the discharge of cavities and the breakdown of contact spots on the interfacial breakdown strength are examined separately based on the corresponding submodels introduced in Chapter 4 by following the sequence of mechanisms hypothesized in Section 4.2. It should be emphasized that the mechanisms controlling the interface breakdown are investigated for samples assembled in an optimal, dry laboratory (dry-mate) conditions. The effect of either water- or oil-ingress (wet-mate or oil-mate) is also discussed at the end of this chapter

using the results of AC breakdown experiments and FEM simulations for wet- and oil-mate interfaces.

12.2.1 Effect of Discharge of Cavities on the Interfacial Breakdown

In this section, the effect of discharged cavities on the interfacial breakdown is thoroughly investigated using the measured AC BDS values, measured PDIE values, and estimated PDIE values. It should be noted that an AC voltage ramp with the rate of 1 kV/s was utilized for both the AC breakdown experiments and the PD inception field tests for a fair comparison. This is because the rate of the voltage rise is likely to affect the mechanisms controlling the interfacial breakdown by varying the build-up of space charges as well as concentration and distribution thereof [143–148]. Besides, the interfacial BDS or AC BDS implies a short-term interfacial breakdown phenomenon due to the selected rate of rise of the AC ramp voltage in the experiments. In other words, the breakdown strength investigated in this work is short-term interfacial breakdowns and mechanisms related to the short-term failure.

Correlation between the Measured PD Inception Field Strength and Measured AC Breakdown Strength at Solid-Solid Interfaces

The main purposes of this section are to examine how the measured PDIE is correlated with the measured AC breakdown field and to reveal the interconnection between the measured PDIE and the estimated PDIE. To begin with, the results of the AC breakdown experiments are compared to the measured PDIE values ($PDIE^m$). Figure 12.2(a) shows the comparison between the measured PDIE and the measured AC BDS of XLPE–XLPE #500 interface. The difference between the 63.2% BDS and $PDIE^m$ is found to be only around 10%. This small difference strongly supports the interface breakdown model that suggests that discharged cavities in the XLPE samples evolve to a complete flashover in a short time because the contact spots are less likely to withstand the enhanced fields for a long time due to the relatively low estimated interfacial tracking resistance of XLPE. In contrast, in the case of PEEK–PEEK #500 interface in Figure 12.2(b), the mean $PDIE^m$ values are lower than the measured mean BDS values by a factor of 1.55. Thereby, it can be claimed that the contact spots in PEEK could withstand the discharged cavities for a longer time (applied voltage is higher by 1 kV at every next second) since the estimated interfacial tracking resistance of the PEEK is higher than that of XLPE. Overall, the correlation between the measured PDIE and BDS values, despite the limited number of data points, agree with the hypothesis that the interfacial tracking resistance is an essential electrical insulation property in the solid-solid breakdown of interfaces.

Secondly, the estimated and measured PDIE values are plotted in Figure 12.3 to examine the correlations between them. The results suggest that the estimated

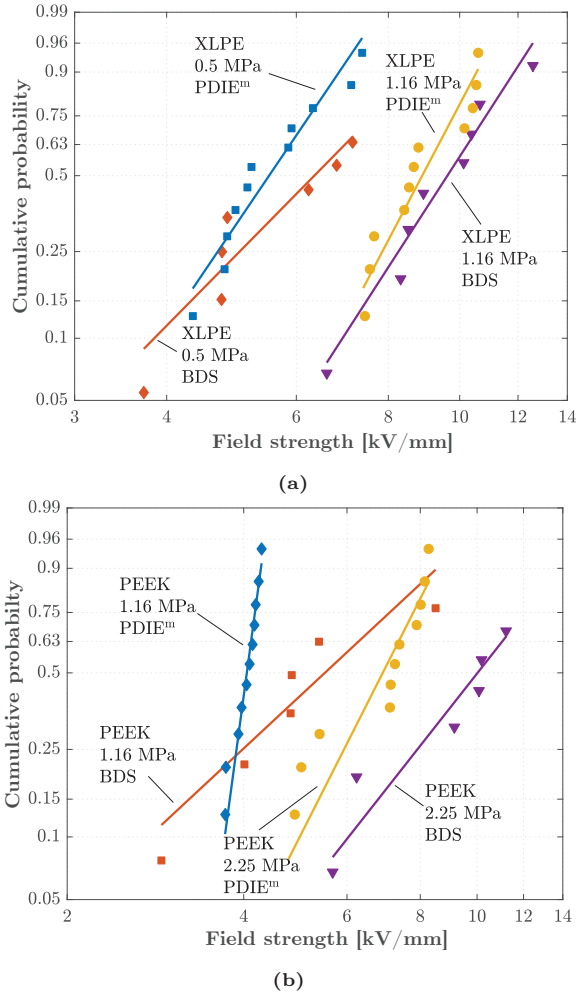

Figure 12.2: Comparison of measured PDIE and AC BDS of dry-mate: (a) XLPE–XLPE #500 interface. (b) PEEK–PEEK #500 interface.

and measured PDIE values show a clear correlation, but the number of data points is possibly too low to make a comprehensive interpretation. Nevertheless, using the available data, it can be inferred that the trends of the PDIE values as a function of the contact pressure are consistent. Apparently, at low contact pressures, the estimated PDIE values are generally higher than the measured PDIE values. Vented channels in real life, as illustrated in Figure 12.1(b), could be the primary culprit for this deviation since the simplified 2D model takes only the enclosed cavities into consideration. Another reason for the deviation could be that due to normally distributed asperity peaks and heights—observed in the normality analyses appended in Appendix D.3.3.2—there are at least some cavities larger than the average-sized cavities, in which the PD activity presumably commences first while there is still no

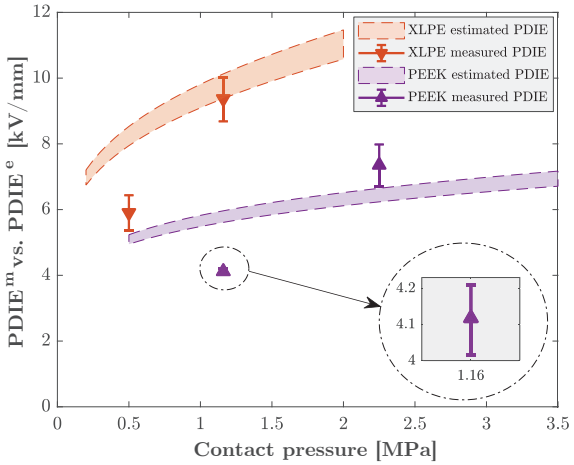

Figure 12.3: Comparison of the measured PDIE and the estimated PDIE of dry-mate XLPE–XLPE #500 and PEEK–PEEK #500 interface.

PD activity in the average-sized cavities. The deterministic interface contact model reveals that the largest cavities could be 3–4 times as large as the average-sized cavities (see Figure 11.14). Consequently, depending upon the number and size of larger cavities, the accuracy of the estimated PDIE might decrease. Accordingly, an improved contact model containing the influence of the size and number of the largest cavities may potentially be more effective.

Finally, it should be noted that the measured PDIE values do not necessarily characterize the inception field of the discharged cavities that initiate/trigger the interfacial breakdown, as mentioned in Chapter 9. As explained in Section 12.1, interfacial tracking is likely to be tortuous due to the presence of contact spots obstructing the propagation of streamers. The endurance of the contact spots against propagating streamers is designated using the interfacial tracking resistance of the contact spots which is an insulation property of the bulk material. Moreover, cavity sizes are essential for the theoretical analysis of the interface breakdown phenomenon. However, sizes of the interfacial cavities cannot be extracted from the measured PDIE (i.e., $\mathrm{PDIE^m}$) data without using an analytical model. For these reasons, the statistical interface model is developed to determine the sizes of cavities as a function of the surface roughness, elasticity and applied contact pressure. The estimated sizes of cavities are then used to estimate the cavity discharge inception field (i.e., $\mathrm{PDIE^e}$) to directly relate the cavity size to the interface breakdown. Consequently, in the following section, the estimated PDIE values are used to further investigate the correlation between discharged cavities and interface breakdown by considering the sizes of the cavities and the ratio of the real area of contact to the nominal interfacial area.

Correlation between the Estimated PD Inception Field Strength and Measured AC Breakdown Strength at Solid-Solid Interfaces

First, the results of the AC breakdown experiments performed using XLPE samples with different roughnesses (see Figure 8.1) and the corresponding estimated PDIE values i.e., $PDIE^e$ (see Figure 11.3(b)) are plotted in Figure 12.4.[19] As a reminder, the $PDIE^e$ values are estimated with the assumption that all cavities are vented, and the pressure inside remains at 1 atm (see Section 11.1). The effect of increased gas pressure inside enclosed cavities on the interfacial BDS will be discussed in Section 12.2.3.

Figure 12.4 indicates that, at higher contact pressures, smoother interfaces tend to yield a stronger correlation between the estimated PDIE and the measured BDS. For instance, $PDIE^e$ values slightly deviate from the measured BDS data at higher pressures in the cases of XLPE #180 and XLPE #500.[20] In contrast, an opposite tendency is observed in the cases of XLPE #1000 and XLPE #2400.

Second, the results from the AC breakdown experiments performed using SiR, XLPE, EPOXY, and PEEK with the same surface roughness of #500 (see Figure 8.2) and the interface breakdown model (see Figure 11.1) are used. The estimated PDIE values are plotted alongside the measured BDS in Figure 12.5.

The results shown in Figure 12.5 indicate that there is a strong correlation between the BDS values and the $PDIE^e$ values within the covered pressure range in the case of relatively soft interfaces, such as SiR–SiR #500 or XLPE–XLPE #500. The ratio of the mean BDS to the mean $PDIE^e$ ranges from 0.8 to 1.2. The $\pm 20\%$ deviation suggests that the interfacial breakdown is likely to be dominated by the cavity discharge in the case of SiR and XLPE interfaces. Nevertheless, EPOXY–EPOXY #500 and PEEK–PEEK #500 interfaces exhibited a weaker correlation between the cavity discharge and the interface breakdown, especially at relatively high contact pressures. It can be inferred that, at higher elastic modulus, the interfacial breakdown is not solely predominated by the discharge of vented air-filled cavities (channels), particularly at high contact pressures. Electrical insulation properties, such as the interfacial tracking resistance, are likely to play an essential role in determining the endurance of the contact spots against breakdown. The influence of the interfacial tracking resistance of the contact spots on the interfacial breakdown is discussed in the next section. For this purpose, SiR, XLPE, EPOXY and PEEK interfaces (all are #500) that have different elastic moduli are utilized. The relationship between the elastic modulus and the interfacial tracking resistance will be explained as well.

[19] The estimated PDIE and measured PDIE show consistent trends and values. More information on why $PDIE^e$ and measured BDS are compared is given in the previous section.

[20] It should once again be underscored that the discussion is based only on the interfaces formed between identical materials. Therefore, in some places in the text, to reduce wordiness only the name of the polymer is used when representing the interface.

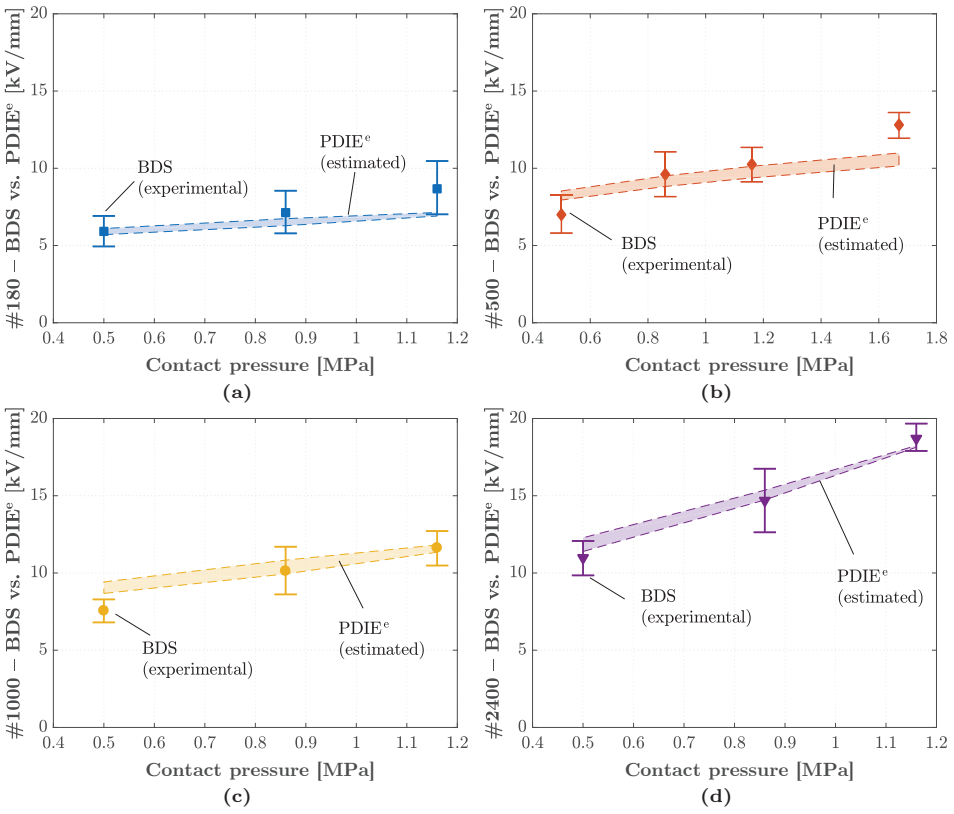

Figure 12.4: Experimental (measured) BDS data set (error bars) from Figure 8.1 vs. estimated $PDIE^e$ (shaded areas) vs. contact pressure: (a) XLPE–XLPE #180. (b) XLPE–XLPE #500. (c) XLPE–XLPE #1000. (d) XLPE–XLPE #2400. Each $PDIE^e$ data set is computed by substituting the d_{avg} values in Figure 11.2(a) into Equations (4.2) and (4.4), respectively.

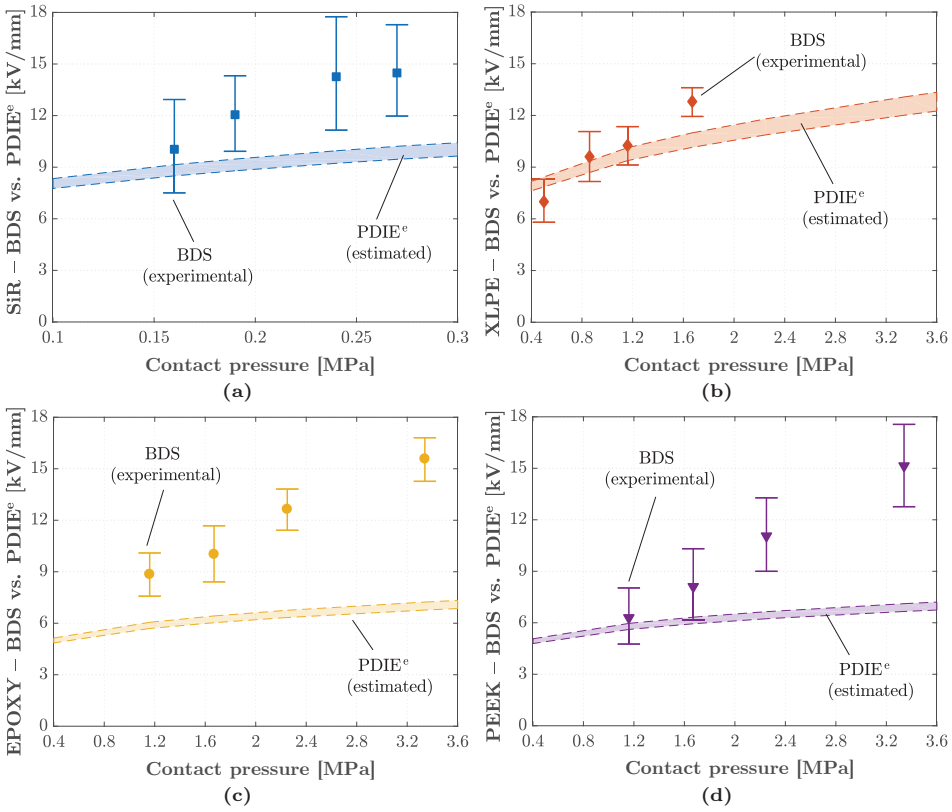

Figure 12.5: Experimental (measured) BDS data set (error bars) from Figure 8.2 vs. estimated PDIE^e (shaded areas) vs. contact pressure: (a) SiR–SiR #500. (b) XLPE–XLPE #500. (c) EPOXY–EPOXY #500. (d) PEEK–PEEK #500. The range of the horizontal axis of SiR–SiR is different from the rest due to the very low pressure range. To estimate the PDIE (i.e., PDIE^e), the minimum and maximum d_{avg} values (from Figure 11.1(a)) were substituted in Equations (4.2) and (4.4), respectively to estimate the minimum and maximum values of the PDIE^e.

12.2.2 Effect of Contact Spots on the Interfacial Breakdown

The results from experimental and theoretical studies suggest that different mechanisms are involved during the interface breakdown. An interfacial surface such as the one illustrated in Figure 12.1(a) indicates that when an interfacial failure occurs, both cavities and contact spots are broken down along the discharge path. However, the existence of vented channels (air-gaps) will enable streamers to propagate by chasing after only interconnected cavities without being obstructed by any contact spots.

Constituents of Contact Spots in Fractal Dimensions

In this section, firstly, constituents of contact spots are elaborated by considering imperfections that cause deviations from an "ideal contact surface."

The multiscale nature of surface roughness is likely to have a role on the interface breakdown such that when a surface is repeatedly magnified, increasing details of roughness can be observed right down to nanoscale owing to the unique property of rough surfaces [16, 149–151]. Consequently, surface texture at all magnifications seems somewhat similar in structure, causing the interfacial surface texture to repeat itself in smaller scales, as illustrated in Figure 12.6. This phenomenon is studied under fractal analysis in the literature [149–151]. Without delving too much into the details of the fractal analysis, the parameter of interfacial tracking resistance is elaborated in the following by discussing what it actually represents.

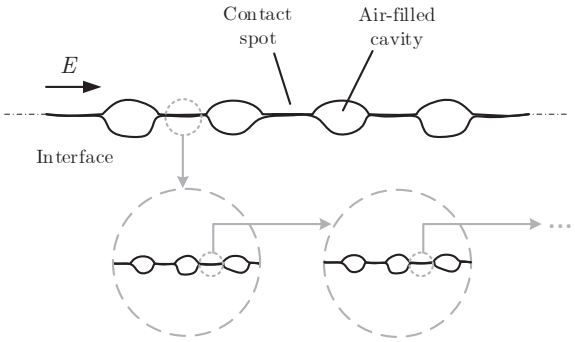

Figure 12.6: Multiscale nature of surface roughness characterized by fractal geometry.

Considering the fractal geometry of a rough surface, contact spots at the microscale incorporate contact spots and cavities at the nanoscale, as illustrated in Figure 12.6. Thus, the breakdown of contact spots is assumed to be equivalent to the discharge of nanoscale cavities and breakdown of nanoscale contact spots. In that case, the air-filled, enclosed nanocavities will have as high a dielectric strength as nanoscale contact spots of the bulk material according to the left of Paschen minimum for air (see Figure E.3 in Appendix E). As a consequence, significantly lower enhanced local fields are required to break down a nanoscale contact spot than a

microscale contact spot. In the proposed interface breakdown model in Chapter 4, air-filled cavities are discharged first while contact spots are subjected to breakdown last. However, discharged cavities will not immediately lead to an interface breakdown because the insulation properties of the solid insulation are likely to affect the endurance of the contact areas against interface breakdown caused by the enhanced fields generated by the discharged cavities.[21] The endurance of contact spots against discharges at an interface is roughly modeled and is estimated using the interfacial tracking resistance of the solid material.

For clarity, a hypothetical case is exemplified as follows. Assume that cavities at two different homogeneous[22] interfaces are identical (identical size, number, and shape) and are discharged at the same voltage, the interface formed between the materials with a higher interfacial tracking resistance is likely to yield a higher breakdown strength, as observed in the AC breakdown experiments.

Effect of Elastic Modulus on the Tracking Resistance of Contact Spots

Different materials with different moduli were used in this work to vary the elastic modulus at the expense of changing other electrical insulation properties in addition to the interfacial tracking resistance. However, electrical insulation features other than the interfacial tracking resistance are not taken into account in the interface breakdown model. Previous studies reported improved electrical insulation properties when the modulus is increased [59–61]. These results are clearly correlated with the proposed model of the interfacial tracking resistance. According to Equation (4.7), the interfacial tracking resistance is proportional to the fourth root of the elastic modulus, i.e., $E_{tr} \propto E'^{1/4}$.[23] Thus, the higher the elastic modulus, the higher the interfacial tracking resistance.

As repeatedly emphasized, both the statistical and deterministic interface models yield larger cavities when the elastic modulus is increased, that strongly affect the width of the tracking path, r in Equation (4.7). Conversely, the interfacial tracking resistance is inversely proportional to the fourth root of the width of the tracking path ($E_{tr} \propto r^{-1/4}$), which is likely to negate the opposite influence of the elastic modulus on the interfacial tracking resistance. Figure 8.8 manifests that lower estimated interfacial tracking resistances of SiR and XLPE might have led to deeper and wider breakdown tracking paths, which supports the correlation between the width of the tracking path and interfacial tracking resistance.

On the other hand, the results from the AC breakdown experiments indicate that materials with lower moduli yield higher interfacial BDS values. At first glance, these results seem to conflict with the observed trends shown in [59–61]. However, there are several reasons why this is not the case. First of all, performances of bulk

[21] The relative permittivities (ε_r) of the materials range from 2.3 to 4.6; therefore, magnitudes of the field enhancements at the edges of air-filled cavities are assumed to not differ significantly from each other.

[22] Interfaces formed between identical pairs of solid dielectrics.

[23] The tracking resistance is represented by E_{tr} rather than R_{tr} because its unit is in kV/mm.

materials, not those of interfaces, were tested in these studies. Likewise, we did not test the BDS of the bulk materials with reference to their elastic moduli because it is not within the scope of this work. Moreover, in the light of the theoretical models we proposed, as the elastic modulus is increased, larger cavities arise at the interface, and in turn, a considerably smaller contact area than the nominal area of the bulk material is predicted. Therefore, the assessment for the impact of the elastic modulus on the interfacial BDS is different from that for the BDS of the bulk material. In agreement with this, Roy et al. [60] concluded in their work that the increase in an interfacial region in dielectric materials creates a zone of altered polymer properties, which drastically reduces the dielectric permittivity of the interface.

Secondly, the opposite effects of r and E' on the interfacial tracking resistance in Equation (4.7) hinders making generalized statements on the correlation between the elastic modulus and the interfacial BDS. With the increased elastic modulus, the effect of the increased size of cavities and number of vented channels might prevail over the influence of the increased interfacial tracking resistance on the interfacial breakdown strength. This is because, in real surfaces, contact spots take up considerably less space than the cavities according to the results from the statistical and deterministic interface models. Thus, the increased interfacial tracking resistance of the contact spots is potentially negated by the lower inception field strength of larger cavities. Overall, the elastic modulus influences the breakdown of bulk insulation at the nanoscale (contact spots) along the interface tracking path.

Correlation between the Interfacial Tracking Resistance of Contact Spots and AC Breakdown Strength at Solid-Solid Interfaces

The estimated results of the interface breakdown model displayed in Figure 11.4 is replotted in a single graph in Figure 12.7(a). Figure 12.7(a) indicates that once the cavities are discharged, the low estimated tracking resistance of the XLPE is not likely to endure the enhanced local fields, and this will probably lead to an interfacial breakdown. Conversely, the estimated enhanced local fields are not sufficiently high to exceed the estimated interfacial tracking resistances in the cases of the EPOXY and PEEK. Although the average-sized cavities are assumed to be discharged, the high estimated interfacial tracking resistances of the EPOXY and PEEK seem to be able to withstand the high local fields longer than the XLPE could last. It can be inferred that the clear correlation between the estimated cavity discharge and the measured interface BDS values in the case of XLPE (observed in Figure 12.5(b)) is supported by the relation between the estimated interfacial tracking resistance and enhanced fields by the submodel of contact spot breakdown. These findings from the submodel of contact spot breakdown also support the weak correlation between the estimated PDIE and the measured interface BDS observed in Figures 12.5(c)–(d). Overall, the interfacial tracking resistance seems to have an essential role in the interfacial breakdown phenomenon.

Similarly, the estimated results of the XLPE samples at different surface roughnesses presented in Figure 11.5 are replotted in Figure 12.7(b). In the cases of the XLPE samples with four different surface roughnesses, when discharge activity starts in the average-sized cavities, the estimated enhanced fields are close to the estimated interfacial tracking resistance of the XLPE as shown in Figure 12.7(b). At smoother surfaces, the estimated enhanced field values are predicted to be sufficiently intense to result in the breakdown of the contact spots. The magnitudes of the estimated local fields do not significantly increase from the PD inception until interface breakdown (between instants I and II in Figure 12.7(b)) because the estimated PDIE^e values are close to the measured BDS values. In some cases, PDIE^e values are estimated to be higher than the measured BDS values. Thus, the clear correlation between the cavity discharge and the interface breakdown observed in the case of XLPE #500 in Figure 12.5(b) is also detected in the case of XLPE samples with different surface roughnesses. Consequently, Figure 11.5 highlights again that once the average-sized cavities are discharged, the low (estimated) interfacial tracking resistance of the XLPE is not likely to withstand the enhanced local fields for a long time and is predisposed to lead to interfacial tracking/breakdown. These findings once again indicate that the interfacial tracking resistances of the polymers strongly affect the interfacial breakdown as well as the discharged cavities. In particular, the results suggest that the influence of the contact spots on the interfacial BDS becomes more prominent at higher contact pressures, harder materials and/or smoother surfaces.

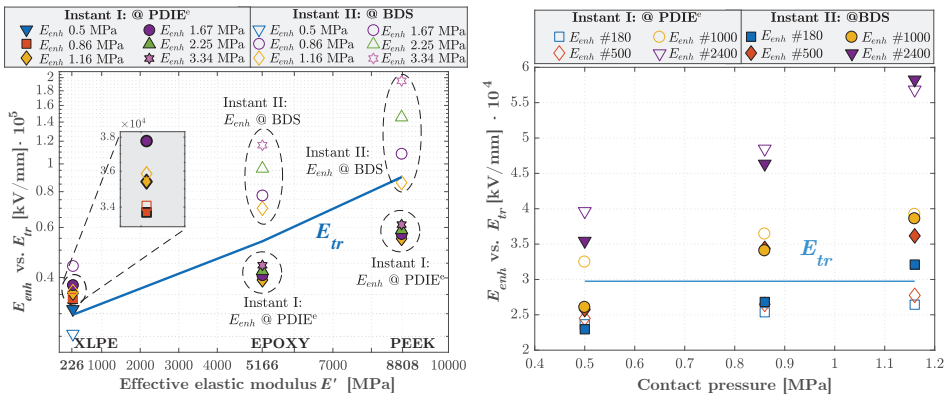

Figure 12.7: Estimated enhanced fields E_{enh} vs. tracking resistance E_{tr} within the covered p_a for each interface at the instants of cavity discharge and breakdown of contact spots: (a) XLPE #500, EPOXY #500, and PEEK #500 interfaces. (b) XLPE #500 interfaces at four different surface roughnesses. Instants I and II represent the moments when PD and BD take place, respectively in the interface BD model presented in Figure 4.6.

Turning now to the deterministic interface model, the results reveal that the ratios of real contact area to the nominal area, A_{re}/A_a, of the XLPE–XLPE and PEEK–PEEK interfaces (see Figure 11.13(d)) are very close, in fact, the maximum deviation is only 5%. Based on the similarity in A_{re}/A_a values, it can be claimed that if the interfacial tracking resistances of materials were ineffective on the interfacial breakdown, the interfacial BDS values obtained from the AC breakdown experiments would be very close to each other. The experimental results, however, indicated otherwise: significant differences between the BDS vales of XLPE–XLPE and PEEK–PEEK interfaces were observed. These findings thus support the above-mentioned deduction that the interfacial tracking resistance is very likely to affect the interfacial BDS considerably.

Besides, the mechanisms for initiation and propagation stages of interfacial breakdown proposed by Gao et al. [66] are in line with our observations in the discharge-monitoring experiments. For instance, the discharged cavities shown in Figures 10.3 and 10.5 can be associated with the proposed initiation and propagation stages of the breakdown of contact spots by Gao et al. [66], respectively, such that only microcavities are discharged in the initiation stage whereas contact areas isolating the discharged cavities are bridged in the propagation stage as illustrated in Figure 10.11(b).

Finally, interface surfaces inspected using a digital microscope after experiments provide supporting evidence for the effect of contact spots on the interfacial breakdown. Figure 12.8(a) displays the interfacial surface of an XLPE sample that underwent an interface breakdown. The encircled area at the surface indicates interfacial microtracking activity near the top electrode, but the propagation of the streamers was most likely hindered due to contact spots on their way. The interface tracking path shown by the arrows might be one such streamer that could propagate owing to interconnected cavities or by breaking down the contact spots obstructing it. The interfacial surface of a PEEK sample, subjected to an interfacial breakdown, provides more explicit evidence in Figure 12.8(b).

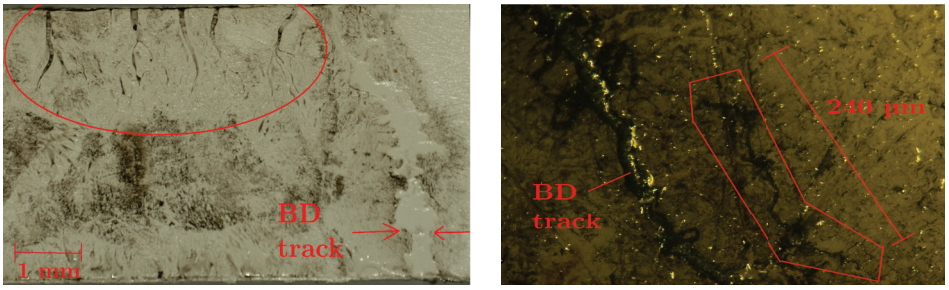

(a) XLPE–XLPE #500 1.16 MPa. **(b)** PEEK–PEEK #500 1.16 MPa.

Figure 12.8: Microtracking observed at interfaces between broken-down samples. The widths of the microtracks range from 4–8 µm.

The enclosed area unveils an interfacial microtrack of a length about 0.24 mm. The tracking path is located near the main breakdown track, but neither of its ends is connected with other tracking paths. Thus, it is an isolated microtrack, which possibly bridged two contact areas but was stopped by the high estimated tracking resistance of PEEK. Furthermore, in Figure A.20, microscope images of the interfacial surfaces of virgin and used PEEK #500 samples are presented at different surface magnifications. The images suggest that there were discharge activities in several cavities/channels that could not evolve to a complete flashover.

12.2.3 Effect of Gas Pressure inside the Cavities on the Interfacial Breakdown Strength

In this section, the results of the AC breakdown experiments, discharge-monitoring experiments, and the deterministic roughness model are used to scrutinize the gas pressure inside the air-filled cavities. The results of the deterministic model revealed that, in the cases of lower contact pressure, rougher surface and/or harder material, vented channels composed of connected cavities emerge at the real interface (see Figures 11.7, 11.8, and 11.9). The continuous discharge channels observed in Figures 10.3 and 10.5 further support the assumption that there are vented channels composed of a number of connected cavities in the real 3D interface. On the other hand, the effect of isolated cavities should also be taken into account, particularly at higher contact pressures, smoother surfaces and/or softer materials.

The results of the simulated interfaces using the deterministic model shown in Figures 11.7 and 11.8 indicate that, when smoother surfaces are assembled at higher contact pressures, the increased contact pressure reduces the number of long air-filled channels, and thus, creates more enclosed cavities at the interface. In particular, in Figure 11.8, the increased contact pressure in the case of XLPE #2400 produces an almost perfect/ideal contact between the XLPE samples, leading to a notably increased estimated contact area (see Figure 11.13(b)). In conjunction with the increased contact area in the simulations, very high BDS values are measured in the AC breakdown experiments in the case of XLPE #2400, particularly at higher contact pressures, as shown in Figure 12.4(d).

In addition, the increased contact pressure from 0.5 to 1.16 MPa in the case of XLPE #180 (see Figure 12.4(a)) yields an increased BDS by a factor of 1.4, while the factor becomes 1.7 in the case of #2400 (see Figure 12.4(d)). These results indicate that the smoother the surface, the higher the influence of the increased pressure on the measured BDS. To sum up, the gas pressure inside the isolated cavities is likely to increase as a function of the change in the size of the cavity, that is dependent on the contact pressure and elastic modulus. Consequently, the increased PDIE values of the isolated/enclosed cavities are likely to have contributed to the very high BDS values achieved at smoother interfaces at high contact pressures in the AC breakdown experiments.

A similar discussion is also valid for softer materials such as SiR. The very high AC BDS values of SiR–SiR #500 displayed in Figure 12.5(a) suggest that there are probably numerous enclosed cavities even at a relatively low contact pressure in which the gas pressure is greater than 1 atm. As shown in Figure 12.9, the simulation results of the SiR–SiR #500 interface also indicate that there are many isolated cavities even at the lowest applied pressure, which are broken into even smaller cavities under the increased contact pressure. Likewise, despite the significant difference in elasticity, at high contact pressures, the presence of enclosed cavities is also suspected due to high BDS achieved in the cases of XLPE #500, EPOXY #500, and PEEK #500 in the AC breakdown experiments. These findings are in line with the reported results by Stewart et al. [53, 54] that vented channels were likely to be subjected to less severe PDs due to the dispersal of by-products and gas refresh through the vent. This is because the variation in gas content and by-products generated by the PD activity in voids affect the space charge build-up on the void walls, the generation rate of initiating electrons, and alter the collision energy; thus changing the PD characteristics [53].

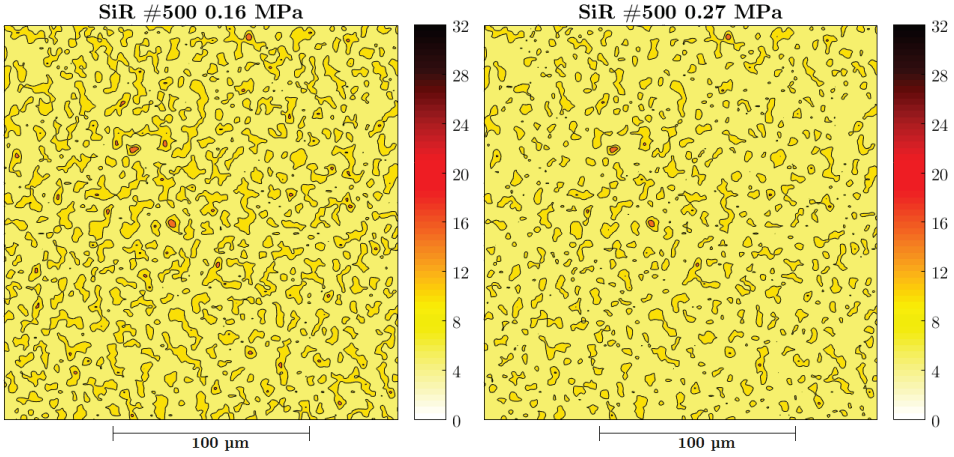

Figure 12.9: Filled-contour plots of the surface asperities of the SiR samples polished with #500 at 0.16 MPa (lowest p_a) and 0.27 MPa (highest p_a), respectively. Color bars are in µm.

When developing the interface breakdown model in Chapter 4, the pressure inside the cavities is assumed to remain at ambient pressure because a large number of connected cavities at the interface are likely to allow the air to be squeezed out and be vented to the surroundings. However, the results of the AC breakdown experiments and the deterministic simulations mentioned above indicate that the assumption of vented cavities is not entirely valid in the cases of smooth surfaces under high contact pressures and/or very soft materials subjected to high contact pressures. In these cases, the number of isolated cavities is very high while there are few, if not none, vented channels according to the interface simulations. Consequently, vented cavities and enclosed cavities at the interface are likely to coexist

in real life. Thus, the gas pressure inside the enclosed cavities is likely to increase as a function of the change in the size of the cavity that is dependent on the contact pressure and elastic modulus, which in turn, increase the discharge field strength of the cavities according to the right of the Paschen minimum.

According to the ideal gas law, the air pressure in the enclosed cavities tends to be higher than 1 atm after the contact pressure is increased from its initial value. To calculate the air pressure inside enclosed cavities, the initial gas pressure p_0—prior to the application of contact pressure—is set to 1 bar ($\approx$ 1 atm). With the increase of the applied pressure, cavities are further compressed, and hence the pressure inside an average cavity, p_c will rise according to the ideal gas law [152]:

$$p_c = \left(\frac{d_{avg_{ref}}}{d_{avg}} \right)^3 p_0 \,, \tag{12.1}$$

where $d_{avg_{ref}}$ is the initial cavity size in the longitudinal direction when p_a is equal to the reference initial applied pressure p_{ref}. Based on the right of Paschen minimum, the discharge field strength of air-filled cavities increases as a function of the gas pressure inside the cavities as shown in Figure 4.2.

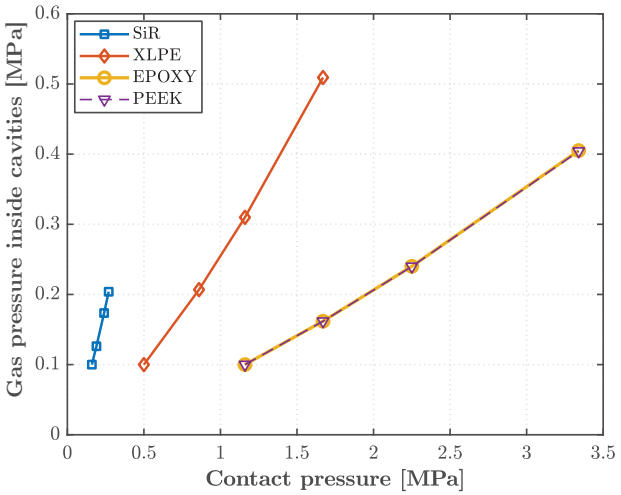

Figure 12.10: Estimated gas pressure inside enclosed cavities as a function of contact pressure based on the ideal gas law, as represented in Equation (12.1).

In a hypothetical case that an interface incorporates only air-filled, enclosed cavities (unvented), the pressure inside the average-sized cavities can be estimated using Equation (12.1). Figure 12.10 demonstrates the calculated gas pressure inside the enclosed, average-sized cavities for SiR, XLPE, EPOXY, and PEEK (all are #500) based on the interface contact model shown in Figure 4.1. As can be seen from the figure, each p_{ref} is selected as the lowest contact pressure opted for each

polymer in the experiments, and the gas pressures at these contact pressures are 1 bar (≡ 0.1 MPa). Since the estimated average sizes of the cavities are similar for PEEK and EPOXY, the gas pressures inside thereof arise to be almost identical. Using the increased gas pressure values inside enclosed cavities, the estimated PDIE values are plotted in Figure 12.11.

As the impact of the interfacial tracking resistance is shown to be significant in the previous section, these estimated PDIE values in the defined hypothetical case could only be used to demonstrate that enclosed cavities are also one of the critical elements affecting the interfacial BDS since the trapped gas pressure inside will have an essential role in determining the dielectric strength of the cavities according to the Paschen's law.

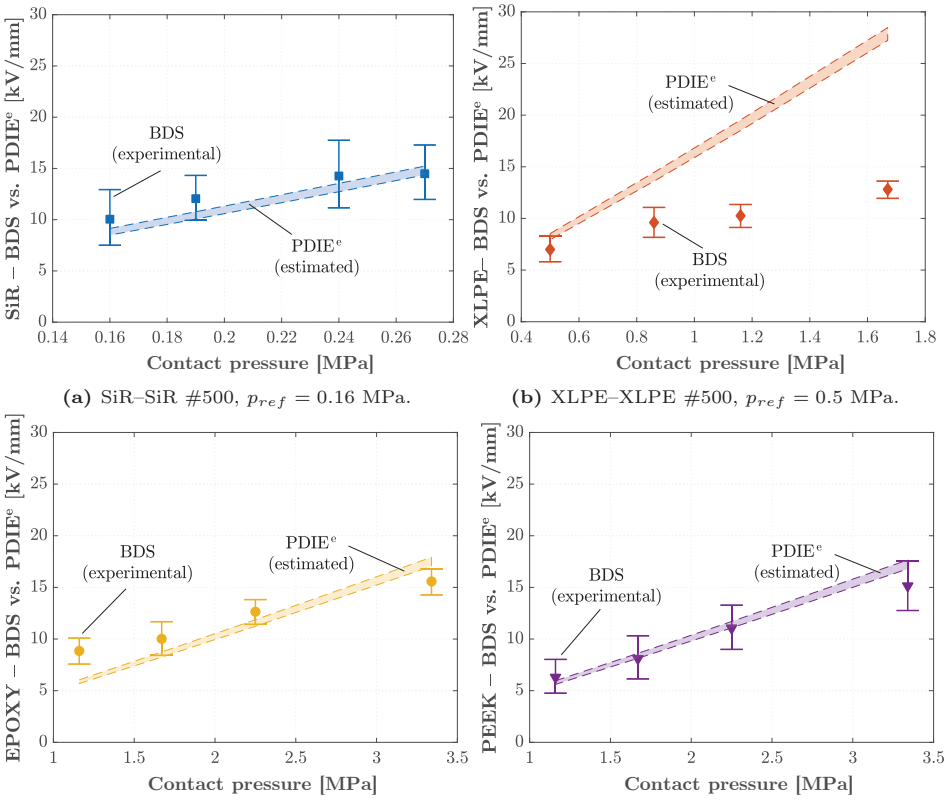

(a) SiR–SiR #500, $p_{ref} = 0.16$ MPa. **(b)** XLPE–XLPE #500, $p_{ref} = 0.5$ MPa.

(c) EPOXY–EPOXY #500, $p_{ref} = 1.16$ MPa. **(d)** PEEK–PEEK #500, $p_{ref} = 1.16$ MPa.

Figure 12.11: Measured BDS data (error bars) from Figure 8.2 vs. estimated PDIE^e (shaded areas) according to ideal gas law with the relation of $p_c \propto {d_{avg}}^{1/3}$: (a) SiR–SiR #500. (b) XLPE–XLPE #500. (c) EPOXY–EPOXY #500. (d) PEEK–PEEK #500. When calculating the estimated PDIE, the minimum and maximum d_{avg} and p_c values were substituted in Equations (4.2) and (4.4), respectively to estimate the minimum and maximum values of the PDIE^e.

12.2.4 Effect of Dielectric Media in Cavities on the Interface Breakdown Strength

In this section, results from the AC breakdown experiments, deterministic model and FEM simulations on the effect of the insulating medium inside interfacial microcavities are used, which incorporate wet-mate and oil-mate XLPE–XLPE and SiR–SiR interfaces, sanded using only #500 grit sandpapers. The results of wet- and oil-mate experiments are discussed below as compared to the dry-mate interfaces explored so far in the discussion.

The results, as shown in Figure 8.6, indicate that the presence of water droplets at the interface reduced the interface breakdown strength drastically. Particularly at low contact pressures, the BDS of the interface is comparable with that of air, leading to the deduction that the water ingress is a critical concern for the design of any HV equipment incorporating solid-solid interfaces, especially in subsea connectors where the hydrostatic pressure can be up to 300 bar at depths around 3000 m [1].

The simulated interface surfaces using the deterministic model indicate that cavities in 3D plane form long vented channels by merging with one another randomly. In the case of wet-mate assembly, water is free to penetrate these channels and is likely to inflict very high local field enhancements around the edges of the contact spots.

Similarly, FEA was used to simulate field distribution at dry-, wet-, and oil-mate XLPE–XLPE interfaces studied in real experiments by defining air, water and oil as the dielectric media filling the cavities, respectively. $\varepsilon_r = 80.1$ is used for water while $\varepsilon_r = 3.8$ is assigned for Midel oil [125]. The FEM simulation results shown in Paper II and in Figure B.8 estimate that very high local field enhancements are likely to emerge at the edges of water-filled voids. Figure 12.12 demonstrates the FEA of all three cases (shown again for convenience). The field enhancement factor is found to be greater than 30 as the field inside the water-filled cavities is virtually zero due to the high relative permittivity of water, and the entire voltage drop is concentrated at the contact spots enclosing the water-filled cavities.

In the case of oil-mate samples, voids are filled with oil. The addition of insulating liquids such as insulating oil prior to assembly showed a promising value to ensure a high breakdown strength and long service life for practical applications. The lubricated interfaces (oil-mate) yielded significantly higher BDS values than those in the cases of dry-mate or wet-mate interfaces, as shown in Figure 8.7. Especially the oil-mate SiR–SiR #500 interface showed an exceptional performance where breakdowns did not occur at the SiR–SiR interface. The field calculations in Figure B.8 indicate that local field enhancements by a factor of about 1.6 occur at the edges of the oil-filled cavities. Since the relative permittivity of the oil ($\varepsilon_{r,\,\mathrm{MIDEL}} \simeq 3.8$ [153]) is comparable with that of XLPE ($\varepsilon_{r,\,\mathrm{XLPE}} \simeq 2.3$), a lower field enhancement occurs compared to water-filled cavities.

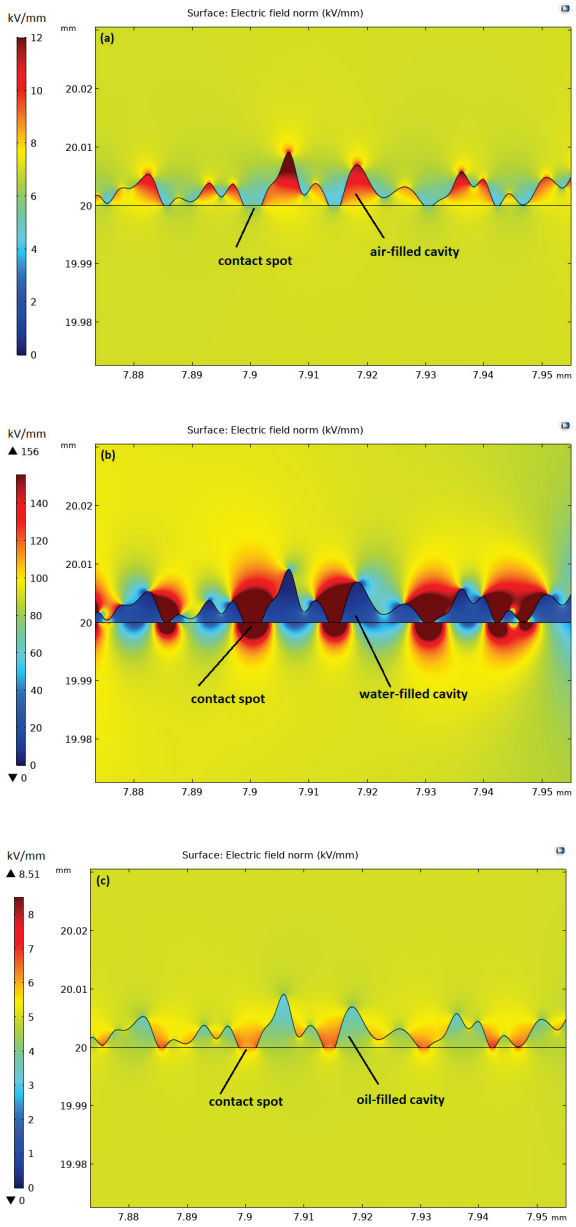

Figure 12.12: Simulation of field distribution at a rough XLPE–XLPE #500 interface in the case of: (a) Air-filled cavities. (b) Water-filled cavities. (c) Oil-filled cavities. The rough surface profile of the equivalent rough surface in 2D, obtained using the profilometer, is exported to COMSOL Multiphysics®.

Moreover, the PDIV of oil-filled cavities is significantly higher compared to that of air- or water-filled cavities. When PD activity starts at a higher voltage, the high dielectric strength of oil ($\sim$ 21-22 kV/mm based on Figure 8.7 and [153]) could thus withstand these local fields longer than the interfaces in the cases of air-filled or water-filled cavities can endure. Finally, the oil-filled cavities at the nanoscale probably increase the interfacial BDS by preventing/hindering microtracking unlike in the cases of air-filled and water-filled cavities.

Chapter 13

Conclusions and Future Work

The main conclusions on this work and recommendations for future work are presented in this chapter.

13.1 Conclusions

The main conclusions with reference to the research questions presented in Section 1.4 and Chapter 12 are listed below:

- The results of experimental and theoretical studies performed in this work have indicated that different mechanisms are involved in the breakdown of air-filled cavities and contact spots. The main hypothesis—that size, shape and insulating medium inside the cavities strongly affect the discharge inception field of the cavities, whereas, the interfacial tracking resistance of the contact spots enclosing the cavities also has a significant impact on the interfacial breakdown strength—has been verified using the results of the experimental and theoretical studies.

  The interfacial breakdown in the cases of softer materials such as SiR and XLPE has been found to be strongly dominated by the discharged cavities due to the low estimated interfacial tracking resistances of SiR and XLPE. In other words, discharged cavities have led to an interfacial failure more easily because the contact spots could not withstand the enhanced fields for a long time. In addition, different surface roughnesses in the case of XLPE–XLPE interfaces have also shown a clear correlation between the cavity discharge and the interface breakdown in both rough and smooth surfaces. On the other hand, in the case of stiffer materials with higher elastic modulus such as EPOXY and PEEK, contact spots endured the local enhanced fields longer due to the increased estimated interfacial tracking resistance. To conclude, the results

have suggested that the influence of the interfacial tracking resistance of contact spots on the interface breakdown becomes more prominent at higher contact pressures, harder materials and/or smoother surfaces.

- Two different theoretical approaches have been proposed for the modeling of the interfacial cavities and contact spots, namely the statistical and deterministic interface contact models.

  The deterministic interface contact model provides insight on how the real area of contact at solid-solid interfaces varies as a function of the contact pressure, surface roughness, elasticity, and hardness of the solid material. The model has indicated that the increased interfacial pressure reduces the number of long vented channels and thus creates more enclosed cavities at the interface. Likewise, the smoother the surface, the more enclosed, smaller cavities are present. Conversely, the harder the material, the larger the resulting cavities, and in turn, long channels can be formed by the interconnected cavities. The statistical interface contact model has yielded agreeing results in terms of the average cavity size as well as the ratio of the real contact area to the nominal contact area, A_{re}/A_a. Increased contact pressure, increased elastic modulus (harder materials), and/or decreased surface roughness generated smaller average-sized cavities and higher ratios of A_{re}/A_a.

- The proposed interface breakdown model assumes that the pressure inside the cavities remains at ambient pressure because a large number of interconnected cavities at the interface are likely to allow the air to be squeezed out and be vented to the surroundings. However, the results have indicated that the assumption of vented cavities is not entirely valid in the case of smooth interfaces under high contact pressures and/or soft materials subjected to high contact pressures as the number of enclosed cavities are very high while there are few, if any, vented channels according to the surface simulations. Consequently, vented cavities and enclosed cavities at the interface are likely to coexist in real life in 3D geometry. Thus, the gas pressure inside the enclosed cavities is likely to increase as a function of the change in the size of the cavity, the extent of which is dependent on the contact pressure and elastic modulus. Increased gas pressure, in turn, increases the discharge field strength of the cavities according to the Paschen law.

- The results of the discharge-monitoring experiments have elucidated the mechanisms determining how the discharges in the cavities are initiated, how discharge cavities develop to streamers and propagate at the interface, and how they finally evolve to an interface breakdown by bridging the electrodes. In particular, the discharge images have indicated that microcavities in the field direction are in similar sizes to those of the estimated cavities calculated using the statistical roughness model.

- The ingress of water into the cavities has considerably reduced the measured

BDS values due to the strong local field enhancements at the edges of contact spots. On the other hand, the ingress of oil has yielded significantly higher interfacial BDS values. It has been observed that air-filled cavities and water penetration at the interface are the main limiting factors for the BDS of solid-solid interfaces, whereas addition of insulating liquids such as ester oil prior to assembly has indicated a promising potential to ensure a high breakdown strength and long service life for practical applications.

13.2 Recommendations for Future Work

The following list contains suggestions that could be extended for the continuation of the PhD work to improve the proposed models and the discussion on the findings:

- PD experiments were carried out using XLPE #500 and PEEK #500 samples assembled in dry conditions. In order to ensure a more thorough examination of the effect of water and oil ingress and surface roughness, PD inception field of wet-mate and oil-mate samples with different surface roughnesses can be tested.
- As concluded above, the assumption of vented cavities does not completely remain valid in the case of smooth surfaces under high contact pressures or very soft materials subjected to high contact pressures. Therefore, the interface breakdown model can be extended to incorporate the case of unvented cavities.
- Due to normally distributed asperity peaks and heights, there are at least some cavities larger than the average-sized cavities, in which the PD activity presumably commences first while there is still no PD activity in the average-sized cavities. Thereby, depending on the number and size of larger cavities, accuracy of the estimated PDIE might dwindle. Consequently, an improved contact model containing the influence of the size and number of the largest cavities might perform more accurately. The results of the statistical and deterministic interface contact models revealed that the largest cavities could be 3–4 times as large as the average-sized cavities, as shown in Figure 11.14 .
- Discharge-monitoring experiments can also be carried out for wet-mate and oil-mate samples to monitor the PD behavior under those circumstances.
- In the discharge-monitoring experiments, the discharge activity could only be captured in the indispensable presence of a large artificial cavity to initiate PDs at a lower voltage to prevent the discharge channel from bridging the electrodes immediately. The next step can be trying to achieve capturing the discharge activity at the interface without the presence of an artificial cavity. For this purpose, a faster and more sophisticated camera and peripherals might be

needed. Also, as an intermediate step, rather than creating an artificial cavity at the polymer surface, the electrodes can be extended at the interface by using a very thin, conductive layer of paint or other conductive materials that can generate a substantially high, non-homogeneous electric field to initiate PD activity at a considerably lower voltage, in other words, that can cause local field enhancements at lower applied fields.

- To test the validity of the proposed interface tracking model introduced in Section 4.1.2.1, extending the electrodes with sharp needle-like metals or replacing them with needle-plane or needle-needle electrodes to expose a small part of the interface to a high non-homogeneous electric field can be carried out. The same method can also be tried for discharge-monitoring experiments as an alternative to the use of a conductive paint layer.

- The discharge model, for a spherical cavity within a homogeneous dielectric material, proposed by Illias in [50] could be adapted for solid-solid interfaces. The developed surface simulations using real surface texture data of the rough polymer surfaces in the FEA software in this work could be coupled with the MATLAB® and COMSOL Multiphysics® scripts provided in [50] to improve the submodel for the discharges of air-filled cavities.

- Simulation model of partial discharges in solid dielectric materials proposed by Illias [50] could be retrofitted to the deterministic interface contact model proposed in this work so that the PD inception voltage values could be estimated using the entire 3D interfacial surface.

APPENDICES
A-G

Appendix A

Supplementary Experimental Results

In this appendix chapter, raw experimental data for the dry-mate AC breakdown tests are presented for each parameter studied separately. In addition, images of the broken down interfaces are shown that are intended to serve as supporting information on the interfacial BD mechanisms. Similarly, additional data from the PD experiments are also given to provide additional evidence for the AC breakdown experiments and discharge-monitoring experiments, respectively. It is noted that, unless otherwise stated, interfaces at stake are dry-mate, are assembled between identical polymers and are sanded using #500.

A.1 Raw Data of AC Breakdown Experiments

A.1.1 Influence of Surface Roughness

Additional experimental data on the effect of the surface roughness on the interfacial BDS at 0.5, 0.86, and 1.16 MPa contact pressures are displayed in this section using the Weibull plots of the cumulative percent failure, i.e., cumulative probability of failure, in terms of AC BDS. Figure A.1 summarizes the impact of surface roughness and contact pressure on the AC BDS of interfaces using the 63.2% values with their 90% confidence intervals (CIs). There are several BDS values of similar magnitude at the same pressure especially in the case of the roughest surface (#180), as can be seen in Figure A.1. The overlapping portions of the bars, on the other hand, tend to dwindle as the surface roughness decreases. In the case of the smoothest surface, there are not any coincident BDS values, as seen in Figure A.1.

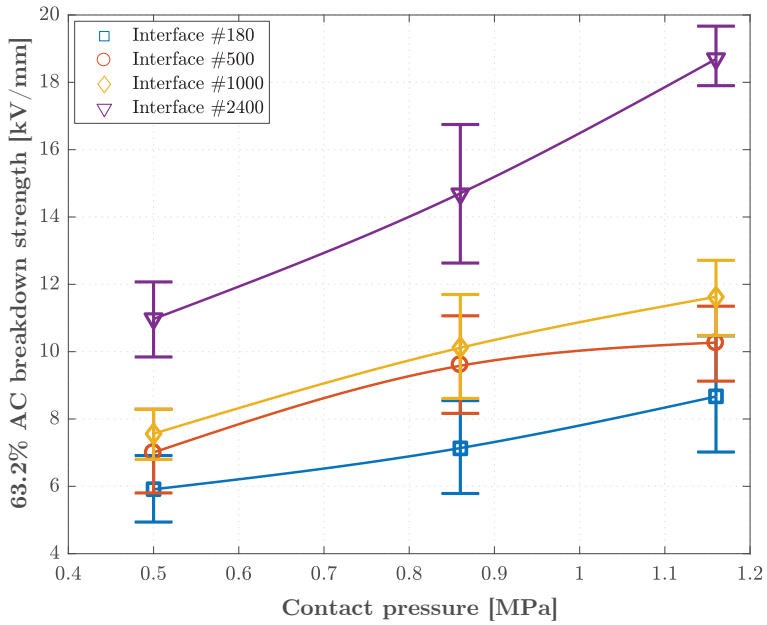

Figure A.1: The experimental AC BDS data set vs. contact pressure. The error bars stand for the 90% CI of the 63.2% AC BDS values, while the markers depict the 63.2% BDS.

Furthermore, the 90% CIs, for the complete cumulative percent failure range are depicted in Figures A.2, A.3, and A.4 by using the cases of the roughest (#180) and the smoothest (#2400) interfaces. The non-overlapping CIs further highlight the strong influence of the surface roughness on the interfacial BDS as well as validate/consolidate the claim that the smoother the interface, the higher the AC BDS.

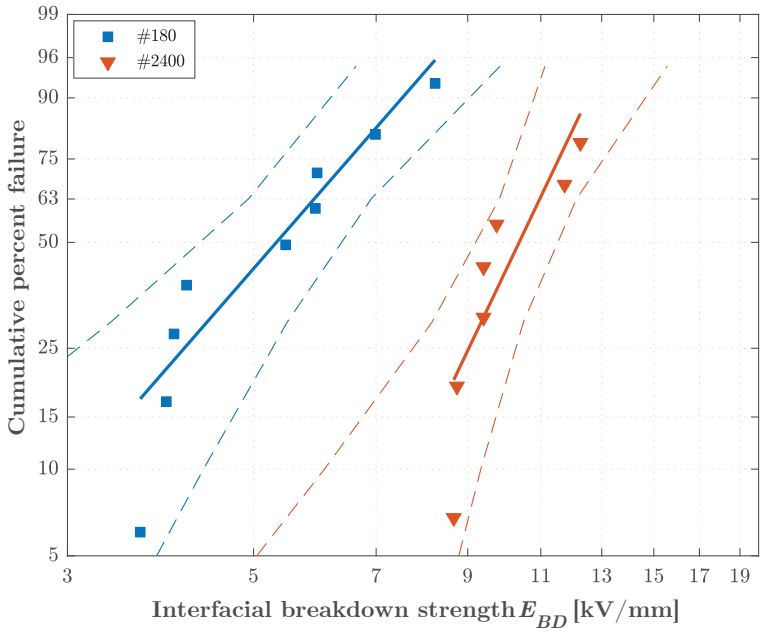

Figure A.2: Weibull plot of cumulative percent failure vs. BDS of XLPE–XLPE interface at 0.5 MPa with the 90% CIs.

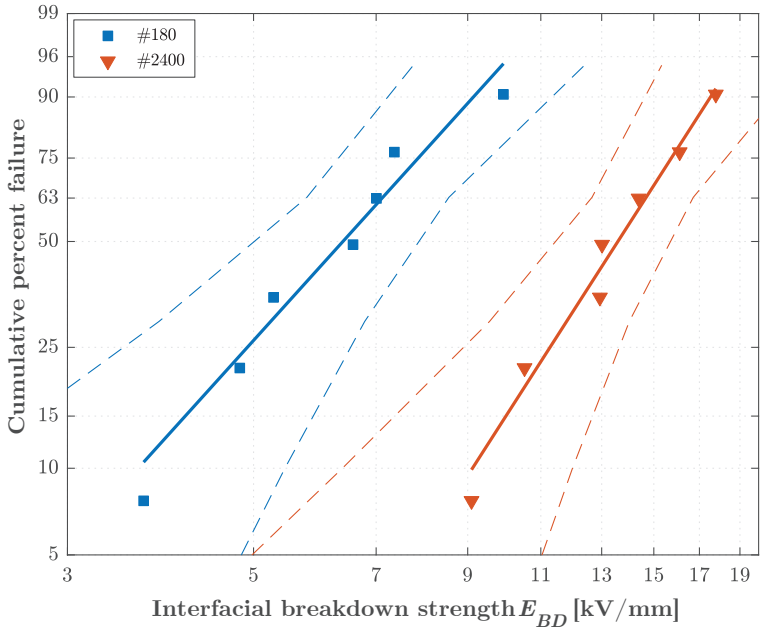

Figure A.3: Weibull plot of cumulative percent failure vs. BDS of XLPE–XLPE interface at 0.86 MPa with the 90% CIs.

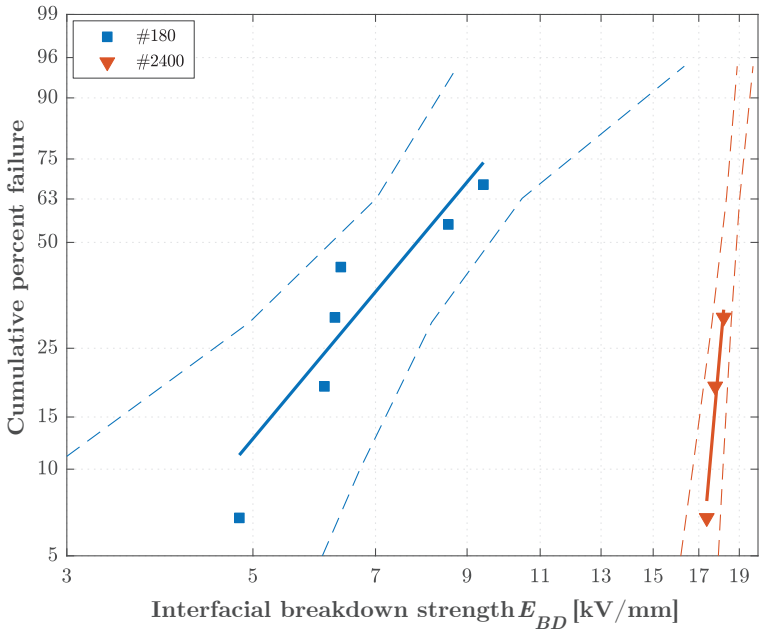

Figure A.4: Weibull plot of cumulative percent failure vs. BDS of XLPE–XLPE interface at 1.16 MPa with the 90% CIs.

A.1.2 Influence of Elastic Modulus

Similarly, Figures A.5, A.7, A.9, and A.11 depict the two-parameter Weibull plot of SiR–SiR, XLPE–XLPE, EPOXY–EPOXY, and PEEK–PEEK interfaces at four different contact pressures, respectively. Each Weibull plot in these figures consists of 7−8 repeated tests at the same conditions using virgin samples. In addition, Figures A.6, A.8, A.10, and A.12 show the BDS values with the 90% CIs at the lowest and highest pressure values. The 90% CIs indicate that augmented contact pressure has a clear impact on the AC BDS of the solid-solid interfaces. Moreover, Weibull plots of the XLPE–XLPE, EPOXY–EPOXY, and PEEK–PEEK (all with #500) interfaces are plotted in the same graphs in Figures A.13 and A.14 at 1.16 and 1.67 MPa to take a closer look at the impact of the elastic modulus on the AC BDS values.

Figures A.15 and A.16 exhibit similar figures for the cases of interfaces between soft-hard materials (relative to each other).

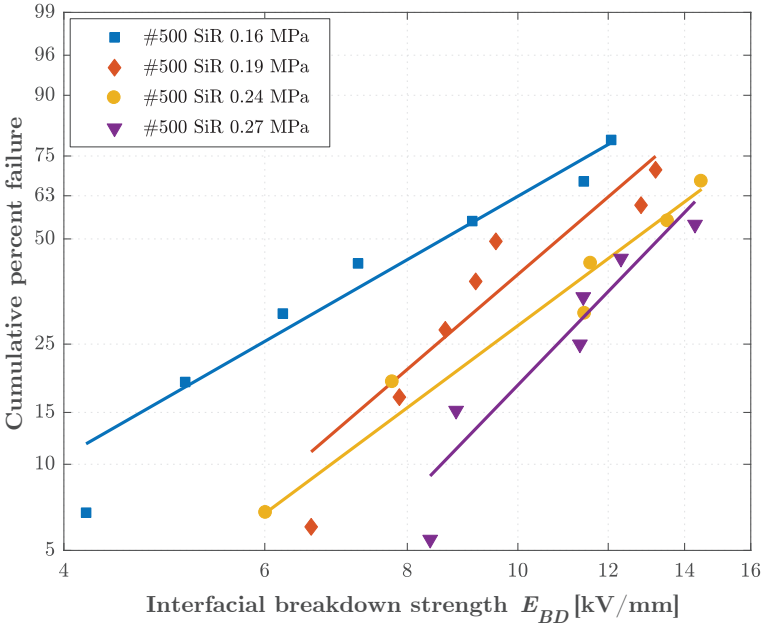

Figure A.5: Weibull plot of cumulative percent failure vs. BDS of dry SiR–SiR interface.

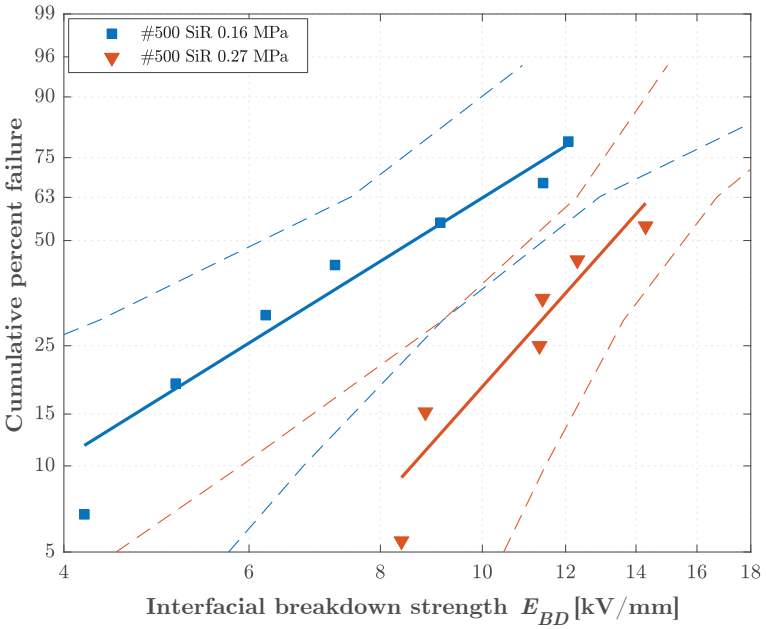

Figure A.6: Weibull plot of cumulative percent failure vs. BDS of dry SiR–SiR interface with the 90% CIs.

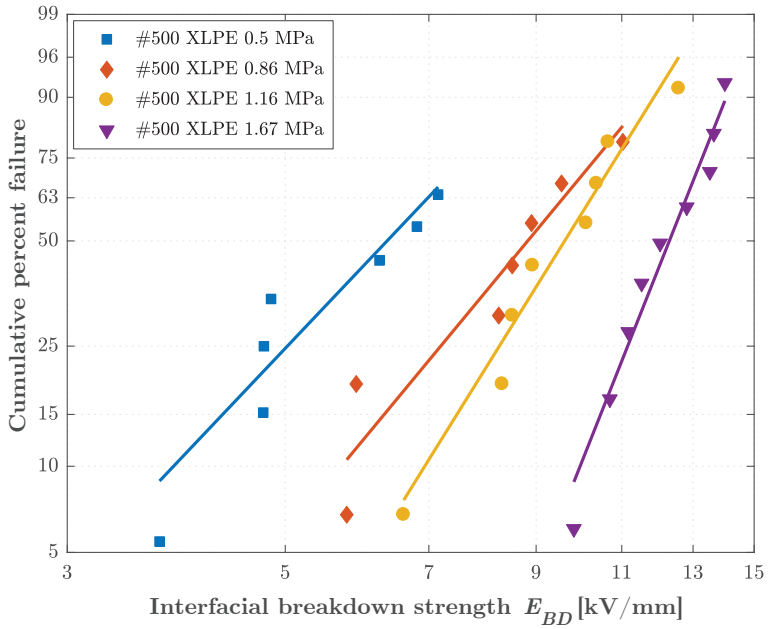

Figure A.7: Weibull plot of cumulative percent failure vs. BDS of XLPE–XLPE interface.

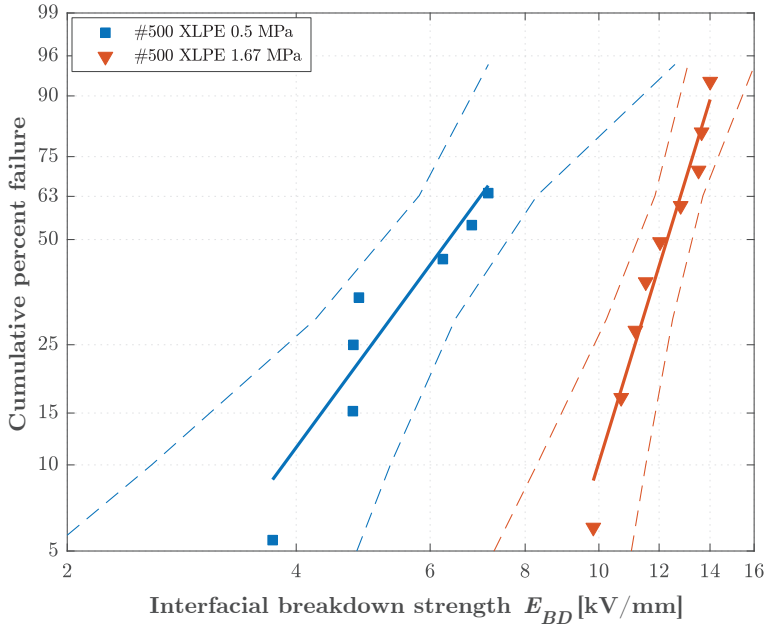

Figure A.8: Weibull plot of cumulative percent failure vs. BDS of XLPE–XLPE interface with the 90% CIs.

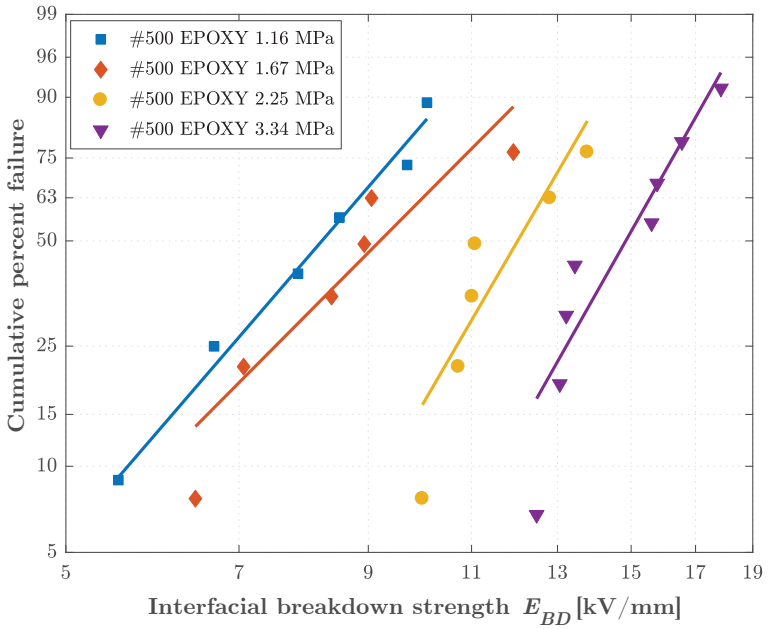

Figure A.9: Weibull plot of cumulative percent failure vs. BDS of EPOXY–EPOXY interface.

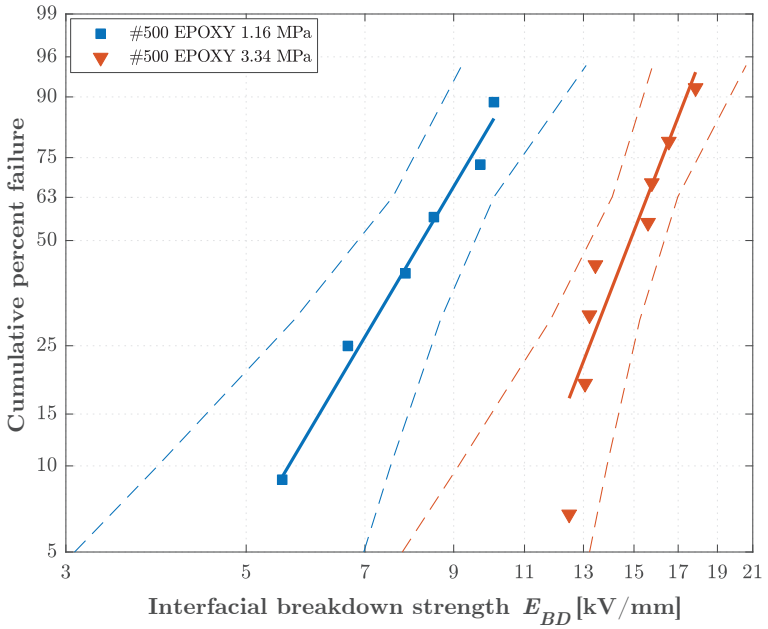

Figure A.10: Weibull plot of cumulative percent failure vs. BDS of EPOXY–EPOXY interface with the 90% CIs.

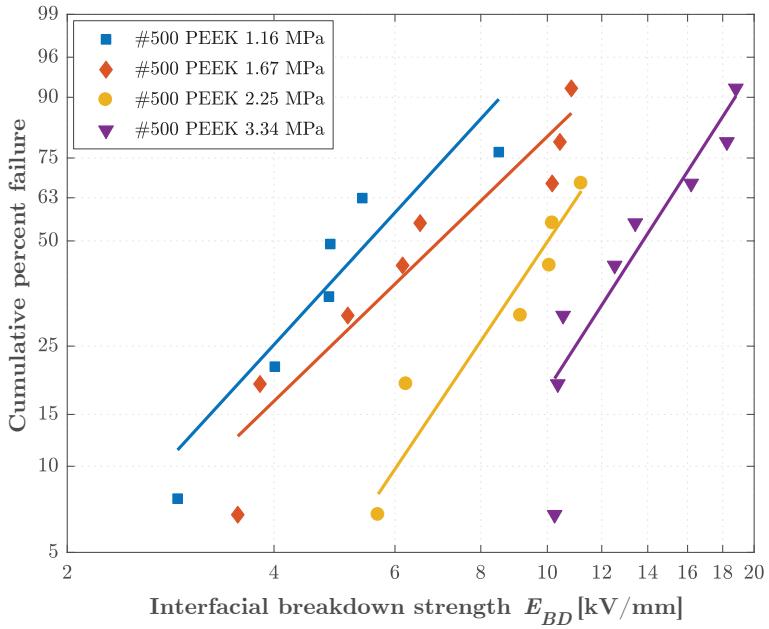

Figure A.11: Weibull plot of cumulative percent failure vs. BDS of PEEK–PEEK interface.

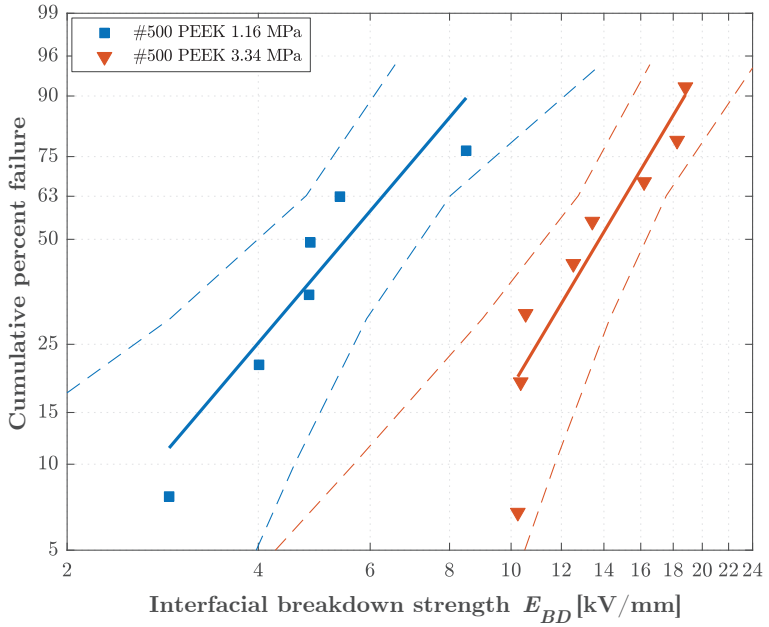

Figure A.12: Weibull plot of cumulative percent failure vs. BDS of PEEK-PEEK interface with the 90% CIs.

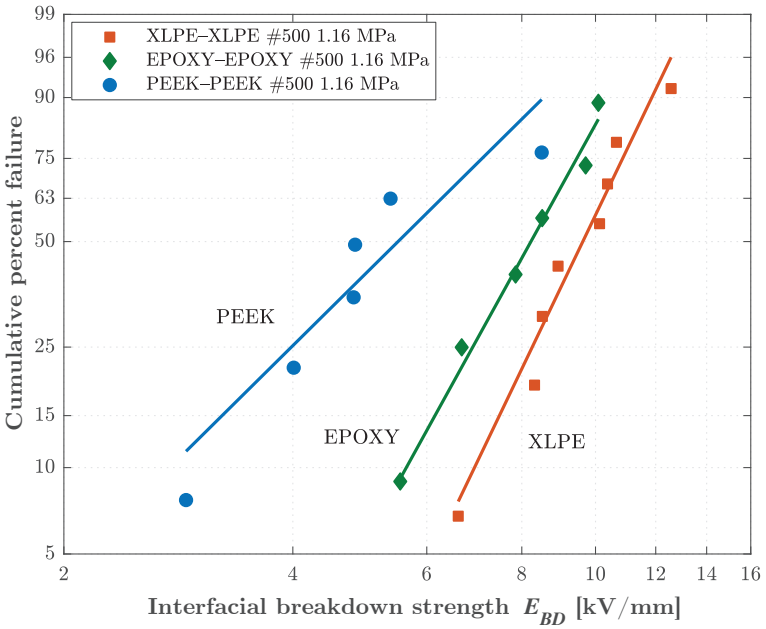

Figure A.13: Weibull plot of cumulative percent failure vs. BDS of XLPE, EPOXY, and PEEK interfaces at 1.16 MPa.

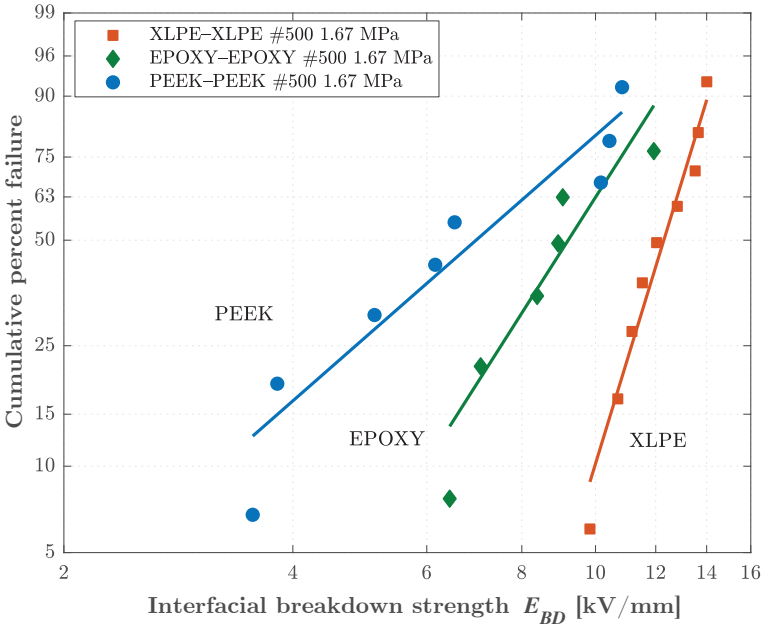

Figure A.14: Weibull plot of cumulative percent failure vs. BDS of XLPE, EPOXY, and PEEK interfaces at 1.67 MPa.

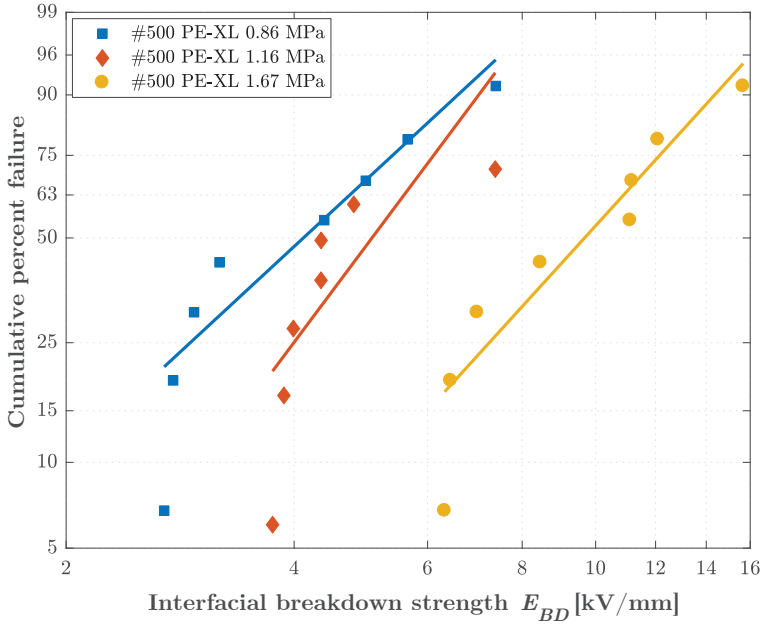

Figure A.15: Weibull plot of cumulative percent failure vs. BDS of PEEK–XLPE interface.

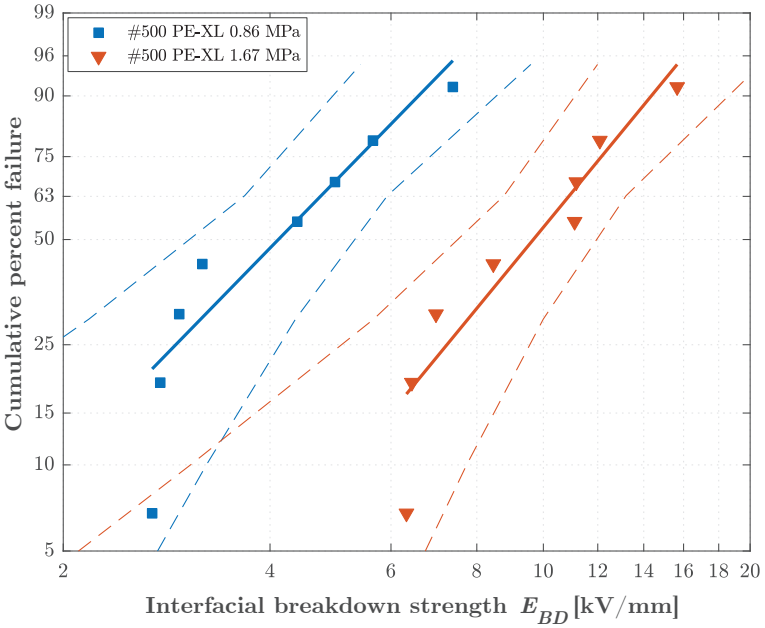

Figure A.16: Weibull plot of cumulative percent failure vs. BDS of PEEK–XLPE interface with the 90% CIs.

A.2 Destructive Effects of Surface Tracking at Interfaces

The energy released during the electrical breakdown resulted in permanent, destructive damages/tracks at the interfacial surface of the specimens. Dry samples exhibited a clear and clean breakdown track as well as incomplete/premature, visible and permanent discharge tracks in both sides starting from the edges adjacent to the electrodes (see Figures A.17(a), A.17(b), A.19(a), and A.19(b)). Carbonization at the interfaces was observed, which were likely to be caused by the heat emanated from breakdown. In the majority of the cases, carbonization caused the specimens to be attached to one another at the points of the BD track. The specimens did not undergo amalgamation; the attachments were weak and easily detachable. Moreover, as in the case of dry-mate EPOXY–EPOXY #500 interface, permanent discharge tracks were explored in the direction of the field at the center of the interface, not at the edges of the sample (see Figures A.19(d) and A.19(e)).

The dry SiR–SiR #500 interface has shown no branches or signs of microtracking after breakdown except for the main BD track, implying that the contact spots withstand the voltage without clear permanent damage until some weaker spots break down (see Figure A.17). It was also observed that less noticeable damage or thinner BD channels were formed at higher contact pressures or reduced surface roughnesses.

Interfacial tracks (microtracks) hint that electrical treeing at the interface was likely to have taken place in the wet-mate case (see Figures A.17(c), A.17(d), and A.19(c)). Interfacial tracking is very likely to form due to the extremely high local fields at the terminals of short-circuited water-filled cavities, as simulated in Figure B.8(c).

In the case of the lubricated XLPE–XLPE #500 and SiR–SiR #500 interfaces, clean and smooth paths were detected, as depicted in Figure A.18, which were presumably created by local Joule heating, as mentioned in Chapter 10. The absence of premature tree-like developing tracks and limited carbonization marks in Figures A.18(e), A.18(f), and A.18(g) suggest that the presence of oil augments the PDIV substantially. Hence, although a higher field strength is reached, the surfaces of the specimens were not profoundly impaired due to high PDIV except for the closest vicinities of the main breakdown path, which was likely to contain air-filled cavities coexisting with the oil-filled cavities. This is because the contact force is likely to squeeze some oil out through vented channels formed by the connected microcavities. As a result, it can be argued that oil-mate interfaces improve not only the breakdown strength but also the overall performance of the interface since no permanent damage occurred due to the pre-breakdown activity.

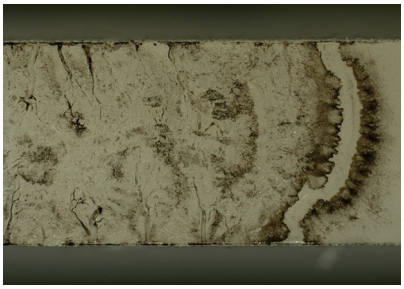

(a) Dry XLPE–XLPE 0.5 MPa.

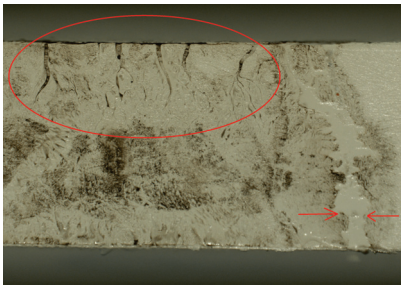

(b) Dry XLPE–XLPE #500 at 1.16 MPa.

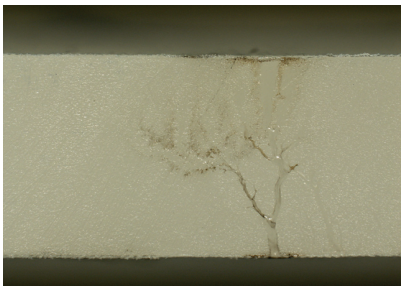

(c) Wet XLPE–XLPE #500 at 0.5 MPa.

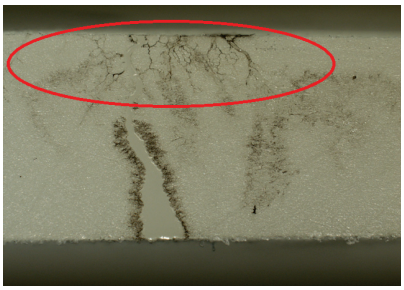

(d) Wet XLPE–XLPE #500 at 1.16 MPa.

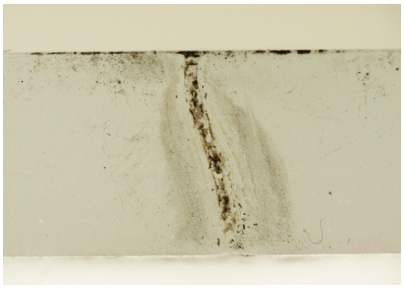

(e) Dry SiR–SiR #500 at 0.16 MPa.

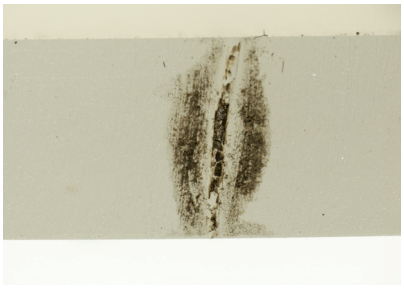

(f) Dry SiR–SiR #500 at 0.27 MPa.

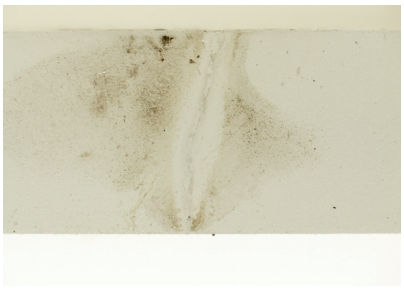

(g) Wet SiR–SiR #500 at 0.16 MPa.

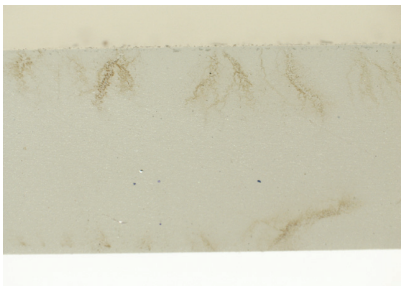

(h) Wet SiR–SiR #500 at 0.27 MPa.

Figure A.17: Breakdown tracks at solid-solid interfaces of 4 mm (part I).

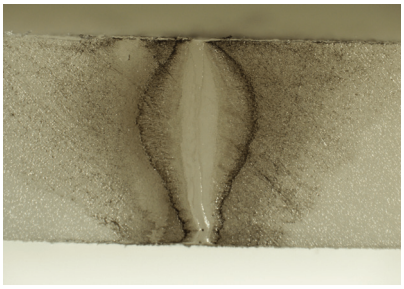

(a) Dry **XLPE**–SiR #500 at 0.27 MPa.

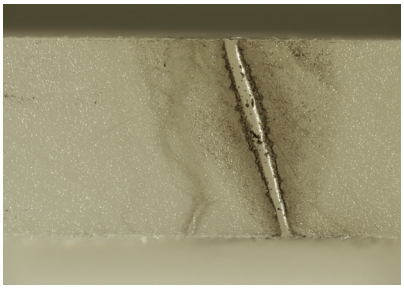

(b) Dry XLPE–**SiR** #500 at 0.27 MPa.

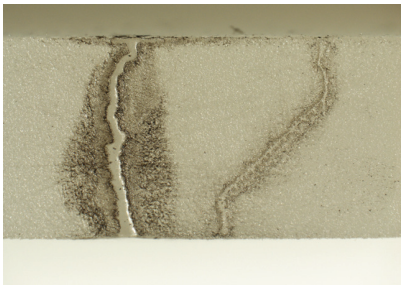

(c) Wet **XLPE**–SiR #500 at 0.27 MPa.

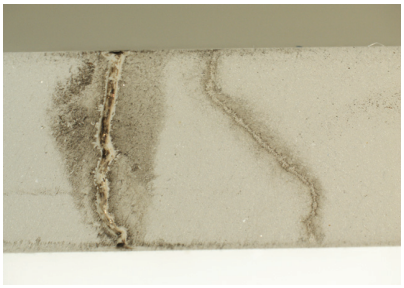

(d) Wet XLPE–**SiR** #500 at 0.27 MPa.

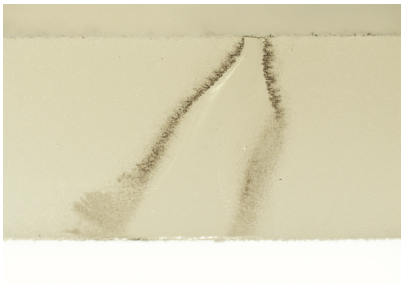

(e) Lubricated XLPE–XLPE #500 at 0.5 MPa.

(f) Lubricated XLPE–XLPE #500 at 1.16 MPa.

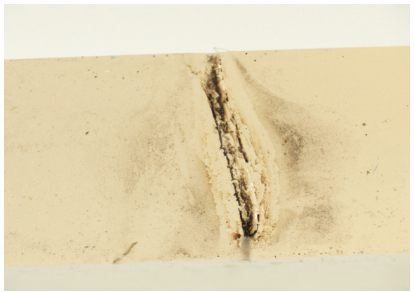

(g) Lubricated SiR–SiR #500 at 0.16 MPa.

Figure A.18: Breakdown tracks at solid-solid interfaces of 4 mm (part II). In the cases of XLPE–SiR #500 interfaces, image of the corresponding sample is emphasized in bold type.

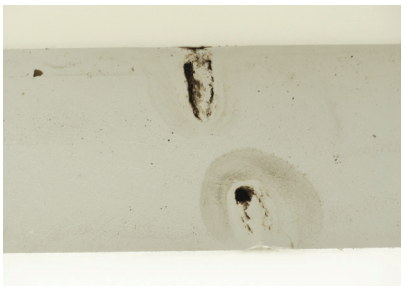

(a) Dry SiR–SiR #500 at 0.27 MPa.

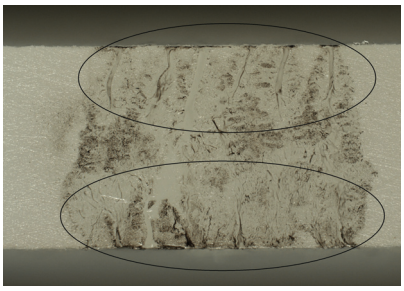

(b) Dry XLPE–XLPE #500 at 0.27 MPa.

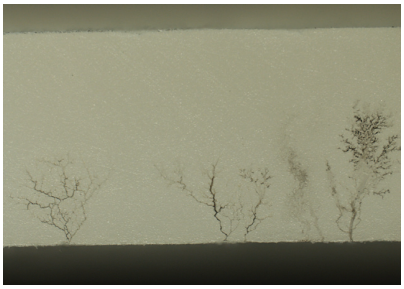

(c) Wet XLPE–XLPE #500 at 1.16 MPa.

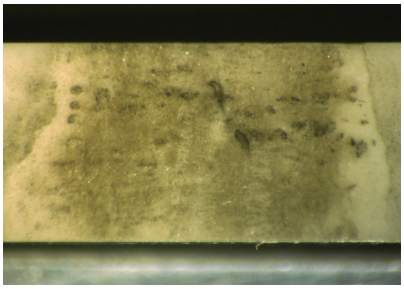

(d) Dry EPOXY–EPOXY #500 at 3.34 MPa.

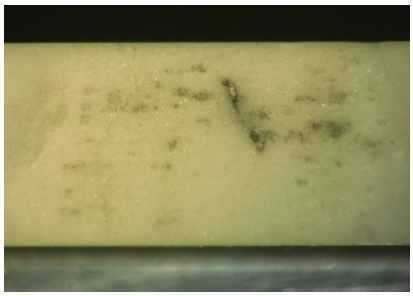

(e) Dry EPOXY–EPOXY #500 at 3.34 MPa (cleaned).

Figure A.19: Breakdown tracks at solid-solid interfaces of 4 mm (part III).

Finally, surface tracking at dry PEEK-PEEK #500 interfaces after AC breakdown tests was also inspected. In Figure A.20, microscope images of the interfacial surfaces of virgin and used PEEK #500 samples are presented at different surface magnifications. We suppose that pre-breakdown activity caused permanent damages at microcavities and the high estimated interfacial tracking resistance of the PEEK presumably prevented the streamers from propagating from the discharged microcavities.

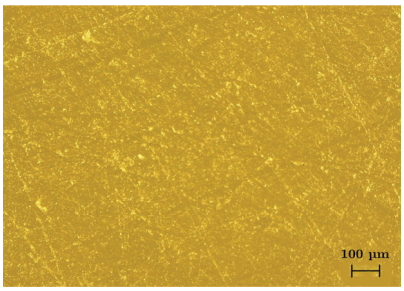

(a) Virgin PEEK #500 at (200X).

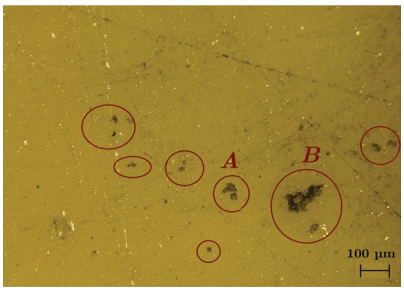

(b) Used PEEK #500 (200X).

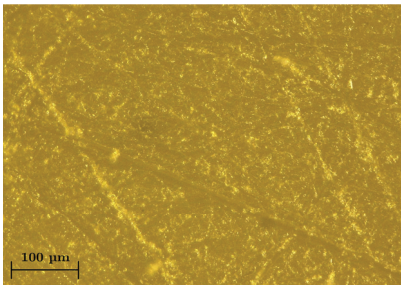

(c) Virgin PEEK #500 at (500X).

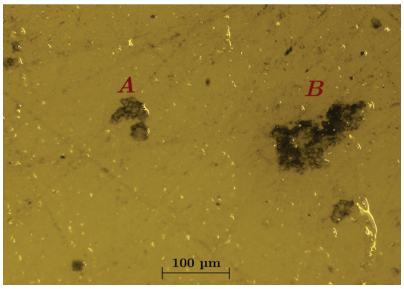

(d) Used PEEK #500 (500X).

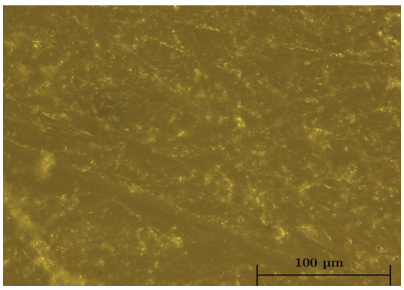

(e) Virgin PEEK #500 at (1000X).

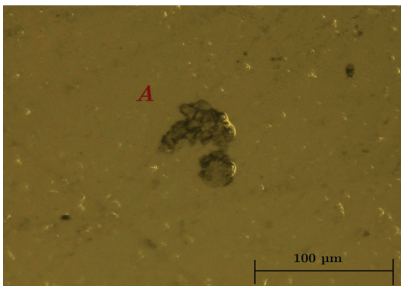

(f) Used PEEK #500 (1000X).

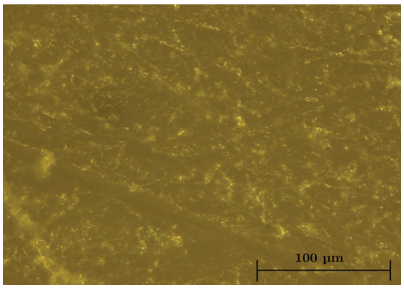

(g) Virgin PEEK #500 at (1000X).

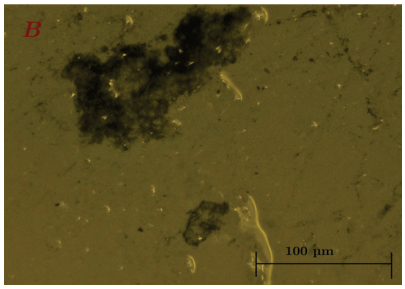

(h) Used PEEK #500 (1000X).

Figure A.20: Surface inspection of virgin and used PEEK #500 samples. Damages shown are not close the main breakdown track.

A.3 Raw Data of PD Experiments

The main differences between the data representation techniques of PRPDA[24] and PSA[25] are such that PRPDA is based on the charge magnitude with reference to voltage phase whereas PSA is based on time and voltage data of PDs. PSA enables users to find out the sequence of PDs whereas PRPDA allows the statistical data to be extracted from the phase-charge magnitude information. The PD sequence information is lost in the PRPDA while statistical data cannot be extracted in the PSA [52].

A.3.1 Polymer–Polymer Interfaces

A.3.1.1 Results using Phase-Resolved Partial Discharge Analysis

The GUI of the Omicron software enables users to export PD data to MATLAB®. The data are exported while the recorded sequence of PD events is replayed in the GUI. However, MATLAB® does not directly recognize the exported data because these data are recorded in binary format [50]. The MATLAB® script developed by Illias [50] is used to extract useful data from the exported binary file. Except for the PD clusters shown in the Omicron GUI, favored PD characteristics in the literature when representing the PRPD patterns are the number of PDs per cycle, total apparent charge per cycle, mean charge and maximum charge magnitude. Details of how to determine these phase distributions are explained in [51] (on pp. $64-65$).

The graphs in Figure A.21 provide statistical, quantitative examination using each PRPD data. The PD data were exported to MATLAB® and were further processed as explained above. In addition to the results shown in Chapter 9, XLPE–XLPE #500 at 0.5 MPa is also displayed to reveal the effect of pressure increase in the case of XLPE. PRPD patterns are shown using 3D histograms in Figure A.22(a)–(c) in the format of $\phi-q_a-n_{PD}$ plots.[26] The build-up of $\phi-q_a-n_{PD}$ distribution is illustrated in Figure A.23. As seen in the histograms, n_{PD} is higher at the PEEK–PEEK interface where as maximum PD charge magnitude is lower compared to those in the XLPE–XLPE intefaces.

[24] Phase-resolved partial discharge analysis.

[25] Pulse-sequence analysis.

[26] ϕ on the x-axis is the voltage phase, q_a on the y-axis is the apparent charge magnitude and n_{PD} on the z-axis is the number of PDs occurring at a specified phase of the applied voltage.

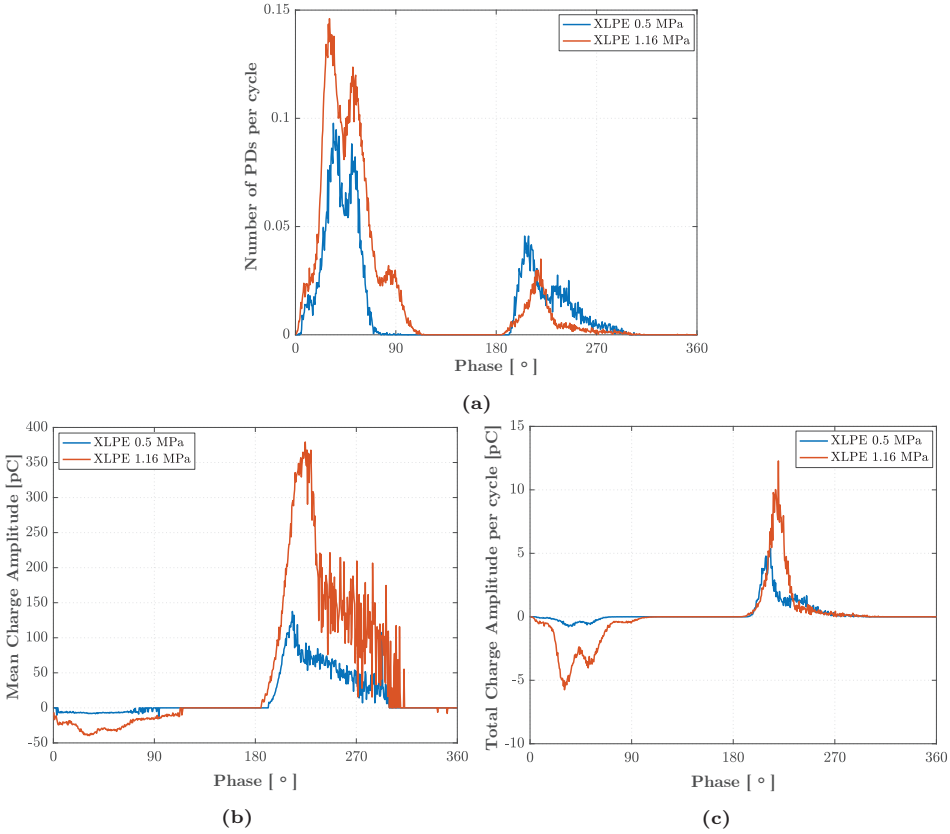

Figure A.21: Results of PD experiments of XLPE–XLPE #500 at 0.5 and 1.16 MPa. (a) Number of PDs per cycle vs. phase angle. (b) Mean charge amplitude vs phase angle. (c) Total charge amplitude per cycle vs. phase angle.

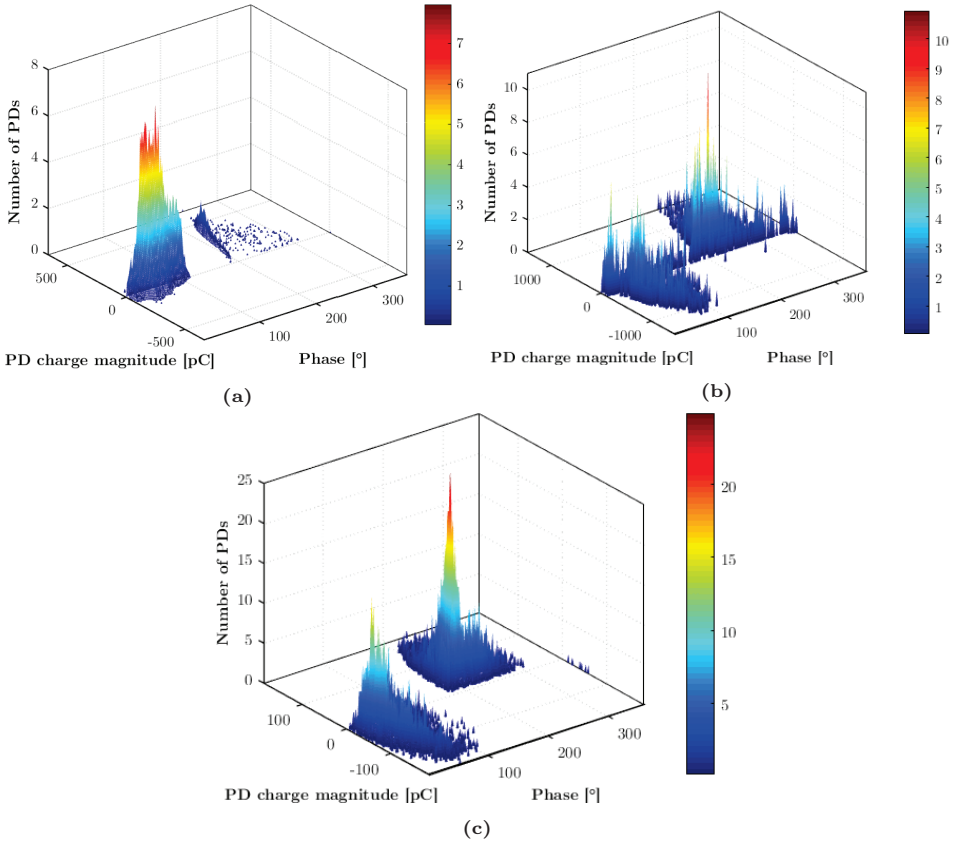

Figure A.22: $\phi - q_a - n_{PD}$ of: (a) XLPE–XLPE #500 at 0.5 MPa. (b) XLPE–XLPE #500 at 1.16 MPa. (c) PEEK–PEEK #500 at 1.16 MPa.

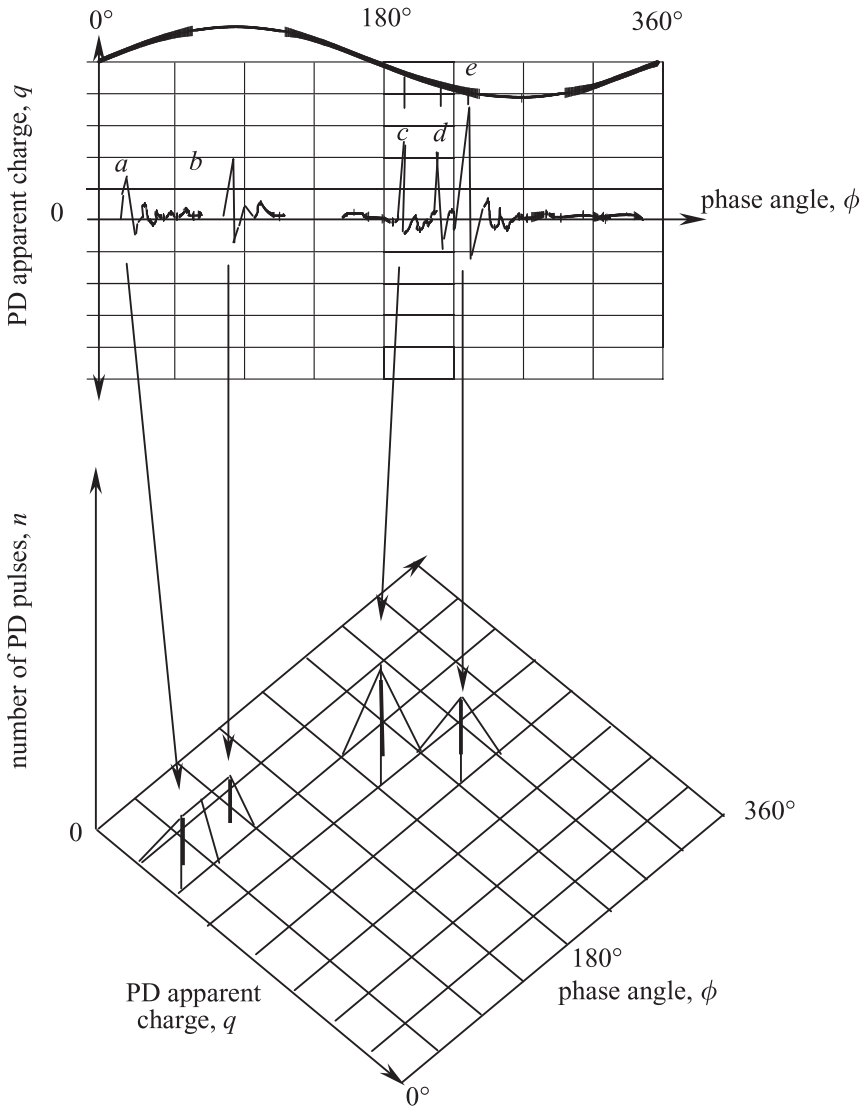

Figure A.23: Build-up of $\phi - q - n$ distribution [154].

Figure A.24 displays the typical PD patterns addressed in the literature with their corresponding sources. For instance, the PD sources are characterized by the pulse patterns where the phase angle ϕ is used in the first place to differentiate between the sources such as internal voids, surface or corona discharges. For instance, PD patterns of corona noise are usually featured as a cluster across the peaks of the positive and negative voltage curve. An unnoticed phase shift of 30° in the PRPD diagram could mislead the interpretation of the PD source in such a way that critical surface PDs indicating a serious defect could be mistaken for corona noise, which is usually classified as a not dangerous phenomenon [155].

When the PD histograms shown in Figure A.22 are compared with the reference PD patterns in Figure A.24, it can be inferred that the likely cause of the resulting PRPD patterns is internal discharges. In other words, discharged cavities either with direct contact to one of the electrodes or without any contact, i.e., floating at the interface are the potential sources. In particular, the PRPD pattern near the voltage zero crossing points (180°) in Figure A.22(a) is relatively similar to the pattern in the third row in Figure A.24. Figure A.22(a) is replotted in Figure A.25(a) in 2D to facilitate the comparison with the reference pattern. Thus, an expanding cavity is likely to yield a pattern such as that in Figure A.25(a), meaning that at a lower contact pressure, cavities are likely to merge and form larger air-filled gaps.

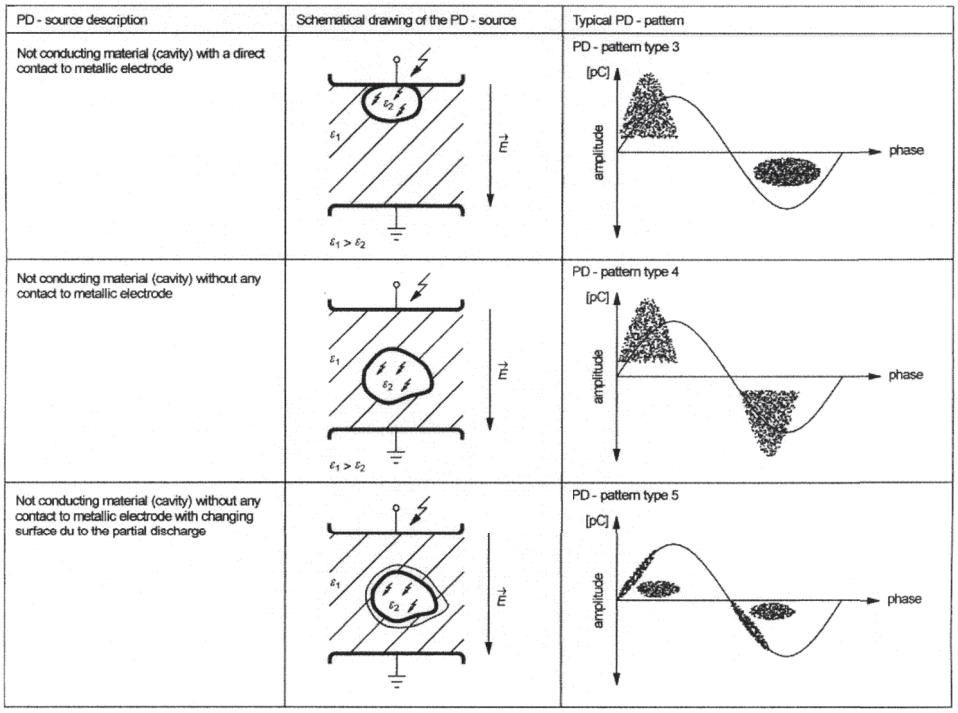

Figure A.24: Typical PD patterns detected in insulating systems [140].

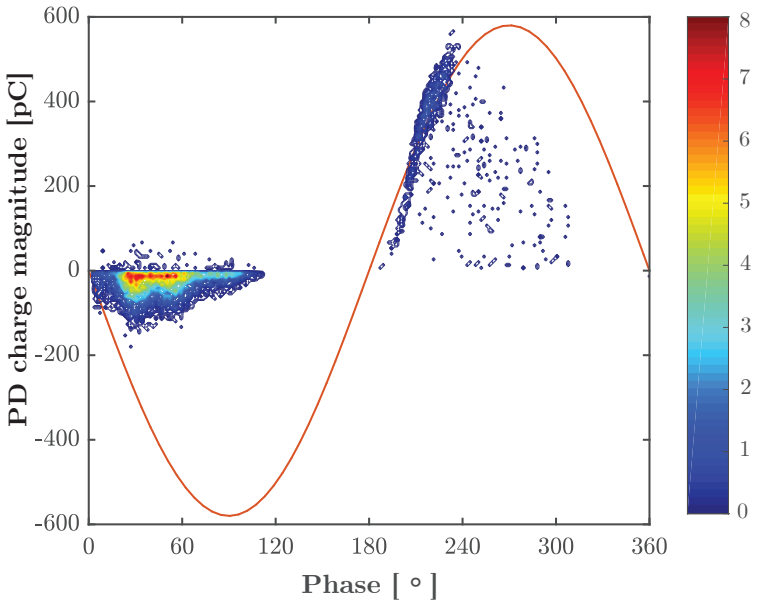

(a) XLPE–XLPE #500 at 0.5 MPa

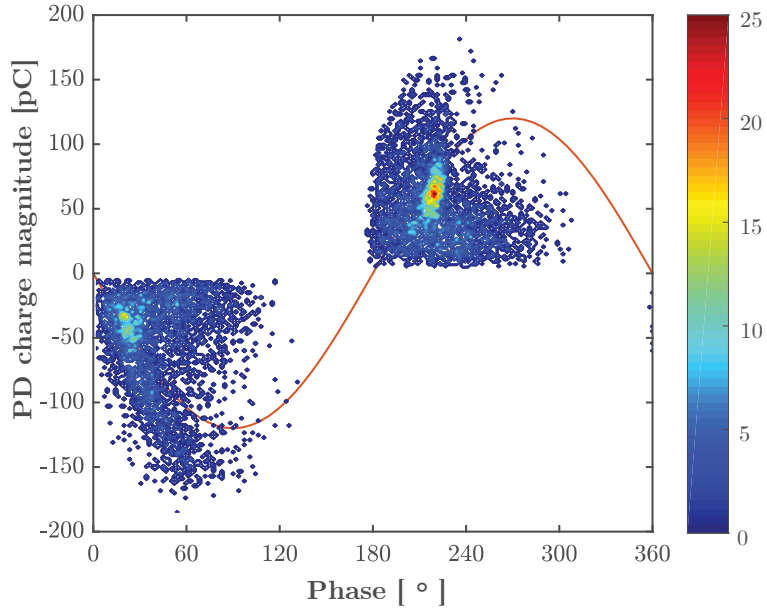

(b) PEEK–PEEK #500 at 1.16 MPa

Figure A.25: PRPD patterns at the interfaces with respect to applied 50 Hz AC voltage. Color bars represent n_{PD}.

On the other hand, higher PDIE value in the case of XLPE–XLPE #500 at 1.16 MPa leads to more scattered PD patterns along the entire voltage phase, especially close to the phases of 0° and 180°. Based on the correlation between PD pattern and source illustrated in the second row in Figure A.24, the expansion of the discharge activity seems to be limited by the increased number of isolated cavities or shorter air-gaps/channels. In the case of PEEK–PEEK #500 at 1.16 MPa, the shape of the PRPD shown in Figure A.25(b) is similar to that of the XLPE–XLPE #500 at 1.16 MPa except for the magnitude of the n_{PD} in accordance with the phase distributions displayed in Figure 9.3.

A.3.1.2 Results using Partial Sequential Analysis Method

In this section, the PSA technique is used to find out the sequence of the PDs at the interface.

Figure A.26 shows PSA patterns by utilizing the voltage U and time t difference between successive discharges occurring at the interface for XLPE and PEEK. For instance, $\Delta(n-1)$, $\Delta(n)$, and $\Delta(n+1)$ are the applied voltage magnitude of previous $U(n-1)$, current $U(n)$, and the next $U(n+1)$ PD occurrences, respectively. A large magnitude of $\Delta(n)$ and $\Delta(n-1)$ indicates that successive PDs take place at the opposite polarity. On the other hand, small magnitudes of $\Delta(n)$ and $\Delta(n-1)$ hints that consecutive PDs occur at the same polarity. The same interpretation is also valid for PSA time plots.

As seen in Figure A.26 at 1.16 MPa, PSA voltage clusters tend to occupy a larger area in the case of PEEK compared to XLPE. Additionally, the increase in pressure leads to an additional increase in the area of PD voltage clusters. The PSA results indicate that in the case of XLPE, the time difference between successive PDs is longer. This means that the expected number of PDs per cycle is lower, which can be seen in the statistical analysis of the PRPD patterns in Figure 9.3(a). Similarly, increased area of PSA patterns in Figure A.26(f) compared to that in Figure A.26(d), can also be explained using the same argument, that is further supported by the PRPD Figure 9.3(a).

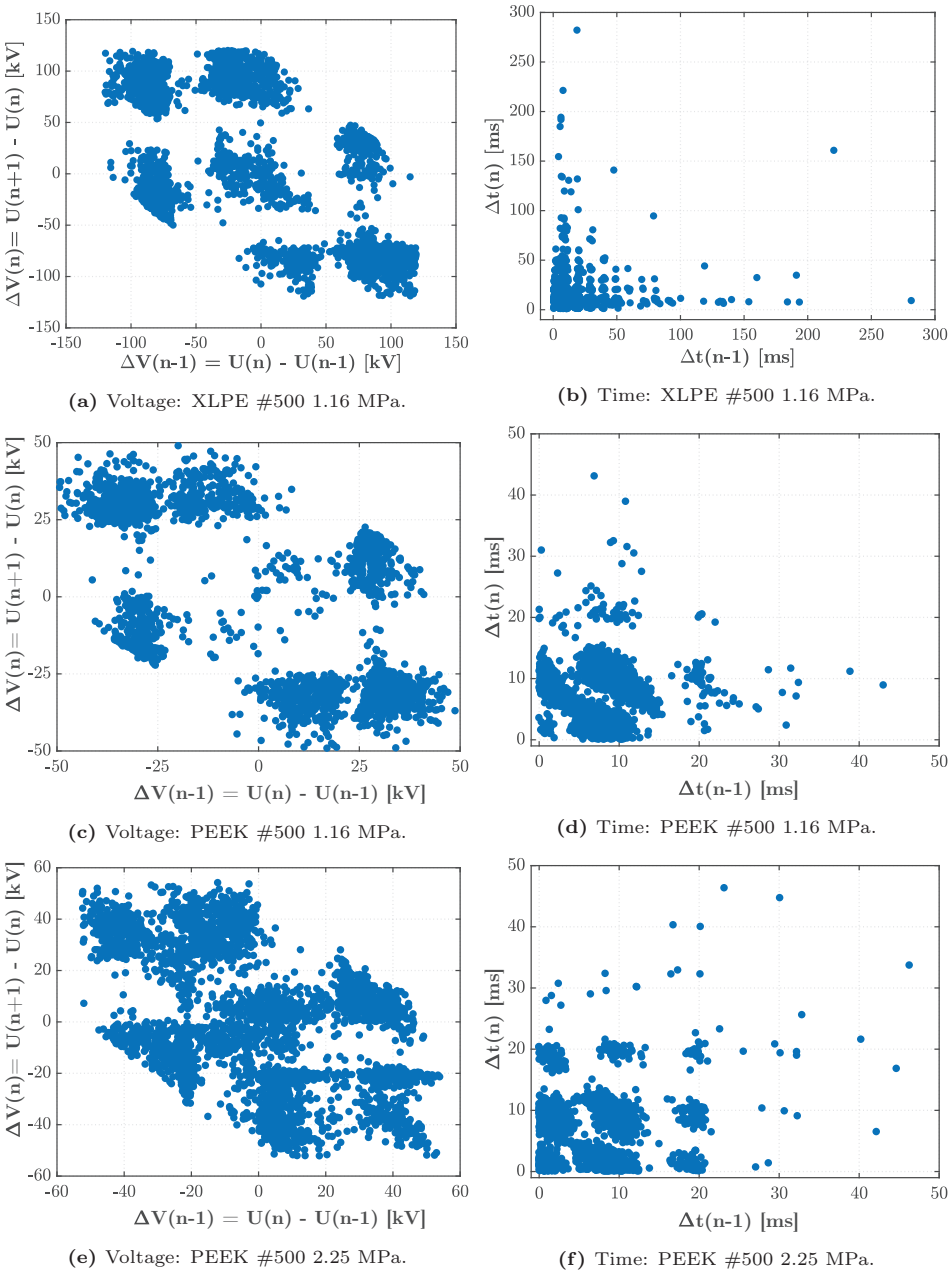

(a) Voltage: XLPE #500 1.16 MPa.

(b) Time: XLPE #500 1.16 MPa.

(c) Voltage: PEEK #500 1.16 MPa.

(d) Time: PEEK #500 1.16 MPa.

(e) Voltage: PEEK #500 2.25 MPa.

(f) Time: PEEK #500 2.25 MPa.

Figure A.26: PSA voltage and time difference patterns of interface discharge.

A.3.2 Polymer–Glass Interfaces

Using the experimental setup shown in Figure 6.7, discharge data were also acquired to correlate the discharge images with the quantitative discharge magnitudes, number of PDs, and their phase distributions. However, it is of vital importance to isolate each PD source to ensure a fair correlation between the discharge images and the PRPD data. There is an exclusive feature called 3FREQ mode in the Omicron GUI that requires an additional license. In the 3FREQ mode, three-cascaded band-pass filters with three different center frequencies with specific bandwidths are used, as depicted in Figure A.27(a). The resulting PD patterns are displayed in a 3D frequency domain, as illustrated in Figure A.27(c). If a specific area is not selected in the 3D frequency domain, all detected discharges are plotted (see Figure A.27(b)). On the other hand, when there are distinct patterns discernible in the 3D frequency domain, any area can be singled out by drawing an enclosed geometrical shape using the mouse pointer. When a specific area is selected, the recorded PD data must be replayed in the GUI, which then plots only the discharges taking place in the frequency bandwidth within the specified geometrical shape. Thus, each PD source can be isolated, and discharges solely generated by interfacial cavities can be extracted.

The PD pattern in Figure A.27(f) indicates that the source of PD can be either corona/external disturbance or surface discharges since the discharge dots clustered symmetrically around the peak voltage values [23]. Due to the presence of the metallic parts in the test setup, which were not submerged in the oil despite being electrically grounded (see Figure F.3), the possibility of corona noise cannot be ruled out. The imperfect contact between the electrodes and the glass sample, due to the glass being very hard, could also be the PD source. Nevertheless, with the proper selection of the bandwidth, these PD sources could be separated, and the useful information of the cavity discharge was extracted. When there was no PD occurring at the interfacial cavities, only surface discharges or corona were present in the PRPD diagram, as delineated in Figure A.27(f).

In addition to results from the discharge-monitoring tests shown in Chapter 10, glass–PEEK #500 interfaces where PEEK samples with the main cavity (1-mm artificial cavity) and without the main cavity are compared at 1.67 MPa to show the effect of the main cavity on the PD results in Figures A.28 and A.29. As seen in the phase distributions and the histograms, n_{PD} is significantly higher in the case at which the PEEK has the artificial cavity. The PDIV values and the recorded charge magnitudes are also provided in Figures A.28(d) and A.28(e).

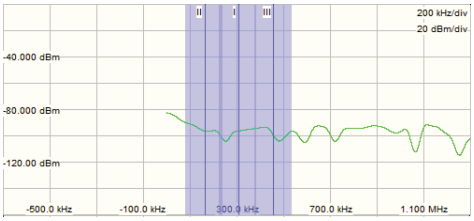

(a) Selected three-cascaded band-pass filters.

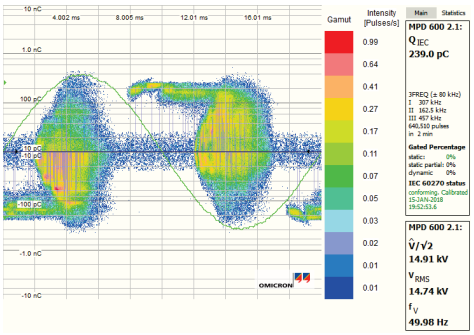

(b) PRPD pattern including all the PD sources.

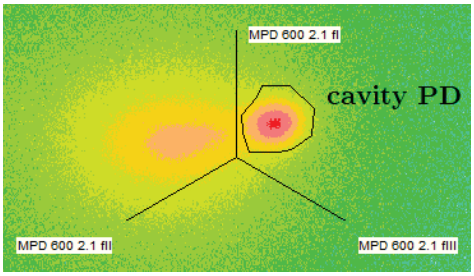

(c) Cavity PD in 3D in the frequency domain.

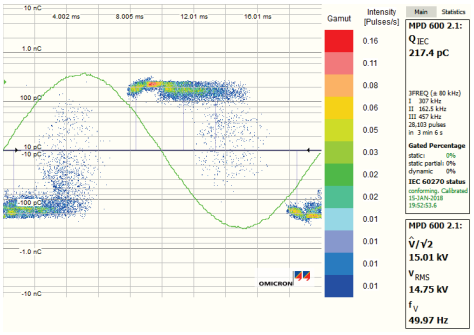

(d) Cavity PD in 2D.

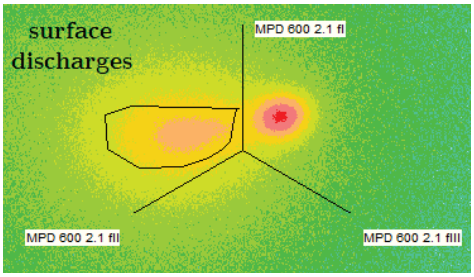

(e) PD related to surface discharges in 3D.

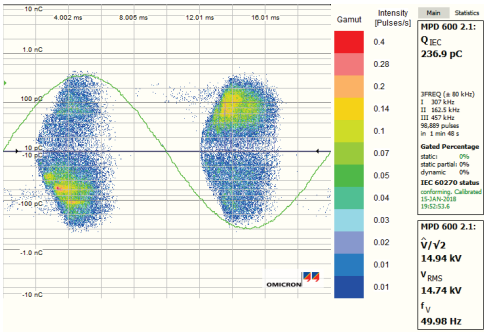

(f) PD related to surface discharges in 2D.

Figure A.27: PD patterns generated by different PD sources in the discharge-monitoring experiments. Three center frequencies for the PD filters are $f_{\mathrm{I}} = 307$ kHz, $f_{\mathrm{II}} = 162.5$ kHz, $f_{\mathrm{III}} = 457$ kHz. PD filter bandwidth = 160 kHz.

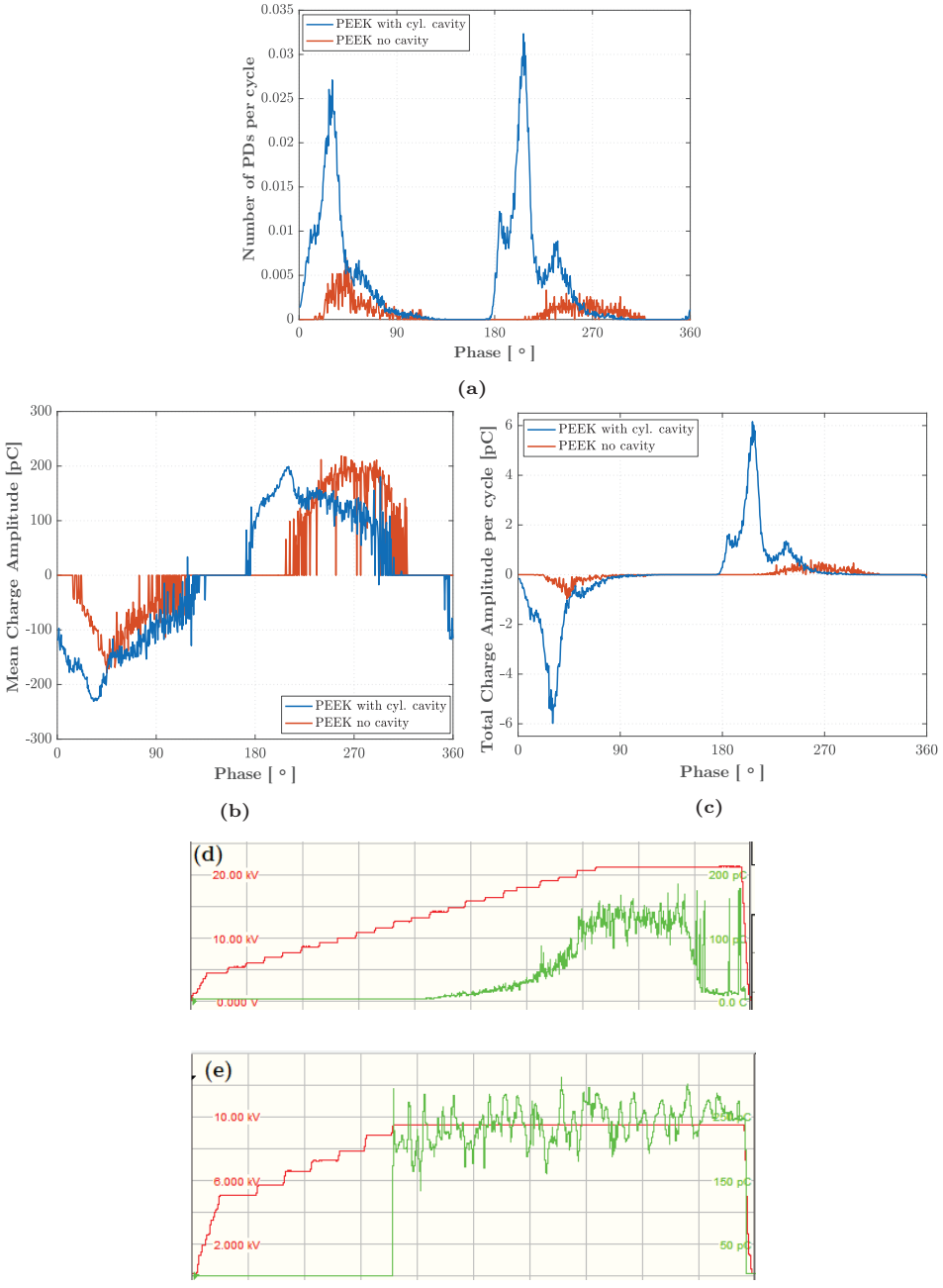

Figure A.28: Results of PD experiments of glass–PEEK #500 at 1.67 MPa with the cylindrical cavity as shown in Figure 6.10 as opposed to the same interface without the cylindrical cavity. (a) Number of PDs per cycle vs. phase angle. (b) Mean charge amplitude vs phase angle. (c) Total charge amplitude per cycle vs. phase angle. Applied ramp AC voltage vs. charge magnitude. (d) PEEK without the main cavity. (e) PEEK with the cavity.

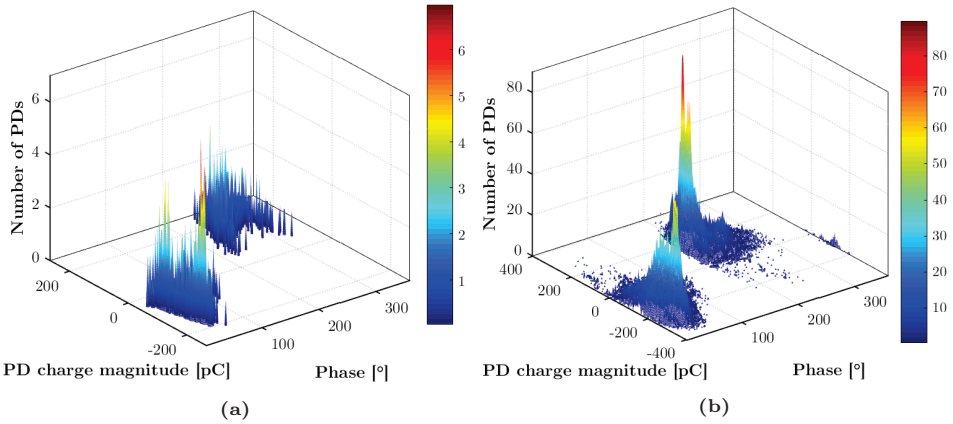

Figure A.29: $\phi - q_a - n_{PD}$ of PEEK #500–glass at 1.67 MPa. (a) Without the cylindrical cavity. (b) With the cylindrical cavity.

A.4 Raw data of Discharge-Monitoring Experiments

In this section, the additional results from the discharge-monitoring experiments are shown.

A.4.1 Long-term Discharge Experiments

The results of a discharge experiment run for 48 hours are shown in this section. The main reason why the results are provided here is that they were obtained after a long-term experiment, and they are not directly answer the research questions because the research questions are primarily seeking answers for the momentary mechanisms of interfacial breakdown, not degradation of the interface over time. However, still, the following results are interesting and give some clues on the amount of heat energy released during interfacial discharges.

Figure A.30 demonstrates the images of a PEEK #500 sample exposed to the discharged artificial cavity for 48 hours. Viscous sediments were observed to be developed at the surface of the glass in a tree-like structure over time, as shown in Figure A.30. This viscous material is presumably melted PEEK under the high temperature of glow discharge, which adhered to the glass surface. To check if the temperature around the discharged main cavity is sufficiently high to cause the melting of the PEEK sample, the following study is referred to.

Nagao et al. [156] worked on estimating the local Joule heating in polyethylene films. They detected high-temperature points before the electrical breakdown at room temperature and reported that the breakdown occurred at the point of

the highest temperature. The concurrence of the breakdown point and the Joule heating point suggests that a thermal process is involved in the electrical breakdown of polymers at room temperature. Consequently, the local electro-thermal deformation is supposed to contribute to the electrical breakdown of polymers [156]. Therefore, if the high-temperature points around the main cavity reached to very high values over time due to the persistent discharges in the main cavity, it would be likely that the contacting area in PEEK, subjected to glow discharge for a long time, melted and grew in a tree-like structure. The melting temperature of PEEK is around 340 °C [123]. The imperfections on the glass surface in Figure 10.10(b) might be the molten, viscous PEEK, which then solidified after the experiment was stopped and temperature decreased.

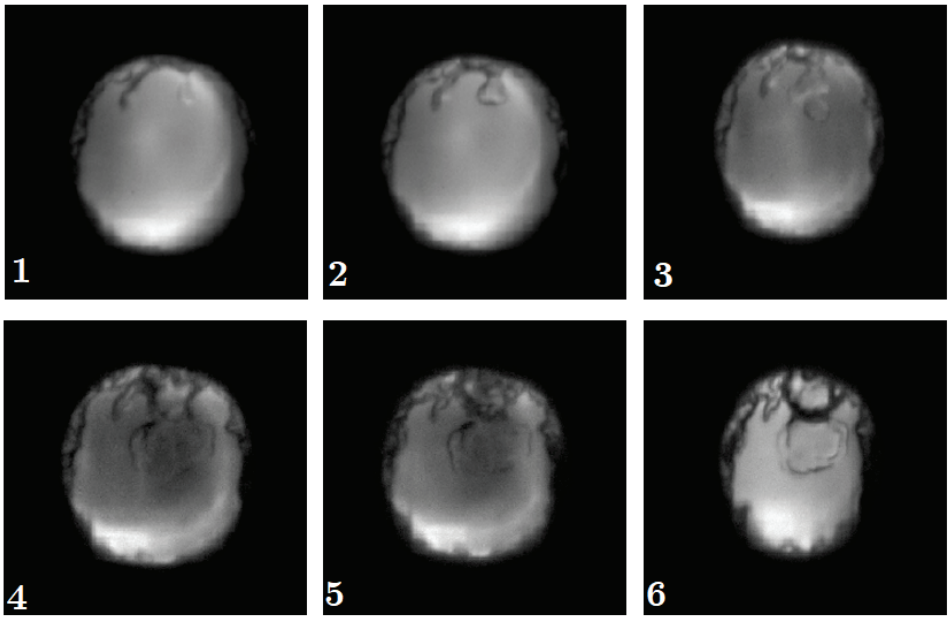

Figure A.30: Formation of tree-like sediments at the interface during a 48-hour discharge testing acquired by using the CCD camera. Each image represent the condition of the interface every eight hours.

A.4.2 Histogram of Emitted Light in Discharge-Monitoring Experiments

Figure A.31 shows the histogram of the emitted light represented by number of pixels at three different events:

i. no discharge observed either in the main cavity (1-mm-cylindrical cavity) or anywhere at the interface;
ii. discharge activity limited solely to the main cavity; and
iii. increased non-homogeneous field caused by the discharged main cavity, resulting in glow discharge streamers spreading to the interface.

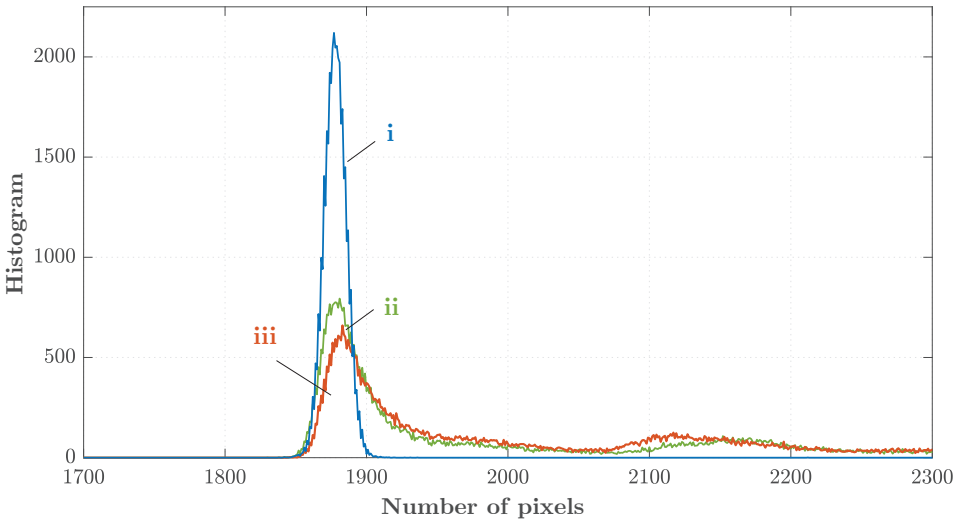

Figure A.31: Histogram of emitted discharge light in terms of number of pixels: (a) No discharge. (b) Discharge in the main cavity only. (c) Simultaneous discharges in the main cavity and in glow discharge filaments from the main cavity towards the electrodes.

Appendix B

Field Simulation Results by Finite Element Analysis

In this chapter, electric field simulations performed for rough solid-solid interfaces are shown. First, field enhancements in voids with defined geometries are provided. Second, simulations for rough XLPE–XLPE #500 interfaces are performed in the cases of air-, water-, and oil-filled voids.

B.1 Field Strength in Air-filled Cavities of Defined Geometries

The test setup used for the AC breakdown and PD experiments was modeled in COMSOL Multiphysics® [157] using the real dimensions of the components. Electric field distributions at interfaces were then simulated using Finite Element Analysis (FEA). Figure B.1 depicts the electrodes and the samples placed on top of each other as well as the simulated normal and tangential field distributions. The simulated field lines verify the homogeneous electric field generated by the selected Rogowski-electrodes in the absence of any imperfections at the interface.

Figures B.4 and B.5 show the electric fields at an XLPE–XLPE interface containing air-filled voids with different geometric shapes such as ellipsoidal (horizontal or vertical according to the tangential field), cylindrical/disk (horizontal or vertical according to the tangential field), triangular and spherical voids. Note that only the voids are fitted in the surface plots (top figures) whereas field distributions are adjusted so that the entire interface (4-mm) is visible in all cases. Therefore, the edges of the distorted fields correspond to the edges of the cavities in each case. In the simulations, to facilitate the calculation of the field intensifications, the electric stress in the bulk insulation is adjusted to be 1 kV/mm by applying 4 kV AC voltage between the electrodes. The most severe field intensification, which is greater than 2, takes place in the cases of vertical ellipsoids or disks.

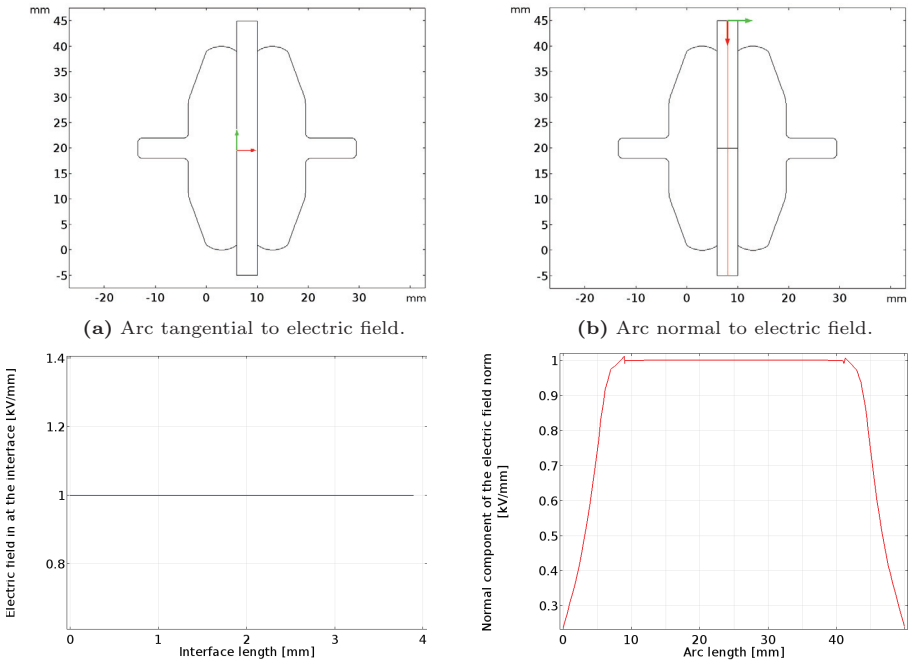

(a) Arc tangential to electric field.

(b) Arc normal to electric field.

(c) Electric field in the tangential direction.

(d) Electric field in the normal direction.

Figure B.1: 2D COMSOL Multiphysics® simulation of a solid-solid interface placed between two Rogowski electrodes. All the dimensions are set in real size. 4 kV AC voltage is applied between the electrodes, resulting in an electric stress of 1 kV/mm at the 4-mm interface.

Spheroidal cavities are categorized as oblate or prolate based on the ratio of tangential length (a) to the perpendicular length (b) with respect to a reference plane. Figure B.3 displays the shape factor γ introduced in Equation (4.3) versus the ratio of a/b where applied field is parallel to a-axis. In the next section, the real surface texture of the XLPE–XLPE #500 is studied to estimate the field intensifications occurring in the air-filled voids.

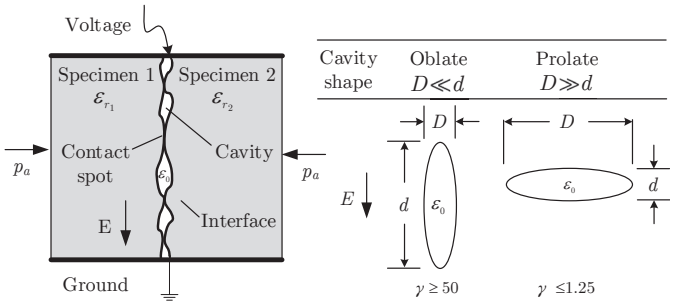

Figure B.2: The field enhancement factor f based on the shape of the air-filled cavities. Figure B.3 provides γ values as a function of the axis ratio d/D. (p_a: Contact pressure). Oblate and prolate are defined with respect to the electric field direction.

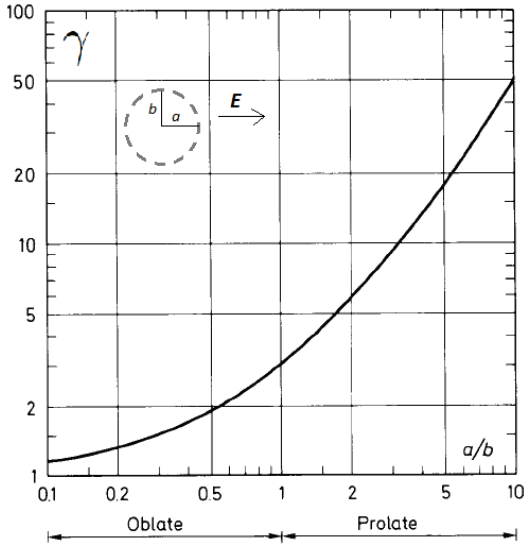

Figure B.3: Variation of the shape factor γ in Equation (4.3) versus the ratio of axes (a/b) for spheroids (ellipsoids). The applied field is parallel to a-axis [99].

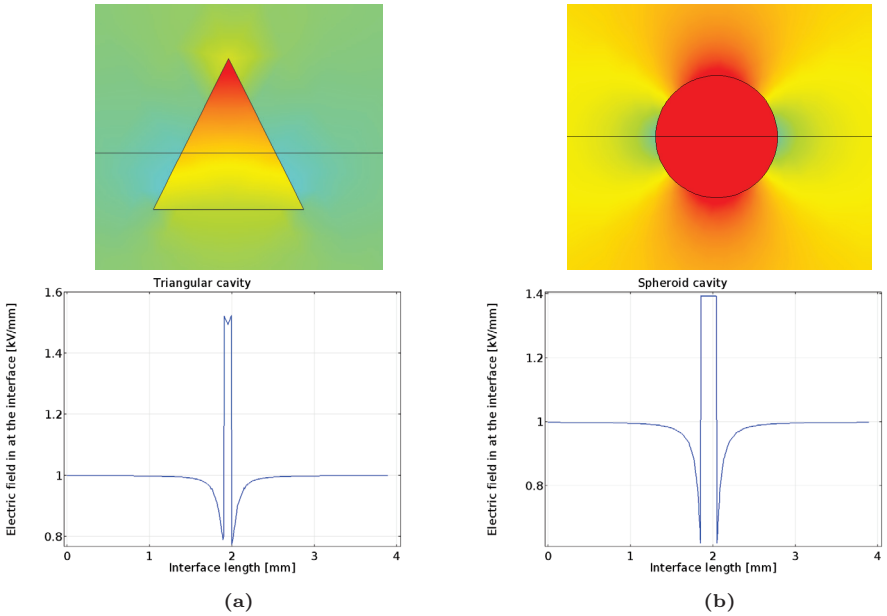

(a) (b)

Figure B.4: Simulated field distribution at an XLPE–XLPE interface with air-filled cavities of various shapes: (a) Triangular cavity with 1-mm side lengths. (b) Spherical cavity with a radius of 0.1 mm. (Surface plots on top and line graphs at the bottom are not to-the-scale).

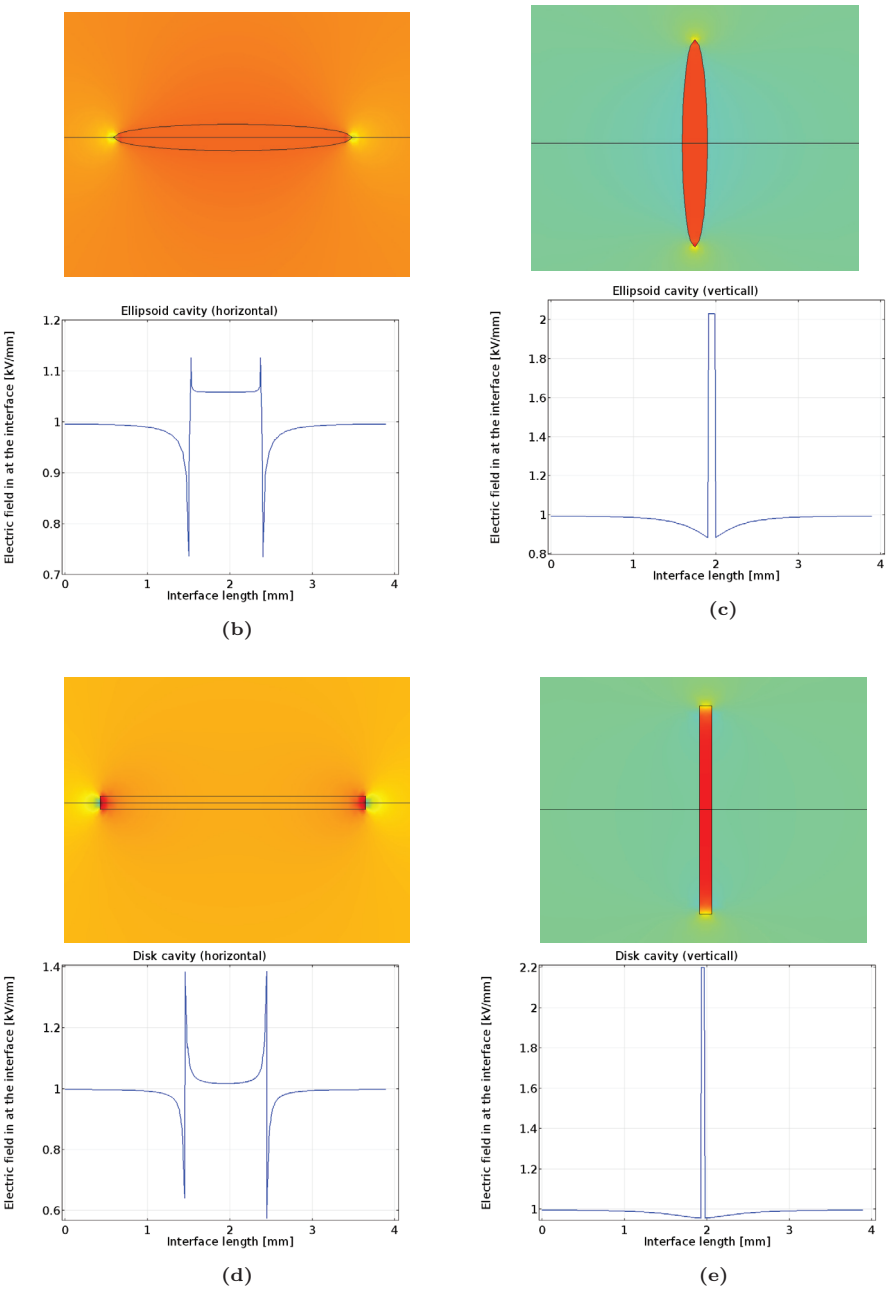

Figure B.5: Simulated field distribution at an XLPE–XLPE interface with air-filled cavities of various shapes: (a) Horizontal ellipsoidal cavity $a = 0.5$ mm, $b = 0.05$ mm. (b) Vertical ellipsoidal cavity $a = 0.05$ mm, $b = 0.5$ mm. (c) Horizontal disk/cylindrical cavity length = 1 mm, width = 0.1 mm. (d) Vertical disk/cylindrical cavity length = 0.1 mm, width = 1 mm. (Surface plots on top and line graphs at the bottom are not to-the-scale).

B.2 Field Strength in Air-filled Cavities at Rough XLPE–XLPE Interfaces

Similarly, FEA is used to simulate electric field distribution at dry-, wet-, and oil-mate XLPE–XLPE interfaces covered in real experiments. The rough surface profile of the sum surface in 2D is exported to COMSOL Multiphysics® and is defined as an enclosed geometry. As the scanned surface was about 1.25 mm, the rough surface constitutes a fraction of the 4-mm interface, the rest of which is perfectly/ideally smooth. Figure B.6 shows a part of the exported, equivalently rough surface in 2D whereas Figure B.8 displays the electric stress at the 4-mm interface. The top sample contains the imported, equivalently rough, real sum surface data. In Figure B.7, the electric field at the part free of cavities is undisrupted and homogeneous at 5 kV/mm while field spikes stand for the intensified field in the air-filled microcavities. It should be noted that the cavities in Figure B.6 are elongated in the $x-$axis in 1:1 aspect ratio, yielding a mean enhancement factor, f, around 1.3.

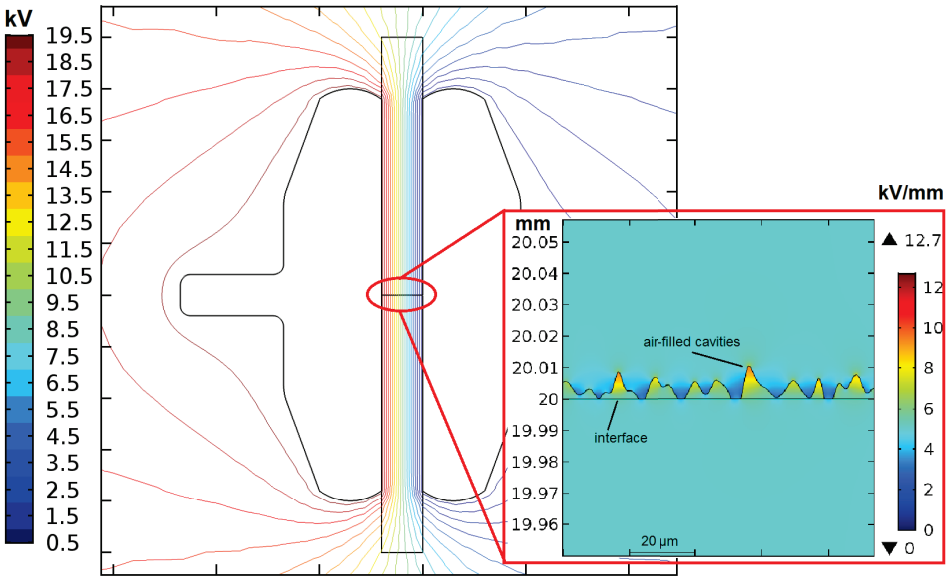

Figure B.6: FEM simulation result of the test setup used in AC breakdown and PD experiments.

The theoretical calculations using Equation (4.3) lead to an field enhancement factor of $f \simeq 1.23$ in an air-filled spherical cavity ($\gamma = 3$ for spherical cavities in Figure B.3) at the XLPE–XLPE interface, where the relative permittivity of XLPE is $\varepsilon_r = 2.3$. For a cavity much larger in the tangential direction, on the other hand, $\gamma \geq 50$ yields $f \approx 1$ (see Figure B.3).

The simulation results are thus consistent with these theoretical calculations such that the field enhancement takes place at the edges of the air-filled cavities with a factor around 1.3 in the micro-cavities whereas the enhancement is negligibly small inside a cylindrical cavity, as depicted in Figures B.6 and B.7. These findings validate the assumption of spherical asperity tips, introduced in Chapter 3.

Likewise, simulations are run for water- and oil-filled cavities in COMSOL Multiphysics® by defining water and oil as the dielectric media filling the cavities, respectively. $\varepsilon_r = 80.1$ is used for water whereas $\varepsilon_r = 3.8$ is assigned for Midel ester oil [125]. Figure B.8 depicts line graphs for field distributions only at the part containing the imported rough surface data for all three cases with the illustration of the surface plots at the interface. As seen in Figure B.8(c), the stress at the contact spots near the edges of the short-circuited cavities are enhanced by a factor of more than 30. On the other hand, the field enhancements in the case of oil-filled cavities are comparable with those in the case of air-filled cavities. It should be noted that the field enhancements take place at the edges of the air-filled cavities whereas they occur at the edges of the oil-filled cavities, i.e., at the contact area surrounding the cavities. Since the relative permittivity of the oil is higher than that of the XLPE, the enhancements occurred in the spots in the case of oil-filled cavities while the opposite occurs in the case of air-filled cavities.

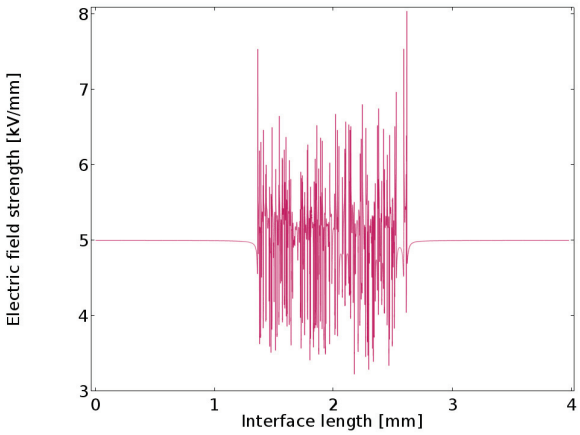

Figure B.7: Simulation of field distribution at a rough interface in air-filled cavities.

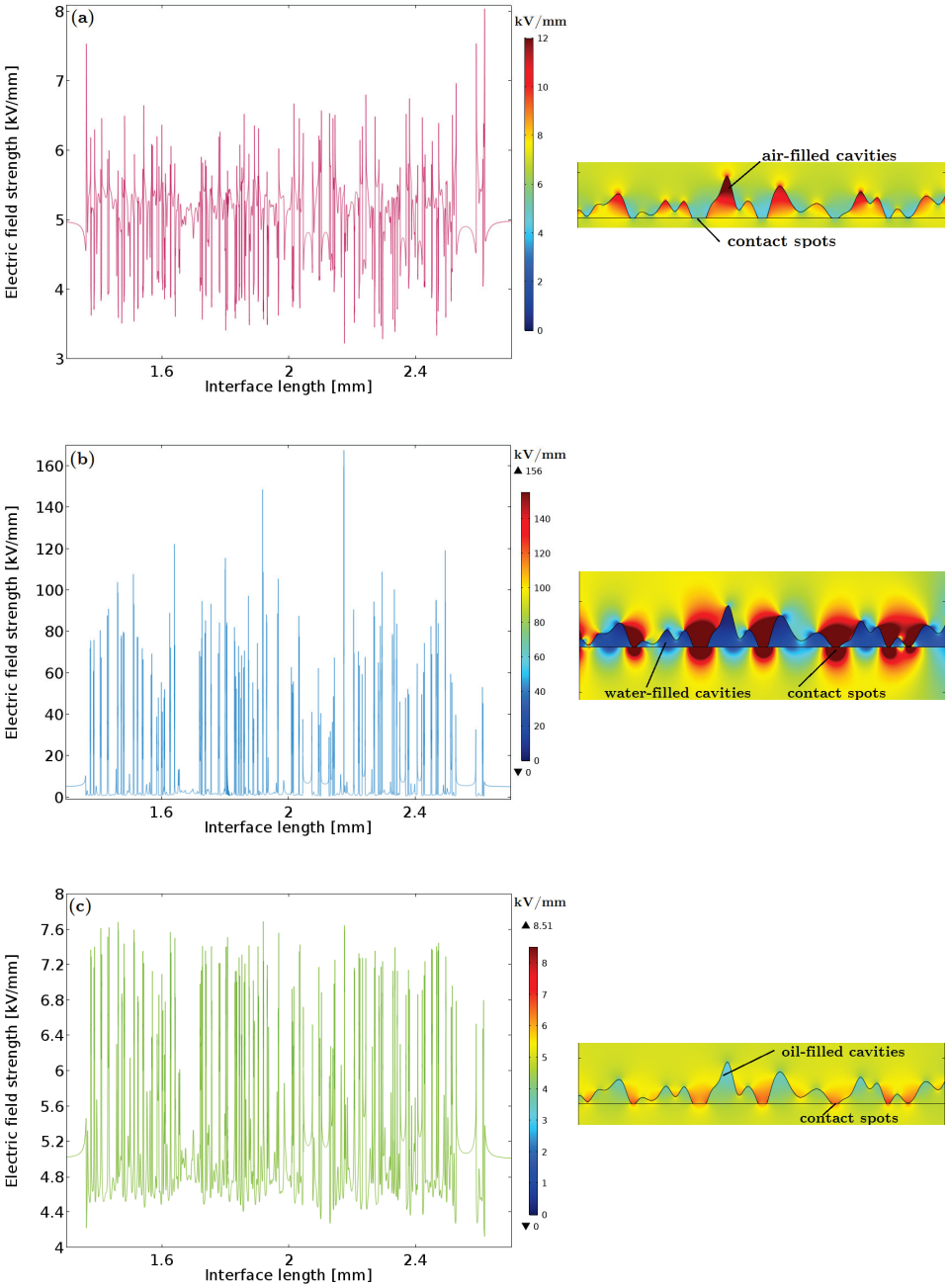

Figure B.8: Simulation of field distribution at a rough XLPE–XLPE interface in the case of: (a) Air-filled cavities. (b) Water-filled cavities. (c) Oil-filled cavities. Color bars stand for the electric field strength in the surface plots shown to the right-hand side.

Appendix C

Additional Results from Deterministic Model

This appendix chapter presents several filled-contour plots and scatter plots obtained using the deterministic model to provide supplementary information on the type of the deformation (i.e., elastic, elasto-plastic, and plastic deformation) taking place at the interface as a function of elasticity, surface roughness, and contact pressure.

C.1 Contour Plots

Contour plots in this chapter represent the amplitudes of the asperities and area of cavities and contact spots at the interface. To increase readability, different levels are colored using color maps where red indicates the highest peak and white indicates the zero level. Contour lines are extracted from the intersection of the surfaces with horizontal planes at different heights, as illustrated in Figure 5.2(a).

Figures C.1–C.4 display the discretized 3D surface data from the obtained profiles as shown in Figure 7.5. Projections of the asperity amplitudes on a 2D plane are also mapped using contour plots. With the help of color bars next to the contour plots, the amplitudes of the peaks are quantitatively displayed where red represents the highest peak, and light yellow/white represents the contact points.

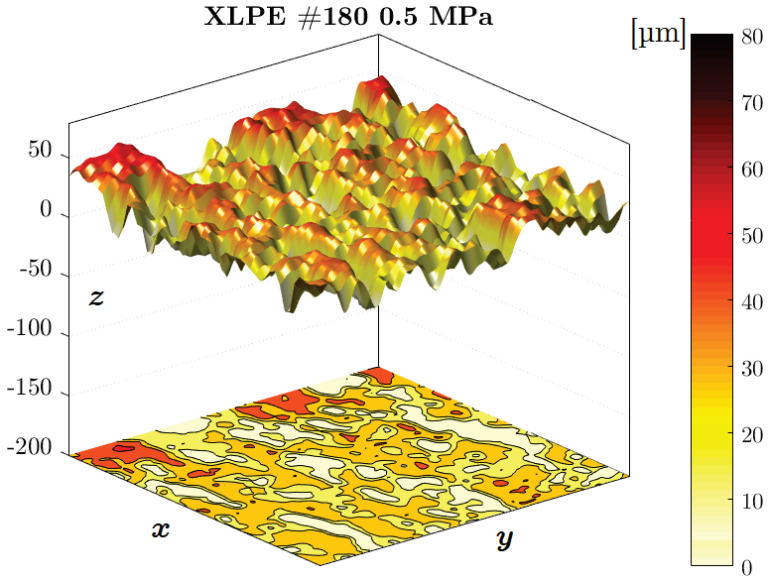

(a)

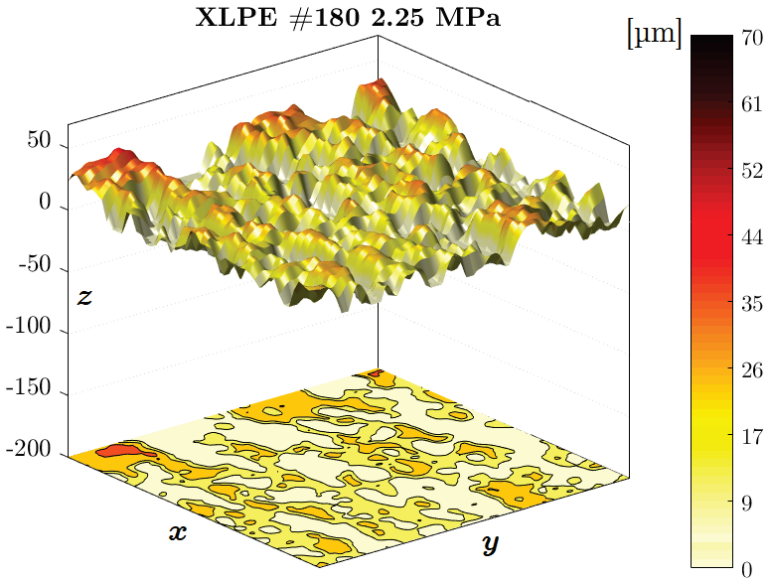

(b)

Figure C.1: Surface plot of XLPE #180 with filled-contour plot of the projection of the 3D surface on a 2D surface at: (a) 0.5 MPa. (b) 2.25 MPa.

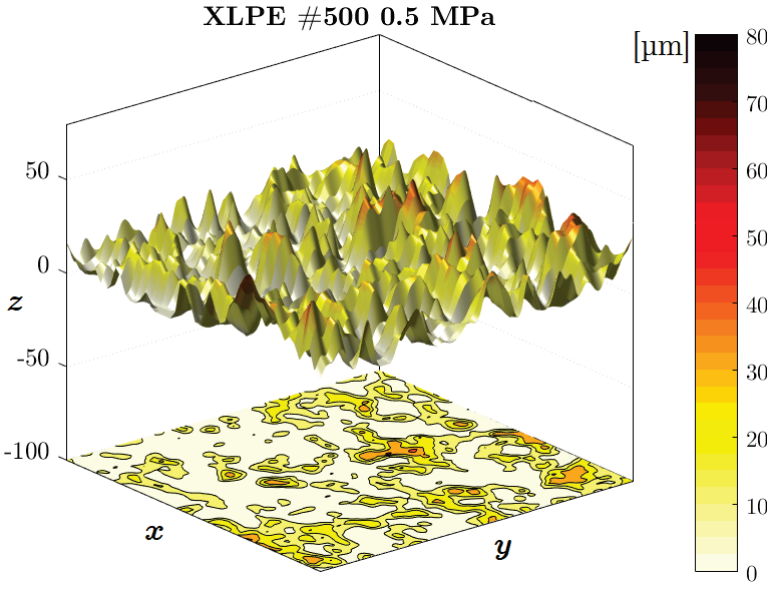

(a)

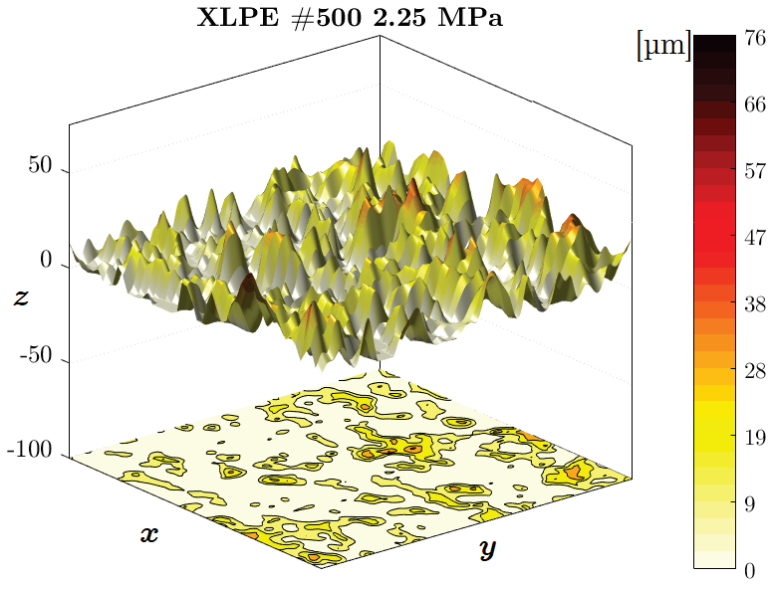

(b)

Figure C.2: Surface plot of XLPE with filled-contour plot of the projection of the 3D surface on a 2D surface at: (a) 0.5 MPa. (b) 2.25 MPa.

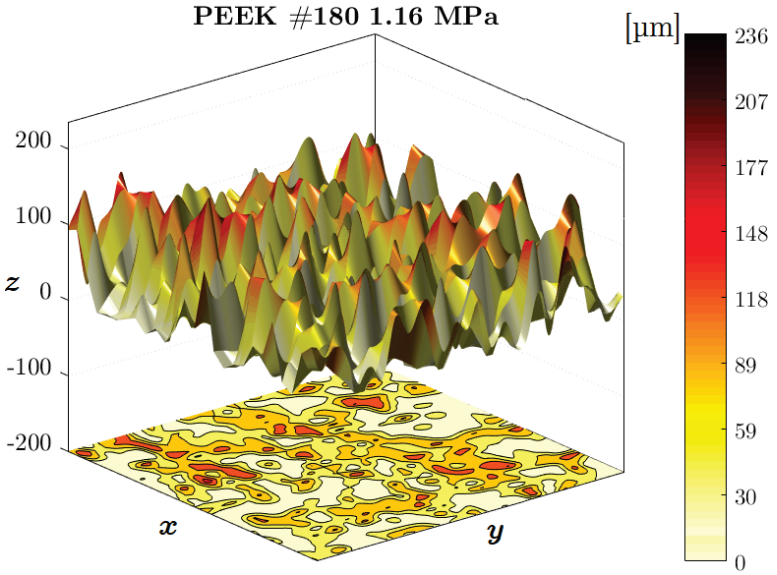

(a)

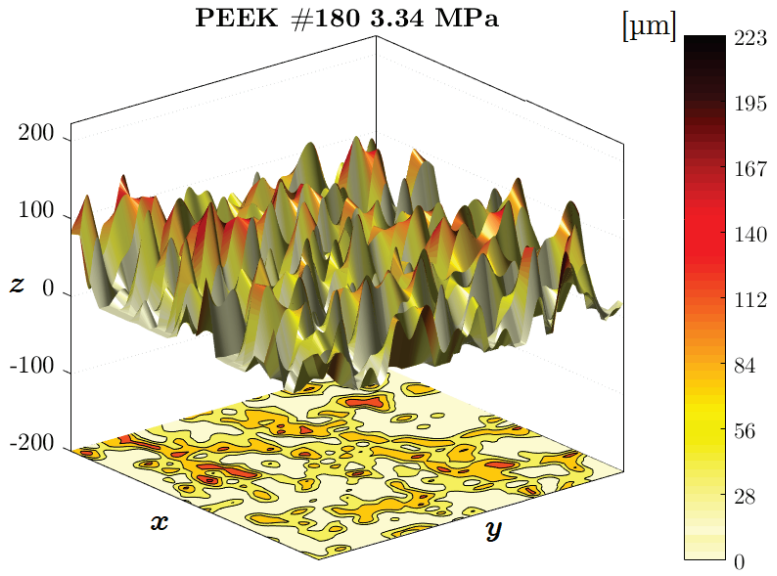

(b)

Figure C.3: Surface plot of PEEK #180 with filled-contour plot of the projection of the 3D surface on a 2D surface at: (a) 1.16 MPa. (b) 3.34 MPa.

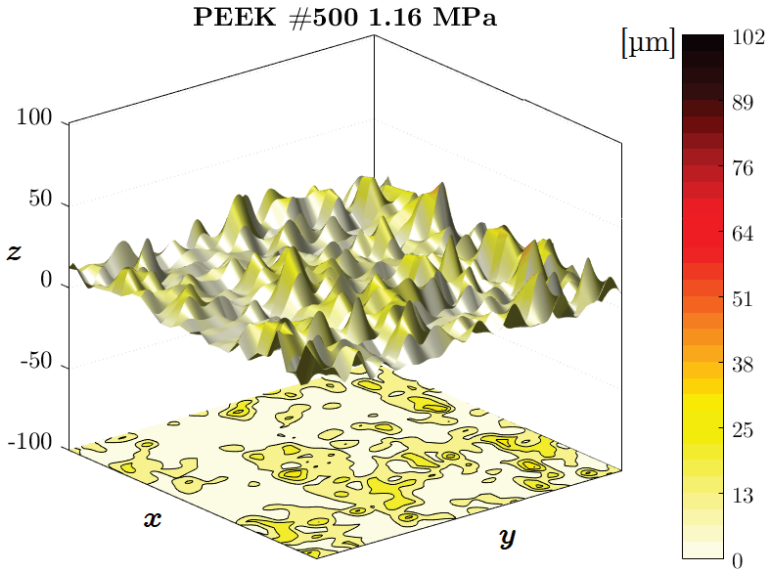

(a)

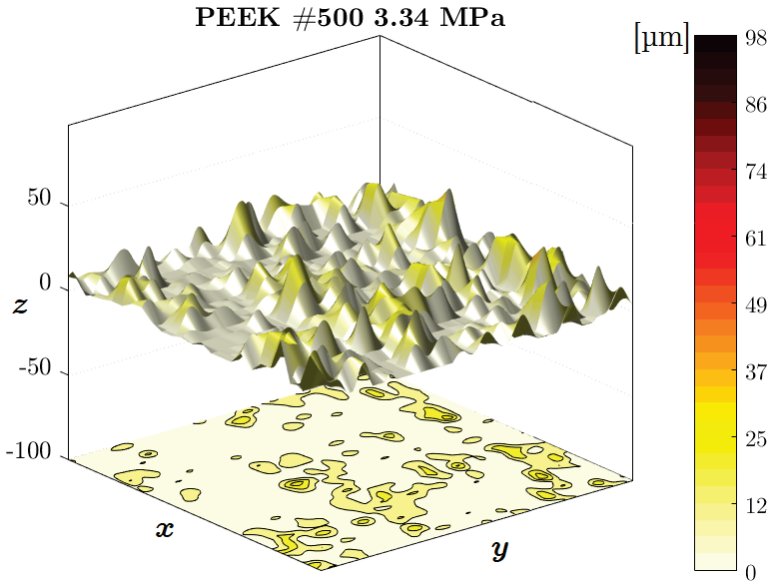

(b)

Figure C.4: Surface plot of PEEK #500 with filled-contour plot of the projection of the 3D surface on a 2D surface at: (a) 1.16 MPa. (b) 3.34 MPa.

C.2 Scatter Plots

The pressure distribution at the contact surface is illustrated in Figure 2.8(b) in 2D. In this section, pressure distributions at the contact surfaces of the XLPE and PEEK samples at two different pressures are shown in 3D plots in order to gain a clear understanding of elastic and plastic deformations. Each spherical marker represents the contact pressure at the shown position. If the contact is elastic, then the contact pressure will lie between zero and the hardness of the material. On the other hand, in the case of a plastic contact, the pressure value will settle at the hardness of the material, and the contact area does not increase any further, irrespective of the applied force.

Figures C.5–C.8 display the pressure distribution at the contacting areas of the XLPE samples with different surface roughnesses. As seen in the plots, at some contact spots, plastic deformation takes place which is equal to the hardness of XLPE. The hardness of the XLPE according to the manufacturer data sheet is $H = 11.2$ MPa.

Similarly, Figures C.9–C.10 shows the deformation of the asperities at the PEEK surface. The hardness of the PEEK according to the manufacturer data sheet is $H = 17.9$ MPa.

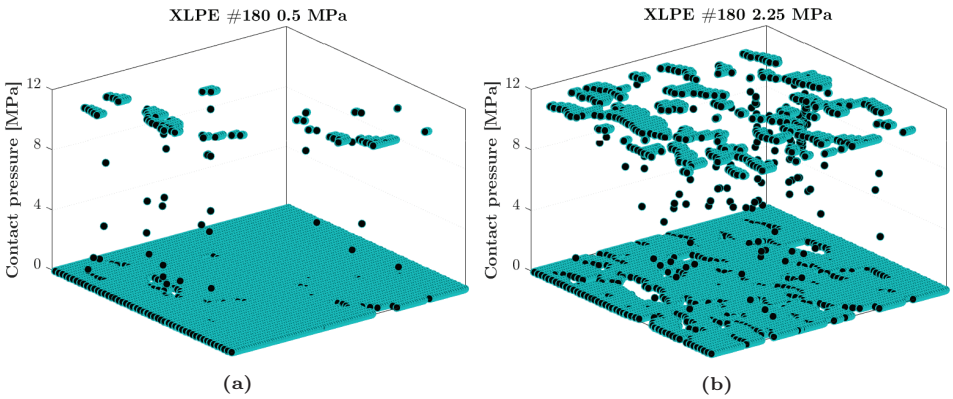

Figure C.5: Surface plot of XLPE #180 at 0.5–2.25 MPa.

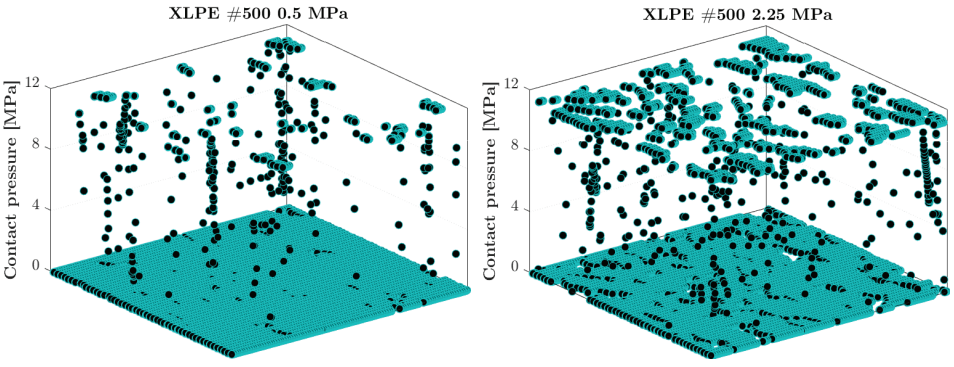

Figure C.6: Surface plot of XLPE #500 at 0.5–2.25 MPa.

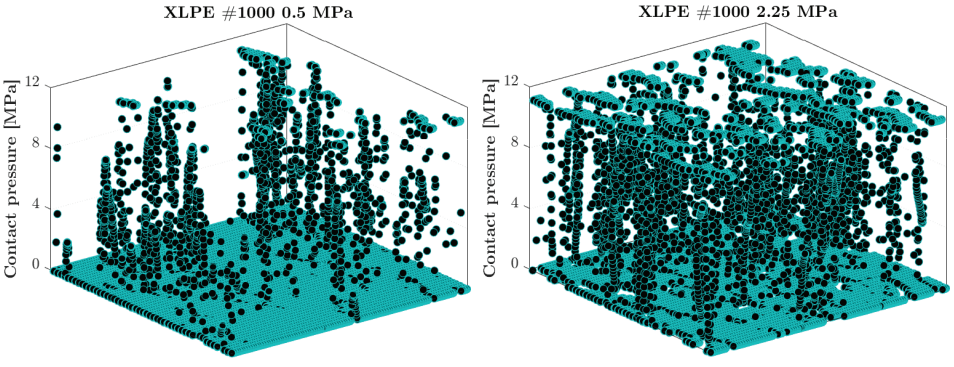

Figure C.7: Surface plot of XLPE #500 at 0.5–2.25 MPa.

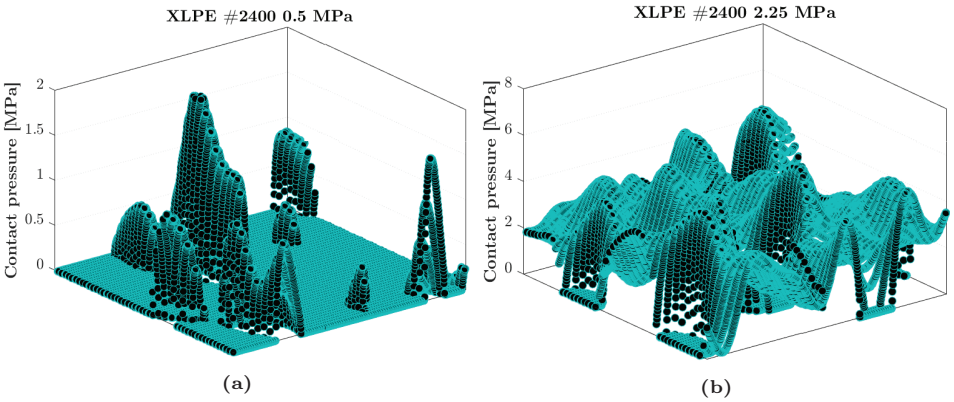

Figure C.8: Surface plot of XLPE #2400 at 0.5–2.25 MPa.

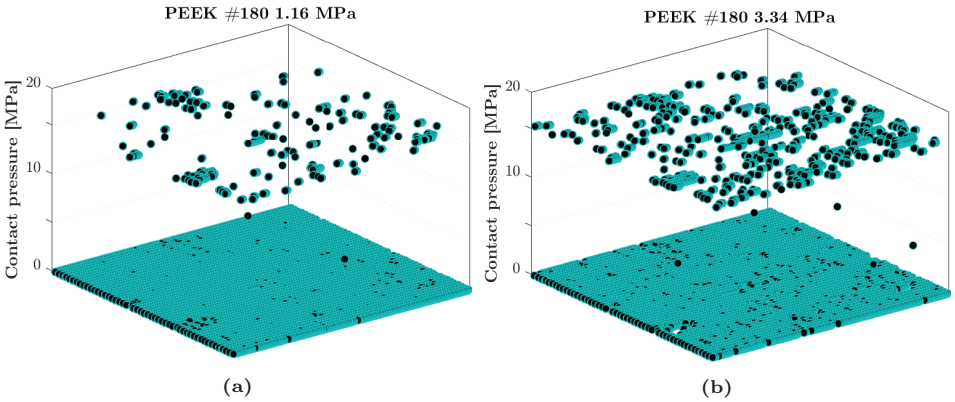

Figure C.9: Surface plot of PEEK #180 at 1.16–3.34 MPa.

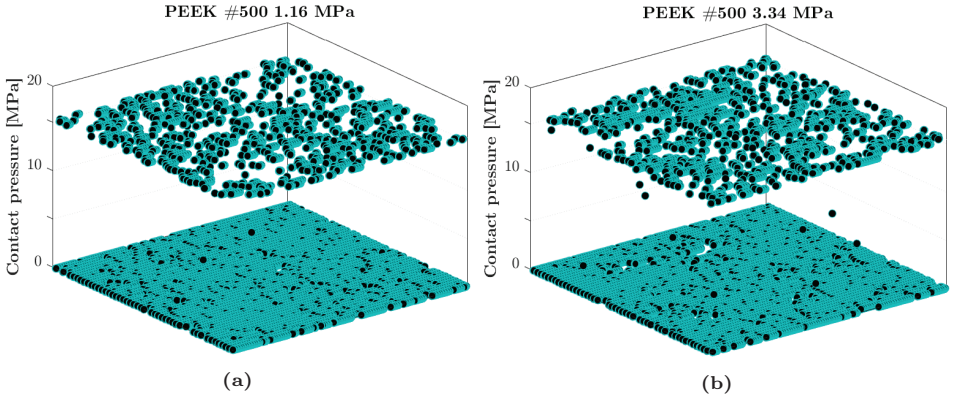

Figure C.10: Surface plot of PEEK #500 at 1.16–3.34 MPa.

Appendix D

Additional Details on Experimental Methodology

In this appendix section, details on the polymer casting, measurement techniques for elastic modulus, surface roughness characterization, which were referred to in the main body of the thesis, are provided.

D.1 Polymer Casting

In this section, casting SiR and epoxy resin are described. The methodology for the SiR casting is presented in detail whereas only the basic information is given for the casting of epoxy resin. Detailed casting and post-curing information for the epoxy is provided in [122].

D.1.1 Silicone Rubber

The silicone rubber (SiR) samples are cast in the laboratory using a mixture composed of two viscous components. The two components (A and B) are transparent and look identical. The mixture is prepared using equal quantities from A and B, by utilizing an electronic scale for precision. It is crucial to have dust- and dirt-free tools when casting. Therefore, all the tools are cleaned with isopropanol and polyester/cellulose blend cleanroom wipers prior to casting.

In order to effectively mix the two components, a rotating stirrer made from PTFE is used.[27] A hole is drilled to avoid the mechanical strain of the rotating equipment (see Figure D.2(a)). The mixing takes place under vacuum to minimize the formation of air bubbles in the mixture (see Figure D.2(b)). The process of mixing process takes about 3 hours in room temperature. Although stirring at a

[27] Polytetrafluoroethylene.

higher temperature eases the mixing by reducing the viscosity of the silicone, it might initiate a premature curing process.

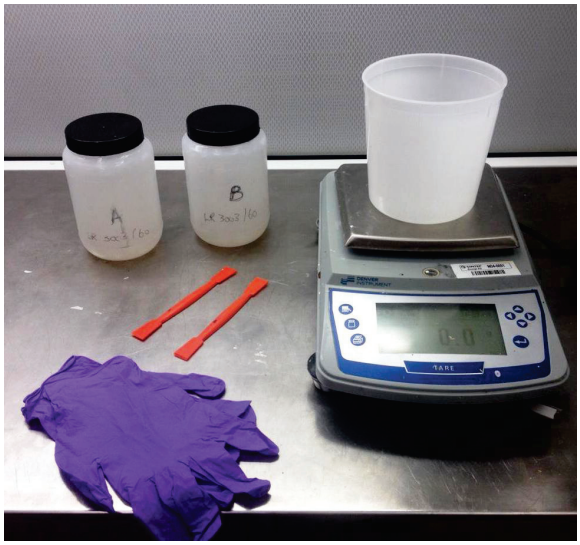

Figure D.1: Viscous silicone components A and B mixed in equal quantities using a sensitive electronic scale [158].

(a) **(b)**

Figure D.2: (a) PTFE stirrer. (b) The silicone rubber components, A and B, are mixed in a vacuum chamber [158].

A steel mold as shown in Figure D.3(a) is used to produce SiR samples in the desired shape and thickness. The mold is a square steel frame with a thickness of 4 mm with inner dimensions of 12 cm × 12 cm. The mixture is carefully poured from the container to the mold to minimize the number of air bubbles in the mixture.

The SiR in the mold is contained with the help of virgin, clean, heat-resistant, plastic foils. The mold is then placed between temperature-regulated plates of the press machine (see Figure D.3(b). Initially, the plates are at ambient temperature to avoid the initiation of the curing process before the full pressure is applied. First, a recipe for low pressure is applied for two minutes to ensure the mixture spreads evenly in the mold. Subsequently, a recipe for high pressure is applied to squeeze the excessive SiR out of the mold to ensure the thickness of 4 mm while the plates are heated gradually to 165 °C. The mold is exposed to the high pressure with heated plates for 20 minutes, and by the end of the process, the SiR is cured. The plates are then cooled down by water circulation for 12 minutes so that the SiR cools to room temperature.

Finally, the post-curing of the SiR is required. Based on the data sheet [120], the post-curing requires four hours in a ventilated oven of 200 °C. After the post-curing, the 120 mm × 120 mm × 4 mm SiR is cut into rectangular prisms in the desired dimensions. The samples are ready for the next step (i.e., surface preparation).

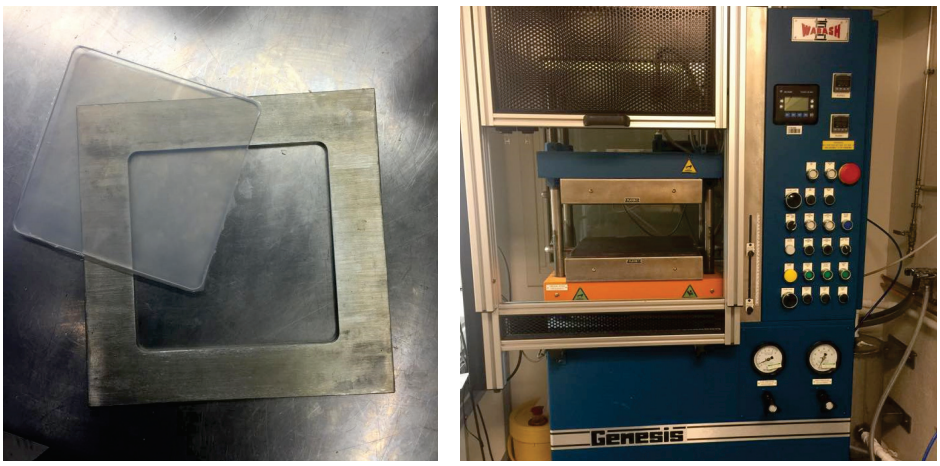

(a) **(b)**

Figure D.3: (a) Steel mold for SiR molding. (b) Mechanical press machine with temperature-regulated plates [158].

D.1.2 Epoxy

The epoxy used to produce samples is prepared in the casting laboratory using a mixture of two components: casting resin XB 5950 and hardener XB 5951 APG. Liquid, toughened, alumina pre-filled, hot-curing epoxy resin system for producing castings with excellent mechanical end-properties and good long-term strength [122]. Some basic properties concerning the casting and molding procedure are shown below:

Density of casting:	2.0 g/cm^3
Filler content:	60%
Mixing ratio:	100/100
Minimum curing time:	6/80 + 10/140
Glass transition temperature (DSC):	140–150 °C
Mold temperatures/demolding times	
APG process:	130–150/12–40 (°C/min)
Vacuum casting:	70–100/5–8 (°C/h)

Although a similar procedure is followed, casting epoxy is considerably more laborious and challenging than casting SiR. Figure D.4(a) shows the tube configuration to inject liquid epoxy resin into the mold, whereas Figure D.4(b) depicts the specifically designed mold for casting the epoxy samples in the desired dimensions.

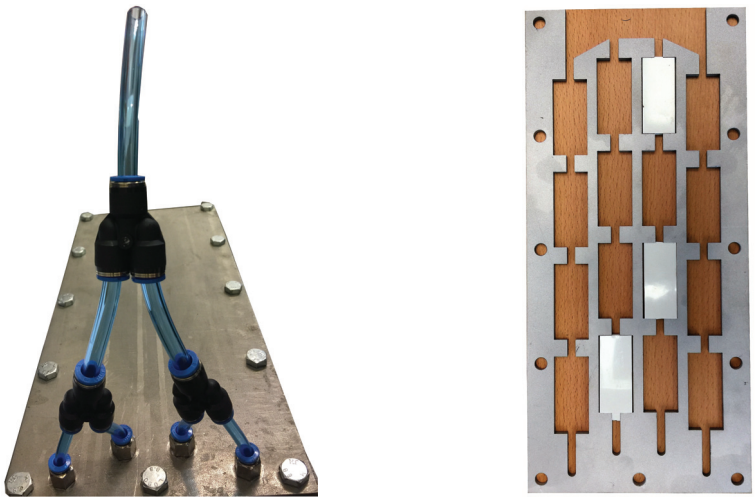

(a) (b)

Figure D.4: (a) Tube configuration to inject viscous epoxy resin into the mold. (b) Specifically designed mold for casting the epoxy samples in the desired dimensions.

D.2 Measurement Techniques of Elastic Modulus

In this study, a Lloyd LR5K gauge was used for tensile and compressive tests. Both methods were tested to check if there is a significant deviation between the outcomes. For tensile and compressive tests, two different test setups were used. The elastic modulus was determined using the average value of five identical measurements.

D.2.1 Tensile Method

The majority of tensile testing of materials shows a linear relationship between the applied force (stress) and the elongation of the specimen (strain), in the initial portion of the test, as illustrated in Figure D.5. The behavior of the material can be likened to the response of a spring under tension and, when the force is removed, the material returns to its original length. In the linear region i.e., elastic stage in Figure D.5, the line obeys the Hooke's Law such that the ratio of stress (σ) to strain (ϵ) curve is constant, i.e. $^{\sigma}/_{\epsilon} = E$, where E stands for the elastic modulus [159].

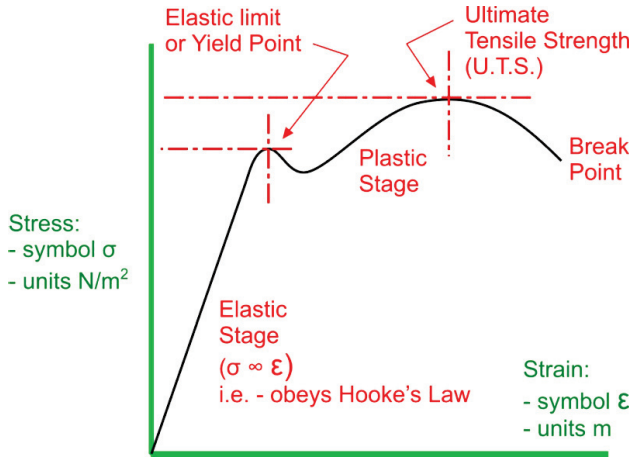

Figure D.5: Illustration of a stress-strain graph [159].

When measuring the elastic modulus of the samples in the tensile method, dog-bone-shaped samples were used where they were free to expand only in one direction (vertical direction). Figure D.6 depicts a specimen prepared for testing along with the nomenclature of what a dog-bone-shaped sample represents. Besides, Figure D.7 shows the methods followed when measuring the modulus of the dog-bone-shaped samples. It is examined by subjecting a sample to a controlled tension until it yields. Tensile specimens are punched out of the polymers used for the electrical breakdown testing. The dimensions of the test specimens are graphically shown below.

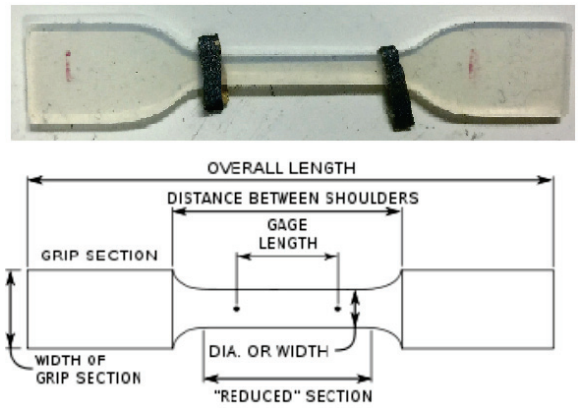

Figure D.6: Nomenclature for dog-bone shaped test specimens [160].

Light-reflecting tapes are attached to the ends of the straight part of a sample for the laser to detect any changes between them (see Figure D.6). The laser beam cast on the sample measures the elongation in the upwards direction between the tapes. The moduli of the materials were then calculated using the slope of the initial portion of the stress-strain curve.

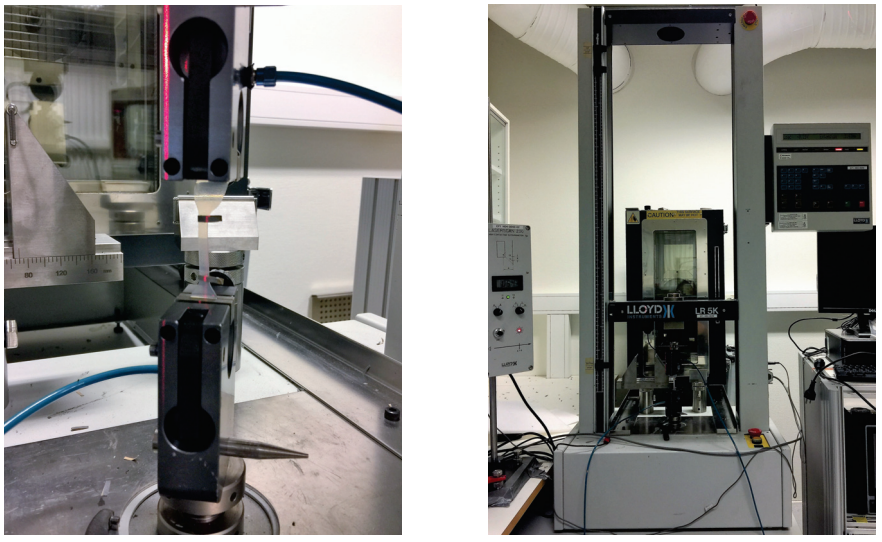

(a) **(b)**

Figure D.7: Lloyd LR5K gauge used for tensile and compressive tests.

D.2.2 Compressive Method

Compressive testing was executed using two rectangular specimens in the same dimensions as the materials used in the AC breakdown experiments. The two specimens were placed in a composite housing holding them on top of each other. The top specimen was pressed at a given speed until the pre-defined force value was reached. The optimal values for these pre-defined values of the speed and force were determined by running some initial tests. The range of the force was selected considering the chosen contact pressure values in the AC breakdown experiments. This method was developed to emulate the conditions that the specimens undergo in the breakdown testing.

The obtained modulus values from both methods concurred, and the deviation between them was less than 10% while the sequence from highest to the lowest modulus did not change.

D.3 Surface Roughness Characterization

D.3.1 Determination of Scan Parameters

Impact of the sampling interval, magnification and scan size on the resolution and scaling of rough surfaces were discussed in detail in [161] by testing four different surface characterization methods with performed by different instruments. Critical remarks from the study by Poon and Bhushan [161] are provided below:

> "Although surface roughness is intrinsic, measured roughness is extrinsic. Instruments using different sampling intervals measure features with different length scales. It can be concluded that a surface is composed of a large number of length scales of roughness that are superimposed on each other. Therefore, it is not that different asperities come in different sizes, but it is that one asperity comes in different sizes. Distribution of size and shape of asperities is dependent on the measurement technique. When the sampling interval at which the surface is examined is reduced, the number of asperities detected and their curvature appears to rise without a limit down to the atomic scale. This means that an asperity is not a *definite object*. Attempts have been made to identify a correct sampling interval, which yields the relevant number of summits and the relevant curvature for a particular application (functional filtering)."

Two parameters can characterize a surface with Gaussian distribution of heights and exponential auto-correlation function: the standard deviation of surface heights (σ_p or S_a or S_q) and correlation length (β_m). Additional parameters that are

commonly measured are peak-to-mean distance (S_p) and peak-to-valley (S_z) distance. A definition of S-parameters are provided in Figure 3.9. Due to the multiscale nature of surfaces, it is found that the surface roughness parameters depend strongly on the resolution of the measuring instrument or any other form of filter, and hence are not unique for a surface. Therefore, predictions of the contact models based on conventional roughness parameters may not be unique to a pair of rough surfaces. Poon and Bhushan [161] also added:

> "Surface measurement is also limited by the resolution of surface measuring instruments where the real surface topography may be misrepresented owing to finite dimension of the stylus tip of stylus instruments, stylus kinematics, stylus load, electrical filtering, size of the photodiode detector and objective lens magnification used by a non-contact optical profiler (NOP) and errors in sampling due to discretization process."[28]

D.3.2 Effect of spatial resolution

The spatial resolution is equivalent to the stylus size of stylus profiler (SP) and atomic force microscopy (AFM) and magnification of the objective lens used in non-contact optical profiler (NOP) in roughness measurements [161]. Based on the selected scan size and sampling interval, the roughness parameters S_q, S_p, S_z and β_m are likely to differ between the measurement methods. In the following section, the appropriate scan size and sampling interval for the NOP-type surface profilometer used in the PhD study are computed.

D.3.2.1 Selection of scan size

Regarding the selection of the optimal scan size, Poon and Bhushan [161] claimed that:

> "It is commonly observed that the roughness parameters of engineering surfaces change with the scan size. In particular, S_q and β_m generally increase with scan size [161]. It is due to longer wavelength features are included as the scan size is increased. In general, S_q, S_p and S_z increase initially with the scan size and each appears to approach a constant value, as the scan size is greater than 16 µm. β_m for different scan sizes was calculated using different cut-off lengths in the cubic spline filtering method. The advantage of using this filtering method is that only one single profile is required in which roughness for different scan sizes can be studied by rejecting the waviness longer than the cut-off length. Therefore, the cut-off length is essentially the same as the scan size. β_m approached a constant value for the cut-off length

[28] The optical profilometer used in this study is of NOP type.

> = 16 µm and therefore the long wavelength limit is 16" (as shown Fig. 13 in [161]).

In this work, long wavelength cut-off was selected to be 8 µm following the ISO 4287 standard [105] as depicted in Appendix D.3.3. Therefore, the scan size should be greater than 8 µm for a proper scan.

D.3.2.2 Selection of sampling interval

On the determination of the optimal sampling interval, Poon and Bhushan [161] suggested that:

> "In elastic contact, sampling interval should be small to include the finer details. The question now arising is what the sampling interval is considered as sufficient to include the finer structure. From SEM images, the surface contains finer and finer details as magnification increases. It suggests that there is no natural limit to the spatial size of features on most engineering surfaces. Intuitively, a natural limit must exist when approaching atomic dimensions, but in view of the scale of the size involved its significance to most engineering applications will be negligible. β_m represents the main wavelength structure for a given size of interest; it is reasonable to use a fraction of β_m, i.e., $\tau = c \cdot \beta_m$, as an appropriate sampling resolution to collect details which are of significance to their contact."

Overall, it was concluded in [161] that the use of $\tau = 0.4\,\beta_m$ for the sampling interval takes the instrument resolution into account and therefore is convenient and practical.

Features of NOP used in this work for surface characterization is shown as follows [133]:

Two objectives:	5X and 50X.
Two extra lenses:	0.55X and 2X.
VSI/VXI mode:	3 nm (white light with vertical resolution).
Lateral resolution:	0.38 µm (Sparrow criterion);
	0.26 µm (with AcuityXR®).

Using the β_m from Table 7.3, the minimum sampling interval should be as low as 0.8 µm as shown below:

Min #180: $\tau_{\min} = 0.4\,\beta_m = 0.4 \cdot 1.94\,\mu\text{m} = 0.8\,\mu\text{m}$.
Max #2400: $\tau_{\max} = 0.4\,\beta_m = 0.4 \cdot 118.19\,\mu\text{m} = 47\,\mu\text{m}$.

An average of five measurements on different sections of the surface of PEEK #180 has been performed. As can be seen in Table D.1, the rougher the surface, the more asperity peaks exist, which results in a much smaller asperity radius β_m

as revealed in Table 7.3. Therefore, the scan size and the sampling length should be selected accordingly. As discussed above, scan size should be greater than 8 µm when using the NOP in this work, which is satisfied under all combinations of the available objectives and lenses as shown Table D.1. Regarding the selection of sampling interval, 10X, 25X and 50X magnifications are found to be satisfactory when scanning the roughest surface. For smoother surfaces, all the magnification combinations are shown to have performed satisfactorily.

Table D.1: List of performance under different NOB magnifications.

NOB magnification	**2.75X**	**5X**	**10X**	**25X**	**50X**
S_q [µm]	30.64	29.72	30.28	29.87	28.33
S_p [µm]	37.01	36.30	37.57	38.02	35.40
Sampling interval [µm]	3.523	1.961	0.973	0.353	0.197
Scan size x [µm] x y [µm]	2254 x 1691	1255 x 942	623 x 467	226 x 176	126 x 95

D.3.3 Roughness and Waviness Profiles

Figure D.8 and Figure D.9 show the roughness and waviness profiles acquired by using the optical profilometer as described in Section 6.6.1. Low-pass and high-pass filters were employed with the following cut-off lengths: $\lambda_s = 8\,\mu m$, $\lambda_c = 0.08\,mm$, $\lambda_f = 0.25\,mm$ with reference to Figure 3.7(a).

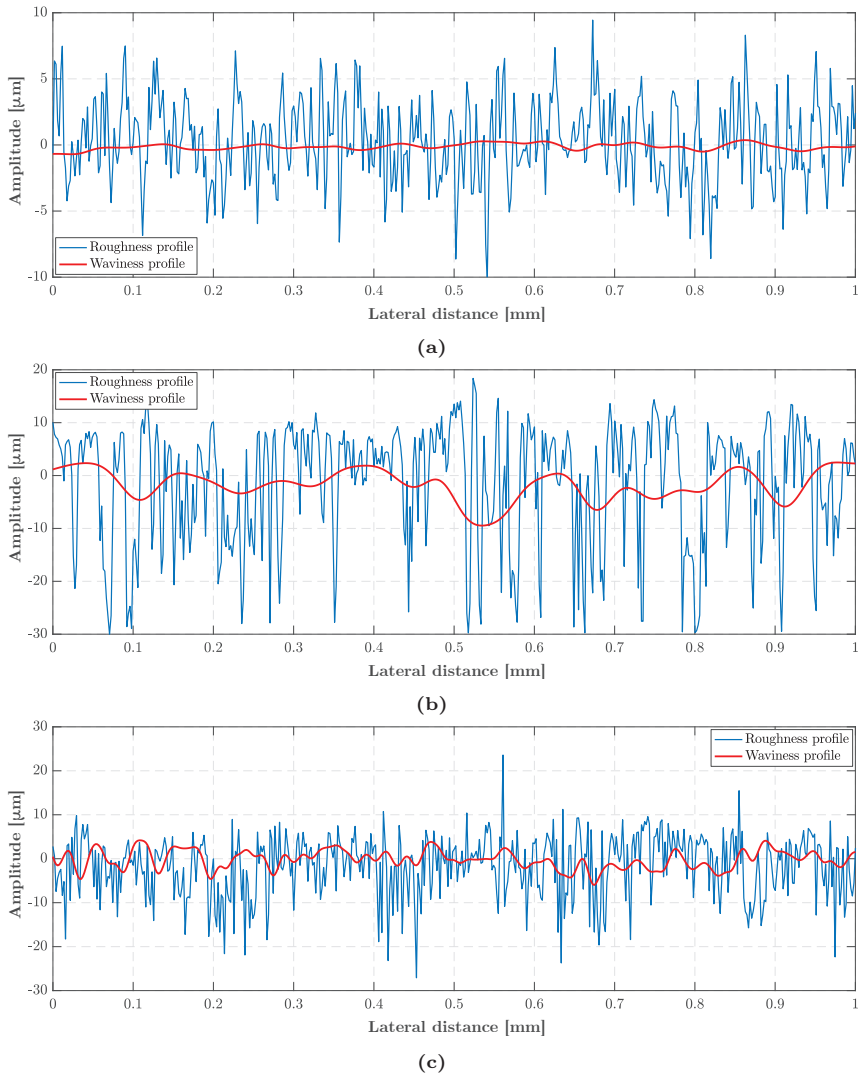

Figure D.8: Obtained roughness and waviness profiles of: (a) SiR #500. (b) EPOXY #500. (c) PEEK #500.

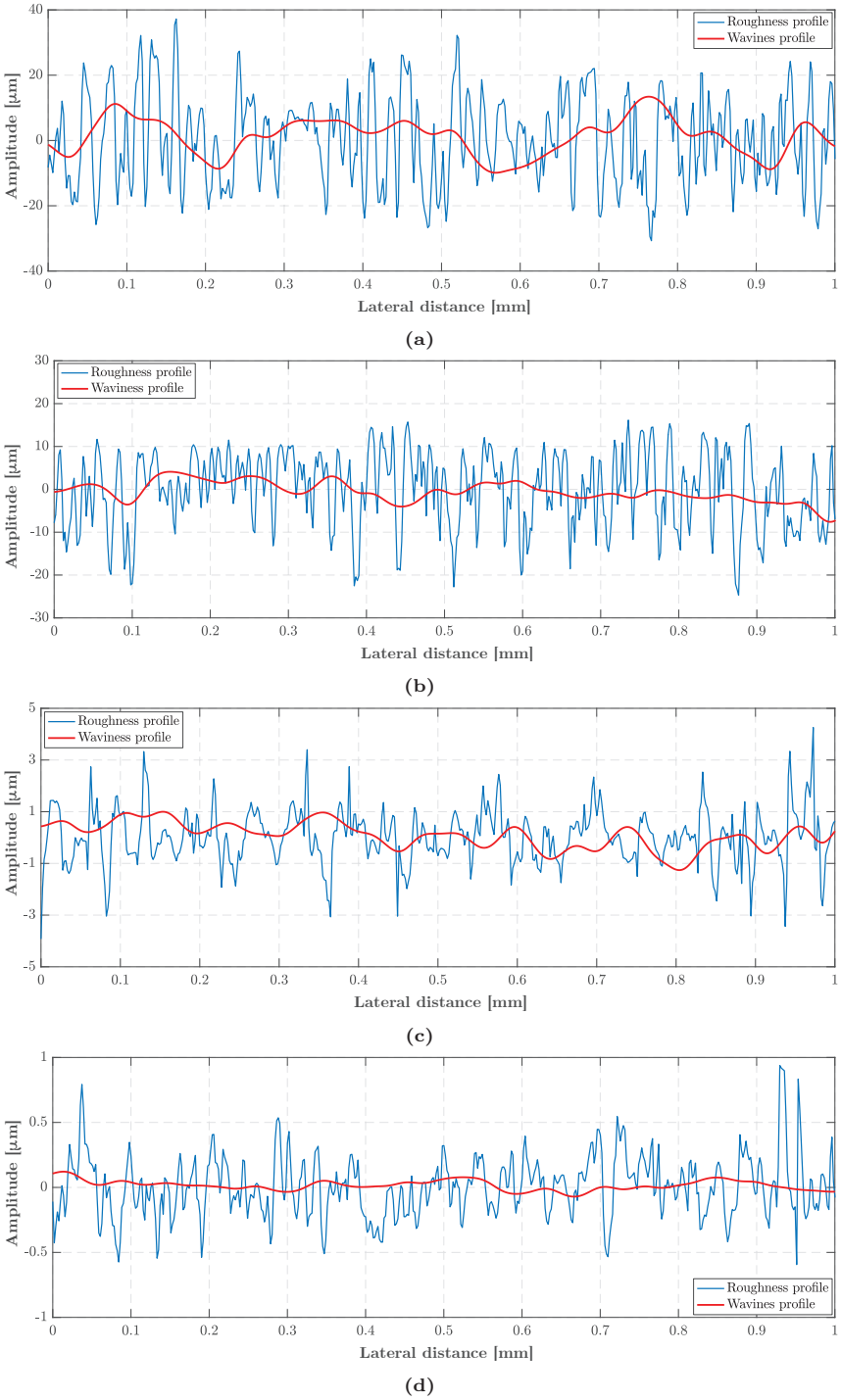

Figure D.9: Obtained roughness and waviness profiles of XLPE samples polished with: (a)#180. (b) #500. (c) #1000. (d) #2400.

D.3.3.1 Surface Histograms

In addition to the results presented in Paper III, the histograms of the amplitudes of raw roughness data are depicted in Figures D.10–D.11 alongside the theoretically fitted Gaussian bell-shaped curves. Although the histogram data seem to be reasonably well-fitted to the normal distribution, to quantitatively assess if the peak-height distributions of the polished sample surfaces are normal, a number of normality tests widely used in the literature [77,162] are performed in the following section.

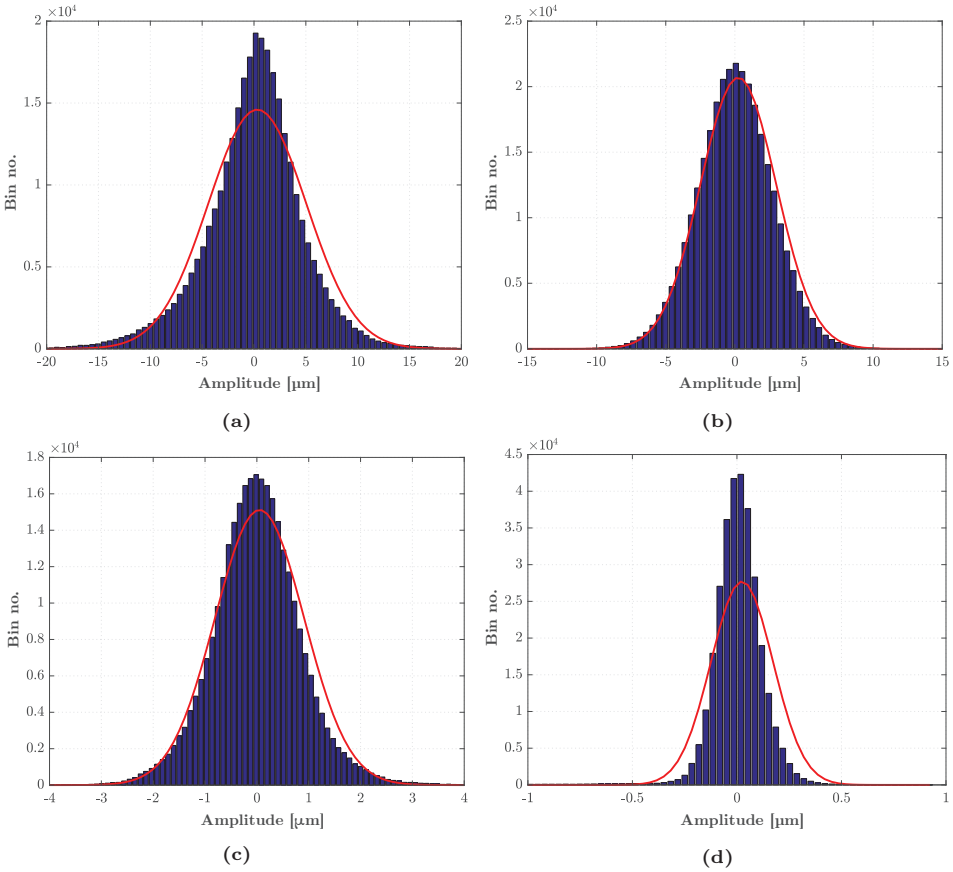

Figure D.10: Histogram of the peak-height distribution of XLPE samples: (a) #180. (b) #500. (c) #1000. (d) #2400.

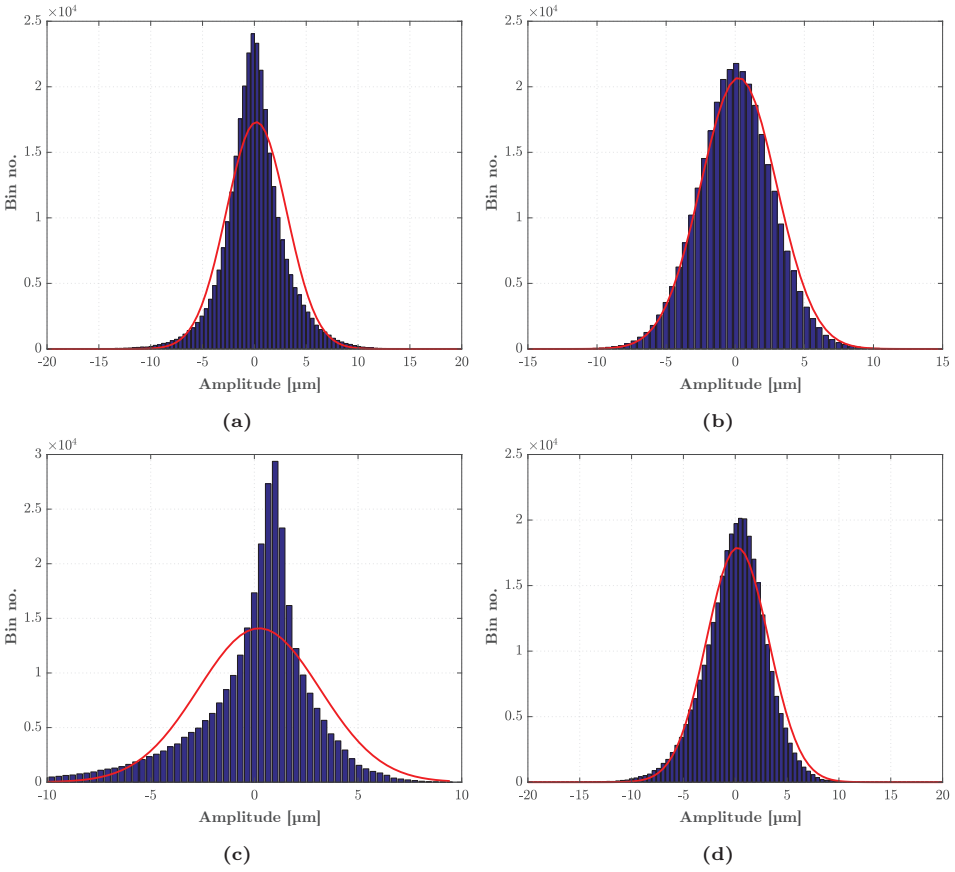

Figure D.11: Histogram of the peak-height distribution of: (a) SiR #500. (b) XLPE #500. (c) EPOXY #500. (d) PEEK #500.

D.3.3.2 Normality Tests

To quantitatively test if the distribution is normal or not, modern statistics has developed many tests of normality [162]. The main tests for the assessment of normality are the Anderson-Darling (AD) test, the Lilliefors (LF) test, the Jarque-Bera (JB) test, the Shapiro-Wilk (SW) test, the D'Agostino-Pearson (DP) test, and the Shapiro-Francia (SF) test [162]. Each test is based on a particular test statistic which is a quantitative estimator of proximity between the theoretical normal distribution and an observed sample of measurements. Based on the test statistic, the test determines the $p-$value. The $p-$value can be interpreted as the significance at the scale between 0–1 that the hypothesis of the normality is true for the observed measurements. If the $p-$value is less than the acceptable significance level, usually selected between $3-5\%$, then the hypothesis of normality is rejected. That is to say, the height distribution is not normal. Note that the acceptable

significance level is a probability to reject the hypothesis of normality even if it is true.

To execute the above-mentioned normality tests, the matrices storing the roughness data, which are used to plot the roughness profiles shown in Figures D.8 and D.9, are processed using MATLAB®'s built-in functions namely: *adtest*, *lillietest*, *jbtest* along with the open source adds-on *swtest*, *sftest*, and *DagosPtest* (available in MATLAB® central file exchange platform [163]). Each test then returns a $p-$value which is assessed to conclude if the sampled population is normally distributed within the given significance, which is set to 0.03, i.e., 3% in this study.

The resulting $p-$values of the executed normality tests are tabulated in Table D.2 and Table D.3. As can be seen in Table D.2, all the XLPE samples with various roughnesses have $p-$values higher than 0.03 in all the tests that conclude that the hypothesis of normality is rejected, i.e. the population is normally distributed. Likewise, $p-$values of SiR, EPOXY, and PEEK samples polished by #500 grit sandpaper have all failed to reject the hypothesis of normality. Only the height distribution of XLPE shows slightly skewed distribution from the normal distribution due to the $p-$values being close to 0.03 in AD and SW tests, which is within acceptable margins and should not cast any doubt on the validity of the hypothesis.

Table D.2: $p-$values of the selected normality tests for the XLPE samples with different roughnesses.

Interface	AD	LF	JB	SW	DP	SF
#180	0.0592	0.1563	0.0365	0.0318	0.0570	0.0318
#500	0.0579	0.1077	0.2115	0.0343	0.1569	0.1129
#1000	0.0510	0.2878	0.0559	0.0781	0.0506	0.0781
#2400	0.0417	0.0610	0.5501	0.1565	0.1651	0.0581

Table D.3: $p-$values of the selected normality tests for the samples with different modulus (#500).

Interface	AD	LF	JB	SW	DP	SF
SiR	0.9255	0.9686	0.8551	0.7436	0.9061	0.5112
XLPE	0.0579	0.1077	0.2115	0.0343	0.1569	0.1129
EPOXY	0.3254	0.7509	0.1163	0.0781	0.1224	0.0579
PEEK	0.9941	0.9593	0.9018	0.0123	0.9415	0.9720

D.4 Probability Density Function of the Radius of the Asperities

The radius of asperities, β_m estimated using Equation (3.28) corresponds to a numerical estimation of the mean radius of the asperities on the surface, which is utilized as the radius value in the Greenwood-Williamson theory [88].

The distribution function of the radius of asperities, β_m is represented with a lognormal distribution [164]. The statistical distribution is not viable to be constructed using a Gaussian distribution, because negative values may occur with the relatively high value of the ratio of the root mean square to the mean [100].

The distribution function of the radius of asperities is calculated using [100]:

$$f(\beta^*) = \frac{1}{c_1\,\beta^*\,\sqrt{2\pi}}\,e^{-\frac{\left(\ln\,\beta^* - c_2\right)^2}{2\,c_1^2}}\,. \tag{D.1}$$

This lognormal distribution is available only for the positive values, and therefore requires a dimensionless parameter β^*:

$$\beta^* = \frac{\beta}{\beta_{rms}}\,, \tag{D.2}$$

where β is the set/space of asperity radii for which the lognormal distribution is plotted, and β_{rms} is the root mean square of β_m. With the parameter β^*, the mean value of the distribution becomes β_m/β_{rms}, and the root mean square becomes 1, which then allows the determination of c_1 and c_2 such as:

$$c_1 = \sqrt{\ln\left(\left(\frac{\beta_{rms}}{\beta_m}\right)^2 + 1\right)}\,, \tag{D.3a}$$

and

$$c_2 = \ln\left(\frac{\beta_m}{\beta_{rms}}\right) - \ln\left(\left(\frac{\beta_{rms}}{\beta_m}\right)^2 + 1\right). \tag{D.3b}$$

The root mean square value β_{rms} of the equivalent rough surface (sum surface) is calculated using:

$$\beta_{rms} = \frac{AY_{eq}^2}{16Y_{eq}}\,\sqrt{\frac{SY_{eq}^2}{Y_{eq}^2} + 4\,\frac{SAY_{eq}^2}{AY_{eq}^2}}\,, \tag{D.4}$$

where Y_{eq} is the arithmetic, mean asperity height, AY_{eq} is the average width of the motifs, SY_{eq} is the root mean square of the mean height values, and SAY_{eq} is

the root mean square of the motifs in a sum surface [100]. As a reminder, β_m is calculated using Equation (3.28).

Using the lognormal distribution in Equation (D.1), distributions of the radii of surface asperities of SiR, XLPE, EPOXY, and PEEK samples polished using #500 grit sandpaper and of XLPE samples with four different surface roughnesses. The set of β ranges from 0 to 10^3 µm. The lognormal distributions of the samples within the defined β range with 1 nm resolution are plotted in Figure D.12. It should be noted that horizontal axes are plotted in logarithmic scale to visualize the distributions in bell-shaped curves.

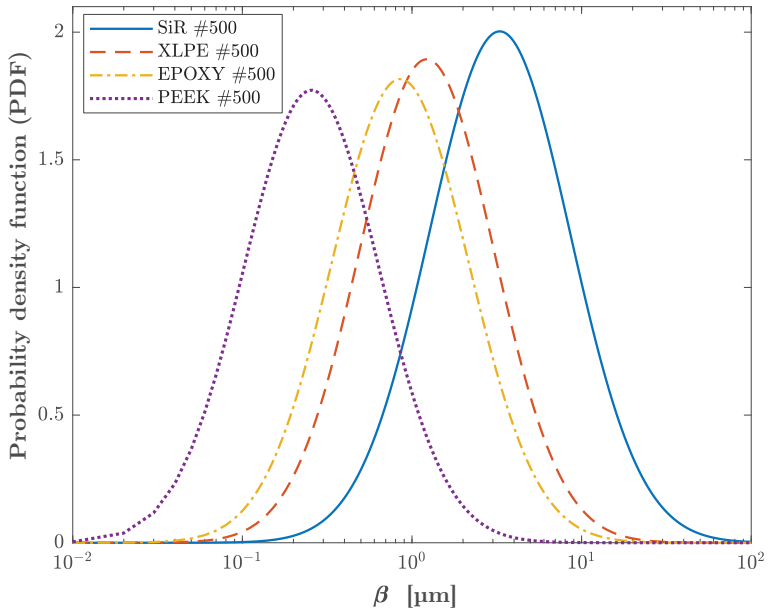

(a)

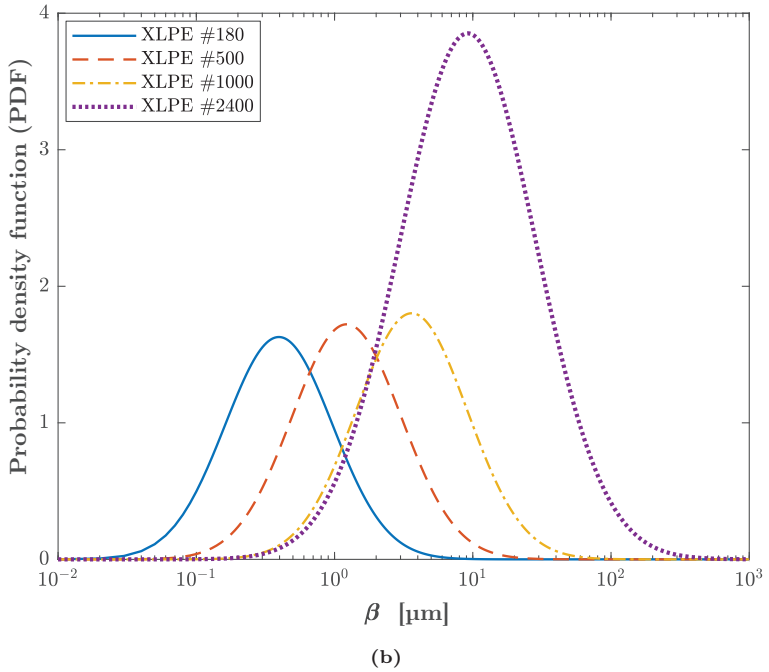

(b)

Figure D.12: Distributions of the asperity radius on the surface obtained by grinding process: (a) Four different materials sanded by sandpaper grit #500. (b) XLPE samples with four different roughnesses.

Appendix E

Estimating Cavity Discharge Field and Voltage

In this appendix chapter, details for the Paschen law modeled using a polynomial fit function introduced in Section 4.1.1 are provided.

The PD inception voltage of a cavity, V_{cav} at a given pressure is derived by multiplying Equation (4.2) by the cavity size d:

$$V_{cav}\left(p_c, d\right) = A\,\frac{p_0/p_c}{d} + B\,\frac{p_c}{p_0}\,d + C + D\sqrt{\frac{p_c}{p_0}\,d}\,, \tag{E.1}$$

where p_c is the pressure inside the cavity, atmospheric pressure $p_0 = 1\,\text{bar}$, $A = 0.00101\ \text{kV}\cdot\text{mm}$, $B = 2.4\ \text{kV/mm}$, $C = -0.0097\ \text{kV}$, $D = 2.244\ \text{kV}\cdot\text{mm}^{-0.5}$ [14]. The waveform in Figure E.1 is plotted using Equation (4.2) for the case of vented cavities, i.e., $p_c = p_0 = 1$ bar.

The Paschen's law predicts the occurrence of a minimum breakdown voltage for $pd = 7.5\cdot10^{-6}$ m·atm, corresponding to 327 V (peak) in the air at standard atmospheric pressure at a distance of 7.5 µm [165]. As seen in Figure E.1, the Paschen minimum is estimated to be around 238 kV (rms) and 336 kV (peak) using the polynomial fit function, which can be deemed to be a sufficiently robust estimation. At 1 atm, the left side of the Paschen minimum represents a gap distance (or a uniform cavity size) less than or equal to around 7.5 µm. The theoretical and experimental studies in this thesis indicated that the cavities at the interfaces are in the orders of several tens of microns. Therefore, the portion to the right of Paschen minimum (RHS of the Paschen's curve) is considered.

A cavity size (or gap distance) from 10 µm to 1 mm is covered in Figure E.2 for both the inception voltage and inception field in the same graph (log-log scale). The inception voltage curve is basically the right side of the Paschen minimum while the inception field is identical to the one plotted in Figure 4.2. As seen in the figure, the slopes of the field and voltage waveforms are opposite.

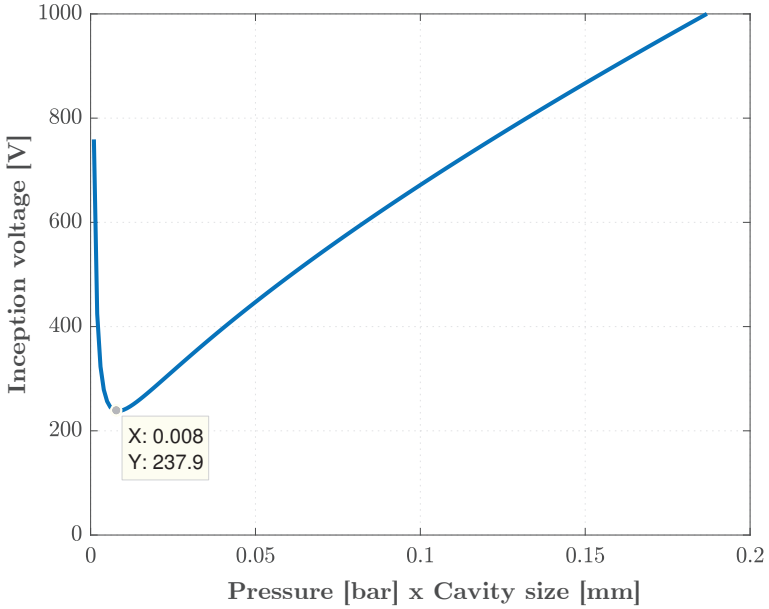

Figure E.1: Paschen's curve for air at atmospheric air pressure (1 bar). Estimated inception voltage is calculated using Equation (E.1).

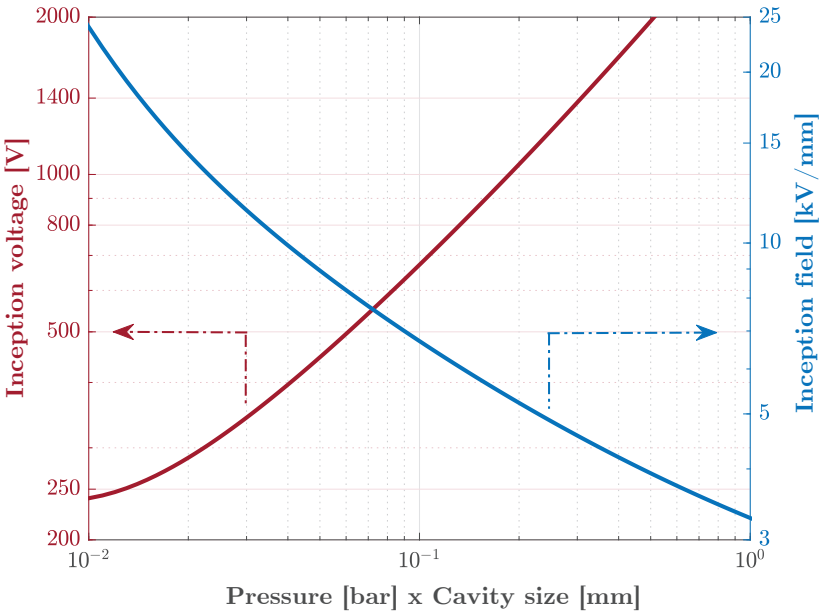

Figure E.2: Paschen's curve for air at atmospheric air pressure (1 bar). Left y-axis: Estimated PD inception voltage (V_{cav}). Right y-axis: Estimated PD inception field (E_{cav}).

The polarity of the slope of the inception voltage V_{cav} waveform is calculated by differentiating V_{cav} with respect to d:

$$\frac{\partial V_{cav}}{\partial d} = A\,\frac{p_0}{p_c}\left(-\frac{1}{d^2}\right) + B\,\frac{p_c}{p_0} + D\sqrt{\frac{p_c}{p_0}}\,\frac{1}{2\sqrt{d}}\,. \tag{E.2}$$

Since B and D are significantly higher than A, the effective sign of the slope is expected to be positive in the spanned range of d. The inception voltage waveform plotted in Figure E.2 concurs with the expected positive polarity of the slope.

Similarly, the polarity of the slope of the inception field E_{cav} curve is calculated by differentiating E_{cav} with respect to d:

$$\frac{\partial E_{cav}}{\partial d} = -A\,\frac{p_0}{p_c}\,\frac{2}{d^3} - \frac{C}{d^2} - D\sqrt{\frac{p_c}{p_0}}\,\frac{1}{2\,d^{3/2}}\,. \tag{E.3}$$

As can be seen in Equation (E.3), the slope is negative in the spanned range of d. Thus, an inverse correlation between E_{cav} and d is expected. Figure E.2 agrees with the expected negative polarity of the slope. It might thus be bewildering in the results and discussion section when the right side of the Paschen minimum is referred to while the field curve is employed because the breakdown field strengths are of interest. Consequently, when the right side of Paschen minimum is referred to in this work, the inception voltage waveform is taken as the reference, as adopted in the literature. This short study is aimed to remedy any ambiguities that might arise related to the use of Paschen's law in this work.

Finally, the air-filled, enclosed nanocavities will have as high a dielectric strength as nanoscale contact spots of the bulk material according to the left of Paschen minimum for air, as shown in Figure E.3.

Alternative Approach for Modeling the Inception Field

The inception field in the cavity, E_{inc} is the minimum field in the cavity required for a PD to occur. The inception field for a streamer type PD in a cavity depends on the cavity geometry, pressure in the cavity, the dielectric permittivity, characteristics of ionization process in the gas, and the distance between the electrodes [50, 99]. For streamer-type discharge, the cavity inception field, E_{inc} is defined as [50, 99]:

$$E_{inc}\,(p,d) = \left(\frac{E}{p}\right)_{cr} p\left[1 + \frac{\mathcal{F}}{(p\,d)^{\mathcal{T}}}\right] \tag{E.4}$$

where $(E/p)_{cr}$, $\mathcal{F}$ and $\mathcal{T}$ are parameters associated with ionization processes in the gas, p is the pressure in the cavity and d is the cavity diameter. For air, $(E/p)_{cr} = 24.2\,\mathrm{VPa^{-1}m^{-1}}$, $\mathcal{T} = 0.5$ and $\mathcal{F} = 8.6\,\mathrm{Pa^{1/2}}$.

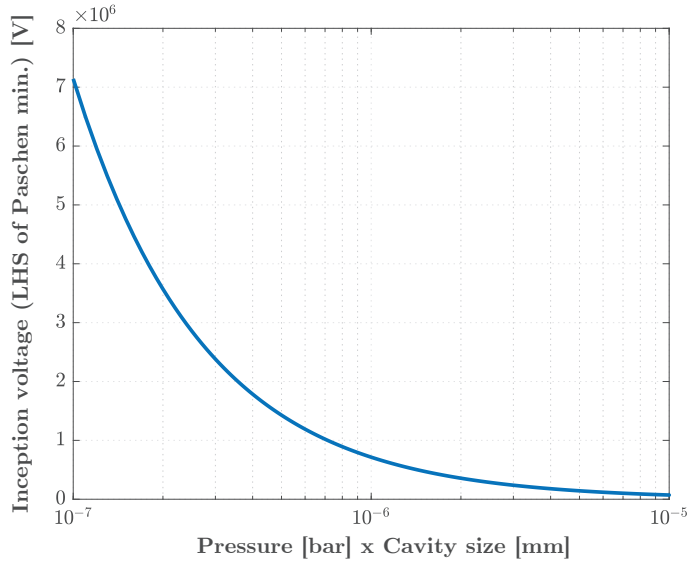

Figure E.3: Left side of the Paschen minimum for air at atmospheric air pressure (1 bar). Estimated inception voltage is calculated using Equation (E.1).

Figure E.4 shows the estimated field strength by the streamer-type discharge (E_{inc}) calculated using Equation (E.4) alongside the estimated field by the right side of the Paschen's curve (E_{cav} in Figure E.2).

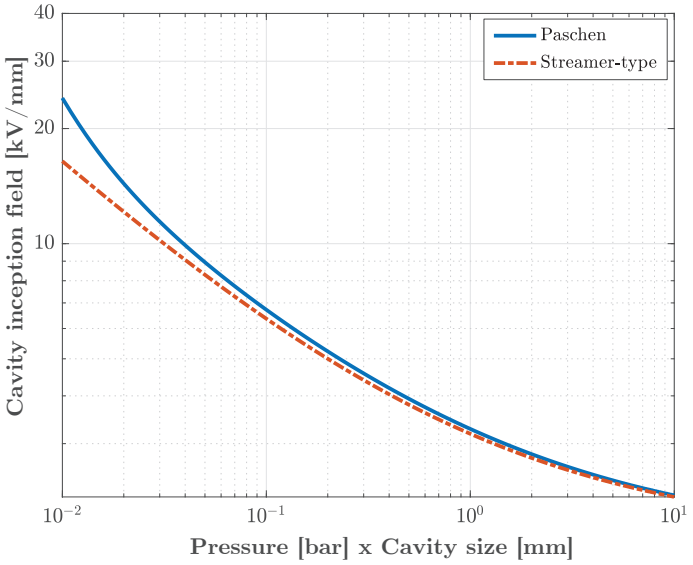

Figure E.4: Right side of the Paschen's curve for air under various air pressure.

Appendix F

Details of Experimental Setups

F.1 AC Breakdown Experiments

The photo of the setup used in the AC breakdown experiments is also shown in Figure F.1. Figure F.2 shows the laboratory test cell used throughout the BDS experiments.[29]

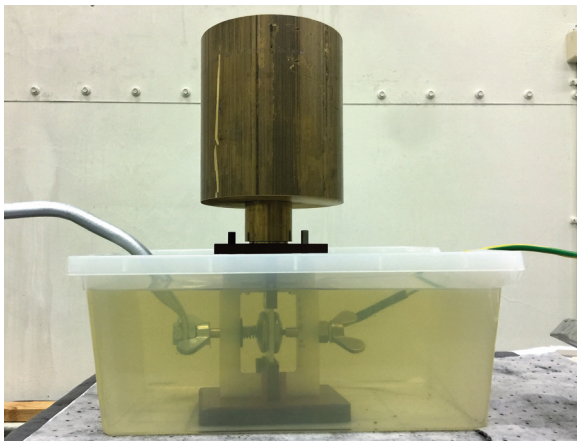

Figure F.1: Photo of the mechanical setup with the Rogowski electrodes and load submerged in an oil-filled container.

[29] Figure 6.5 illustrates the connections of the complete circuit.

(a) The laboratory test cell.

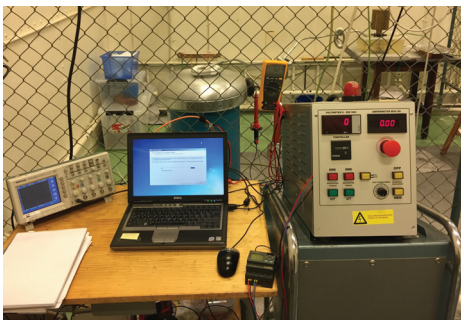

(b) Primary-side variac, PC and oscilloscope.

(c) Data acquisition unit.

Figure F.2: The complete setup used for the AC breakdown testing.

F.2 PD Experiments

Figure F.3 shows the laboratory test cell used throughout the BDS experiments.[30]

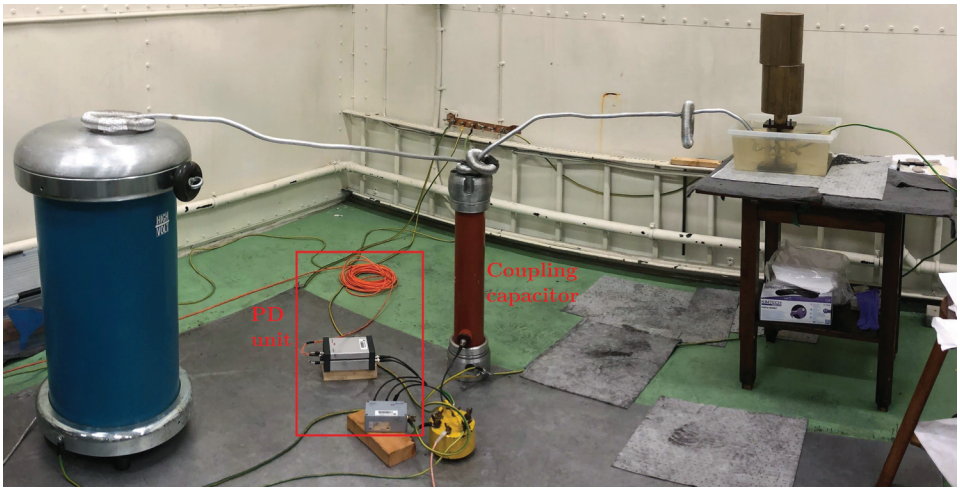

Figure F.3: The complete setup used for the PD testing.

F.2.1 System calibration for PD Testing

Before each experiment, the system needs to be calibrated. The MPD 600 system allows charge calibration to be performed digitally using its user-friendly GUI. A charge calibrator is connected across the terminals of the test object during calibration, which injects a calibration charge at the predefined amplitude and polarity (see Figure F.4).

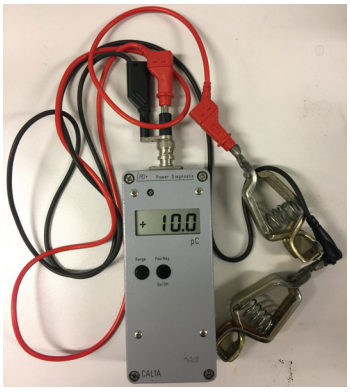

Figure F.4: Impulse injector used for calibration.

Voltage drops in the measuring impedance (i.e., coupling device) due to the injected charge, which ceases when the voltage across the coupling capacitor is the same as across test object. In a circuit, injected charge emulates discharge activity in the test object. The range of calibration charge is from 1 to 100 pC.

As highlighted in Figure F.5, the target value of the charge is set to a value equal to

[30] Figure 6.6 shows the connections of the complete circuit.

the injected charge amplitude, and the charge calibration is completed by pressing 'Compute' button that calculates a divider factor as the calibration constant. Lastly, two of the most common mistakes committed during calibration should be mentioned. First and foremost, disconnecting the grounding stick attached to the HV in the system is usually forgotten since the HV supply is not energized during calibration. Second, the calibrator should be removed from the system before energizing the circuit; otherwise, it gets severely damaged.

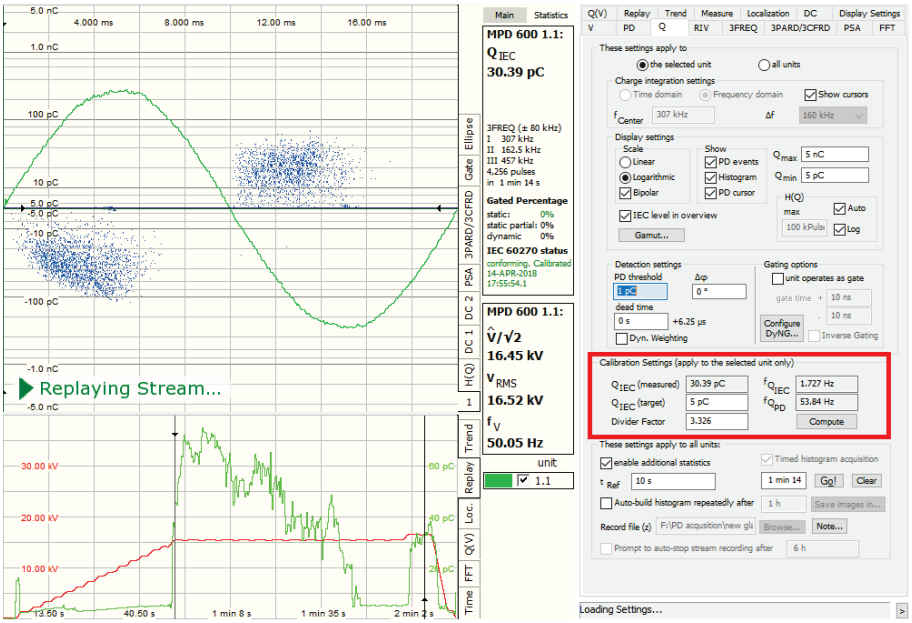

Figure F.5: The graphical user interface of the Omicron software.

F.3 Experiments on Interface Discharge-Monitoring

The mechanical test setup used in the AC breakdown experiments could not be used where the force is applied in the vertical direction. Therefore, a new setup was designed to improve the previous design as well as to enable a CCD camera to be placed over the setup. The first issue to be resolved was the way the force is applied. In the new design, force is applied with the help of screws and bolts, while the applied force is measured using two identical S-shaped load cells connected to two separate PCE Digital Force Gauges (PCE-FB 2K) to ensure the same amount of pressure is exerted at both edges of the top sample. To facilitate repetitive experiments, the volume of the oil chamber is reduced considerably. Only the samples and the electrodes are immersed in oil. The CCD camera is intended to be placed over the setup with some distance concerning the minimum distance

for an achievable focus and electrical safety. For that purpose, a thick steel plate (no.1 in Figure 6.8) with a window of sufficient size to monitor the interface was designed. To provide an extra insulation distance from the electrodes immersed in the oil, an identical wooden plate (no.2) is also used. With the current design, forces up to 2 kN can be applied without any difficulty, which is the maximum force that the load cells can withstand safely. This improvement is a significant step forward when compared to the old design in which cumbersome weights are used, which made performing a large number of experiments a very laborious task. The steel and wooden plates sit only on the top sample; there is thus sufficient clearance between the sides of the plexiglass container and the plates including the compression taking place in the second sample.

A custom-made base for the camera is designed, which enables the camera to move in the horizontal and vertical directions with coarse and fine-tuning options (see Figure F.6).

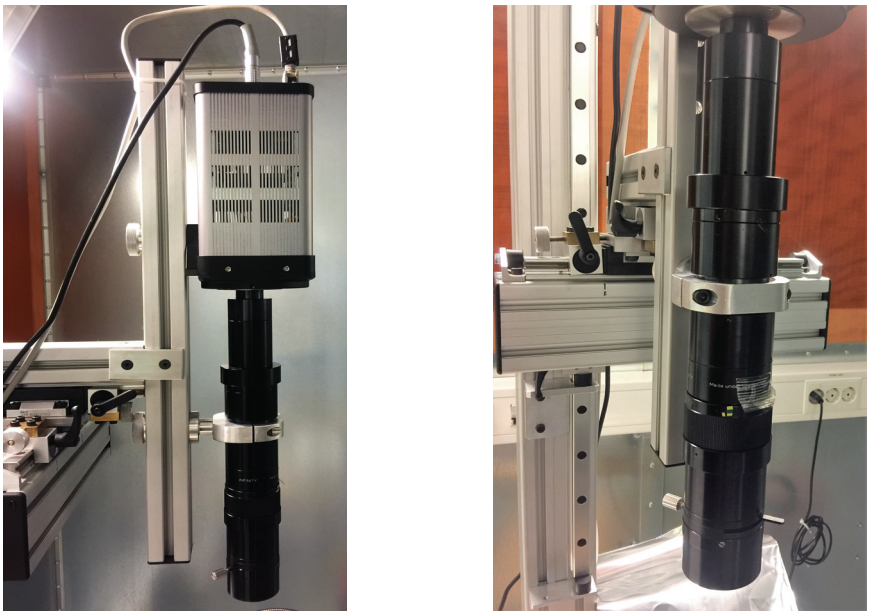

(a) **(b)**

Figure F.6: Photos of mechanical setup for CCD camera: (a) Camera attached to its custom-made base. (b) External camera lens.

Figure F.7(a) shows the full setup with the load cells connected to the force gauges that instantly show the applied force in their displays. Figure F.7(b) shows the setup in the test cell during initial tests, which were performed to determine the PDIV of the setup, limitations regarding maximum admissible voltage and contact pressure and to validate safe operation. Furthermore, Figure F.8 provides a closer look into the electrode pair attached to the oil container made of plexiglass.

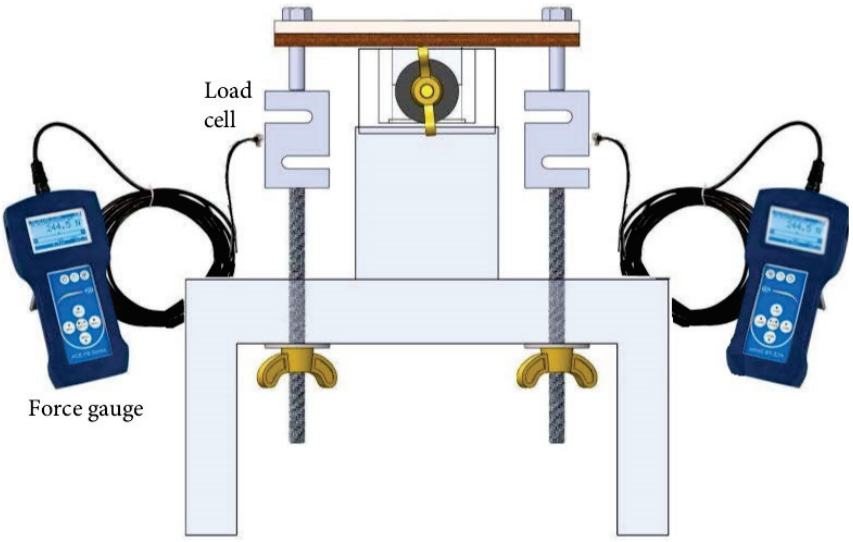

(a)

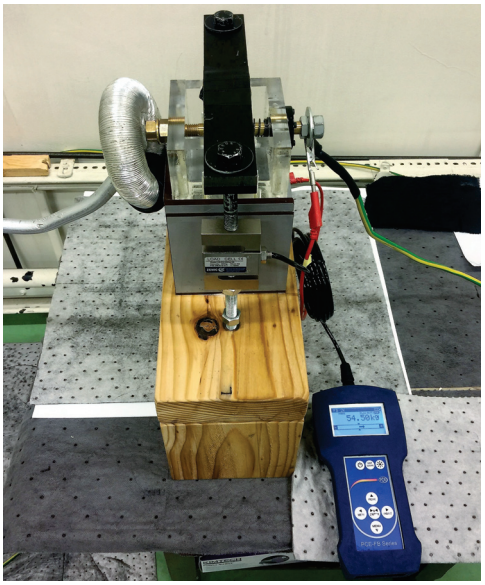

(b)

Figure F.7: The complete test setup with the force gauges. (a) Illustration of the setup. (b) Photo of the setup in the HV hall. The window in the plates were covered with electric tape and polymer pieces during preliminary tests to determine limitations of the system.

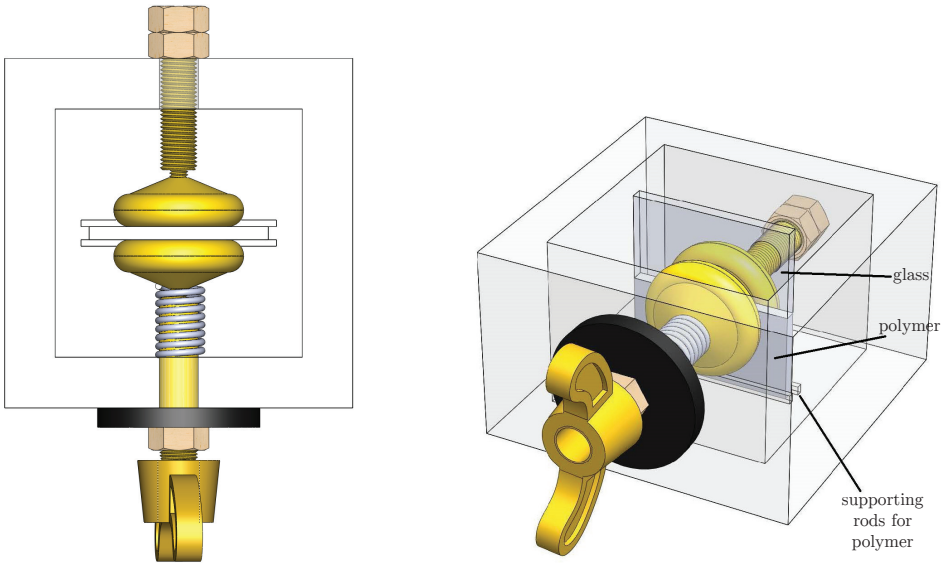

Figure F.8: Plexiglass container in detail: (a) Top view. (b) Trimetric view. (Top sample: glass, bottom sample: polymer. The slender rectangular rods attached to the bottom surface are intended to keep the bottom sample in place).

F.3.1 Challenges Encountered in the Discharge-Monitoring Experiments

First, the challenges encountered during the tests are briefly stated to elucidate how the test methodology presented in the next section was devised.

Challenges are listed as follows:

- Finding the correct focus was somewhat challenging due to the presence of the additional lens. Since the camera is sensitive to light, images need to be captured in a dark environment; otherwise, the image becomes saturated and only shows overexposed lines. Since there is no light source in the system while adjusting the focus, an additional light source was added, and a sharp object such as a needle was placed at the interface to assess if the focus is good enough when the tip of it become visible clearly.
- Since there are metal parts in the mechanical setup, they cause light reflections even in the absence of a strong light source. As the discharge taking place at the interface is not as bright and luminous as the one emitted during the breakdown, any reflection or light leaking from the outside environment reduce the quality of the image and might override the useful part of the image. After many trials, painting all the metal parts with pale black paint reduced the reflections notably.

- Finding the optimal exposure time was also a challenge initially. After many trials, the optimal exposure time inherent to the setup and the type of the samples used were determined to be between 60-180 s. Over 180 s, the images became overexposed and nothing was discernible, while they were blurred below 60 s.

F.3.2 Detailed Test Procedure

1. Samples are assembled at dry conditions between the electrodes following a similar procedure that is adopted for BD and PD experiments.
2. The metal and wooden plates are placed on top of the sample in such a way that the interface is visible through the window.
3. The force gauges are connected to the load cells and are switched on.
4. The wingnuts under the base (see Figure 6.8) are tightened equally until both the force gauges reach the desired force value.
5. The computer controlling the CCD camera is switched on, and the CCD camera is powered. After the CCD camera cools down to its operating temperature, preliminary images are taken via MetaMorph software. Fine-tuning of focus and image quality is exercised until the optimal quality is reached.
6. The values that the force gauges display are checked if a considerable deviation occurred due to improper assembly or sample imperfections. Fine tuning on the force values is performed if necessary.
7. The plexiglass container is filled with Midel ester oil to the brim.
8. The images of the interface are obtained again to check if the interface is still in good condition after filling the container with oil. If not, the procedure starts over. An image of the interface is saved for reference.
9. The force gauges are removed from the system, but the load cells remain connected. The cables sticking out the load cells are secured properly to protect them against external flashover.
10. The grounding connections of the metal parts such as metal plate, bolts, nuts, and load cells are checked.
11. The dark-room environment is set by fixing the black fabric and by switching off the lights.
12. A series of images are shot without the voltage on to check if the light is penetrating the fabric.
13. A background image is shot by setting the exposure time to 180 s to be used in *background subtraction mode*[31] if necessary.
14. The PD acquisition system is activated and is calibrated.
15. The exposure time is set to 20 s.
16. The setup is powered by a ramp voltage of 1 kV/s and the PD pattern is

[31] A feature that MetaMorph camera software allows to maximize image quality.

observed in the meantime.

17. When the PRPD suggest that PD activity starts, an image is taken to check if any discharge is visible.
18. If discharge activity is discernible on the image, the voltage is kept at that value, and the exposure time is set to 60–180 s depending on the preferred image quality. The quality changes depending on the opaqueness of the sample and the darkness of the room. Therefore, several trials are needed to determine the optimal exposure time. For top-quality images, the 180-second duration is suggested, while the 60-second duration provides the lowest satisfactory quality. It should be noted that as the diaphragm is kept open during the exposure time, the obtained image contains all the changes taking place during that period. Thus, in case more intervals between the images are needed, a 60-second duration can be selected.
19. The tests are usually run for at least 8 hours, sometimes for a couple of days. Stream acquisition or time-lapse acquisition modes are selected in MetaMorph software to capture the images automatically and continuously. For instance, when the exposure time is set to 180 s, and the stream acquisition is set to continue for 10 hours, the camera takes images for 10 hours continuously whereas an image represents the entire activity taking place during the 180-second period. The images can then be viewed in a sequence. Omicron software is run to save the PRPD patterns simultaneously.

Appendix G

Selected Publications

Paper I:

E. Kantar, D. Panagiotopoulos, and E. Ildstad, "Factors Influencing the Tangential AC Breakdown Strength of Solid–Solid Interfaces,"*IEEE Transactions on Dielectrics and Electrical Insulation*, vol. 23, no. 3, pp. 1778–1788, June 2016.

Paper II:

E. Kantar, F. Mauseth, and E. Ildstad, "Effect of Pressure and Elastic Modulus on Tangential Breakdown Strength of Solid–Solid Interfaces," *IEEE Electrical Insulation Conference (EIC)*, Montreal, QC, 2016, pp. 431–435.

Paper III:

E. Kantar, F. Mauseth, E. Ildstad, and S. Hvidsten, "Longitudinal AC Breakdown Voltage of XLPE–XLPE Interfaces Considering Surface Roughness and Pressure," *IEEE Transactions on Dielectrics and Electrical Insulation*, vol. 24, no. 5, pp. 3047–3054, Oct. 2017.

Paper IV:

E. Kantar, F. Mauseth, E. Ildstad, and S. Hvidsten, "A Stochastic Model for Contact Surfaces at Polymer Interfaces Subjected to an Electrical Field," *Tribology International*, vol. 127, pp. 361–371, Nov. 2018.

Paper V:

E. Kantar, S. Hvidsten, and, E. Ildstad, "Effect of Material Elasticity on the Longitudinal AC Breakdown Strength of Solid-Solid Interfaces," *IEEE Transactions on Dielectrics and Electrical Insulation*, vol. 26, no. 2, pp. 655–663, Apr. 2019.

Paper I

E. Kantar, D. Panagiotopoulos, E. Ildstad, "Factors influencing the tangential AC breakdown strength of solid-solid interfaces", IEEE Trans. Dielectr. Electr. Insul., vol. 23, no. 3, pp. 1778–1788, Jan. 2016.

Paper II

E. Kantar, F. Mauseth and E. Ildstad, "Effect of pressure and elastic modulus on tangential breakdown strength of solid-solid interfaces," IEEE Electr. Insul. Conf. (EIC), pp. 431–435, June 2016.

Effect of Pressure and Elastic Modulus on Tangential Breakdown Strength of Solid-Solid Interfaces

Emre Kantar*, Frank Mauseth and Erling Ildstad
Department of Electric Power Engineering
Norwegian University of Science and Technology (NTNU)
Trondheim, Norway
*emre.kantar@ntnu.no

***Abstract*—Breakdown strength (BDS) of the interface between the two solid dielectrics is much lower than the BDS of the bulk materials due to formation of microscopic cavities at the interface. The main motivation of this paper is to explore the impact of the applied contact pressure and composite elastic modulus on the AC tangential BDS of dry-mate, wet-mate and oil-mate solid-solid interfaces experimentally. In the experiments, two different contact pressures were applied using different mechanical loads with two different materials having different elastic moduli, i.e. cross-linked polyethylene (XLPE) and silicon rubber (SiR). Two rectangular prism shaped samples were placed between two vertical Rogowski shaped electrodes in air, water or oil. Field simulations were also performed on the test objects to assess the electric field distribution and they show a good agreement with the experiments. The experiments show that the elastic modulus, contact pressure and void-filling medium (air/water/oil) have a significant impact on the tangential BDS.**

Keywords—breakdown strength; dielectric breakdown; silicon rubber; surface breakdown; solid interface; XLPE.

I. INTRODUCTION

Cable connectors and terminations allow swift, reliable and in situ connection of units to main modules, providing adaptability and modularity of expensive equipment and cables. They are indispensable components because in some cases total system design is dictated by availability of connector technology [1, 2]. However, driving force to provide more power mandates significant and cost-effective developments in cable connector technologies, which should be able to withstand and operate under higher voltage levels/power ratings, higher temperatures and longer step-out lengths [1, 2].

A problem peculiar to any cable connector and termination is the existence of solid-solid interfaces between materials. The combination of two solid dielectrics increases the risk of interfacial tracking failure defined as formation of a conductive path due to the existence of microscopic cavities and imperfections (contaminant and water droplets) on the interface. These cavities/imperfections reduce the breakdown strength (BDS) of the interface considerably, particularly when the electric field has a tangential (longitudinal) component [1-3]. Although the magnitude of electric field is much lower than the dielectric strength of the bulk insulation, the existence of local microscopic cavities and imperfections at the interface cause electric field enhancements. The field enhancements are likely to result in initiation of partial discharge (PD) and when the PDs persist for a significant time, the discharge energy induces channels that bridge the electrodes and breakdown (BD) follows immediately [1-3].

Study of insulating materials and BDS of applications for power apparatus such as cables and accessories have been covered to a large extent in the literature. However, little is known about the features of solid-solid interfaces as they appear in connectors, as the majority of research articles focus on the complete designs of connectors as a whole without exercising due attention on the interfaces [4, 5]. Therefore, the specific parameters that influence the breakdown of solid-solid interfaces when the electric field has a component tangential to the interface must be examined separately. In [3, 4] the effect of contact pressure and surface roughness on the tangential BDS was studied and it was reported that a higher interfacial pressure and smoother surfaces lead to increase in the BDS. However, the interfaces formed by materials with different elastic moduli have not been investigated, although combination of different materials exists in subsea connectors.

The focus of this paper is to investigate the impact of the contact pressure together with the influence of composite elastic modulus and the void-filling medium on the tangential BDS of solid-solid interfaces experimentally. Two different contact pressures are applied using two different solid materials with different elastic moduli, namely cross-linked polyethylene (XLPE) and silicon rubber (SiR). In order to investigate the impact of the void-filling medium on the dielectric strength, air-filled (i.e. dry-mate), water-filled (i.e. wet-mate) and oil-filled (i.e. oil-mate) void cases are compared by repeating the same set of experiments.

II. THEORETIC BACKGROUND AND EXPERIMENTAL METHODS

A. Test Setup, Specimen Preparation and Data Handling

A simple illustration of the test arrangement along with the dimensions of the basic components is depicted in Fig. 1. In the setup, two rectangular shaped samples (4 mm x 55 mm x 25 mm) were placed on top of each other between two Rogowski shaped electrodes forming a 4.0 mm wide interface traversed by the tangentially applied field strength. XLPE samples were

The authors acknowledge the financial support of the Norwegian Research Council and the SUBCONN Project Consortium.

cut from the insulation of commercially available 145 kV power cables while the SiR samples (ELASTOSIL® LR 3003/60 A/B) were cast in the laboratory [2]. The desired contact pressure was exerted by pressing the samples against each other vertically using weights ranging from 3.5 kg to 26 kg. All breakdown tests were performed with the setup immersed in transformer oil to prevent any external flashover prior to breakdown (see Fig. 2). In order to prevent ingress of oil into the cavities, surface pressure was applied prior to filling the test chamber with the oil for dry-mate and wet-mate cases. Besides, the interface was subjected to the injection of tap water and insulating oil droplets with a definite volume (approx. 10 µl) using a laboratory pipette prior to the interface was formed for wet-mate and oil-mate cases, respectively. The 50 Hz AC voltage was generated using a 100 kV transformer and increased at a constant rate of 1 kV/s. For each test sample, 7-8 breakdown measurements were taken using a new pair of samples and the results were statistically evaluated using the two-parameter Weibull distribution. The adequacy of the two-parameter Weibull distribution was tested for each curve using the check curve provided in [6] and obtained goodness-of-fit (adequacy) parameter ρ are provided in the figures.

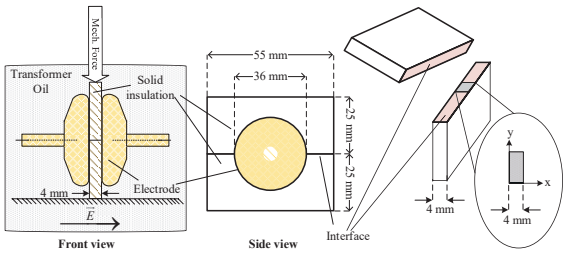

Fig. 1. Sketch of the test specimens with the Rogowski-shaped electrodes with their dimensions.

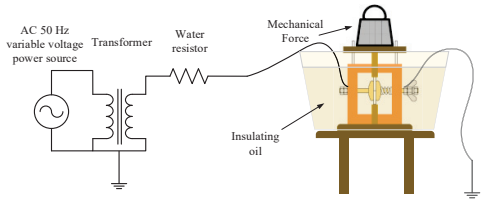

Fig. 2. Sketch of the experimental setup for AC breakdown voltage tests.

B. Contact Surface Preparation and Interface Modeling

The impact of surface roughness on the BDS was not examined in this work. Hence, surface roughness was kept constant and the surfaces of each of the XLPE and SiR samples were made plane and smooth by means of a rotating grinding/sanding disc using a SiC sandpaper with grit no. 500. The samples were sanded for approximately one minute with continuous flow of water to remove any by-products. Subsequently, the samples were rinsed in tap water and were left to dry. Then, the dry samples were cleaned using filtered compressed air before the clean samples were washed briefly in isopropanol. Finally, the samples were dried at room temperature. Fig. 3 shows the measured original surface profiles of a specimen after grinding using a 3D non-contact profilometer (Bruker 3D Optical). The assessment length of the profile is 0.13 mm, which is about 3% of the total width of interface (4 mm). A similar profile for the rest of the surface was observed. Five different surface measurements were obtained from different sections of the specimen and their mean value was computed. Regarding the obtained surface roughness analysis and the contact theory in [3], a simplified profile of contact asperities using an ideally flat and a rough surface (equivalent to two rough surfaces) can be modeled as shown in Fig. 4. In the subsequent sections, experimental results are interpreted using this model and the simulation model revealing the varying field strength in the cavities and on the contact spots is developed considering this model.

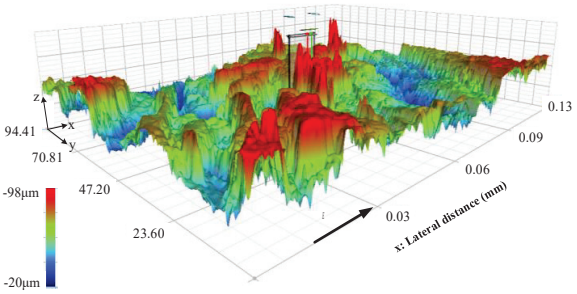

Fig. 3. The measured surface roughness profile of a specimen grinded with a 500 grit no. SiC sandpaper by Bruker 3D Optical Surface Profilometer.

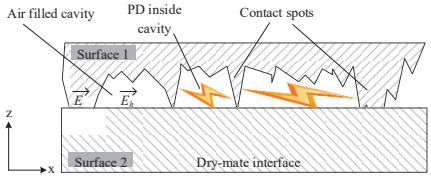

Fig. 4. The electrical model a dry-mate interface where $\vec{E}$ is the electric field strength on solid, $\vec{E_h}$ is the field strength inside the voids.

III. Experimental Results and Discussion

In this section, test results for the dry-mate and the wet-mate XLPE-XLPE, SiR-SiR and XLPE-SiR interfaces are presented. Separate results for the oil-mate interface follow in a similar manner. The results are compared in terms of the *63.2 percentile* values derived from Weibull plots. A brief overview of the experiments is tabulated in Table I.

TABLE I. Overview of the Experimental Study

Interface type	Contact Pressure [MPa]	
	Dry-mate	Wet-mate
XLPE-XLPE	0.27, 0.5 & 1.16	0.27, 0.5 & 1.16
SiR-SiR	0.16 & 0.27	0.16 & 0.27
XLPE-SiR	0.27	0.27

A. Dry-mate Surface Examination after Breakdown

Initiated PDs give rise to formation of a breakdown channel at the interface and the channel does not necessarily follow a straight line at the interface by tracing all the contact spots and the voids one by one. There are strong evidences on the broken down specimens revealing that breakdown channel propagates in such a way that it can evade the contact spots on the same direction (e.g. x-axis) acting as barriers and find the nearest voids or easier barriers (i.e. smaller contact spots) in the nearest vicinities and form the channel. In this case, all the voids on the string/channel become vented and the pressure inside them

remains at 100 kPa (1 bar) regardless of the applied contact pressure [3]. The images of broken down samples are shown in Fig. 5. These images support validity of the assumed model consisting of micro-voids and contact spots. Thus, enhanced field strength in the cavities and their resulting impact on the BDS can be associated with the assumed model in Fig. 4.

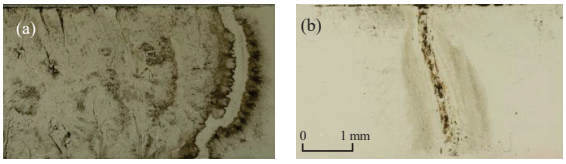

Fig. 5. Breakdown channels of a dry (a) XLPE interface (b) SiR interface.

B. Dry-mate vs. Wet-mate XLPE-XLPE Interface

Increasing the contact pressure from 5 to 11.6 bar (i.e. 132% increase) results in an 18% increase of the *63.2 percentile breakdown strength* (E_{63}) (see Fig. 6(a)). The small increase confirms the dependency of the BDS on the interfacial pressure of dry-mate XLPE samples since the impact of the increased pressure affects the cavity size on the interface. Furthermore, the presence of water at the interface has a detrimental effect on its BDS such that the resulting BDS of the wet-mate XLPE-XLPE interface is very low at 5 bar. In fact, they are comparable with the dielectric strength of air (about 2.12 kV_{rms}/mm [6]), showing that the water ingress is a critical concern of the connector design due to the high local field enhancement around the water-filled cavities ($\varepsilon_{r,water} \approx 80$ whereas $\varepsilon_{r,XLPE} \approx 2.3$ and $\varepsilon_{r,SiR} \approx 2.8$).

When the pressure is increased from 5 to 11.6 bar (132% increase), an increase by 68% of the E_{63} results. Consequently, the positive impact of pressure increase on the BDS of wet-mate XLPE-XLPE interface becomes evident. It can be argued that the increase in contact pressure removes more water from the interface, bringing the trend of the interface closer to that of dry-mate case —consisting of air-filled and water-filled cavities simultaneously— thus increasing the BDS significantly. In addition, Fig. 6 shows that the Weibull shape factor β (slope) relates to the width of 90% confidence interval, such that the higher β, the narrower the confidence bounds.

C. Dry-mate vs. Wet-mate SiR-SiR Interface

The BDS values of the dry-mate and wet-mate interface formed by the softer SiR are shown in Fig. 6(b). The pressure levels are considerably lower than that of in the XLPE-XLPE case since pressure higher than about 2.7 bar was unfeasible during experiments because of the considerable deformation of the silicon rubber. As the graphs show, increasing the pressure from 1.6 to 2.7 bar (i.e. 70% increase) causes a 44% increase of the E_{63}, clearly showing that the BDS augments significantly with the increased pressure for the SiR-SiR interface. The wet-mate SiR-SiR interface was also tested at 1.6 bar and 2.7 bar. The negative impact of the presence of water-filled voids is also quite evident due to the resulting local field enhancements. Most of the recorded BDS values are comparable with that of air, with the lowest being about 2 kV_{rms}/mm. Moreover, increasing the pressure from 1.6 bar to 2.7 bar has a limited effect on the BDS of the wet-mate SiR-SiR interface such that the E_{63} increases only about 20% against the pressure increase of 69%. As a result, it can be inferred that the wet SiR-SiR interface yields a poor BDS increase against the pressure increase unlike the XLPE-XLPE wet-mate case. It can be argued that a softer material (i.e. lower elastic modulus) tends to be less hydrophobic and hence, less of the water droplets are pushed away the interface with the pressure increase.

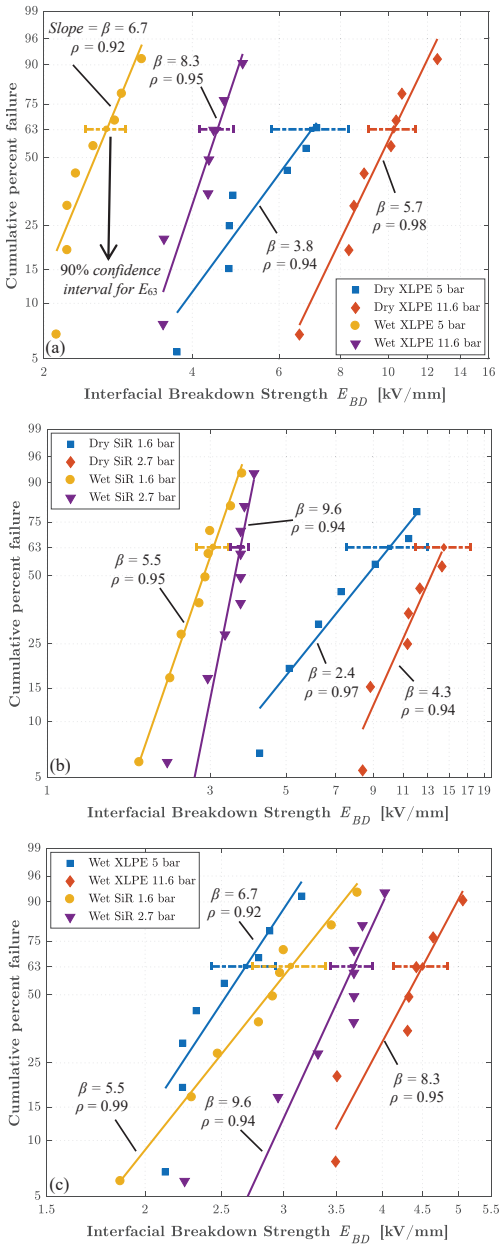

Fig. 6. Breakdown strength of dry-mate and wet-mate (a) XLPE-XLPE interface at 0.5 MPa (5 bar) and 1.16 MPa (11.6 bar) (b) SiR-SiR interface at 0.16 MPa (1.6 bar) and 0.27 MPa (2.7 bar) (c) Comparison of wet-mate XLPE-XLPE and SiR-SiR interfaces.

The physical reason for the increase in BDS with the applied pressure increase under all cases can be attributed to the mean diameter size of the voids as follows: Increased

contact pressure pushes the tall summits of the contact spots (see Fig. 4) further, yielding smaller voids and hence higher BDS according to the Paschen's curve. Similarly, a softer material enables the tall summits to be compressed even further compared to a harder material resulting in much smaller cavities providing a higher BDS.

Comparing the Weibull plots of the XLPE-XLPE and the SiR-SiR under wet-mate conditions (see Fig. 6(c)), it is noted that the BDS of the XLPE-XLPE interface is more sensitive to the pressure change in terms of the E_{63} than the SiR-SiR is. However, in both cases the BDS is relatively low, revealing the detrimental effect of local field enhancements on the BDS of the interface. Nevertheless, the wet-mate XLPE-XLPE at 11.6 bar case revealed that the increase in pressure (from 5 bar to 11.6 bar) appears to push more of the water droplets off the interface, and hence, the BDS reaches higher values. This assumption was also examined using the breakdown channel images under a microscope (see Fig. 5). Further details can be found in [1, 2] while the simulation studies of the field enhancements for the dry and wet-mate cases are shown in Section IV.

D. Dry-mate vs. Wet-mate XLPE-SiR Interface

In Fig. 7, the Weibull plots representing the BDS of all the dry-mate and wet-mate interfaces at 2.7 bar are compared. As can be seen, the presence of SiR makes a significant difference with a greater measurement dispersion in such a way that the E_{63} value of the dry-mate XLPE-SiR interface increases by 43% compared to that of dry-mate XLPE-XLPE whereas it is 39% lower than that of dry-mate SiR-SiR.

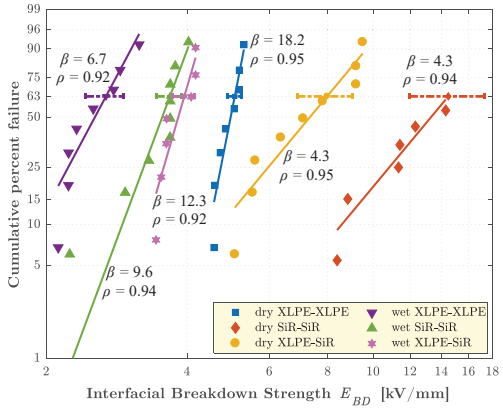

Fig. 7. Breakdown strengths of dry and wet-mate interfaces at 0.27 MPa (2.7 bar) with 90% confidence intervals for E_{63}.

In the wet-mate case, it is obvious that the combination of the two different materials has the highest E_{63}. Yet, the 90% confidence bounds of the E_{63} for the wet-mate SiR-SiR and XLPE-SiR are overlapping partly, thus it is difficult to claim that one is better than the other is, although the XLPE-SiR have a slightly higher value. However, the XLPE-XLPE interface having the lowest values under dry-mate and wet-mate might be associated with the different elastic modulus features (tensile elasticity) of the XLPE and SiR. In addition, the Weibull shape factor β of the XLPE and SiR lines deviate much less from each other than what the case is for the dry-mate interface, yielding that the water droplets override the mechanism taking place in dry-mate case. Hence, the dominating mechanism in the wet-mate case shows a stable trend regardless of the type of the material.

E. Dry-mate vs. Wet-mate vs. Oil-mate Interfaces

In this section, the BDS of the oil-mate XLPE-XLPE and SiR-SiR are presented. Fig. 8 depicts the results for XLPE-XLPE at 5 bar and SiR-SiR at 1.6 bar. As can be seen, the presence of oil at the interface results in much higher BDS values, particularly in the SiR-SiR case. For the XLPE-XLPE case, when comparing the dry-mate with the wet-mate interface, there is a decrease of 42% of the E_{63} value, while comparing the dry-mate with the oil-mate interface, the E_{63} increases about 178%.

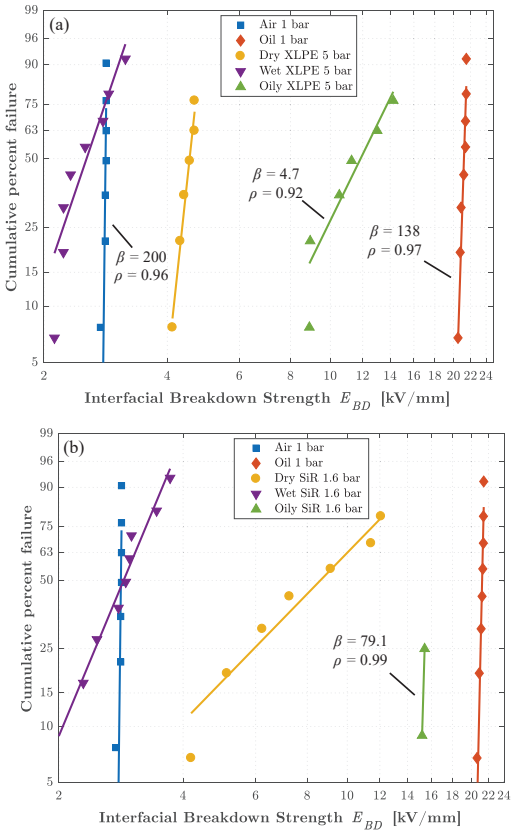

Fig. 8. BDS of the dry-mate, wet-mate and oil-mate interfaces (a) XLPE-XLPE interface at 0.5 MPa (5 bar) (b) SiR-SiR interface at 0.16 MPa (1.6 bar) along with the BDS of air and transformer oil at 100 kPa (1 bar) where E_{63} = 2.9 kV_{rms}/mm (air) and 21.3 kV_{rms}/mm (oil).

For the SiR-SiR case, when comparing the dry-mate interface with the wet-mate, water droplets appear to cause a substantial decrease of 70% of the E_{63} value. On the other hand, from dry-mate to oil-mate interface, there is a significant increase of 56% of the E_{63}. In some of the experiments, the BDS of the oil-mate SiR-SiR interface was so high that a flashover occurred around the electrodes in the oil, thus not at the interface. This data were then recorded as singly censored data and treated accordingly [6]. An experiment of SiR-SiR at 0.27 MPa (2.7 bar) was also attempted, but breakdown never occurred at the interface (at about 90 kV_{rms} when the BDS of

the transformer oil around the electrodes was reached). The Weibull plots of air and transformer oil at 100 kPa (1 bar) are also included in Fig. 8 for comparison. It unveils that air-enclosed cavities limit the BDS of the interface remarkably and the BDS deteriorates when water ingresses at the interface. Besides, varying results amidst dry, wet and oil-mate cases validate the competency of the constructed setup, which succeeded in preventing oil ingress for dry and wet-mate cases.

IV. Simulation Studies

The laboratory test setup was also modeled in Comsol Multiphysics® and simulation studies covering dry-mate and wet-mate interfaces were conducted to analyze the electric field distribution at the interface. Two-dimensional approximation was used to simulate the test cases. In the simulations, given dimensions of the specimens and electrodes were adopted (Fig. 1), applied AC voltage U_{AC} was fixed to 30 kV_{rms} and the applied contact pressure was assumed 2.7 bar.

Using the contact theory in [3] (at 2.7 bar) and the simplified profile of contact asperities using an ideally flat and a rough surface (Fig. 4); the obtained surface roughness data (see Fig. 3) was processed. Then, the resulting flat-rough model of the interface was imported (3% of the entire interface) into the simulation model and the remaining portion was modeled as the ideal flat surface. Fig. 9(a) displays the electric field strength at the dry-mate interface where it is uniform except at the part where the obtained roughness pattern had been implemented. Fig. 9(b) views the enhanced field strength in detail where the dielectric strength of the XLPE and the SiR are $2.3\varepsilon_0$ and $2.8\varepsilon_0$, respectively. Considering the sizes of micro-voids (Fig. 3) along with the Paschen's curve for air-filled cavities in [1], it can be inferred that the enhanced field of 8 kV_{rms}/mm (Fig. 9(b)) can initiate PDs at a lower voltage and an eventual BD might follow at a much lower field strength.

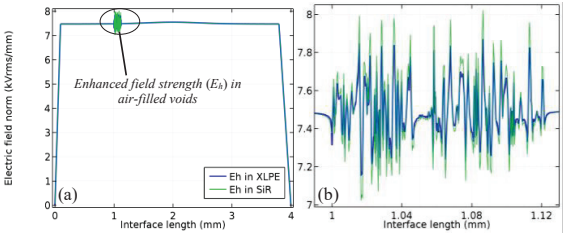

Fig. 9. (a) Enhanced field strength (E_h) in air-filled voids. (b) Zoomed view.

Fig. 10(a) depicts the field strength in the cavities for the wet-mate case where all the voids are filled-with tap water with $\varepsilon_r = 80$. Since the dielectric permittivity of water is much higher than that of the insulation, the field strength inside the voids reduces to about 0.2 kV_{rms}/mm, resulting in negligible voltage drops over the voids. Thus, it can be inferred that water-filled cavities reduce the nominal interface width and the effective interface width becomes much shorter in practice. As a result, the applied voltage cumulates at the contact spots and the field strength enhances to 2-3 times of the BDS in the insulation (7.5 kV_{rms}/mm) as seen in Fig. 10(b). Considering the enhanced BDS at the contact spots, it is likely to expect the BDS of the wet-mate interface to become extremely low accounting for the very low BDS values obtained in the experiments.

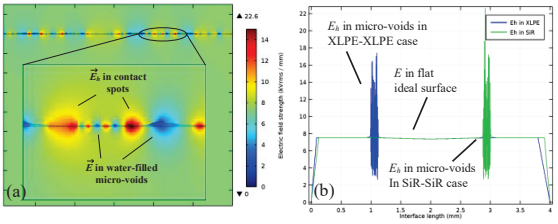

Fig. 10. (a) Field gradient. (b) Enhanced field strength of water-filled micro-voids at 0.27 MPa (2.7 bar) with $U_{AC} = 30$ kV_{rms}.

The aggregate impact of having a rough surface can be further analyzed such that the experimentally obtained E_{63} value (~ 5.5 kV_{rms}/mm) of XLPE-XLPE dry-mate interface at 1.16 MPa (11.6 bar) is used when calculating the field strength inside the voids by means of

$$\vec{E}_h = \left(3\varepsilon_r \big/ 1+2\varepsilon_r\right)\vec{E}, \qquad (1)$$

where ε_r stands for the dielectric strength of the insulation [1].

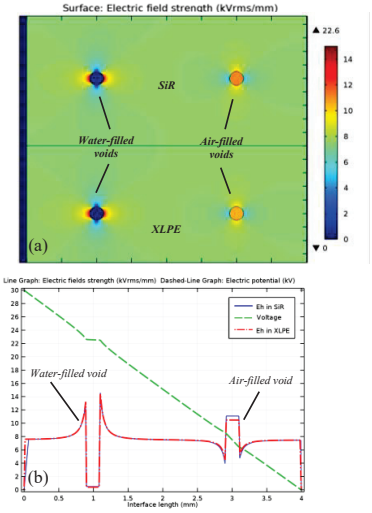

Fig. 11. (a) Field gradient. (b) Enhanced field strength of air-filled and water-filled voids at 0.27 MPa (2.7 bar) with $U_{AC} = 30$ kV_{rms}.

Equation (1) yields $E_h / E = 1.23$ and 1.27 for XLPE and SiR, respectively. Then, a mean diameter of $d = 0.17$ mm is attained from the Paschen's curve at 100 kPa (assuming vented spherical voids and the pressure inside the voids remains at 100 kPa). Thus, the test results were emulated in the simulation (see Fig. 11) by adding a single sphere-shaped void with the diameter of 0.17 mm, which can be regarded as the sum of all the voids on the interface according to Paschen's law. Two identical voids were placed in the XLPE and the SiR (one air-filled, one water-filled) to examine the field gradient inside the voids for the dry-mate and wet-mate cases. As depicted in Fig. 11, high dielectric permittivity of water gives rise to negligible voltage drops inside the voids, thus the BDS becomes almost zero. Yet, the field strength upsurges on the contact spots where the left and right sides of the spherical voids are in contact with the insulation. Accordingly, the sharp edges of the field waveform in Fig. 11(b) account for the field enhancement

on the contact spots. In contrast, the field strength is enhanced inside the spherical air-filled voids as a function of (1). As a result, the voltage drop inside the cavity is higher (Fig. 11(b)). In conclusion, conducted simulation study aids significantly on revealing the potential ongoing mechanisms at the dry and wet-mate interfaces. They are all in line with the test results.

V. Conclusion

The tangential BDS of the solid-solid interfaces was shown to be governed by the BDS of the micro voids as a function of void-filling medium and contact pressure. A lower elastic modulus made a significant improvement in the BDS since it results in smaller voids, in turn yields a higher BDS in line with Paschen's curve. However, the BDS values of SiR-SiR interface disclosed wider scatter with much wider 90% confidence intervals that increases the uncertainty when designing equipment. In oil-mate case, the insulating oil filled the cavities on the interface and hence the BDS was improved significantly. Thus, air-filled cavities are the limiting factor in the overall dielectric strength of the interface where the water ingress degrades the BDS even further due to the strong local field enhancements at the contact spots unveiled by the field calculations. In brief, the examination of solid-solid interfaces in this work can be considered useful for any insulating equipment containing solid interfaces.

References

[1] E. Kantar, D. Panagiotopoulos, and E. Ildstad, "Factors Influencing the Tangential AC Breakdown Strength of Solid-Solid Interfaces," *IEEE Trans. Dielectr. Electr. Insul.,* In press (accepted).

[2] D. Panagiotopoulos, "AC Electrical Breakdown Strength of Solid Solid Interfaces: A study about the effect of elasticity, pressure and interface conditions," M.S. thesis, Dept. Elect. Eng., TU Delft, 2015.

[3] M. Hasheminezhad and E. Ildstad, "Application of contact analysis on evaluation of breakdown strength and PD inception field strength of solid-solid interfaces," *Dielectrics and Electrical Insulation, IEEE Transactions on,* vol. 19, pp. 1-7, 2012.

[4] D. Fournier and L. Lamarre, "Interfacial breakdown phenomena between two EPDM surfaces," in *Dielectric Materials, Measurements and Applications, 1992., Sixth International Conf. on*, 1992, pp. 330-333.

[5] T. Takahashi, T. Okamoto, Y. Ohki, and K. Shibata, "Breakdown strength at the interface between epoxy resin and silicone rubber-a basic study for the development of all solid insulation," *Dielectrics and Electrical Insulation, IEEE Transactions on,* vol. 12, pp. 719-724, 2005.

[6] "IEC/IEEE Guide for the Statistical Analysis of Electrical Insulation Breakdown Data (Adoption of IEEE Std 930-2004)," *IEC 62539 First Edition 2007-07 IEEE 930,* pp. 1-53, 2007.

Paper III

E. Kantar, F. Mauseth, E. Ildstad, and S. Hvidsten, "Longitudinal AC breakdown voltage of XLPE-XLPE interfaces considering surface roughness and pressure," IEEE Trans. Dielectr. Electr. Insul., vol. 24, no. 5, pp. 3047–3054, Oct. 2017.

Paper IV

E. Kantar, F. Mauseth, E. Ildstad, S. Hvidsten, “A stochastic model for contact surfaces at polymer interfaces subjected to an electrical field”, Tribology Int., vol. 127, pp. 361–371, 2018.

Tribology International 127 (2018) 361–371

Contents lists available at ScienceDirect

Tribology International

journal homepage: www.elsevier.com/locate/triboint

A stochastic model for contact surfaces at polymer interfaces subjected to an electrical field

Emre Kantar[a,*], Sverre Hvidsten[b], Frank Mauseth[a], Erling Ildstad[a]

[a] Department of Electric Power Engineering, NTNU, O.S. Bragstads Plass 2E, 7491 Trondheim, Norway
[b] SINTEF Energy Research, Stiftelsen SINTEF, P.O. Box 4760 Torgarden, 7465 Trondheim, Norway

ARTICLE INFO

Keywords:
Cables
Contact surface
Contact mechanics
Elastic
Optical microscopy
Polishing
Polymer
Texture
XLPE

ABSTRACT

Morphology of the contact area between solid insulation materials ultimately determines the short- and long-term electrical properties of the complete insulation system. The main purpose of this paper is to propose a statistical model to examine the real area of contact between solid dielectric surfaces and secondly to verify and correlate the model outputs with experiments. The model computes real area of contact, number of contact spots and average cavity size at the interface as a function of elasticity, contact force and surface roughness. Then, using the average cavity size and the Paschen's law, the discharge inception field of the cavity (CDIE) is estimated. AC breakdown strength (BDS) testing of solid-solid interfaces was carried out, where cross-linked polyethylene (XLPE) samples with four different surface roughnesses were tested at various contact pressures.

Following the increased contact force, the calculated average cavity size decreased by a factor of 4.08 − 4.82 from the roughest to the smoothest surface, corresponding to increased CDIEs by a factor of 2.01 − 2.56. Likewise, the experimentally obtained BDS values augmented by a factor of 1.4 − 1.7 when the contact pressure was elevated from 0.5 MPa to 1.16 MPa.

A linear correlation between the CDIE and BDS was assumed, yielding a correlation coefficient varying within 0.8 − 1.3. When the 90% confidence intervals were considered, the range reduced to 0.86 − 1.05. This correlation suggests that interfacial breakdown phenomenon is strongly related to the interfacial cavity discharge. Hence, the proposed model is verified with experiments.

1. Introduction

The series connection of two or more dielectric materials constitute the electrical insulation system in most high voltage apparatus. The alternating current (AC) breakdown strength (BDS) of insulation systems is limited by the lowest BDS of either the bulk insulating materials or the interface between the adjacent insulating materials. The interfacial breakdown between two solid insulating materials is complex and accounts for one of the principal modes of failure for power cable joints [1]. The interface increases the risk of reduced/low BDS due to the local electric field enhancements caused by the imperfections at the interface such as microscopic cavities, protrusions and impurities [2–6].

Cable accessories as power cable joints, outdoor composite terminations, and subsea connectors have solid-solid interfaces, which undergo electrical stress during service life by the tangential component of the electric field [3]. Hence, it is very important to have a high surface BDS. By studying and identifying the parameters affecting the breakdown strength of such interfaces cost-effective, long-lasting, and most importantly, reliable high voltage apparatus and equipment can be developed [2–7]. The impacts of contact pressure and surface roughness on the interfacial BDS were studied in Refs. [1–5], where a higher interfacial pressure and a smoother surface reportedly led to an increased tangential BDS. However, mostly only empirical studies have been performed using the complete designs of connectors, accessories, and apparatus. The polymer interfaces should be scrutinized separately and diligently by considering the contact surface texture, type of the contact (i.e., elastic or plastic), surface roughness, elasticity modulus and applied contact force. Thus, comprehensive theoretical models incorporating these parameters should be developed in addition to the experimental studies in the literature because the understanding of tribological principles dominating in solid interfaces paves the path for the successful design of advanced apparatus.

The primary motivation of this paper is to model the contact surfaces between solid materials as a function of the applied mechanical contact pressure, surface texture/roughness, and elastic modulus using the tribological principles presented in Refs. [8–15]. For this purpose, a stochastic model of multiple-asperity dry contacts formed at a solid-solid interface is developed in 2 − D, which estimates the average size of

* Corresponding author.
E-mail address: emre.kantar@ntnu.no (E. Kantar).

https://doi.org/10.1016/j.triboint.2018.03.003
Received 15 October 2017; Received in revised form 30 January 2018; Accepted 2 March 2018
Available online 16 March 2018
0301-679X/

cavities at the given interface. Then, discharge inception field of the average-sized cavity (CDIE) is calculated by employing the Paschen's law. To test the validity of the model, experiments on the tangential AC BDS of solid-solid interfaces under various contact pressure were performed. Subsequently, the correlation between the calculated CDIE values and the experimental BDS is discussed in detail. In the experiments, cross-linked polyethylene (XLPE) samples with four different surface roughness were used to realize the polymer interfaces since XLPE can withstand high pressures without any significant deformation over a broad contact pressure range experienced in real-life applications. Besides, XLPE is one of the most prevalent materials preferred in the cable industry and is readily available for research activities.

2. Background

2.1. Contact surfaces of dielectric materials

Although cable accessories are prefabricated and pretested for partial discharges (PD), they are assembled/fitted on site under sub-optimal and less controllable conditions [3]. Assembly procedure, thus, does not incorporate an automated process under clean room conditions, which makes them somewhat vulnerable to bad installations. As a consequence, interfacial surfaces become rife with imperfections such as cavities, protrusions, and contaminants/impurities [1]. The existence of such imperfections at the interface causes local electric field enhancements [3,16]. They are, hence, likely to initiate partial discharges (PD) and trigger electric treeing, which might give rise to a premature tracking failure [1–6,17,18].

The cavities on a solid dielectric surface have various sizes and distribution depending on the methods concerning surface polishing, manufacturing, and assembly [3]. When two nominally flat surfaces are assembled, surface asperities cause contact to occur at discrete contact spots whereas manifold cavities arise between the contact spots as schematically represented in Fig. 1. The real contact area is, thus, much smaller than the nominal area. A typical cavity formed at the interface is much larger in the tangential direction ($x-$axis or y-axis) as indicated in Fig. 2 [10]. The parameters that influence the distribution and size of the contact spots and the cavities are discussed in the next section.

2.2. Electrical properties of solid-solid interfaces

When the interface is assembled under dry conditions, the cavities are filled with air. The applied voltage is then distributed along the strings of the cavities and contact spots. The exact size and number of the cavities are however unknown and depend heavily on the following

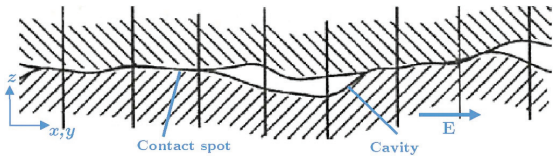

Fig. 2. An illustration of the cavities at the interface in 2−D profile [11].

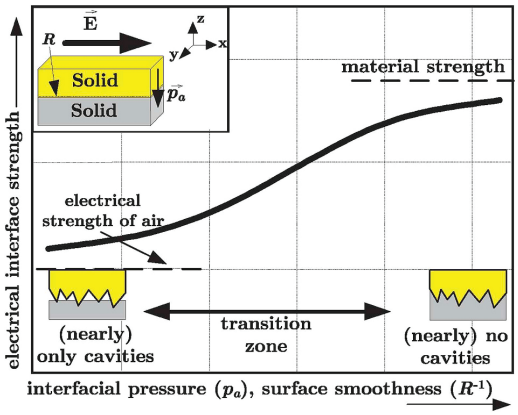

Fig. 3. The relation between tangential breakdown strength of interfaces, interfacial pressure and the surface roughness/smoothness [19].

parameters: the elasticity of the material, the applied contact pressure, and the surface roughness as depicted in Fig. 3.

The interfacial breakdown voltage and time to breakdown are strongly dependent on these parameters. The interfacial BDS is, for instance, slightly higher than that of air whereas it is not as strong as the bulk material strength, even under a higher contact pressure or a smoother surface as shown in Fig. 3. Besides, the increased contact pressure causes the interfacial BDS to become higher because the increased pressure further deforms the tips of the protrusions and makes the cavities smaller that will increase the interfacial BDS [19]. Likewise, smoother surfaces indicate as similar an influence on the BDS as the increased pressure, due to the mitigated cavity size at the interface. Since the dielectric strength of air is much lower than that of the bulk insulation, the dielectric breakdown will hence first occur in the air-filled cavities, followed by a complete flashover.

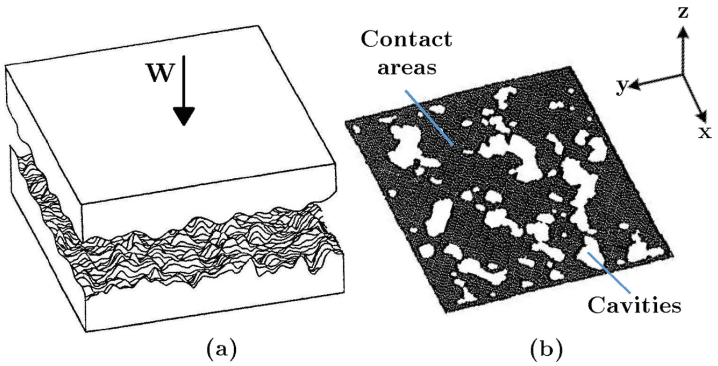

Fig. 1. Schematic drawing of: (a) Two 3-D rough surfaces in contact. (b) Corresponding contact areas/spots [10].

2.3. Approaches to rough surfaces

There are various approaches to the description of rough engineering surfaces in the history of tribology, such as statistical approaches, fractal approaches, approaches based upon the surface power spectrum [20] as well as numerical deterministic roughness models [21]. One of the earliest statistical models of contact between rough elastic solids was offered by Zhuravlev (1940) [22]. Johnson (1975) [23] and Greenwood (1990) [24] are among the first scientists having cited the Zhuravlev model. With the aim of developing the Zhuravlev model, Greenwood and Williamson [12] later proposed a contact model of nominally flat surfaces, where both Gaussian and exponential distribution of the asperity peaks were tested to show that the real contact area is proportional to the applied load. More recently, Borodich's introduction to Zhuravlev's historical paper [25] highlighted that the Greenwood-Williamson's theory (1966) [12] assuming the asperities having the same radii with various heights is a development of Zhuravlev's model for purely elastic contact published in 1940 [22]. In fact, the Greenwood and Williamson [12] modified the Zhuravlev model by covering elasto-plastic transition of asperities. On the other hand, Archard [26] worked on multilevel structure of the roughness where a sphere of radius consists of manifold spherical protuberances whose radii are much smaller. The idea of iterative hierarchical structure of roughness was further developed in Ref. [27]. Also, Nayak [28] and Whitehouse and Archard [29] studied modeling of surfaces as random processes; however, it later turned out that the mean radius of curvature is scale dependent [20]. With the aim of providing a scale-invariant characterization of roughness to obtain the contact area more accurately, fractal approaches have been introduced more recently [20,30,31]. Fractal characterization supplies information of the surface roughness at all the length scales that depict the fractal behavior [31]. It was, however, argued that empirical fractals do not yield scale-independent parameters for description of rough surfaces [20,32]. Thus, fractal approach is still an active area of research [20]. Last but not least, approaches to surface roughness based on the surface power spectrum have not been widely approved due to lack of mathematical justification [20].

The Greenwood and Williamson model [12] together with Bhushan's modifications [10] are adopted to develop the proposed statistical model in the next section.

3. Stochastic modeling of multiple asperity dry contacts of rough surfaces in tribology

3.1. Statistical analysis of surface contacts

If the two rough surfaces as depicted in Fig. 4, which are both nominally flat, are brought in contact until their reference planes are separated by a distance d, numerous discrete contact spots then arise at those asperities whose total heights $z_1 + z_2$ are greater than d [8–10]. Greenwood and Williamson [12] analyzed a rough surface against a smooth surface, where the contacts are either elastic or plastic, and stated that:

- the rough surface incorporates a large number of asperities, which are of spherical geometry at least near their summit;
- asperities on each surface have a constant summit radius, whereas their heights vary randomly;
- most surfaces found in engineering applications have normally distributed asperities and peak heights.

Williamson et al. [13] addressed that assessing surfaces with cumulative processes (either single-point processes or extreme-value processes) resulted in a Gaussian-height distribution, whereas peak heights had a Gaussian distribution in all cases. On the other hand, Greenwood and Tripp [15] studied the contact surface of two rough surfaces as opposed to examining one rough surface against a nominally flat surface as performed in Greenwood and Williamson [12]. There, contact spots occur on the summits of the two adjacent hills since the asperity pairs are not aligned. Based on this, they discovered that as long as peak-height distribution is Gaussian, the asperity shape and whether the asperities exist on one or both surfaces are unimportant. In the light of this finding, Bhushan [9] addressed that the assumption of the spherical asperity tips for the sake of simplicity (first bullet point) does not affect real-area calculations. Besides, Greenwood and Tripp [15] showed that the contact of two rough surfaces could be reduced to an equivalent sum surface, consisting of a single, rough surface with a smooth rigid plane. O'Callaghan and Cameron [33] and Francis [34] also published supporting results such that the contact of two rough surfaces negligibly differs from the sum surface consisting of a perfectly smooth and an equivalent rough surface. The asperity-peak curvature, β_m of the equivalent rough surface (sum surface) is then defined as the sum of the asperities of two rough surfaces:

$$1/\beta_m = 1/\beta_{m1} + 1/\beta_{m2}. \tag{1}$$

Also, elementary statistics suggests that if the peak-height distributions of two rough surfaces are independent (as is likely when two surfaces are prepared separately) and are distributed randomly (not necessarily Gaussian) with standard deviations of the asperities σ_{p1} and σ_{p2}, the distribution of the equivalent rough surface will have a standard deviation of σ [9,10]:

$$\sigma_p = \sqrt{\sigma_{p1}^2 + \sigma_{p2}^2}. \tag{2}$$

When the contact pressure between the two contacting samples is applied, elastic deformation initially takes place as a function of their Young's moduli of elasticity [12]. As the load is further increased, one of the two samples begins to deform plastically. The load at which the plastic flow or yield begins depends on the yield point of the softer material in a simple tension test via a suitable yield criterion [10,12]. Subsea connectors, for instance, experience up to 30-MPa-hydraulic pressure in a 300-m-deep seabed [35]. In the experiments, the performed contact pressure values were selected accordingly, which were within the elastic contact region for the XLPE samples (plastic flow after 44−MPa pressure). Therefore, the next section covers only elastic contacts.

3.2. Elastic surface contacts

In the light of the assumptions/simplifications made by Greenwood

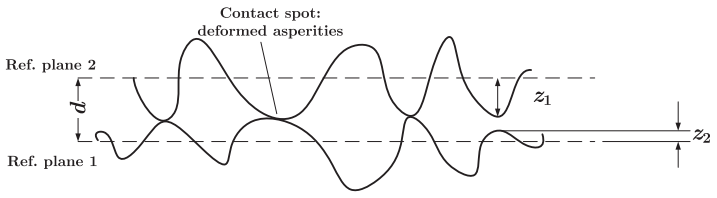

Fig. 4. Contact of two rough surfaces [9].

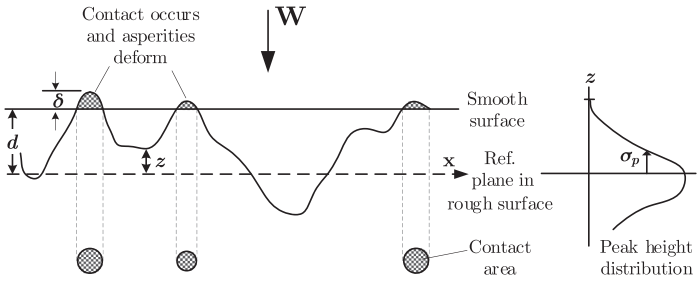

Fig. 5. Schematic drawing of the contact between a rough surface and a smooth surface (rigid plane) [10].

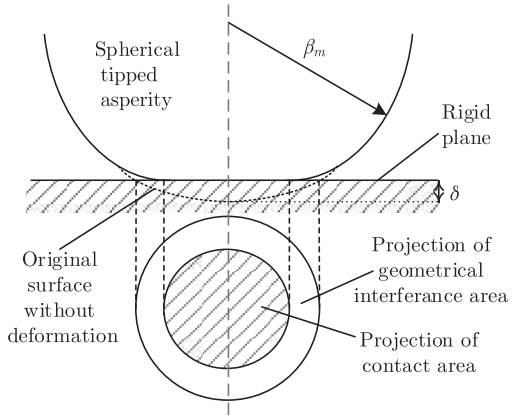

Fig. 6. Contact area between a spherical asperity and a rigid plane, which is circular $\pi\beta_m\delta$ with the radius of $a = \sqrt{\beta_m\delta}$ [14].

and Williamson [12], Bhushan [10] showed that the apparent pressure p_a, mean real pressure p_r, (elastic) real area of contact , the number of contact spots n, and mean asperity real area of contact as a function of separation d can be calculated. For this purpose, the contact between a plane and a nominally flat surface incorporating numerous spherically tipped asperities of the same radius β_m was considered with their peak heights represented by a probability density function of $p(z)$ as shown in Fig. 5. Contact mechanics of an individual cavity under a definite load is known from the Hertzian equations [12,36], in which the contact radius a, area A_i, and load W_i are represented in terms of total peak displacement δ. Each elastic contact area for a peak displacement δ equals to $A_i = \pi\beta_m\delta$ and is circular with the radius $a = \sqrt{\beta_m\delta}$ as depicted in Figs. 5 and 6; whereas, the load is given by $W_i = (4/3)E'\beta_m^{1/2}\delta^{3/2}$ [36].

When two surfaces are brought to contact until their reference planes are separated by d, contact spots will arise at any asperity whose height was formerly greater than d. Thus, the probability of having a contact at a given asperity height z is [10,12,36]:

$$P(z > d) = \int_d^\infty p(z)dz. \tag{3}$$

Moreover, if there are N asperities in total, the expected number of contacts n will then become

$$n = N\int_d^\infty p(z)dz. \tag{4}$$

In addition, since the total displacement δ is equal to $z - d$, the total real area of contact becomes

$$A_{re} = \pi N\beta_m \int_d^\infty (z - d)p(z)\,dz. \tag{5}$$

Similarly, the expected total load ($W = NW_i$) is

$$W = \frac{4}{3}NE'\beta_m^{1/2}\int_d^\infty (z - d)^{3/2}p(z)\,dz, \tag{6}$$

where E' is the composite/effective elastic modulus (i.e., Young's modulus) of two materials in contact. Effective elastic modulus can be calculated by using elastic modulus of each surface in contact E, using the relation of

$$\frac{1}{E'} = \frac{1}{2}\left(\frac{1 - \nu_1^2}{E_1} + \frac{1 - \nu_2^2}{E_2}\right), \tag{7}$$

where E_1, ν_1 and E_2, ν_2 are the elastic modulus in Pa and Poisson's ratio of each material, respectively [21]. Note that Eqs. (3) – (6) hold for any type of surface peak-height distribution. For instance, in the case of Gaussian peak-height distribution:

$$p(z) = \frac{1}{\sigma\sqrt{2\pi}}\, e^{-\frac{1}{2}\left(\frac{z-\mu}{\sigma}\right)^2}, \tag{8}$$

where μ is expected value and σ^2 is variance of the random variable. Likewise, in case of an exponential asperity height distribution $p(z)$ becomes: $p(z) = \lambda e^{-\lambda z}$, where λ is the rate parameter provided that $\lambda > 0$.

Bhushan [8–10] manipulated the above formulae by introducing non-dimensional variables and standardized probability density functions, and then correlated the real area of contact with the nominal contact area A_a in the elastic regime as:

$$A_{re} \cong 3.2\frac{p_a A_a}{E'\sqrt{\sigma_p/\beta_m}}, \tag{9}$$

where p_a is the apparent contact pressure in Pa and $p_a = W/A_a$ with W being the exerted force in N and A_a in m^2. The expected number of contact spots n is then yielded as

$$n = 1.21\eta A_a\left(\frac{p_a}{\eta\sigma_p\beta_m E'\sqrt{\sigma_p/\beta_m}}\right)^{0.88}, \tag{10}$$

where η stands for the surface density of asperities [8–10]. With the help of Eqs. (9) and (10), the number of contacting points and the area that the contact spots take up as a fraction of the nominal contact area can be computed.

3.3. Average size of air-filled cavities

By further manipulating Eqs. (9) and (10), the total area the interfacial cavities occupy could also be computed. As stated in Section 3.1, the equivalent rough surface simplification does not affect the real area calculation [15]. In this study, we aim to develop a simple, two-dimensional contact surface model. This model incorporates the average cavity size for simplicity. To determine the types of cavities that exist on polymer surfaces, surface morphology of a polished XLPE sample is examined by following the methodology described in Section 5.

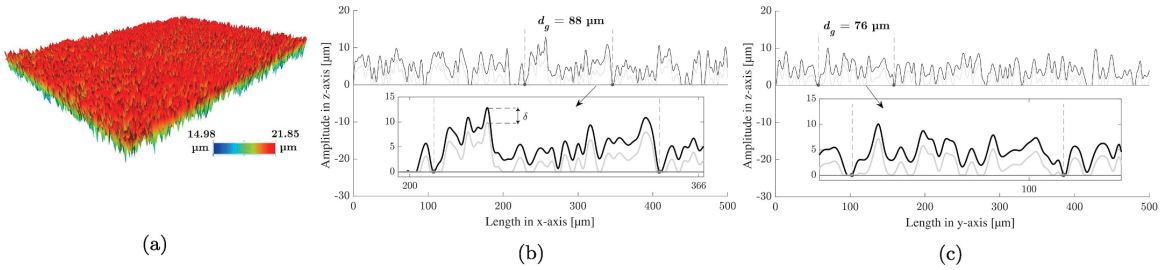

Fig. 7. (a) Surface profilometer scan in 3 − D. Interface between an equivalent rough surface and a perfectly smooth plane: (b) Cursor x−axis data. (c) y−axis data.

Fig. 7(a) shows the obtained three-dimensional surface profile whereas Fig. 7(b) and (c) depict two-dimensional profiles at the cursor position in x− and y−axes, respectively. It should be noted that these profiles account for the interface between the equivalent rough surface and the perfectly smooth plane. The gray-solid lines represent the displaced asperity position under a heavier load, whereas the difference between the lines is the peak displacement δ. The details on how to transform two rough surfaces into an equivalent rough surface and a smooth rigid plane can be found in Ref. [37].

What is observed in Fig. 7(b) and (c) is that the surface topographies both in the x− and y−axes have similar distributions of peaks and valleys with comparable amplitudes i.e., isotropic, and the cavities formed in xz− or yz−planes can be approximated with an ellipsoid whose length parallel to the electric field (d_g) is approximately 8 − 9 times larger than the length normal to the field (h_z). However, in addition to the cavity shape, the cavity size parallel to the electric field component is of importance when determining the CDIE because the minimum value of CDIE is associated with the maximum path length in the field direction (critical avalanche length) [18]. Thus, the assumed interfacial cavity can be illustrated as in Fig. 8, whose tangential length is much larger than the height h_z.

As the average cavity shape is defined, the cavity area on the xy−plane should be determined next. For simplicity, the projection area on the xy−plane is considered square with the side length . A cavity in 3 − D can, thus, be envisaged as an ellipsoid whose height h_z is much smaller than its side lengths ( ). On that account, is calculated as follows:

$$\sum_{j=1}^{n} A_{cav,j} = A_a - A_{re}, \tag{11a}$$

$$\overline{A}_{cav} = \frac{A_a - A_{re}}{n}, \tag{11b}$$

$$d_g = \sqrt{\frac{A_a - A_{re}}{n}}, \tag{12a}$$

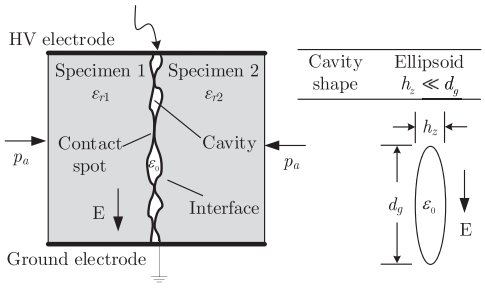

Fig. 8. Defined cavity shape at the polymer interface.

$$d_g = \frac{\left(E'\sqrt{\frac{\sigma_p}{\beta_m}} - 3.2p_a\right)^{0.5} \beta_m^{0.47}\sigma_p^{0.41}}{\sqrt{1.21}\,E'^{0.06}\eta^{0.06}p_a^{0.44}}, \tag{12b}$$

where $A_{cav,j}$ and $\overline{A}_{cav}$ stand for the respective area of the j^{th} cavity and the average cavity area, respectively.

The three surface topography parameters σ , β_m and η in Eq. (12b) need to be determined to calculate the average cavity size . For that purpose, the motif profiles namely, roughness and waviness profiles, proposed in Refs. [38,39], are employed as explained in the following section.

3.4. Motif profiles: roughness and waviness

Motif parameters offer a statistical description of asperity shapes and locations spread out on a broad range of micro-geometry from periodic to random profiles, where the primary asperities on isotropic rough surfaces are scrutinized by employing the summit and the radius of the altitude of each asperity [38]. Statistical analysis using probability density functions e.g., Gaussian or log-normal are used to describe each of these geometrical characteristics, where the distributions are redimensioned with the extracted characteristic values of the *roughness* and *waviness* parameters following the so-called *motif* procedure [38,39].

The procedure in determining the motif parameters is described according to ISO 4287 [40]. First, the total surface profile is obtained using a surface characterization instrument. Second, a short-wave cut-off noise filter (λ_s) is applied to the total profile to obtain the primary profile. The roughness profile is then extracted by applying a band-pass filter with the short-wave cut-off wavelength λ_s and the long-wave cut-off wavelength λ_c to the primary profile P [41]. Likewise, a band-pass filter with the short-wave cutoff wavelength λ_c and the long-wave cut-off wavelength λ_f is applied to extract the waviness profile [41]. For proper selection of cut-off lengths, ISO 4287 [40] or ASME B46.1 [42] should be referred. Resulting profiles and motifs are schematically represented in Fig. 9.

A motif stands for a portion of the primary profile between the highest points of two local peaks of the profile, which are not necessarily adjacent [43]. The geometrical characteristics of a motif with the index i are as follows (see Fig. 10):

- H^i is the height difference between the left peak and the deepest

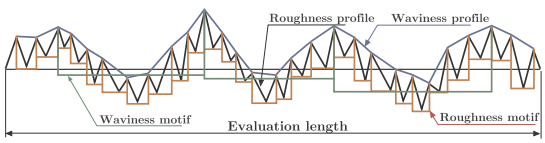

Fig. 9. Schematic drawing of roughness and waviness motifs and extracted profiles from the primary profile [43].

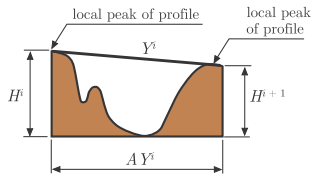

Fig. 10. Length measured parallel to the general direction of the profile [43].

valley;
- H^{i+1} is the height difference between the right peak and the deepest valley;
- Y^i is the mean height (of H^i and H^{i+1}) of the i^{th} motif;
- AY^i is the horizontal distance between the peaks of the i^{th} motif.

The following four conditions give the principal peaks and permit the calculation of roughness parameters of a surface consisting of a number of motifs:

- Y is the average of the height values Y^i of the motifs (i.e., arithmetic mean asperity height);
- AY is the average of the width values AY^i of the motifs;
- SAY is the root mean square of the AY^i of the motifs.

Likewise, waviness parameters W and SW—the mean value and root-mean-square of the height values W^i of the waviness motifs, respectively—are determined following the same procedure using the waviness profile.

Belghith et al. [39] derived micro-geometry characteristics of the sum surface (i.e., an equivalent rough surface and a smooth surface) from each surface in contact. Thus, the parameters of the sum surface results from parameters of each surface with the subscripts 1 and 2 as [39]:

$$Y_{eq} = Y_1 + Y_2, \tag{13a}$$

$$W_{eq} = W_1 + W_2, \tag{13b}$$

$$AY_{eq} = \frac{1}{2}(AY_1 + AY_2), \tag{14a}$$

$$D = 1/AY_{eq}, \tag{14b}$$

$$SAY_{eq} = \sqrt{SAY_1^2 + SAY_2^2}, \tag{15a}$$

$$SW_{eq} = \sqrt{SW_1^2 + SW_2^2}. \tag{15b}$$

Robbe-Valloire [38] revealed the surface characterization parameters of η, β_m and σ such that the density of asperities on a profile D are converted to the surface density of asperities η by using the correlation:

$$\eta = 1.2D^2. \tag{16}$$

The standard deviation of the distribution of the peak heights σ and the mean value of the summit radius β_m—considering two spherically shaped summits—are respectively given by

$$\sigma_p = 0.35\sqrt{W_{eq}^2 + SW_{eq}^2}, \tag{17}$$

$$\beta_m = \frac{AY_{eq}^2 + SAY_{eq}^2}{16Y_{eq}}. \tag{18}$$

To sum up, the motif parameters of the equivalent rough surface are computed using Eqs. (13a) and (15b). The resulting parameters are then substituted in Eqs. (17) and (18). As a remark, β_m and σ of the sum surface could be calculated in an alternative way. Eq. (18) can be employed to calculate β_{m1} and separately by using the Y, AY, and SAY motif parameters of each surface. The resulting β_m is then computed using Eq. (1). A similar procedure is followed for σ, too.

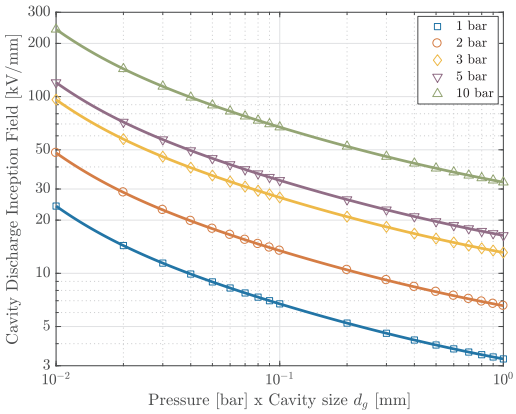

Fig. 11. The Paschen's curve for air under various air pressure. (1 bar = 0.1 MPa.)

As Leach [41] suggested, the arithmetic mean asperity height Y represents an overall measure of the surface texture, and it can be used in identifying different rough surfaces under consideration. Thus, Y or Y_{eq} will be utilized in the first place when a brief comparison is made.

4. Hypothesis

The electric field at which the breakdown strength of the gas in the cavity is exceeded is defined as the cavity inception field strength E_i (i.e., CDIE). Under a homogeneous electric field, the CDIE of an air-filled cavity is characterized by the Paschen's law [7,18]. The portion of the Paschen's curve that covers a cavity size within 10 μm– 1 mm is shown in Fig. 11 for five different air-pressures in the cavity (p_c). The curves suggest a reduced inception field strength as the cavity size increases.

The curves in Fig. 11 are plotted by using the following polynomial fit equation to the empirical data:

$$E_i(p_c, d_g) = A\frac{p_0/p_c}{d_g^2} + B(p_c/p_0) + \frac{C}{d_g} + D\sqrt{\frac{p_c/p_0}{d_g}}, \tag{19}$$

where p_0 = 1 bar, A= 0.00101 kV·mm, B= 2.4 kV/mm, C= −0.0097 kV, D= 2.244 kV·mm$^{-0.5}$ [18].

As can be seen from Fig. 1(b), cavities can either be isolated/trapped or form larger channels by connecting with other cavities. Thus, it is likely that vented channels coexist with isolated cavities. Initially compressed air in the cavities/channels is probably squeezed out due to the openings available at the interface, and the pressure inside the cavities is vented to surroundings and remains around the ambient pressure i.e., $p_c \approx 1$ bar. Previous work [7,44–47] also indicated that the interfacial BDS correlates much better with the CDIE estimated at 1 bar whereas the assumption of increased gas pressure inside the cavities provided highly deviated results from the interface BDS experimental data [55].

The inception field strength of a vented cavity is much lower than that of an interlocked cavity according to Paschen's law. Thereby, in our hypothesis, we propose that vented cavities are the principal governing mechanism in the interfacial breakdown phenomenon. The captured images of interfacial discharge activity also strongly support this assumption [37].

A flashover in a cavity at the interface is analogous to the onset of the interfacial partial discharge (PD) activity [44]. When PD starts, discharge extends from one end of the cavity surface and traverses

through the gas-filled cavity and reaches the other end of the cavity surface. Hence, it only bridges the cavity not the whole insulation between electrodes. Whether discharges in these cavities can cause a complete flashover across the interface or the duration until a PD evolves to a complete flashover is highly stochastic and are not covered here. However, there is voltage and time difference between the CDIE and the BDS since the former is the initial stage (cause) whereas the latter is the ultimate consequence (effect). This is because the process depends on the factors such as availability of a free electron to start the avalanche process, the energy of the electron, the field strength in the cavity accelerating the electrons, and so forth [18]. Thus, we will implement a simple relationship between the estimated CDIE and the measured BDS as follows.

To correlate cavity discharge and interfacial breakdown phenomenon, we hypothesize that experimentally obtained interfacial BDS (i.e., applied field stress by the power source—BDS_{exp}) is linearly proportional to the CDIE:

$$BDS_{exp} = \alpha \cdot CDIE, \tag{20}$$

where α is a numerical coefficient. As a remark, the electric field strength in the air-filled cavities is enhanced by a factor f, depending on the cavity shape since the permittivity of air is less than the permittivity of the bulk material [48,49]. For the defined cavity shape in Section 3.3, $f \approx 1$ [49]. According to the proposed statistical model, discharges take place in the cavities with the size of equal to d_g or greater, and the impact of f is incorporated in α. In the discussion, the strength and limitations of the tribological contact model will be assessed using the computed α values.

5. Experimental procedure

5.1. Sample preparation: cutting and polishing

Samples were taken from a commercial XLPE-insulated 145 kV power cable. Each sample was cut in rectangular prisms with the dimensions of 55 mm x 30 mm x 4 mm where the nominal contact area A_a is 4 mm x 55 mm as shown in Fig. 12. We then polished the contact surfaces of the samples using a tabletop, rotating grinding machine. Four different sandpapers of different grits (#180, #500, #1000, and #2400) were used. The specimens were fixed on a steel rotating disk, and a round-SiC sandpaper of the desired grit was placed on the rotating plane (see Ref. [44]). The speed of the rotating plane was set to 150 rpm, and the force pressing the steel disk towards sandpaper was fixed to 300 N during polishing of all the samples, ensuring that surfaces underwent the same procedure. The speed and the force values were determined based on a number of initial tests [37].

The instrument polished the samples for 2 − 3 minutes with a continuous flow of water to remove any by-products and polymer remnants, and to avoid heating caused by the friction. Subsequently, the samples were rinsed in tap water and were left to dry in air. Dry samples were then cleaned using filtered compressed air before they were washed in isopropanol. Finally, the samples were left to dry again at room temperature.

5.2. Sample characterization

5.2.1. Elastic modulus measurement

The elastic modulus (Young's modulus) of five virgin XLPE samples were measured using Lloyd LR5K gauge under tensile testing that makes use of the initial slope of the obtained stress-strain curve following the ASTM D 790 standard [50]. Next, the effective elastic modulus E' of the mated XLPE-XLPE interface was calculated using Eq. (7).

5.2.2. Surface roughness characterization

A 3D-optical profilometer (Bruker Contour GT-K [51]) was used to characterize the surface topography of the polished surfaces of the samples. 50X magnification was selected with 0.2 μm lateral sampling resolution and 3 nm vertical resolution by following the detailed study performed in Ref. [52]. Scanned surface area was 125 μm × 95 μm. Several scans were performed at different sections to examine variations of surface roughness in the samples.

5.3. High voltage testing

5.3.1. Mechanical test setup

The test set-up with the dimensions of the core components is demonstrated in Fig. 12. There, two samples were positioned on top of each other under dry ambient conditions and were placed between two Rogowski-profile electrodes. The width of the contact surface i.e., interface is 4 mm. Then, the contact pressure was applied before filling the test chamber with synthetic ester (Midel 7131) to avoid the ester from penetrating the interface. The interfacial BDS due to ester penetration was tested in Ref. [7], and the samples assembled in the ester yielded much higher BDSs than dry-mated samples.

5.3.2. Setup for AC breakdown tests

Fig. 13 shows the complete electrical test setup. A 50-Hz variac (0 − 230 V) was used to energize the primary side of a 100 kV transformer, generating AC ramp voltage on the secondary winding at the rate of 1 kV/s. A water resistor was employed to limit the breakdown current. Also, a voltage divider was connected in parallel to measure the applied voltage recorded by a computer via a data acquisition unit.

5.3.3. Test procedure & data handling

The required contact pressure was applied using weights ranging between 11 − 26 kg as illustrated in Fig. 12. The average contact pressure is then calculated using $p_a = F/A_a$, where F is the exerted contact force in N and A_a is the interface area in m^2 (4 mm x 55 mm).

Each set of experiments was composed of eight repeated tests using a virgin pair of samples each time. The obtained results were statistically evaluated using the two-parameter Weibull distribution [18,53].

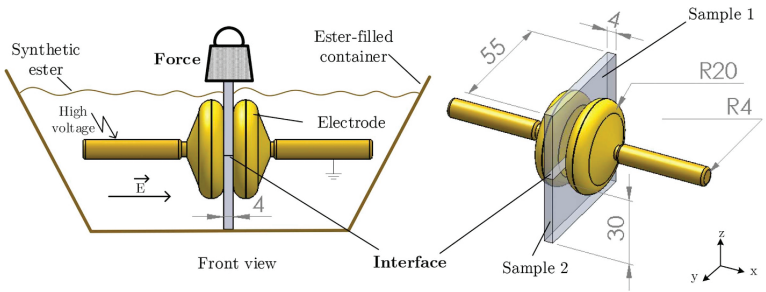

Fig. 12. Simplified sketch of the mechanical test setup. Dimensions are given in mm. Details of the mechanical setup is shown in Refs. [37,44].

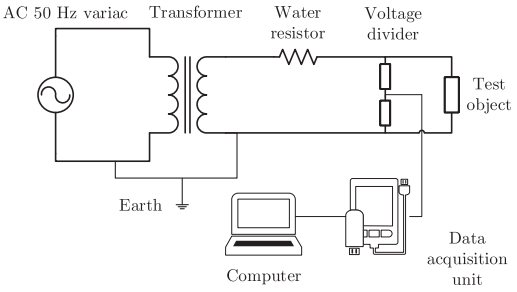

Fig. 13. Sketch of the electrical test setup.

For further evaluation, the nominal value of the Weibull (i.e. 63.2 percentile) with the 90% confidence interval was employed. Goodness-of-fit in each case was tested by following the guidelines in Ref. [53].

6. Results and discussion

6.1. Experimental results

6.1.1. Elastic modulus

Average of five Young's modulus measurements of XLPE samples was calculated to be 200 MPa with the Poisson's ratio 0.46, yielding a resulting effective/composite elastic modulus of 226 MPa for the XLPE-XLPE interface.

6.1.2. Surface characterization

The calculated roughness and waviness motif parameters of the XLPE-XLPE sum surface are shown in Table 1. In addition, Table 2 shows the obtained surface characterization parameters of σ , β_m, and η following the procedure described in Section 3.4. Extracted surface roughness and waviness profiles are also shown in Fig. 14.

6.1.3. AC breakdown tests

Experimental results displaying the influence of the surface roughness on the interfacial BDS under 0.5, 0.86, and 1.16 MPa contact pressures are shown in Fig. 15. 63.2% values are plotted with their 90% confidence intervals (CI); whereas, each curve represents a different roughness degree. As a remark, Y_{eq} in Table 1 stands for the aggregate roughness of the XLPE-XLPE interface accounting for the roughness of the each XLPE surface as depicted in Eq. (13a). The results suggest, in each case, that an increased roughness (i.e., higher Y_{eq}) results in an reduced BDS whereas an increased contact pressure results in an increased BDS as evident in Fig. 15. Table 3 supplies the quantitative data points for Fig. 15.

The 63.2% BDS in the case of the surface polished by #2400 is nearly twice as high as that of in the case of #180 under each contact pressure. As Y_{eq} is reduced by a factor of 36 from #180 to #2400, the BDS increases by a factor ranging in 1.85 − 2.15 at p_a=0.5 − 1.16 MPa. The improvement in the 63.2% BDS from #180 to #500 or from #180 to #1000 is; however, not as notable, only by a factor of 1.2 − 1.3. The change in the BDS from #1000 to #2400 culminates under all pressures

Table 1
Motif parameters of the XLPE-XLPE interface.

Interface	Roughness [μm]			Waviness [μm]	
	Y_{eq}	AY_{eq}	SAY_{eq}	W_{eq}	SW_{eq}
#180	17.79	19.30	13.97	11.39	9.80
#500	5.65	20.61	12.38	5.43	4.87
#1000	1.98	21.47	13.23	1.25	1.08
#2400	0.50	27.59	13.44	0.34	0.35

Table 2
Surface characterization parameters.

Interface	σ_p[μm]	β_m[μm]	η[μm]
#180	5.26	1.94	$3.22{\cdot}10^{15}$
#500	2.55	6.39	$2.83{\cdot}10^{15}$
#1000	0.58	19.91	$2.64{\cdot}10^{15}$
#2400	0.17	118.19	$1.58{\cdot}10^{15}$

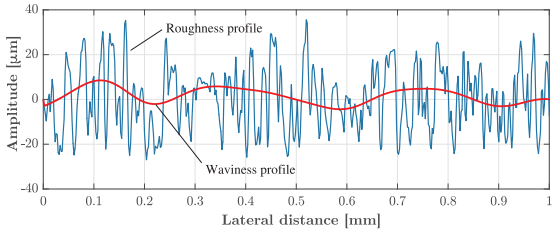

Fig. 14. Obtained roughness and waviness profiles by the optical profilometer. Filters employed with the following cut-off lengths: λ_s = 8 μm, λ_c = 0.08 mm, λ_f = 0.25 mm.

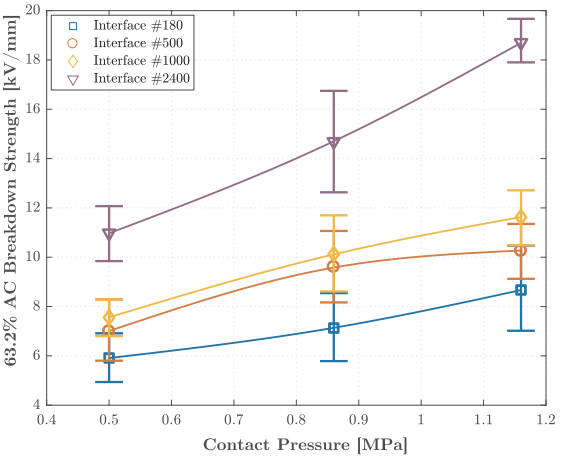

Fig. 15. The experimental BDS data vs. contact pressure. The errorbars stand for the 90% CI; whereas, the markers point the 63.2 percentile.

Table 3
Overview of the experimental results.

XLPE-XLPE Interface	63.2% BDS [kV/mm]		
	0.5 MPa	0.86 MPa	1.16 MPa
#180	5.92	7.13	8.67
#500	6.99	9.61	10.26
#1000	7.56	10.13	11.62
#2400	10.98	14.69	18.70

as evident in Fig. 15, where the highest increase is detected at 1.16 MPa by a factor of 1.6. It can, thus, be claimed that the smoothness of the surface can play as vital a role as the contact pressure in improving the BDS of the interfaces under dry-mated conditions.

As the pressure is raised from 0.5 MPa to 1.16 MPa, the 63.2 percentile BDS becomes 1.4 times as high for #180 (Y_{eq}= 17.79 μm); whereas, it increases by a factor of 1.7 for #2400 (Y_{eq}= 0.50 μm). Thus, the strongest dependence on contact pressure is observed in the case of

Table 4
Parameters calculated using the proposed contact model.

Param.	0.5 MPa			0.86 MPa			1.16 MPa		
Interface	A_{re}/A_a [%]	n [1/mm^2]	d_g [μm]	A_{re}/A_a [%]	n [1/mm^2]	d_g [μm]	A_{re}/A_a [%]	n [1/mm^2]	d_g [μm]
#180	0.41	221	75.6	0.70	357	59.7	0.94	464	52.1
#500	1.06	335	61.3	1.82	540	48.1	2.45	703	42.0
#1000	3.91	1433	29.2	6.73	2309	22.7	9.08	3005	19.6
#2400	17.55	3082	18.5	30.18	4967	13.4	40.71	6464	10.8

the smoothest interface. Eq. (12b) supports the discussion herein such that the increased interfacial pressure creates more isolated cavities and reduces the channels/open sections at the interface, where the biggest change in BDS by a factor of 1.7 was observed in the case of the smoothest surface.

6.2. Correlation between CDIE and BDS

The resulting variables of the contact model—A_{re}, n, and the average cavity size d_g— are tabulated in Table 4. For a complete assessment, the sizes of average cavities are calculated with two-sigma significance (i.e. equivalent to 90% CI [54]) via the standard deviation of the asperity radius σ_p. Thus, an estimated cavity size is represented with its 90% CI by a hatched-region while the markers in Fig. 16 signify the experimentally applied pressure values for reference.

A_{re}/A_a data in Table 4 suggest that the real area of contact increases considerably as the surface roughness decreases. The most significant change in A_{re}/A_a is observed from #1000 to #2400 by a factor of 4.5 under each contact pressure, which accords well with the experimental data shown in Fig. 15. Likewise, the average cavity size decreases by a factor of 4.08 − 4.82 from the roughest interface #180 to the smoothest interface #2400 as the contact pressure p_a is increased from 0.5 MPa to 1.16 MPa. The bottom line is expanded real contact area results in a substantial increase in the number of contact spots n (can be envisaged in Fig. 7 as well) and hence a reduced average cavity size.

Based on the hypothesis in Section 4, the estimated CDIE values are calculated and are plotted in Fig. 17 alongside the experimentally obtained BDS values. Each CDIE data-set is computed by substituting the values (in Fig. 16) into Eq. (19). Also, the CDIE and the experimental BDS data with their corresponding CIs are plotted versus equivalent mean asperity height Y_{eq} in Fig. 18, which additionally incorporates the CIs of the experimental BDS values.

As observed in Fig. 17, the smoother the surface, the stronger the correlation between the cavity inception field CDIE and the experimental BDS data, especially at higher contact pressures. Besides, the CDIE values are lower than the experimental data in the case of rougher surfaces toward higher pressures (see Fig. 17). Likewise, CDIE values tend to deviate from the experimental data in the cases of the two roughest surfaces (#180 and #500) as the pressure is raised from 0.5 MPa to 1.16 MPa. In contrast, an opposite tendency is observed in the case of smoother surfaces (#1000 and #2400). The resulting α coefficients in Eq. (20) are plotted in Fig. 19, where α ranges from 0.8 to 1.05 at 0.5 MPa while it spans 0.98 − 1.3 at 1.16 MPa. As seen, α

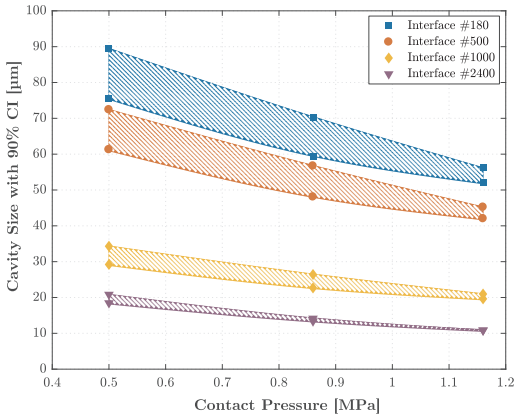

Fig. 16. Calculated cavity size via Eq. (12b) and plotted versus the applied contact pressure.

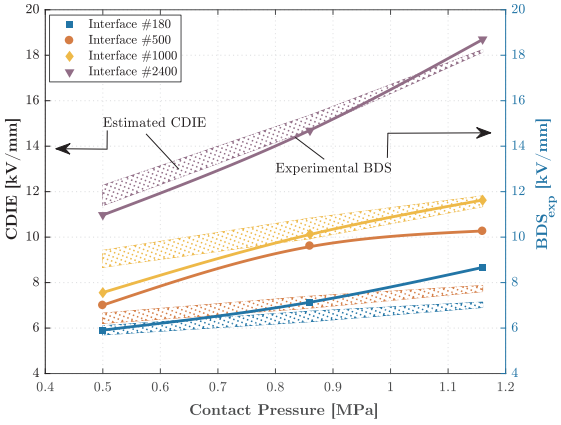

Fig. 17. Experimental BDS data and scaled theoretical CDIE vs. contact pressure. (Solid lines: Experimental data. Hatched-regions: Calculated CDIE via Eqs. (12b), (19) and (20).

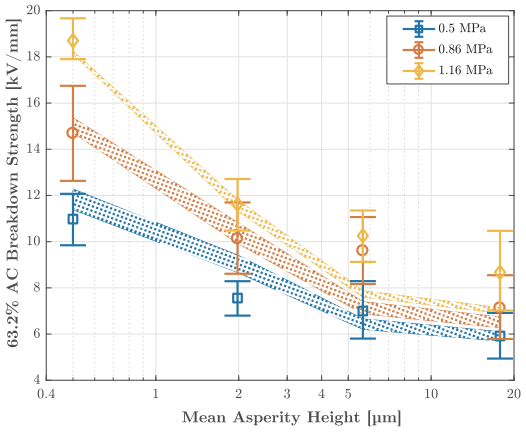

Fig. 18. Experimental BDS and CDIE vs. mean asperity height: (a) 0.5 MPa. (b) 0.86 MPa. (c) 1.16 MPa.

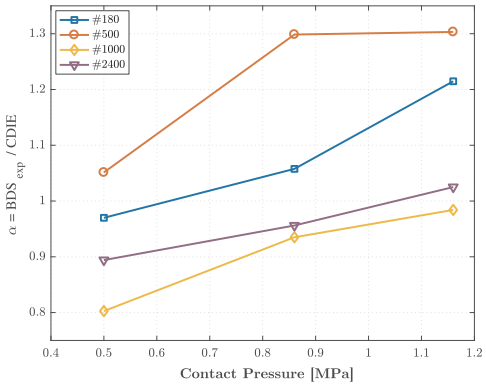

Fig. 19. α vs. contact pressure under four different roughnesses.

digresses from unity by 30% at most toward higher p_a, however when the CIs in Fig. 18 are considered, the range even reduces to 0.86 − 1.05. The strong correlation between the cavity discharge and the interface breakdown suggests that the interfacial breakdown phenomenon is strongly related to the cavity discharges.

Due to normally distributed cavity peaks and heights, there are at least a number of cavities larger than the average-sized cavities, in which the PD activity is likely to start, whereas there is still no PD activity in the average-sized cavities. Thereby, depending on the number and size of such larger cavities, accuracy of the estimated CDIE values might decrease. Consequently, an improved tribological contact model that incorporates the influence of the size and number of the largest cavities can better explain the experimental data. It is also important to underline that the cavity discharge model is developed in two-dimensional plane by considering the length parallel to the applied electric field and the height in the normal direction. However, as can be seen in Fig. 1(b), cavities are likely to form larger vented channels in three-dimensional plane randomly. Thereby, although the cavities are illustrated by being confined between two contact spots in the model, the pressure inside them assumed constant. By further work, the model can be upgraded to cover the entire surface in 3-D for improved accuracy. Furthermore, testing different polymers with different modulus in addition to the analysis performed in this work can improve the model and increase the understanding of the interface breakdown phenomenon. Last but not least, unpublished results in Ref. [37], where the discharge activity is monitored at the interface using a CCD camera setup, suggested that the discharge activity first commences in the larger cavities. Then, when the cavities are completely ionized, discharge extends from one end of the cavity surface and traverses the gas-filled cavity. The interfacial breakdown then follows eventually. The magnitude and phase of the discharges were also measured using a PD measuring unit (Omicron MPD600). These results offer a promising tool to define a more complex correlation between the cavity discharge and the interfacial breakdown strength for future work.

7. Conclusion

A novel contact surface model for solid dielectric materials was proposed, and the results generated by the model (CDIE) were verified and correlated with the experimental data. The calculated average cavity size decreased by a factor of 4.08 − 4.82 from the roughest to the smoothest surface, that in turn yielded increased CDIEs by a factor of 2.01 − 2.56. Likewise, the experimentally obtained BDS values augmented by a factor of 1.4 − 1.7 when the contact pressure was increased from 0.5 MPa to 1.16 MPa. The calculated CDIE was correlated with the experimental BDS using a linear correlation coefficient, which varied between 0.8 − 1.3. Taking the 90% CIs into account has even reduced the range to 0.86 − 1.05. This strong correlation between the cavity discharge and the interface breakdown suggests that the cavity discharge determines the interfacial breakdown phenomenon to a significant extent. To our knowledge, the proposed approach is one of the first models blending tribology and high voltage engineering in the literature. Because of the clear agreement between the model outputs and experimental results, we believe that the model should be studied further.

Acknowledgment

This work is funded by the project "High Voltage Subsea Connections (SUBCONN)." The project is supported by The Research Council of Norway (Grant No. 228344/E30), and by the following industrial partners: ABB AS, Aker Solutions AS, Deutsch Offshore, Chevron Norge AS, Det Norske Oljeselskap ASA, Nexans Norway AS, Shell Technology Norway AS and Statoil Petroleum AS.

References

[1] Kunze D, Parmigiani B, Schroth R, GocNenbach E. Macroscopic internal interfaces in high voltage cable accessories. CIGRE. 2000. p. 15–203.
[2] Fournier D, Lamarre L. Interfacial breakdown phenomena between two epdm surfaces. Proc. 6th int. Conf. Dielectr. Mater. Meas. App. 1994. p. 330–3.
[3] Peschke E, von Olshausen R. Cable systems for high and extra-high voltage: development, manufacture, testing, installation and operation of cables and their accessories. Wiley-VCH; 1999.
[4] Du B, Gu L. Effects of interfacial pressure on tracking failure between XLPE and silicon rubber. IEEE Trans Dielectr Electr Insul 2010;17(6):1922–30.
[5] Du B, Zhu X, Gu L, Liu H. Effect of surface smoothness on tracking mechanism in XLPE-si-rubber interfaces. IEEE Trans Dielectr Electr Insul 2011;18(1):176–81.
[6] Takahashi T, Okamoto T, Ohki Y, Shibata K. Breakdown strength at the interface between epoxy resin and silicone rubber-a basic study for the development of all solid insulation. IEEE Trans Dielectr Electr Insul 2005;12(4):719–24.
[7] Kantar E, Panagiotopoulos D, Ildstad E. Factors influencing the tangential AC breakdown strength of solid-solid interfaces. IEEE Trans Dielectr Electr Insul 2016;23(3):1778–88.
[8] Bhushan B. Principles and applications of tribology. John Wiley & Sons; 2013.
[9] Bhushan B. Analysis of the real area of contact between a polymeric magnetic medium and a rigid surface. J Tribol 1984;106(1):26–34.
[10] Bhushan B. Contact mechanics of rough surfaces in tribology: multiple asperity contact. Tribol Lett 1998;4(1):1–35.
[11] Bhushan B, Tian X. A numerical three-dimensional model for the contact of rough surfaces by variational principle. ASME J. Tribol 1996;118:33–42.
[12] Greenwood J, Williamson J. Contact of nominally flat surfaces. Proc. R. Soc. A, vol. 295. The Royal Society; 1966. p. 300–19.
[13] Williamson J, Pullen J, Hunt R. The shape of solid surfaces. ASME Surf. Mechanics 1969;9:334.
[14] Greenwood J. The area of contact between rough surfaces and flats. J Lubric Tech 1967;89(1):81–7.
[15] Greenwood J, Tripp J. The contact of two nominally flat rough surfaces. Proc. Instit. Mech. Eng 1970;185(1):625–33.
[16] Kantar E, Hvidsten S, Mauseth F, Ildstad E. Tangential AC breakdown strength of solid-solid interfaces considering surface roughness. IEEE conf. Electr. Insul. And dielectr. Phen. (CEIDP), vol. 1. 2017. p. 580–3.
[17] Fournier D. Effect of the surface roughness on interfacial breakdown between two dielectric surfaces. Proc. Conf. IEEE int. Sympos. Elect. Insul, vol. 2. IEEE; 1996. p. 699–702.
[18] Dissado LA, Fothergill JC. Electrical degradation and breakdown in polymers vol. 9. 1992. IET.
[19] CIGRE J. 21/15: interfaces in accessories for extruded hv and ehv cables. Electra 2002;203:53–9.
[20] Borodich FM, Pepelyshev A, Savencu O. Statistical approaches to description of rough engineering surfaces at nano and microscales. Tribol Int 2016;103:197–207.
[21] Almqvist A. On the effects of surface roughness in lubrication PhD. thesis Luleå tekniska universitet; 2006.
[22] Zhuravlev V. On the question of theoretical justification of the Amontons-Coulomb law for friction of unlubricated surfaces. Proc. IMechE Part J 2007;221(8):895–8.
[23] Johnson K. Non-hertzian contact of elastic spheres. In: de Pater AD, Kalker JJ, editors. IUTAM symposium. 1975. p. 26–40.
[24] Greenwood J. Surface modelling in tribology. In: Creasy CFM, Craggs C, editors. App. surf. model. 1990. p. 61–75.
[25] Borodich F. Introduction to Zhuravlev's historical paper: on the question of theoretical justification of the Amontons-Coulomb law for friction of unlubricated surfaces. Proc. IMechE Part J 2007;221(8):893–5.
[26] Archard J. Elastic deformation and the laws of friction. Proc. R. Soc. A, vol. 243. The Royal Society; 1957. p. 190–205.
[27] Borodich F, Onishchenko D. Similarity and fractality in the modelling of roughness by a multilevel profile with hierarchical structure. Int J Solid Struct 1999;36(17):2585–612.

[28] Nayak PR. Random process model of rough surfaces. J Lubric Tech 1971;93(3):398–407. http://dx.doi.org/10.1115/1.3451608.
[29] Whitehouse DJ, Archard J. The properties of random surfaces of significance in their contact. Proc. R. Soc. Lond a, vol. 316. The Royal Society; 1970. p. 97–121.
[30] Ciavarella M, Demelio G, Barber J, Jang YH. Linear elastic contact of the weierstrass profile. Proc. R. Soc. Lond a, vol. 456. The Royal Society; 2000. p. 387–405.
[31] Majumdar A, Bhushan B. Fractal model of elastic-plastic contact between rough surfaces. J Tribol 1991;113(1):1–11.
[32] Whitehouse D. Fractal or fiction. Wear 2001;249(5–6):345–53.
[33] O'Callaghan M, Cameron M. Static contact under load between nominally flat surfaces in which deformation is purely elastic. Wear 1976;36(1):79–97.
[34] Francis H. Application of spherical indentation mechanics to reversible and irreversible contact between rough surfaces. Wear 1977;45(2):221–69.
[35] Midttveit S, Monsen B, Frydenlund S, Stenevik K, et al. SS on implications of subsea processing power distribution-subsea power systems—a key enabler for subsea processing. Offshore technol. Conf., Offshore technol. Conf. 2010.
[36] Greenwood JA, Tripp JH. The elastic contact of rough spheres. J Appl Mech 1967;34(1):153–9.
[37] Kantar E. Characterization of longitudinal AC electric breakdown strength of solid dielectric interfaces PhD. thesis Norwegian University of Science and Technology; 2018.
[38] Robbe-Valloire F. Statistical analysis of asperities on a rough surface. Wear 2001;249(5):401–8.
[39] Belghith S, Mezlini S, BelhadjSalah H, Ligier J-L. Modeling of contact between rough surfaces using homogenisation technique. Compt Rendus Mec 2010;338(1):48–61.
[40] Geometrical product specifications (GPS)–Surface texture: profile method–terms, definitions and surface texture parameters. ISO; 2000.
[41] Leach R. Characterisation of areal surface texture. Springer; 2013.
[42] ANSI. Surface texture (surface roughness, waviness, and lay) B46. The American Society Mechanical Eng.; 1985. p. 1.
[43] TOKYO SEIMISU, Surface texture contour measuring instruments, http://www.inspectionengineering.com/Images/SurfaceFinishExplain.pdf.
[44] Kantar E, Hvidsten S, Mauseth F, Ildstad E. Longitudinal AC breakdown voltage of XLPE-XLPE interfaces considering surface roughness and pressure. IEEE Trans Dielectr Electr Insul 2017;24(5):3047–54.
[45] Kantar E, Mauseth F, Ildstad E. Interfacial breakdown between dielectric surfaces determined by gas discharge. IEEE conf. Electr. Insul. And dielectr. Phen. (CEIDP), vol. 1. 2017. p. 556–9.
[46] Kantar E, Ildstad E. Modeling longitudinal breakdown strength of solid-solid interfaces using contact theory. 2016 IEEE int. Conf. On dielec. (ICD), vol. 1. 2016. p. 398–401.
[47] Kantar E, Hvidsten S, Ildstad E. Examination of longitudinal AC breakdown strength of dielectric surfaces as a function of elastic modulus. Proc. Nordic insul. Sympos 2017;25(1):1–5. http://dx.doi.org/10.5324/nordis.v0i25.2360.
[48] Illias HA. Measurement and simulation of partial discharges within a spherical cavity in a solid dielectric material PhD. thesis 2011.
[49] Crichton GC, Karlsson PW, Pedersen A. Partial discharges in ellipsoidal and spheroidal voids. IEEE Trans Electr Insul 1989;24(2):335–42.
[50] ASTM D20.10. Standard test methods for flexural properties of unreinforced and reinforced plastics and electrical insulating materials D790–17. 2007.
[51] Bruker, ContourGT-K 3D optical microscope, https://www.bruker.com/products/surface-and-dimensional -analysis/3d-optical-microscopes/contourgt-k/overview.html.
[52] Poon CY, Bhushan B. Comparison of surface roughness measurements by stylus profiler, AFM and non-contact optical profiler. Wear 1995;190(1):76–88.
[53] IEC/IEEE guide for the statistical analysis of electrical insulation breakdown data (adoption of ieee std 930-2004). 2007. p. 1–53. IEC 62539 First Edition 2007-07 IEEE 930.
[54] Leon-Garcia A. Probability, statistics, and random processes for electrical engineering. Pearson Education; 2017.
[55] Hasheminezhad M, Ildstad E. Application of contact analysis on evaluation of breakdown strength and pd inception field strength of solid-solid interfaces. IEEE Trans. Dielectr. Electr. Insul. 2012;19(1):1–7.

Paper V

E. Kantar, S. Hvidsten, and, E. Ildstad, "Effect of Material Elasticity on the Longitudinal AC Breakdown Strength of Solid-Solid Interfaces," *IEEE Transactions on Dielectrics and Electrical Insulation*, vol. 26, no. 2, pp. 655–663, Apr. 2019.

References

[1] S. Midttveit, B. Monsen, S. Frydenlund, K. Stenevik *et al.*, "SS on implications of subsea processing power distribution-subsea power systems-a key enabler for subsea processing," in *Conf. Offshore Tech.*, 2010.

[2] P. Weiss, S. Beurthey, Y. Chardard, J. Dhedin, T. Andre, K. Rabushka, C. Tourcher, F. Gauch, and C. Micoli, "Novel wet-mate connectors for high voltage and power transmissions of ocean renewable energy systems," in *Proc. 4th Int. Conf. Ocean Energy*, 2012.

[3] I. Østergaard, A. Nysveen, and T. Romanisko, "MECON: A High Voltage Subsea Connector." Conf. Offshore Tech., Jan. 1999. [Online]. Available: https://www.onepetro.org/conference-paper/OTC-10948-MS

[4] J. T. Myklatun, "Condition monitoring of subsea connectors," Master's thesis, Norwegian University of Science and Technology, 2014.

[5] D. Kunze, B. Parmigiani, R. Schroth, and E. Gockenbach, "Macroscopic internal interfaces in high voltage cable accessories," in *CIGRE Session*, 2000, pp. 15–203.

[6] E. Peschke and R. von Olshausen, *Cable systems for high and extra-high voltage: development, manufacture, testing, installation and operation of cables and their accessories.* Wiley-VCH, 1999.

[7] T. Takahashi, T. Okamoto, Y. Ohki, and K. Shibata, "Breakdown strength at the interface between epoxy resin and silicone rubber-a basic study for the development of all solid insulation," *IEEE Trans. Dielectr. Electr. Insul.*, vol. 12, no. 4, pp. 719–724, 2005.

[8] D. Fournier, C. Dang, and L. Paquin, "Interfacial breakdown in cable joints," in *Proc. IEEE Int. Electr. Insul. Symp.*, 1994, pp. 450–452.

[9] D. Fournier and L. Lamarre, "Interfacial breakdown phenomena between two EPDM surfaces," in *Proc. 6th Int. Conf. Dielectr. Materials, Meas. App.*, 1994, pp. 330–333.

[10] C. Dang and D. Fournier, "Dielectric performance of interfaces in premolded cable joints," *IEEE Tran. Power Delivery*, vol. 12, no. 1, pp. 29–32, 1997.

[11] D. Fournier, "Effect of the surface roughness on interfacial breakdown between two dielectric surfaces," in *IEEE Int. Symp. Electr. Insul.*, vol. 2. IEEE, 1996, pp. 699–702.

[12] B. Du and L. Gu, "Effects of interfacial pressure on tracking failure between XLPE and silicon rubber," *IEEE Trans. Dielectr. Electr. Insul.*, vol. 17, no. 6, 2010.

[13] B. Du, X. Zhu, L. Gu, and H. Liu, "Effect of surface smoothness on tracking mechanism in XLPE-Si-rubber interfaces," *IEEE Trans. Dielectr. Electr. Insul.*, vol. 18, no. 1, pp. 176–181, 2011.

[14] L. A. Dissado and J. C. Fothergill, *Electrical degradation and breakdown in polymers*. IET, 1992, vol. 9.

[15] E. Ildstad, *TET 4160 Insulating Materials for High Voltage Applications*. Department of Electric Power Engineering, Norwegian University of Science and Technology, 2015.

[16] B. Bhushan, "Contact mechanics of rough surfaces in tribology: multiple asperity contact," *Tribology Letters*, vol. 4, no. 1, pp. 1–35, 1998.

[17] S. Alam, Y. V. Serdyuk, and S. M. Gubanski, "Effect of interfaces on surface potential decay on double layered HTV silicone rubber samples," in *IEEE Int. Conf. on Dielec. (ICD)*, vol. 1, Jul. 2016, pp. 309–312.

[18] J. Andersson, S. M. Gubanski, and H. Hillborg, "Properties of interfaces in silicone rubber," *IEEE Trans. Dielectr. Electr. Insul.*, vol. 14, no. 1, pp. 137–145, Feb. 2007.

[19] J. Andersson, S. M. Gubanski, and H. Hillborg, "Properties of interfaces between silicone rubber and epoxy," *IEEE Trans. Dielectr. Electr. Insul.*, vol. 15, no. 5, pp. 1360–1367, Oct. 2008.

[20] D. Fournier and L. Lamarre, "Effect of pressure and length on interfacial breakdown between two dielectric surfaces," in *IEEE Int. Symp. Electr. Insul.*, 2005, pp. 270–272.

[21] D. Fournier and L. Lamarre, "Effect of pressure and temperature on interfacial breakdown between two dielectric surfaces," in *IEEE Conf. Electr. Insul. Dielectr. Phen.* IEEE, 1992, pp. 229–235.

[22] B. Du, L. Gu, X. Zhang, and X. Zhu, "Fundamental research on dielectric breakdown between XLPE and silicon rubber interface in HV cable joint," in *IEEE 9th Int. Conf. Prop. Appl. Dielectr. Mat. (ICPADM)*. IEEE, 2009, pp. 97–100.

[23] F. H. Kreuger, *Partial discharge detection in high-voltage equipment*. Butterworths London, 1989.

[24] X. Chen, Y. Xu, X. Cao, and S. M. Gubanski, "Electrical treeing behavior at high temperature in XLPE cable insulation samples," *IEEE Trans. Dielectr. Electr. Insul.*, vol. 22, no. 5, pp. 2841–2851, 2015.

[25] X. Xu, T. Bengtsson, J. Blennow, and S. M. Gubanski, "On excess current during and after partial discharge activity," in *IEEE Conf. Electr. Insul. and Dielectr. Phen. (CEIDP)*, Oct. 2014, pp. 27–30.

[26] T. Hammarstrom, T. Bengtsson, J. Blennow, and S. M. Gubanski, "Evidence for changing PD properties at short voltage rise times," *IEEE Trans. Dielectr. Electr. Insul.*, vol. 18, no. 5, pp. 1686–1692, Oct. 2011.

[27] T. J. Å. Hammarström, T. Bengtsson, and S. M. Gubanski, "Partial discharge characteristics of electrical treeing in XLPE insulation exposed to voltages of different rise times," in *Int. Symp. Electr. Insul. Mat. (ISEIM)*, vol. 1, Sep. 2017, pp. 407–410.

[28] S. M. Gubanski, "Insulating materials for next generations of HVAC and HVDC cables," in *IEEE Int. Conf. High Voltage Eng. App. (ICHVE)*, Sep. 2016, pp. 1–6.

[29] E. M. Jarvid, A. B. Johansson, J. H. M. Blennow, M. R. Andersson, and S. M. Gubanski, "Evaluation of the performance of several object types for electrical treeing experiments," *IEEE Trans. Dielectr. Electr. Insul.*, vol. 20, no. 5, pp. 1712–1719, Oct. 2013.

[30] A. B. Johansson, "Characterising resistance to electrical treeing in new XLPE-based materials for high-voltage cables," Ph.D. dissertation, Chalmers University of Technology, 2015.

[31] G. Chen and C. Tham, "Electrical treeing characteristics in XLPE power cable insulation in frequency range between 20 and 500 Hz," *IEEE Trans. Dielectr. Electr. Insul.*, vol. 16, no. 1, pp. 179–188, 2009.

[32] M. Akyuz, L. Gao, V. Cooray, T. G. Gustavsson, S. M. Gubanski, and A. Larsson, "Positive streamer discharges along insulating surfaces," *IEEE Trans. Dielectr. Electr. Insul.*, vol. 8, no. 6, pp. 902–910, Dec. 2001.

[33] Y. V. Serdyuk, S. M. Gubanski, J. Blennow, and M. Sjoberg, "Electrical discharge in an air gap with dielectric-covered electrodes," in *IEEE Conf. Electr. Insul. and Dielectr. Phen. (CEIDP)*, vol. 1, Oct. 2000, pp. 397–400 vol.1.

[34] M. L. Sjoberg, H. J. M. Blennow, S. M. Gubanski, and M. A. S. Leijon, "On discharge phenomena in a covered electrode system in air," in *IEEE Conf. Electr. Insul. and Dielectr. Phen. (CEIDP))*, Apr. 2000, pp. 345–348.

[35] A. Bulinski, S. Bamji, E. So, G. C. Montanari, A. Motori, and S. Gubanski, "Diagnostic measurements of high voltage polymeric cable insulation," in *Proc. Int. Symp. Electr. Insul. Mat.*, Sep. 1995, pp. 19–26.

[36] S. M. Hasheminezhad, "Tangential electric breakdown strength and PD inception voltage of solid-solid interface," Ph.D. dissertation, Norwegian University of Science and Technology, 2016.

[37] A. Almqvist, "On the effects of surface roughness in lubrication," Ph.D. dissertation, Luleå tekniska universitet, 2006.

[38] Siemens. Spectron. [Online]. Available: https://www.energy.siemens.com/co-/pool/hq/industries-utilities/oil-gas/applications/subsea/downloads/ SpecTRON-brochure.pdf

[39] A. Nysveen *et al.*, "Coupling-and switch system for subsea electrical power distribution," U.S. Patent 5 834 721, 1998.

[40] P. Argaut, J. Becker, P. M. Dejean, S. Sin, and E. Dorison, "Studies and development in France of 400 kV cross-linked polyethylene cable systems," in *CIGRE Session*, 2000, pp. 15–203.

[41] G. Bogoeva-Gaceva, D. Dimeski, and V. Srebrenkoska, "Friction mechanism of polymers and their composites," *Maced. J. Chem. Chem. Eng.*, vol. 37, no. 1, pp. 1–11, 2018.

[42] B. Bhushan and X. Tian, "A numerical three-dimensional model for the contact of rough surfaces by variational principle," *ASME J. Tribol*, vol. 118, pp. 33–42, 1996.

[43] X. Chen, L. Gu, X. He, and H. Liao, "Tracking failure process of XLPE–Silicone rubber interface under impulse voltage," in *IEEE Int. Conf. High Voltage Eng. App. (ICHVE)*. IEEE, 2012, pp. 51–54.

[44] L. Gu and X. He, "Microcavity on tracking failure of XLPE-SiR interface," in *Asia-Pacific Power Energy Eng. Conf. (APPEEC)*. IEEE, 2012, pp. 1–4.

[45] M. Hasheminezhad and E. Ildstad, "Application of contact analysis on evaluation of breakdown strength and PD inception field strength of solid-solid interfaces," *IEEE Trans. Dielectr. Electr. Insul.*, vol. 19, no. 1, pp. 1–7, 2012.

[46] M. Hasheminezhad and E. Ildstad, "Partial discharge inception of interface voids versus mechanical surface pressure," in *IEEE Int. Conf. High Voltage Eng. App. (ICHVE)*, Oct 2010, pp. 397–400.

[47] S. M. Hasheminezhad, E. Ildstad, and A. Nysveen, "Breakdown strength of solid-solid interface," in *10th Int. Conf. Solid Dielectr. (ICSD)*, July 2010, pp. 1–4.

[48] S. M. Hasheminezhad, "Breakdown strength of solid | solid interfaces," in *Trondheim PowerTech*. IEEE, 2011, pp. 1–7.

[49] M. Hasheminezhad and E. Ildstad, "Breakdown strength of solid-solid interfaces," *Proc. Nordic Insul. Symp. (NORD-IS)*, June 2011.

[50] H. A. Illias, "Measurement and simulation of partial discharges within a spherical cavity in a solid dielectric material," Ph.D. dissertation, University of Southampton, 2011.

[51] H. Illias, G. Chen, and P. L. Lewin, "Modeling of partial discharge activity in spherical cavities within a dielectric material," *IEEE Electr. Insul. Mag.*, vol. 27, no. 1, pp. 38–45, Jan. 2011.

[52] H. Illias, T. S. Yuan, H. Mokhlis, G. Chen, P. L. Lewin *et al.*, "Partial discharge patterns in high voltage insulation," in *IEEE Int. Conf. Power and Energy (PECon)*. IEEE, 2012, pp. 750–755.

[53] D. Adhikari, D. M. Hepburn, and B. G. Stewart, "PD characteristics and degradation in PET insulation with vented and unvented internal voids," *Electr. Power Systems Research*, vol. 100, pp. 65–72, Jul. 2013.

[54] D. Adhikari, D. M. Hepburn, and B. G. Stewart, "Analysis of partial discharge characteristics in artificially created voids," in *45th In. Uni. Power Eng. Conf. (UPEC)*, Aug. 2010, pp. 1–4.

[55] A. A. Mas'ud and B. G. Stewart, "An investigative study on the influence of correlation of PD statistical features on PD pattern recognition," in *IEEE 2nd Int. Conf. Dielectr. (ICD)*, Jul. 2018, pp. 1–5.

[56] F. P. Mohamed, W. H. Siew, B. Sheng, and B. Stewart, "Effect of voltage reduction in minimising partial discharge activity in cables — Experimental study," in *IEEE Conf. Electr. Insul. and Dielectr. Phen. (CEIDP)*, Oct. 2017, pp. 331–334.

[57] D. Adhikari, D. M. Hepburn, and B. G. Stewart, "Comparison of partial discharge characteristics and degradation in several polymeric insulators," *IET Science, Meas. Tech.*, vol. 6, no. 6, pp. 474–484, Nov. 2012.

[58] A. J. Reid, D. M. Hepbum, and B. G. Stewart, "The influence of external magnetic fields on the partial discharge characteristics of voids," in *IEEE Electr. Insul. Conf. (EIC)*, Jun. 2013, pp. 147–150.

[59] S. Albayrak, C. Becker-Willinger, M. Aslan, and M. Veith, "Influence of nano-scaled zirconia particles on the electrical properties of polymer insulating materials," *IEEE Trans. Dielectr. Electr. Insul.*, vol. 19, no. 1, pp. 76–82, Feb. 2012.

[60] M. Roy, J. K. Nelson, R. K. MacCrone, L. S. Schadler, C. W. Reed, and R. Keefe, "Polymer nanocomposite dielectrics-the role of the interface," *IEEE Trans. Dielectr. Electr. Insul.*, vol. 12, no. 4, pp. 629–643, Aug. 2005.

[61] H. Z. Ding and B. R. Varlow, "Effect of nano-fillers on electrical treeing in epoxy resin subjected to AC voltage," in *17th IEEE Lasers Electro-Optics Soc., (LEOS)*, 2004, pp. 332–335.

[62] R. Huuva, V. Englund, S. M. Gubanski, and T. Hjertberg, "A versatile method to study electrical treeing in polymeric materials," *IEEE Trans. Dielectr. Electr. Insul.*, vol. 16, no. 1, pp. 171–178, Feb. 2009.

[63] J. C. Fothergill, "Filamentary electromechanical breakdown," *IEEE Trans. Electr. Insul.*, vol. 26, no. 6, pp. 1124–1129, 1991.

[64] R. M. Eichhorn, "Treeing in solid extruded electrical insulation," *IEEE Trans. Electr.Insul.*, vol. EI-12, no. 1, pp. 2–18, 1977.

[65] J. H. Mason, "Assessing the resistance of polymers to electrical treeing," *IEE Proc. A: Phys. Sci. Meas. Instrum. Manage. Edu. Reviews*, vol. 128, no. 3, pp. 193–201, 1981.

[66] Y. Gao, Y. Yuan, L. Chen, J. Li, S. Huang, and B. Du, "Direct fluorination induced variation in interface discharge behavior between polypropylene and silicone rubber under AC voltage," *IEEE Access*, vol. 6, pp. 23 907–23 917, 2018.

[67] E. Kantar, S. Hvidsten, F. Mauseth, and E. Ildstad, "Longitudinal AC breakdown voltage of XLPE-XLPE interfaces considering surface roughness and pressure," *IEEE Trans. Dielectr. Electr. Insul.*, vol. 24, no. 5, 2017.

[68] E. Kantar, S. Hvidsten, F. Mauseth, and E. Ildstad, "On the tangential AC breakdown strength of polymeric interfaces considering elastic modulus," in *IEEE Conf. Electr. Insul. and Dielectr. Phen. (CEIDP)*, 2017, pp. 816–819.

[69] P. A. Roseen, S. M. Gubanski, and U. W. Gedde, "External PD resistance of thermoplastic and XLPE containing voltage stabilizers," *IEEE Trans. Dielectr. Electr. Insul.*, vol. 5, no. 2, pp. 189–194, Apr. 1998.

[70] X. Chen, D. Murdany, D. Liu, M. Andersson, S. M. Gubanski, U. W. Gedde, and Suwarno, "AC and DC pre-stressed electrical trees in LDPE and its aluminum oxide nanocomposites," *IEEE Trans. Dielectr. Electr. Insul.*, vol. 23, no. 3, pp. 1506–1514, Jun. 2016.

[71] X. Chen, Y. Xu, X. Cao, and S. M. Gubanski, "On the conducting and non-conducting electrical trees in XLPE cable insulation specimens," *IEEE Trans. Dielectr. Electr. Insul.*, vol. 23, no. 1, pp. 95–103, Feb. 2016.

[72] Y. Zheng, Y. V. Serdyuk, and S. M. Gubanski, "Space charge controlled electric field preceding inception of electric tree in XLPE at AC voltage," in *IEEE 11th Int. Conf. Prop. Appl. Dielectr. Mat. (ICPADM)*, Jul. 2015, pp. 132–135.

[73] X. R. Chen, L. B. Hu, Y. Xu, X. L. Cao, and S. M. Gubanski, "Investigation of temperature effect on electrical trees in XLPE cable insulation," in *IEEE Conf. Electr. Insul. and Dielectr. Phen. (CEIDP)*, Oct. 2012, pp. 612–615.

[74] M. Jarvid, A. Johansson, V. Englund, S. Gubanski, and M. R. Andersson, "Electrical tree inhibition by voltage stabilizers," in *IEEE Conf. Electr. Insul. and Dielectr. Phen. (CEIDP)*, Oct. 2012, pp. 605–608.

[75] B. Sonerud, J. Blennow, S. M. Gubanski, S. Nilsson, and T. Bengtsson, "Continuous monitoring of dielectric properties of LDPE samples during electrical treeing," in *10th IEEE Int. Conf. Solid Dielectr.*, Jul. 2010, pp. 1–4.

[76] P. A. Roseen, T. Reitberger, S. M. Gubanski, and U. W. Gedde, "PD resistance of thermally aged polyethylene and carbonyl-containing model polymers," *IEEE Trans. Dielectr. Electr. Insul.*, vol. 6, no. 2, pp. 191–201, Apr. 1999.

[77] F. M. Borodich, A. Pepelyshev, and O. Savencu, "Statistical approaches to description of rough engineering surfaces at nano and microscales," *Tribol. Int.*, vol. 103, pp. 197–207, 2016.

[78] J. Archard, "Elastic deformation and the laws of friction," in *Proc. R. Soc. A*, vol. 243, no. 1233. The Royal Society, 1957, pp. 190–205.

[79] F. Borodich and D. Onishchenko, "Similarity and fractality in the modelling of roughness by a multilevel profile with hierarchical structure," *Int. J. Solids and Structures*, vol. 36, no. 17, pp. 2585–2612, 1999.

[80] P. R. Nayak, "Random process model of rough surfaces," *J. of Lubrication Tech.*, vol. 93, no. 3, pp. 398–407, 1971.

[81] D. J. Whitehouse and J. Archard, "The properties of random surfaces of significance in their contact," in *Proc. R. Soc. Lond A.*, vol. 316, no. 1524. The Royal Society, 1970, pp. 97–121.

[82] M. Ciavarella, G. Demelio, J. Barber, and Y. H. Jang, "Linear elastic contact of the weierstrass profile," in *Proc. R. Soc. Lond A.*, vol. 456, no. 1994. The Royal Society, 2000, pp. 387–405.

[83] A. Majumdar and B. Bhushan, "Fractal model of elastic-plastic contact between rough surfaces," *J. Tribology*, vol. 113, no. 1, pp. 1–11, 1991.

[84] D. Whitehouse, "Fractal or fiction," *Wear*, vol. 249, no. 5–6, pp. 345–353, 2001.

[85] V. Zhuravlev, "On the question of theoretical justification of the Amontons-Coulomb law for friction of unlubricated surfaces," *Proc. IMechE Part J.*, vol. 221, no. 8, pp. 895–898, 2007.

[86] K. Johnson, "Non-hertzian contact of elastic spheres," *IUTAM Symp. (Eds. A.D. de Pater and J.J. Kalker)*, pp. 26–40, 1975.

[87] J. Greenwood, "Surface modelling in tribology," *App. surf. model. (Eds C. F. M. Creasy and C. Craggs)*, pp. 61–75, 1990.

[88] J. Greenwood and J. Williamson, "Contact of nominally flat surfaces," in *Proc. Royal Soc. London A: Math., Phys. Eng. Sci.*, vol. 295, no. 1442. The Royal Society, 1966, pp. 300–319.

[89] F. Borodich, "Introduction to Zhuravlev's historical paper: On the question of theoretical justification of the Amontons-Coulomb law for friction of unlubricated surfaces," *Proc. IMechE Part J.*, vol. 221, no. 8, pp. 893–895, 2007.

[90] B. Zhu, Z. Jia, H. Hu, X. Ouyang, and X. Wang, "Relationship between the Interfacial DC Breakdown Voltage and the Morphology of the XLPE/SiR Interface," *IEEE Trans. Dielectr. Electr. Insul.*, vol. 26, 2019.

[91] B. Bhushan, *Principles App. Tribology.* John Wiley & Sons, 2013.

[92] B. Bhushan, "Analysis of the real area of contact between a polymeric magnetic medium and a rigid surface," *J. Tribology*, vol. 106, no. 1, pp. 26–34, 1984.

[93] J. Williamson, J. Pullen, and R. Hunt, "The shape of solid surfaces," *Surface Mechanics, ASME*, vol. 9, p. 334, 1969.

[94] J. Greenwood, "The area of contact between rough surfaces and flats," *J. Lubrication Tech.*, vol. 89, no. 1, pp. 81–87, 1967.

[95] J. Greenwood and J. Tripp, "The contact of two nominally flat rough surfaces," *Proc. Instit. Mech. Eng.*, vol. 185, no. 1, pp. 625–633, 1970.

[96] M. O'Callaghan and M. Cameron, "Static contact under load between nominally flat surfaces in which deformation is purely elastic," *Wear*, vol. 36, no. 1, pp. 79–97, 1976.

[97] H. Francis, "Application of spherical indentation mechanics to reversible and irreversible contact between rough surfaces," *Wear*, vol. 45, no. 2, pp. 221–269, 1977.

[98] J. A. Greenwood and J. H. Tripp, "The elastic contact of rough spheres," *J. Appl. Mechanics*, vol. 34, no. 1, pp. 153–159, 1967.

[99] G. C. Crichton, P. W. Karlsson, and A. Pedersen, "Partial discharges in ellipsoidal and spheroidal voids," *IEEE Trans. Dielectr. Electr. Insul.*, vol. 24, no. 2, pp. 335–342, Apr. 1989.

[100] F. Robbe-Valloire, "Statistical analysis of asperities on a rough surface," *Wear*, vol. 249, no. 5, pp. 401–408, 2001.

[101] S. Belghith, S. Mezlini, H. BelhadjSalah, and J.-L. Ligier, "Modeling of contact between rough surfaces using homogenisation technique," *Comptes Rendus Mécanique*, vol. 338, no. 1, pp. 48–61, 2010.

[102] ANSI, *Surface Texture (Surface Roughness, Waviness, and Lay). B46. 1.* The American Society Mech. Eng., 1985.

[103] ISO 25178-2, *Geometrical Product Specifications (GPS)–Surface Texture: Areal–Part 2: Terms, Definitions and Surface Texture Parameters.* Int. Org. for Standard., 2012.

[104] ISO 12085, *Geometrical Product Specifications (GPS)–Surface Texture: Profile Method–Motif parameters.* Int. Org. for Standard., 1996.

[105] ISO 4287, *Geometrical Product Specifications (GPS) – Surface Texture: Profile Method–Terms, Definitions and Surface Texture Parameters.* Int. Org. for Standard., 2000.

[106] R. Leach, *Characterisation of areal surface texture.* Springer, 2013.

[107] TOKYO SEIMISU. Surface texture contour measuring instruments. [Online]. Available: http://inspectionengineering.com/wp-content/uploads/2018/03/SurfaceFinishExplain.pdf

[108] J. Archard, "Surface topography and tribology," *Tribology*, vol. 7, no. 5, pp. 213–220, 1974.

[109] K. J. Stout, *The Development of Methods for the Characterisation of Roughness in Three Dimensions.* Penton Press, 2000.

[110] ANSI, *Surface Texture Symbols. Y14.36.* The American Society Mech. Eng., 1996.

[111] R. Leach, *Fundamental Principles of Engineering Nanometrology.* Elsevier, 2009.

[112] L. Blunt and X. Jiang, *Advanced Techniques for Assessment Surface Topography.* Elsevier, 2003.

[113] E. Kantar, D. Panagiotopoulos, and E. Ildstad, "Factors influencing the tangential AC breakdown strength of solid-solid interfaces," *IEEE Trans. Dielectr. Electr. Insul.*, vol. 23, no. 3, pp. 1778–1788, 2016.

[114] J. Kuffel and P. Kuffel, *High voltage engineering fundamentals.* Elsevier, 2000.

[115] F. Kreuger, *Industrial high voltage: electric fields, dielectrics, constructions.* Delft University Press, Delft, The Netherlands, 1991.

[116] L. Niemeyer, "A generalized approach to partial discharge modeling," *IEEE Trans. Dielectr. Electr. Insul.*, vol. 2, no. 4, pp. 510–528, 1995.

[117] F. Gutfleisch and L. Niemeyer, "Measurement and simulation of PD in epoxy voids," *IEEE Trans. Dielectr. Electr. Insul.*, vol. 2, no. 5, pp. 729–743, 1995.

[118] R. Schifani, R. Candela, and P. Romano, "On PD mechanisms at high temperature in voids included in an epoxy resin," *IEEE Trans. Dielectr. Electr. Insul.*, vol. 8, no. 4, pp. 589–597, 2001.

[119] A. Cavallini, R. Ciani, M. Conti, P. Morshuis, and G. Montanari, "Modeling memory phenomena for partial discharge processes in insulation cavities," in *Conf. Electr. Insul. Dielectr. Phen.* IEEE, 2003, pp. 723–727.

[120] *ELASTOSIL LR 3003/60 A/B Data Sheet*, Wacker Chemie AG, Munich, Germany.

[121] J. Chan, M. Hartley, and L. Hiivala, "Performance characteristics of XLPE versus EPR as insulation for high voltage cables," *IEEE Electr. Insul. Mag.*, vol. 9, no. 3, pp. 8–12, 1993.

[122] *Casting Resin XB 5950 Hardener XB 5951 APG Data Sheet*, Huntsman Int. LLC, The Woodlands, Texas.

[123] *PI-VESTAKEEP-4000G-EN Data Sheet*, Evonik Industries AG, Essen, Germany.

[124] Crystran. Silica Glass (SiO_2). [Online]. Available: https://www.crystran.co.uk/optical-materials/silica-glass-sio2

[125] Products of M & I Materials Ltd. MIDEL 7131 Synthetic Ester. [Online]. Available: https://www.midel.com/productsmidel/midel-7131

[126] F. Kreuger, *Industrial high voltage: co-ordinating, measuring, testing.* Delft University Press, Delft, The Netherlands, 1992.

[127] IEC 62539 First Edition 2007-07 IEEE 930, "IEC/IEEE Guide for the Statistical Analysis of Electrical Insulation Breakdown Data (Adoption of IEEE Std 930-2004)," pp. 1–53, 2007.

[128] S. A. Boggs, "Partial discharge. II. Detection sensitivity," *IEEE Electr. Insul. Mag.*, vol. 6, no. 5, pp. 35–42, 1990.

[129] M. Soto Martinez, "Electrical treeing in insulation materials for high voltage AC subsea connectors under high hydrostatic pressures," Master's thesis, NTNU, 2017.

[130] PCE Instruments. Force Gauge PCE-FB Series. [Online]. Available: https://www.pce-instruments.com/english/slot/2/download/378303/man-force-gauge-pce-fb-series-en1078867.pdf

[131] OPT–The Telescope Authority. CCD Cameras. [Online]. Available: https://optcorp.com/collections/ccd-cameras?limit=all&order=name&page=6

[132] A. C. D20.10, "Standard test methods for flexural properties of unreinforced and reinforced plastics and electrical insulating materials D790–17." American Society for Testing Materials, 2007.

[133] Bruker. ContourGT-K 3D Optical Microscope. [Online]. Available: https://www.bruker.com/products/surface-and-dimensional-analysis/3d-optical-microscopes/contourgt-k/overview.html

[134] BIO-RAD Microscience Division. E5100 Series II 'Cool' Sputter Coater. [Online]. Available: https://www.quorumtech.com/assets/pdf/Manuals/E5100-manual.pdf

[135] KEYENCE Corporation. VHX-500FE Digital Microscope. [Online]. Available: https://www.keyence.com/products/microscope/digital-microscope/vhx-500f/models/vhx-500fe/index.jsp

[136] D. Askeland, P. Fulay, and W. Wright, *The Science and Engineering of Materials, 6th Edition*. Nelson Education, 2011, pp. 211–213.

[137] M. Song and Z. Jia, "Calculation and simulation of mechanical pressure of XLPE-SR surface in cable joints," in *Proc. 12th Int. Conf. Properties and App. of Dielectr. Materials (ICPADM)*, May 2018, pp. 1001–1005.

[138] T. Sun, Y. Zhang, X. Guo, and Y. Xu, "Partial discharge behavior of 220 kV prefabricated cable termination induced by inadequate interface pressure," in *Proc. 12th Int. Conf. Properties and App. of Dielectr. Materials (ICPADM)*, May 2018, pp. 381–384.

[139] B. X. Du, Z. L. Ma, X. X. Cheng, and Y. Liu, "Hydrophobicity evaluation of silicone rubber insulator using PD-induced electromagnetic wave," *IEEE Trans. Dielectr. Electr. Insul.*, vol. 19, no. 3, pp. 1060–1067, Jun. 2012.

[140] J. Fuhr, "Procedure for identification and localization of dangerous PD sources in power transformers," *IEEE Trans. Dielectr. Electr. Insul.*, vol. 12, no. 5, pp. 1005–1014, 2005.

[141] L. A. Dissado, "Understanding electrical trees in solids: from experiment to theory," *IEEE Trans. Dielectr. Electr. Insul.*, vol. 9, no. 4, pp. 483–497, 2002.

[142] A. Leon-Garcia, *Probability, Statistics, and Random Processes for Electrical Engineering*. Pearson Education, 2017.

[143] J. Li, B. X. Du, X. X. Kong, and Z. L. Li, "Nonlinear conductivity and interface charge behaviors between LDPE and EPDM/SiC composite for HVDC cable accessory," *IEEE Trans. Dielectr. Electr. Insul.*, vol. 24, no. 3, pp. 1566–1573, Jun. 2017.

[144] J. Li, B. X. Du, and H. Xu, "Suppressing interface charge between LDPE and EPDM for HVDC cable accessory insulation," *IEEE Trans. Dielectr. Electr. Insul.*, vol. 24, no. 3, pp. 1331–1339, 2017.

[145] B. X. Du, J. S. Xue, and M. M. Zhang, "Effect of pulse duration on electrical tree and breakdown process of epoxy resin in LN2," *IEEE Trans. Dielectr. Electr. Insul.*, vol. 24, no. 1, pp. 359–366, Feb. 2017.

[146] B. X. Du and J. Li, "Surface charge coupling behavior of fluorinated polyimide film under DC and pulse voltage," *IEEE Trans. Dielectr. Electr. Insul.*, vol. 24, no. 1, pp. 567–573, Feb. 2017.

[147] B. X. Du, W. B. Zhu, J. G. Zhang, and X. L. Li, "Surface and interface charge accumulation and decay of oil-paper insulation under DC voltage," *IEEE Trans. Dielectr. Electr. Insul.*, vol. 24, no. 2, pp. 939–946, Apr. 2017.

[148] B. X. Du and J. Li, "Interface charge behaviors between LDPE and EPDM filled with carbon black nanoparticles," *IEEE Trans. Dielectr. Electr. Insul.*, vol. 23, no. 6, pp. 3696–3703, 2016.

[149] A. Majumdar and B. Bhushan, "Role of fractal geometry in roughness characterization and contact mechanics of surfaces," *J. Tribology*, vol. 112, no. 2, pp. 205–216, 1990.

[150] S. Ganti and B. Bhushan, "Generalized fractal analysis and its applications to engineering surfaces," *Wear*, vol. 180, no. 1-2, pp. 17–34, 1995.

[151] B. Bhushan, *Handbook of micro/nano tribology*. CRC press, 1998.

[152] E. Kantar, F. Mauseth, and E. Ildstad, "Interfacial breakdown between dielectric surfaces determined by gas discharge," in *IEEE Conf. Electr. Insul. and Dielectr. Phen. (CEIDP)*, 2017, pp. 556–559.

[153] I. V. Timoshkin, R. A. Fouracre, M. J. Given, S. J. MacGregor, P. Mason, and R. Clephan, "Dielectric Properties of Diala D, MIDEL 7131 and THESO Insulating Liquids," in *IEEE Conf. Electr. Insul. and Dielectr. Phen. (CEIDP)*, Oct. 2008, pp. 622–625.

[154] A. Haddad and D. Warne, *Advances in High Voltage Engineering*. IET Digital Library, 2004.

[155] I. Dottore, "Wireless Detection of PD Patterns: Applications in Smart Grids and Modern Power Systems," Ph.D. dissertation, Università degli Studi di Palermo, 2018.

[156] M. Nagao, T. Kitamura, Y. Mizuno, M. Kosaki, and M. Ieda, "Localized heat generation before dielectric breakdown of polyethylene films," in *3rd Int. Conf. Conduction Breakdown Solid Dielectr.*, 1989.

[157] COMSOL, Inc. COMSOL Multiphysics Reference Manual, version 5.4. [Online]. Available: https://www.comsol.com

[158] D. Panagiotopoulos, "AC Electrical Breakdown Strength of Solid Solid Interfaces: A study about the effect of elasticity, pressure and interface conditions," M.Sc. thesis, TU Delft, Elect. Sustainable Energy Dept., 2015.

[159] Design and Technology Online. Young's Modulus. [Online]. Available: http://wiki.dtonline.org/index.php/Youngs-Modulus

[160] O. A. Hammerøy, "DC tangential electric breakdown strength of silicone rubber interfaces under dry, wet and oily conditions," Master's thesis, NTNU, 2016.

[161] C. Y. Poon and B. Bhushan, "Comparison of surface roughness measurements by stylus profiler, AFM and non-contact optical profiler," *Wear*, vol. 190, no. 1, pp. 76–88, 1995.

[162] H. C. Thode, *Testing for normality*. CRC press, 2002, vol. 164.

[163] MathWorks. File Exchange. [Online]. Available: https://se.mathworks.com/matlabcentral/fileexchange

[164] E. L. Crow and K. Shimizu, *Lognormal distributions*. Marcel Dekker New York, 1987.

[165] E. Husain and R. S. Nema, "Analysis of Paschen Curves for air, N2 and SF6 Using the Townsend Breakdown Equation," *IEEE Trans. on Electr. Insul.*, vol. EI-17, no. 4, pp. 350–353, Aug 1982.